Development of a 1-D oxygen isotope photochemical model and its application to atmospheric O_2

Bethan Sarah Gregory

A thesis submitted for the degree of PhD
at the
University of St Andrews

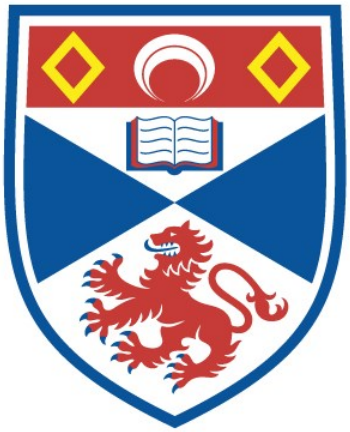

2021

Candidate's declaration

I, Bethan Sarah Gregory, do hereby certify that this thesis, submitted for the degree of PhD, which is approximately 60,000 words in length, has been written by me, and that it is the record of work carried out by me, or principally by myself in collaboration with others as acknowledged, and that it has not been submitted in any previous application for any degree. I confirm that any appendices included in my thesis contain only material permitted by the 'Assessment of Postgraduate Research Students' policy.

I was admitted as a research student at the University of St Andrews in September 2016.

I received funding from an organisation or institution and have acknowledged the funder(s) in the full text of my thesis.

Date 20/05/2021 Signature of candidate

Supervisor's declaration

I hereby certify that the candidate has fulfilled the conditions of the Resolution and Regulations appropriate for the degree of PhD in the University of St Andrews and that the candidate is qualified to submit this thesis in application for that degree. I confirm that any appendices included in the thesis contain only material permitted by the 'Assessment of Postgraduate Research Students' policy.

Date 20/5/21 Signature of supervisor

Permission for publication

In submitting this thesis to the University of St Andrews we understand that we are giving permission for it to be made available for use in accordance with the regulations of the University Library for the time being in force, subject to any copyright vested in the work not being affected thereby. We also understand, unless exempt by an award of an embargo as requested below, that the title and the abstract will be published, and that a copy of the work may be made and supplied to any bona fide library or research worker, that this thesis will be electronically accessible for personal or research use and that the library has the right to migrate this thesis into new electronic forms as required to ensure continued access to the thesis.

I, Bethan Sarah Gregory, confirm that my thesis does not contain any third-party material that requires copyright clearance.

The following is an agreed request by candidate and supervisor regarding the publication of this thesis:

Printed copy

No embargo on print copy.

Electronic copy

Embargo on all of electronic copy for a period of 1 year on the following ground(s):

- Publication would preclude future publication

Supporting statement for electronic embargo request

I would like to publish papers from the work in my thesis before the information is made available to the public.

Title and Abstract

- I agree to the title and abstract being published.

Date 20/05/21 Signature of candidate

Date 20/5/21 Signature of supervisor

Underpinning Research Data or Digital Outputs

Candidate's declaration

I, Bethan Sarah Gregory, understand that by declaring that I have original research data or digital outputs, I should make every effort in meeting the University's and research funders' requirements on the deposit and sharing of research data or research digital outputs.

Date 20/05/2021 Signature of candidate

Permission for publication of underpinning research data or digital outputs

We understand that for any original research data or digital outputs which are deposited, we are giving permission for them to be made available for use in accordance with the requirements of the University and research funders, for the time being in force.

We also understand that the title and the description will be published, and that the underpinning research data or digital outputs will be electronically accessible for use in accordance with the license specified at the point of deposit, unless exempt by award of an embargo as requested below.

The following is an agreed request by candidate and supervisor regarding the publication of underpinning research data or digital outputs:

Embargo on all of electronic files for a period of 1 year on the following ground(s):

- Publication would preclude future publication

Supporting statement for embargo request

I would like to publish papers from the data before the information is made available to the public.

Date 20/05/2021 Signature of candidate

Date 20/5/21 Signature of supervisor

Abstract

Oxygen is the second most abundant gas in the Earth's atmosphere, but this has not always been the case. A suite of geochemical, palaeobiological, and geological proxies have been presented over the last few decades to better constrain the evolution of pO_2 over the history of our planet, but uncertainty remains. Here, we use numerical modelling with the 1-D photochemical model *Atmos*, firstly by exploring the boundary conditions of the model, and secondly by developing it to predict $\Delta^{17}O$ values – a fairly novel proxy for Proterozoic and Phanerozoic pO_2. Our study of boundary conditions highlights the importance of choosing and describing boundary conditions carefully, as our flux-driven models produce somewhat different results to previous fixed mixing ratio-driven models. Our results provide a potential constraint on pO_2, suggesting that atmospheres with $6\times10^{-7} < pO_2 < 2\times10^{-3}$ may have been unlikely to exist for long periods of Earth history. We review these conclusions using our newly-developed oxygen isotope model, tuned to predict modern atmospheric $\Delta^{17}O$. Preliminary results predict the production and preservation of non-zero $\Delta^{17}O$ in the geological record can occur for palaeo-atmospheres with $pO_2 > 10^{-4}$, but even the minimum values observed at 1.4 Ga and 635 Ma do not require such low concentrations, especially if pCO_2 is higher than modern. The development of the oxygen isotope model allows the better prediction of $\Delta^{17}O$ under various atmospheric conditions, and will be a useful tool in the interpretation of anomalous oxygen isotope compositions in the geological record.

Acknowledgements

I am so grateful to the many people who have supported me throughout my time in St Andrews while working on this thesis. Particular thanks go to Dr Mark Claire, who I am incredibly thankful to have had as a primary supervisor. This acknowledgements page could never really do justice to how much he has done for me over the last few years. I am so glad he chose to take on someone convinced she wanted to do a PhD involving numerical modelling, but actually knowing basically nothing about what that meant, and invested so much time into encouragement, help and training. Not only did this allow the production of this work, but it gave me a deeper appreciation of a careful and objective scientific approach, and excitement to find out what's going on on this 'pale blue dot.' Thank you also for rescuing me with a broom from a bog in the driest place on Earth (and for taking me to the Atacama in the first place). Huge thanks also go to my supervisor Dr Sarah Rugheimer, whose encouragement and advice has been so constructive during my postgraduate years. I am grateful to have her as a mentor and an inspiring role model for women in science. In particular, her efforts and challenges were instrumental in taking me from a nervous, weak public speaker to someone voluntarily performing a stand-up comedy routine about my research…twice.

Many thanks also go to the Geobiology, Centre for Exoplanet Sciences, and Mass-Independent Fractionation in Atmospheres (MIFIA) research groups, which have broadened my horizons of scientific research, and helped me to understand how this work might fit into that. From the latter, I am particularly grateful to Dr Aubrey Zerkle, Dr Matthew Warke, Dr Fernando Gázquez-Sánchez and Dr Sonny Harman, for great discussions about MIF and the model, and for their interest in and support of this work. I am also indebted to Dr Claire Cousins and Dr Tim Raub for their support and advice as part of my postgraduate review panel.

My experience of studying at St Andrews over the last four years would not have been the same without the support of all at the School of Earth and Environmental Sciences, for creating an encouraging and friendly atmosphere in which to work. I couldn't have wished for better office mates, who have motivated and helped me in this project, as well as being wonderful friends. I am particularly thankful for Arola, Eloise and Natalya and their friendship, the opportunity to produce this thesis alongside them, and their patience in sitting through many iterations of my practice conference talks. We have had a great time, both in and out of the office (and further afield!), and I hope that the adventures continue!

Constant encouragement has come from many other friends, including my housemates who survived being locked down with both my thesis and I. Constant support and friendship has also come from the church family at St Andrews Free Church, who welcomed me so warmly and have reminded me that I have every spiritual blessing in Christ. I am very grateful to all of my family, including my sister Cerys, and want to thank my wonderful parents, Jenny and Peter Gregory, in particular, for their continual love and support. They have worked so hard over the last twenty-seven years to look after and guide me, as well as giving me every opportunity to learn and enjoy learning.

Finally, I am thankful to God for making the world we live in so interesting, and for giving me the opportunity to study it for four years. I am grateful that "The earth is the LORD's, and everything in it," and that the One who made the intricacies of different oxygen isotopes, as well as the vast expanses of the Universe, loves and cares for me.

Funding

This project was funded by the European Research Council (ERC) grant awarded to Mark Claire, under the European Union's Horizon 2020 Research and Innovation programme (grant agreement No. 678812), without which my studies would not have been possible.

Research data

Research data underpinning this thesis are available at:
https://doi.org/10.1016/j.epsl.2021.116818,
http://dx.doi.org/10.17632/pd659h3fmd.1 and
https://doi.org/10.17630/ee60d0c4-b1e0-4cc9-b4a5-10d90c2e1d8b.

Contents

List of Figures

List of Tables

Chapter 1

Introduction & Literature Review

The composition of the Earth's modern atmosphere is well-understood, but it has not always been the same. Over the last 4.5 billion years, the atmosphere and life have co-evolved to produce the world we see today.

The study of past atmospheres is of interest for several reasons. Firstly, an understanding of how the atmosphere has developed over Earth history can contribute to an understanding of the chemistry and dynamics of the modern atmosphere. Though only a thin layer of gas compared to the rest of the planet, the atmosphere greatly influences conditions on the surface and is constantly changing. Topically, anthropogenic CO_2 released to the atmosphere is having huge effects on the climate, with far-reaching implications for sea-level, ocean circulation, meteorology and ecology. The geological record shows that swings in the partial pressure of CO_2 (pCO_2) have occurred in the Earth's past, so a study of how the Earth's atmosphere has changed and how that has affected surface conditions gives insight as we seek to predict and solve global problems today. For example, a better understanding of how the atmosphere works and has done in the past can feed important global circulation models used to predict modern changes.

Secondly, the evolution of life may have been closely linked to the evolution of the atmosphere, and in particular, the increase in molecular oxygen (O_2) levels. For example, a question under much debate pertains to the relationship between the rise of oxygen at the Great Oxidation Event (GOE) and the development of oxygenic photosynthesis as a metabolism (Fischer et al., 2016; Lyons et al., 2014). The evolution of macroscopic organisms and resulting Cambrian explosion may be

related to a second potential step-increase in atmospheric O_2 towards modern levels of 21%, but it is debated whether the evolution of these organisms was enabled by the increase in oxygen, or a causal mechanism, if there is any link at all (Cole et al., 2020; Erwin et al., 2011; Lyons et al., 2014). Throughout the Phanerozoic, rises in oxygen seem to roughly coincide with advances in evolution. For example, increases in pO_2 (the partial pressure of molecular oxygen) are coeval to the development of land plants during the Palaeozoic (e.g. Dahl et al., 2010; Dahl and Arens, 2020; Krause et al., 2018; Lenton et al., 2016). Therefore, an understanding of atmospheric composition in the past can help to unravel some of the intricacies of the co-evolution of life and the atmosphere.

Thirdly, we are in an age of rapidly advancing space exploration. At the time of writing, more than 4000 exoplanets (planets outside our own Solar System) have been found and confirmed within more than 3000 planetary systems in the last ~30 years (NASA Exoplanet Exploration, 2020). Over the course of the composition of this thesis, more than 828 new worlds have been discovered. These exoplanets range from water worlds, to rocky or gas planets, ranging in size and temperature, and with different orbital positions in relation to their parent stars. Some, such as TRAPPIST-1e, appear to be similar to the Earth in size and bulk density, as well as being in the apparent habitable zone of the parent star (Gillon et al., 2017). Over the next few years, telescopes such as NASA's James Webb Space Telescope (JWST) and ESA's Characterising Exoplanet Satellite (CHEOPS), along with ground-based telescopes will allow for an increased discovery of exoplanets and characterisation of atmospheres through, e.g. spectroscopy of transiting planets, whereby the absorption of certain wavelengths of starlight as the planet moves in front of the star indicates the constituents of the atmosphere (e.g. Charbonneau et al., 2007). The relationship between oxygen, ozone and methane levels is significant, as the simultaneous occurrence of large amounts of oxygen (and/or related ozone) and a reducing gas such as CH_4 or N_2O is considered a potential biosignature (Hitchcock and Lovelock, 1967; Lederberg, 1965; Lovelock, 1965), although caution is required due to possible false positives (e.g. Domagal-Goldman et al., 2014). Developed discernment of the way in which atmospheric constituents relate, as well as the way

Earth's atmosphere and life have co-evolved have the potential to contribute to an improved understanding of these unknown planets and their potential for life, either now or in the future.

In this thesis therefore, my aim is to contribute towards a clearer picture of how the atmosphere has evolved over the Earth's history, with a particular interest in pO_2 and some consideration of pCO_2. More specifically, I use a 1-D photochemical model, *Atmos*, as a tool to provide sharper constraints. The ultimate goal is the development of a triple oxygen isotope photochemical model, to aid the interpretation of anomalous oxygen isotope ratios measured in the geological record.

The remainder of this introduction is an appraisal of existing literature focussing firstly on the current understanding of oxygen (and secondarily, carbon dioxide) levels in the atmosphere over Earth history, highlighting some of the areas of uncertainty attracting the most debate and discussing some existing proxies. I also describe the relationship between O_2 and ozone. Secondly, I introduce anomalous triple oxygen isotope ratios (denoted by $\Delta^{17}O$), and explain how this proxy has been used to better understand processes in the atmosphere in the modern and the past. Thirdly, I outline the structure of this thesis and how it seeks to address questions of atmospheric evolution.

1.1 – Oxygen in the atmosphere over Earth history

Today, oxygen makes up 21% of the modern atmosphere, but oxygen levels over Earth history have not been constant (see reviews by Canfield, 2005; Catling and Claire, 2005; Catling and Kasting, 2017; Farquhar et al., 2014; Kump, 2008; Lyons et al., 2014). Figure 1-1 shows the current understanding of atmospheric oxygen evolution (Kump, 2008; Lyons et al., 2014). The summary from Kump's (2008) review, shown by grey boxes, demonstrates three different sets of broad constraints for the Archaean, the Proterozoic and most of the Phanerozoic, and highlights the large uncertainty, especially in the Earth's middle ages.

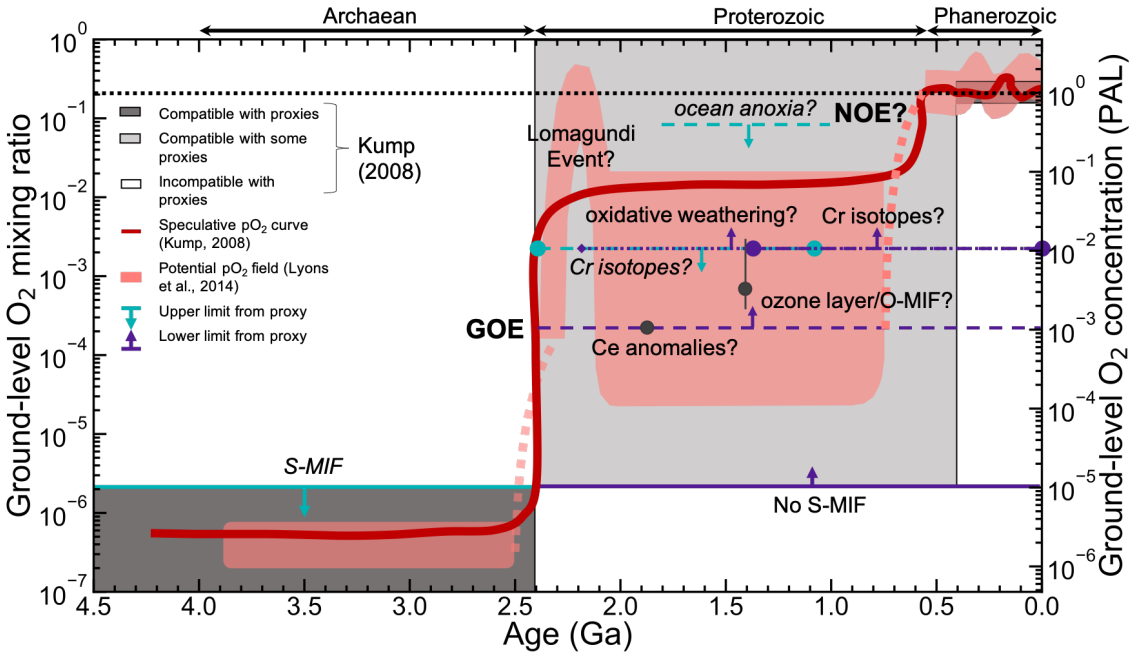

Figure 1-1: The current understanding of oxygen levels over Earth history. Grey boxes and dark red line are from Kump (2008). Pink areas show constraints from Lyons et al. (2014). Purple lines and arrows show lower limits from existing proxies. Teal lines and arrows with annotations in italics show upper limits from existing proxies. Length of lines corresponds to intervals in Earth history for which the proxy constrains pO_2. Solid lines are for constraints from S-MIF, since this is a widely-accepted limit (Bekker et al., 2004; Farquhar et al., 2000). Coloured dashed or dotted lines are for pO_2 suggested by proxies for which there is some disagreement (Canfield et al., 2018, Crockford et al. 2019; Gilleaudeau et al., 2016; Planavsky et al., 2014; 2018; 2020). Purple and teal circles for the Cr isotope proxy are shown for clarity, indicating only the ends of the lines. Grey circles show estimates of pO_2 for 1.87 Ga (Bellefroid et al., 2018) and 1.4 Ga (Planavsky et al., 2020). The dotted line shows present atmospheric levels (1 PAL) of O_2.

One of the main features of Earth history in Figure 1-1 is that oxygen levels have increased from low levels since the Archaean. Arguments for the 'Great Oxidation Event' (GOE) at the end of the Archaean have been present for several decades, with original evidence primarily constituting increased oxidation of minerals. For example, Archaean riverine sediments have been shown to include reduced heavy minerals such as pyrite, uraninite and siderite (e.g. Holland, 1962; Rasmussen and Buick, 1999), indicative of a lack of free atmospheric oxygen, since these would otherwise have become oxidised during erosion and transport. Also, after the GOE, there was a replacement of ubiquitous Banded Iron Formations with sandstones rich in oxidised iron minerals such as haematite ('red beds'), indicating the increased oxidation of soluble, mobile ferrous iron to insoluble ferric iron, with a rise in free atmospheric oxygen (Cloud, 1968; Klein, 2005). The higher solubility of

reduced rather than oxidised forms of iron (Fe) and cerium (Ce) also means that low concentrations of these elements in Archaean palaeosols have been used as evidence for low pO_2 (e.g. Murakami et al., 2011; Utsunomiya et al., 2003;).

Such proxies indicating a distinct change in concentration of atmospheric O_2 at the GOE were greatly supported by measurements of multiple sulphur isotope ratios (Bekker et al., 2004; Farquhar et al., 2000). Mass-independent fractionation of sulphur isotopes (S-MIF), specifically the deviation of $\delta^{33}S$ and $\delta^{36}S$ from mass-dependent fractionation predicted from $\delta^{34}S$, was observed in pyrites and barites in the geological record from before ~2.45 Ga, but disappeared in younger rocks (see blue points in Figure 1-2). Tight constraints on the timing of the disappearance of S-MIF have recently been published as between 2.501 and 2.434 Ga (Warke et al., 2020b). In 2002, Pavlov and Kasting used a 1-D photochemical model (a distant precursor to the models we will describe and develop in Chapters 2-6) including sulphur isotopes to suggest that the disappearance of the S-MIF signal at this time could be accounted for by an increase in atmospheric oxygen from some mixing ratio[1] less than 2.1×10^{-6} to mixing ratios higher than this threshold. It was recognised that the preservation of S-MIF in the geological record is significantly more likely when sulphur exits the atmosphere via several divergent exit channels, which occurs only when oxygen concentrations are low (Claire et al., 2014; Pavlov and Kasting, 2002). At higher O_2, the S_8 exit channel does not occur, and most atmospheric sulphur is oxidised to sulphate, so the S-MIF signal is homogenised and negative and positive S-MIF signals cancel out. In addition, higher atmospheric oxygen levels result in sufficient ozone concentrations to absorb UV radiation which

[1] In this thesis, we predominantly describe O_2 concentrations in terms of 'mixing ratio,' where the mixing ratio is a unitless measure equal to the number of molecules of the species (e.g. O_2) divided by the total number of molecules, within a certain volume. An alternative description, and one occasionally implemented in this thesis is O_2 concentration in units of present atmospheric levels (PAL), which is equal to the mixing ratio divided by the mixing ratio of O_2 in the modern atmosphere (0.21, or 1 PAL).

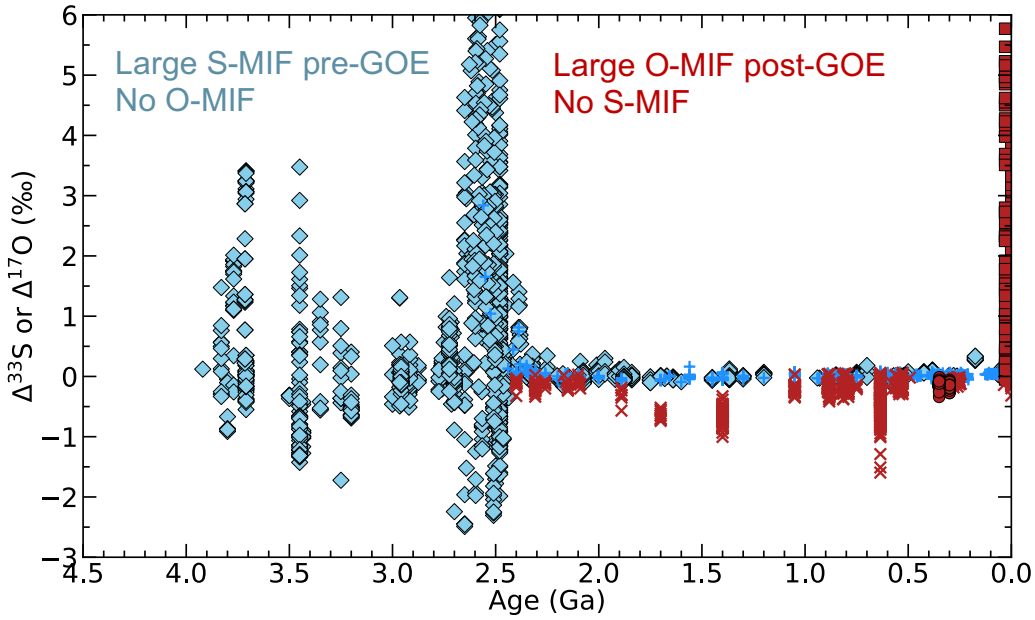

Figure 1-2: S-MIF ($\Delta^{33}S$; blue diamonds and '+' symbols) and oxygen isotope mass-independent fractionation (O-MIF, $\Delta^{17}O$; red crosses, circles, and squares) data from the geological record plotted against age throughout Earth history, adapted from Bao (2015). Large S-MIF and no O-MIF before ~2.45 Ga indicate low pO_2. Non-zero O-MIF and no S-MIF since ~2.45 Ga indicate O_2 mixing ratios greater than 2.1×10^{-6}. S-MIF data shown by blue '+' symbols and O-MIF data shown by red crosses was compiled by Crockford et al. *(2019). S-MIF data shown by blue diamonds and O-MIF data shown by red squares was compiled by Bao (2015). O-MIF data shown by red circles is from Warke* et al. *(2020a) and Pettigrew* et al. *(2020).*

is thought to otherwise cause mass-independent separation of sulphur isotopes in the first place (Danielache et al., 2008).

While the disappearance of non-zero S-MIF in Proterozoic sediments is considered strong evidence for a GOE in which oxygen levels increased to exceed 2.1×10^{-6}, the cause or causes of the GOE remain under debate. However, an oxic atmosphere requires the sources of oxygen to outweigh the sinks, which include reducing gases such as H_2, CH_4 and H_2S (e.g. Catling and Claire, 2005; Claire et al., 2006). Therefore, the development of oxygenic photosynthesis, either before or concurrent to the GOE, increased burial of organic matter (e.g. Karhu and Holland, 1996), hydrogen escape to space (Zahnle et al., 2013) and a decrease in reducing gases, specifically methane (Zahnle et al., 2006) have been proposed as potential contributing factors.

The large regions marked 'compatible with some proxies' in Kump's (2008) summary (pale grey shading on Figure 1-1) show that significant uncertainty remains for the Proterozoic (~2.45 Ga – 542 Ma). The lack of S-MIF in Proterozoic sediments indicates oxygen mixing ratios over 2.1×10^{-6}, as mentioned, but there is a lack of other such compelling evidence to reduce uncertainty further. Various proxies, including chromium isotope ratios, palaeosol proxies and oxygen isotope ratios have been used to further constrain oxygen levels during this interval, as explained below, but uncertainty remains. For most of the Phanerozoic (542 Ma – present), oxygen mixing ratios are thought to have been fairly high (> ~10%), in the wake of either a 'Neoproterozoic Oxygenation Event' (NOE; Och and Shields-Zhou, 2012; Shields-Zhou and Och, 2011) or a more-recently proposed 'Neoproterozoic Oxygenation Window' followed by a 'Palaeozoic Oxygenation Event' (Krause et al., 2018; Lenton et al., 2018; Tostevin and Mills, 2020).

Thus, the Earth's atmosphere has been transformed from one with trace amounts of free molecular oxygen, to one in which it is its second greatest constituent (after N_2, which makes up around 78%). In this thesis, I am particularly concerned with constraining oxygen levels since the GOE, with an aim towards reducing uncertainty evident from Figure 1-1. In the next two subsections, I discuss in further detail the existing evidence that has been used to put constraints on oxygen levels in the Proterozoic and Phanerozoic.

1.1.1 – Proterozoic oxygen levels

The red shading in Figure 1-1 shows the oxygen levels over Earth history as summarised by Lyons et al. (2014). For the Proterozoic, this review shows a little more detail, and contests the traditional assumption that oxygen variation over Earth history has been purely unidirectional. In particular, the proposed large increase in oxygen levels just after the GOE, followed by a decrease within ~200 Myr is known as the Lomagundi Event. Subsequently, Lyons et al. (2014) extend their constraints on the lower limit of pO_2 after the Lomagundi Event to values more than an order of magnitude smaller than the traditional lower limit of 2.1×10^{-3}. Here, I

discuss the different proxies proposed to give insight as to oxygen levels during the Proterozoic.

1.1.1.1 – Lomagundi carbon isotope excursion

A large carbon isotope excursion in carbonates has been proposed to indicate a rapid increase to temporarily high pO_2 between 2.22 Ga and 2.06 Ga (Karhu, 1993; Karhu and Holland, 1996). The high $\delta^{13}C$ values suggest increased organic carbon burial, which could have been an increased source of O_2 to the atmosphere. Further evidence includes high carbonate-associated sulphate concentrations and relatively small variations in $\delta^{34}S$ in such sulphates (Planavsky et al., 2012; Schröder et al., 2008). Evaporites have also recently been shown to indicate seawater sulphate concentrations of more than 10 ppm at ~ 2 Ga (Blättler et al., 2018). These features indicate increased oxidation of sulphur as opposed to burial of reduced sulphur as pyrite. Minerals with increased phosphate concentrations (phosphates) increased in occurrence during this period, indicative of an increase in oxidative weathering and a potential cause of increased biological production of O_2 (Lepland et al., 2013; Papineau, 2010). In geological time, this excursion was short, and decreased fluxes of phosphate from weathering have been proposed as a cause of a decline in productivity resulting in a return to lower O_2 concentrations (Bekker and Holland, 2012).

However, uncertainty remains for this period of Earth history. Concurrent low and high $\delta^{13}C$ in the same sedimentary sequence, calculations of the huge and potentially unrealistic quantity of organic carbon required to be buried to produce the excursion, facies-associated changes in $\delta^{13}C$, and basinal-scale explanations of sulphur isotope measurements have led others to suggest that the carbon isotope excursion may represent regional rather than global Earth system changes (Bakakas-Mayika et al., 2020; Frauenstein et al., 2009; Paiste et al, 2020).

1.1.1.2 – The remainder of the Proterozoic

Traditionally, pO_2 during the Proterozoic is thought to have been between 1% and 40% PAL (corresponding to mixing ratios between 2.1×10^{-3} and 8.4×10^{-2}). The lower limit came from evidence supporting the occurrence of oxidative weathering for the duration of the Proterozoic (Holland, 1994; Rye and Holland, 1998), and the upper limit from evidence for some anoxia in oceans within this time period (Canfield, 1998; 2005). For example, low $\delta^{98/95}$Mo values have indicated deep ocean euxinia locally for at least parts of the Proterozoic (Arnold et al., 2004).

However, more recently these limits have been contested (see e.g. reviews by Lyons et al., 2014; Planavsky et al., 2018). In particular, it has been proposed that pO_2 may have been lower than 1% PAL. The picture of pO_2 levels over Earth history is complicated by disconnects between the atmosphere and the ocean – i.e. the atmosphere may become oxygen-rich, but the ocean may lag behind (Canfield, 1998). This makes the use of marine pO_2 proxies more problematic for direct application to the atmosphere.

Some workers navigate this issue with careful ocean-atmosphere system consideration. For example, detailed ocean mixing models have been used in the extrapolation of low-O_2 waters (indicated by low cerium concentrations in mid-Proterozoic marine carbonates) to atmospheric O_2 mixing ratios of $\sim 2.1\times10^{-4}$ at 1.87 Ga (Bellefroid et al., 2018). Alternative avenues of research focus on the development of proxies for terrestrial (as opposed to marine) oxidation, as follows.

Chromium isotope ratios are a proxy for Proterozoic pO_2, since their fractionation is highly dependent on redox reactions and requires a lower limit of atmospheric oxygen (Frei et al., 2009). They are considered an indicator of terrestrial rather than marine processes, which strengthens them as a proxy for atmospheric pO_2 (Frei et al., 2009; Planavsky et al., 2018). Small δ^{53}Cr values in geographically-widespread and later, temporally-widespread sediments older than 0.8 Ga compared to larger fractionations in the Neoproterozoic and Phanerozoic have been interpreted to suggest predominantly low redox cycling of chromium isotopes in the mid-

Proterozoic, due to pO_2 levels of less than 1% PAL (Cole et al., 2016; Planavsky et al., 2014). This constraint comes from the requirement of oxidised Mn from which Cr can become oxidised, and oxidised Fe, such that oxidised Cr is not subsequently reduced (Planavsky et al., 2018). An observed increase in chromium isotope fractionations during the late Neoproterozoic has been used as evidence for the NOE as a second step-increase in oxygen (Frei et al., 2009).

However, other authors report more variable $\delta^{53}Cr$ values also between 0.8 and 1.1 Ga (Gilleaudeau et al., 2016), and even further back in the Mesoproterozoic (Canfield et al., 2018), with the latter authors arguing that this instead requires $pO_2 > 1\%$ PAL. In addition to discrepancies regarding the presence or absence of chromium isotope fractionation, uncertainty also remains pertaining to the maximum pO_2 levels that can be implied by a lack of fractionation.

A fairly novel and promising alternative proxy for ancient atmospheric pO_2 is triple oxygen isotope signatures. The details of these observations and their application to modern and ancient environments is a major theme of this thesis, and will be discussed in more detail in Section 1.5. However, it is important to introduce the proxy here, and briefly review how it has aided thinking about oxygen levels over time.

Anomalous triple oxygen isotope signatures, denoted by non-zero $\Delta^{17}O$ values, are, in contrast to other existing geochemical proxies, a record of isotopic ratios of directly captured oxygen atoms from palaeo-atmospheric O_2. Such signatures are produced by mass-independent fractionation of oxygen isotopes (O-MIF) in ozone formation processes (Section 1.5). Non-zero $\Delta^{17}O$ therefore requires the presence of a stratospheric ozone layer, and photochemical modelling by Kasting and Donahue (1980) and Segura et al. (2003) has indicated that O_2 mixing ratios must be 2.1×10^{-4} (10^{-3} PAL) or greater to allow an ozone layer to exist. The presence of non-zero $\Delta^{17}O$ in Proterozoic and Phanerozoic sulphates (in which O-MIF is predominantly preserved in the geological record) has therefore been used to propose that pO_2 must have been at least 2.1×10^{-4} for intervals of geologic time since the GOE

(Crockford et al., 2019). In Chapter 3, we will revise and extend the photochemical models on which this value is based.

The non-zero $\Delta^{17}O$ values provide a potential lower limit for Proterozoic pO_2, but extremely negative values of less than -0.5‰ (see Figure 1-2), especially during the mid-Proterozoic, have been counter-intuitively suggested to require a very low photosynthetic O_2 flux to the atmosphere, which is intricately linked to pO_2 (Crockford et al., 2018; Ozaki et al., 2018; Planavsky et al., 2018; 2020). Like Cr isotopes, the $\Delta^{17}O$ record is a terrestrial proxy, because non-zero $\Delta^{17}O$ values are incorporated into geological sulphates via oxidation in the atmosphere. Development of an O-MIF proxy for pO_2 levels requires systematic exploration of O-MIF in a 1-D photochemical model, which is the subject of Chapters 4, 5 and 6.

1.1.2 – Phanerozoic oxygen levels

Phanerozoic oxygen levels are, in comparison, relatively well constrained as above ~10%. Evidence for elevated Phanerozoic pO_2 relative to the bulk of the Proterozoic includes interpretation of carbon and sulphur isotope ratios ($\delta^{13}C$ and $\delta^{34}S$; see e.g. review by Berner et al., 2003). Burial of organic carbon and pyrite are sources of O_2 to the atmosphere and processes which result in the removal of lighter isotopes from the seawater in which carbonates and sulphates form (Berner, 2006; Berner and Canfield, 1989). Increased burial can therefore be detected in increased $\delta^{13}C$ and $\delta^{34}S$ in these rocks. Accordingly, additional structure in pO_2 variation for the Phanerozoic has been calculated from $\delta^{34}S$ and $\delta^{13}C$ by several biogeochemical model studies. These include inverse (e.g. GEOCARBSULF (Berner, 2006; 2009); GEOCARBSULFOR (Krause et al., 2018)) and forward (e.g. COPSE (Bergman et al., 2004; Lenton et al., 2018; Tostevin and Mills, 2020)) modelling approaches. One of the most recently-developed models predicts pO_2 oscillating between 2% and 11% during the Cambrian and Ordovician, before a step increase to higher pO_2, close to modern concentrations in the Devonian (Krause et al., 2018). The model then predicts high pO_2 for the remainder of the Phanerozoic, with a peak of between 30% and 35% in the early Mesozoic. Further constraints for the last ~400 Myr come from

a continuous charcoal record, probably requiring pO_2 within the following lower and upper limits. Wood would not burn at levels lower than ~15%, but oxygen levels higher than 30% would cause spontaneous and runaway forest fires, which would consume all plant matter (Bergman et al., 2004; Glasspool and Scott, 2010; Glasspool et al., 2015; Lenton, 2013).

One reason the nature of O_2 concentrations during the Proterozoic and Phanerozoic is of particular interest to a multidisciplinary scientific community is the implications on the relationship between atmospheric composition and biological evolution, since changes in atmospheric composition and evolutionary steps appear to be temporally coeval at several points in Earth history. Some believe the NOE to be a necessary step to allow for the emergence and evolution of animals, which is a hypothesis supported by evidence for low pO_2 previous to the NOE, and challenged by evidence for established high pO_2 by the late Neoproterozoic (see review by Cole et al., 2020). More recently in the Earth's history, the evolution of land plants and large-bodied organisms are often connected to hypothesised peaks in pO_2 (e.g. Dahl et al., 2010; Lenton et al., 2018). A better understanding of the history of atmospheric O_2 is therefore of importance to a number of fields, and further work in this arena will aid both the understanding of our own planet's history and that of other terrestrial planets in the galaxy.

1.2 – Carbon dioxide in the atmosphere over Earth history

Although the evolution of pO_2 in the Earth's atmosphere is the dominant theme of this thesis, changes in pCO_2 in palaeo-atmospheres are also important in forming a picture of the ancient Earth's conditions and habitability. Estimates of CO_2 levels over Earth history are of particular interest for this thesis, because the oxygen isotope model developed in Chapters 4-6 is able to predict $\Delta^{17}O$ values under various pCO_2 conditions, and is able to attempt to explain geological $\Delta^{17}O$ measurements in terms of potential pCO_2. In this section, I therefore briefly introduce existing proxies and estimates for pCO_2 over the Earth's history, which are illustrated in Figure 1-3.

Early estimates for CO_2 evolution were based on the faint young Sun paradox (Sagan and Mullen, 1972). Since the Sun has been increasing in luminosity over its lifetime, giving out only 70% of its current radiation during the Archaean, the assumed continuous presence of liquid water indicates the influence of a stronger greenhouse effect in the past. Assuming that CO_2 was an important greenhouse gas over the Earth's history, theoretical estimates suggested that at 4.5 Ga, the atmosphere had 0.1-10 bar CO_2 (~350-35,000 times preindustrial atmospheric levels (PAL)), decreasing to 0.02-0.25 bar (~71-890 PAL) at ~2.5 Ga and 10^{-4}-0.025 bar (~0.35-90 PAL) by ~0.8 Ga (Kasting 1987, 1990, 1993). (Here, we define 'preindustrial atmospheric levels' as 280 ppm, a mixing ratio of 2.8×10^{-4} or a surface concentration of 2.8×10^{-4} bar.) Other climate models have also used a similar approach. For example, the 1-D climate model of Haqq-Mirsa et al. (2008) required more than ~70-110 PAL at around 2.8 Ga. Also, Wolf and Toon (2014), used a 3-D global circulation model (GCM) to propose that pCO_2 between ~50 and ~700 PAL for 3.8 Ga and between ~9 and ~140 PAL for 2.5 Ga was sufficient to sustain modern surface temperatures with weaker solar fluxes.

In addition, various proxies from the geological record have been proposed to indicate pCO_2. One of the most promising is palaesol proxies, in which pCO_2 can be estimated from the extent of weathering of cations, by measuring cation/trace element concentrations (Driese et al., 2011; Mitchell and Sheldon, 2010; Sheldon, 2006; Sheldon, 2013). Sheldon (2013) thereby suggested a long-term decline in pO_2 between 1.8 Ga and 1.1 Ga of 45.2 PAL to 1.18 PAL. GCM results show that the fairly low pCO_2 estimates from this method for the mid-Proterozoic can be consistent with the faint young Sun and a lack of glaciation if the concentrations of other greenhouse gases such as methane were higher (Fiorella and Sheldon, 2017).

Other proxies include carbon isotope fractionations in 1.4 Ga microfossils, indicating that the carbon fixation pathway of the organism seems to have required pCO_2 between 20 and 100 times PAL (Kaufman and Xiao, 2003). Evidence for

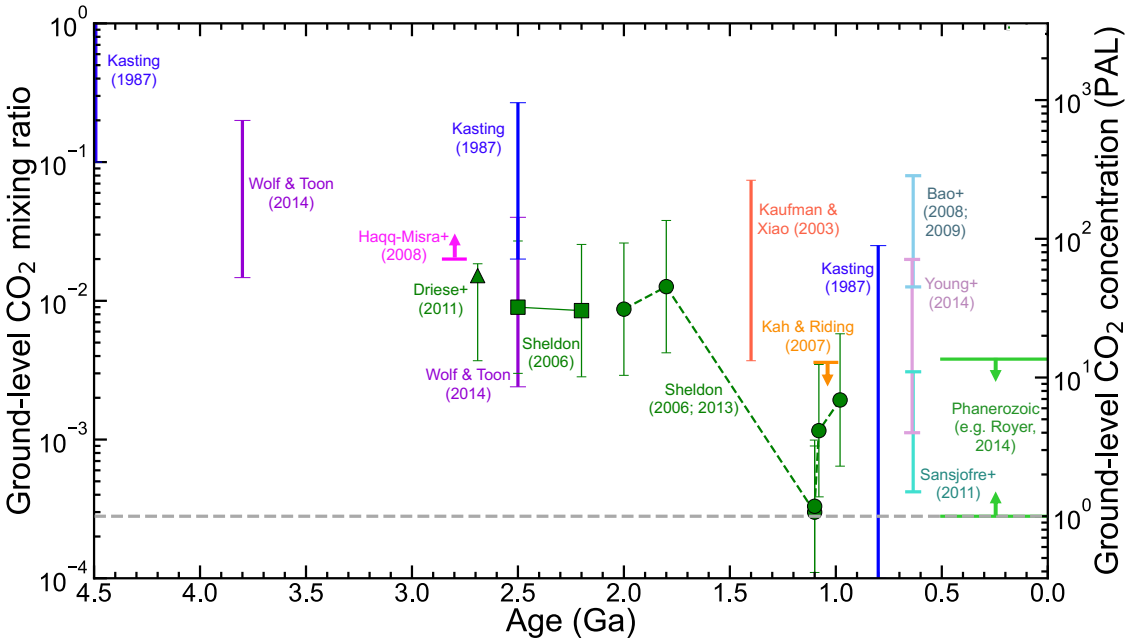

Figure 1-3: Proxies and modelling constraints for carbon dioxide levels over Earth history. Model estimates of pCO_2 from considerations of the faint young Sun are shown by dark blue (Kasting, 1987) and purple (Wolf and Toon, 2015) vertical bars, and pink arrow indicating upper limit from Haqq-Misra (2008). Green points indicate pCO_2 estimates for palaeosol studies from Driese et al. (2011; triangle), Sheldon (2006; squares) and Sheldon (2006; 2013; circles). Error bars (thin green lines) are shown with each green point, and the dotted line indicates the proposed decrease in pCO_2 between 1.8 Ga and 1.1 Ga (Sheldon, 2013). Other vertical bars are not error bars, but indicate estimates from microfossils (Kaufman and Xiao, 2003; dark orange), and three estimates of pCO_2 at 635 Ma (Bao et al., 2008; 2009 (pale blue); Sansjofre et al., 2011 (teal); Young et al., 2014 (pale pink)). The upper limit from Kah and Riding (2007) is shown by the pale orange arrow; note the date was revised from 1.2 Ga by Gibson et al. (2018). Crude upper and limits for the Phanerozoic are indicated by the pale green lines and arrows (based on Berner (2008) and Royer (2014)). Grey dotted line indicates preindustrial atmospheric levels (PAL), assumed to be 2.8×10^{-4} here. Please note that, where authors have presented data in PAL (where they either mean preindustrial or present atmospheric levels), I have assumed that 1 PAL is equal to a mixing ratio of 3.7×10^{-4} for Driese et al. (2011), Kaufman & Xiao (2003) and Sheldon (2006; green squares only), and that 1 PAL is equal to a mixing ratio of 2.8×10^{-4} for Sheldon (2013; green circles).

calcification by cyanobacteria at 1.047 Ga (date revised from 1.2 Ga by Gibson et al. (2018)) requires pCO_2 less than ~13 PAL (Kah and Riding, 2007).

As well as potentially addressing mid-Proterozoic pO_2, large, negative $\Delta^{17}O$ values from 635 Ma sulphates have been proposed as evidence for high pCO_2 in the aftermath of a Snowball Earth event, though this is debated (Bao et al., 2008; 2009; Cao and Bao. 2013; Sansjofre et al., 2011; Young et al., 2014). A more detailed review of pCO_2 for this time period can be found in Section 1.5.2.

For the Phanerozoic, carbon (and sulphur) cycle models account for sinks and sources of these elements over a range of timescales to calculate the atmospheric pCO_2, consistent with C and S isotope values from the geological record (e.g. the GEOCARB family of models; Berner, 2006; Royer et al., 2014) or cycles of other nutrients and primary productivity (e.g. COPSE, Berner et al., 2004; Lenton et al., 2018).

Model outputs can be compared to proxies such as plant stomata densities (Royer, 2001; Woodward, 1987), boron isotope fractionations ($\delta^{11}B$) and B/Ca ratios in carbonates (e.g. Pearson and Palmer, 1999; Yu et al., 2007), the carbon isotope composition of phytoplankton and liverworts (Figge and White, 1995; Fletcher et al., 2005; Popp et al., 1989; White et al., 1994), the presence of the mineral nahcolite (Eugster, 1966; Jagniecki et al., 2015) and temperature reconstructions for the last ~70 Ma from $\delta^{18}O$ values (e.g. Zachos et al., 2008). Ice cores provide a direct record of pCO_2 for the last 800 kyr. Since Phanerozoic pCO_2 is not a key aspect of this thesis, I will not go into the details of these proxies, but for a review, see Royer (2014).

Overall, the evolution of pCO_2 seems to have been a broad decrease from much higher levels during the Archaean. For periods closer to modern, evidence is more abundant and finer details can be resolved through a range of geochemical proxies and modelling methods. For the application of the oxygen isotope model developed in this thesis, we focus mostly on intervals in which large, negative $\Delta^{17}O$ values have been found (i.e. 1.4 Ga and 635 Ma). Our discussion in Chapter 6 regarding pCO_2 will therefore focus on these two points in time.

1.3 – Ozone and O_2

Ozone is also an important gas in the modern atmosphere, which features considerably in this thesis. Ozone is closely related to O_2 and is a key species in the production of O-MIF in the atmosphere. In this section, I briefly describe the relationship between atmospheric O_2 and O_3 formation. For model predictions of ozone with proposed O_2 level (e.g. Kasting and Donahue, 1980; Kasting et al., 1985;

Segura et al., 2003; Zahnle et al., 2006), which we build on in this thesis, see Chapter 3.

O_3 is a trace gas whose formation is dependent on O_2 and its photolysis products (simplified here as O), as shown by the Chapman reactions (Chapman, 1930) below:

$$O_2 + h\nu \rightarrow O + O \text{ for } \lambda < 242\ nm \quad \text{(R1.1)}$$

$$O + O_2 + M \rightarrow O_3 + M \quad \text{(R1.2)}$$

$$O_3 + h\nu \rightarrow O_2 + O \text{ for } \lambda < 290\ nm \quad \text{(R1.3)}$$

$$O_3 + O \rightarrow O_2 + O_2 \quad \text{(R1.4)}$$

where M is a third body (generally N_2 or O_2), and $h\nu$ are photons of the stated wavelength.

Reactions R1.2 and R1.3 are kinetically fast, so O_3 can be considered to be instantly produced and destroyed, with overall steady-state concentrations set by variations in the slower reactions R1.1 and R1.4. The net rate of R1.4 is catalytically enhanced by additional species (e.g. OH, NOx, ClOx). Ozone concentrations in the modern (pre-anthropogenic) atmosphere peak in the stratosphere, whereas the number densities of many other atmospheric species decrease upwards following the barometric law. This stratospheric 'ozone layer' results from a balance between increased O_3 formation by reaction R1.2 at lower altitudes with greater atmospheric density and increased O production at higher altitudes due to O_2 photolysis (R1.1).

1.4 – Models and triple oxygen isotopes

The discussion in Sections 1.1 and 1.2 shows that various models, in combination with geological proxies, have been used to help interpret geological observations in terms of atmospheric oxygen and CO_2 evolution. For O_2, the main focus of this thesis, these include 1-D photochemical models incorporating sulphur isotopes, which examine reducing and oxidising atmospheres either side of the GOE in particular (Claire et al., 2014; Pavlov and Kasting, 2002), as well as biogeochemical models,

many of which centre on the interpretation of geochemical proxies over more recent geological history (e.g. Krause et al., 2018). I have also highlighted the growing potential of the utility of O-MIF, dependent on O_3 formation (Section 1.3), which has already been investigated by box models implementing Monte Carlo approaches to account for uncertainty (e.g. Crockford et al., 2018; Planavsky et al, 2018; 2020). For the remainder of this chapter, I examine the background, mechanisms and existing and potential applications of this upcoming proxy.

1.5 – Mass-independent fractionation of oxygen isotopes

There are three stable isotopes of oxygen. The lightest isotope, ^{16}O contributes 99.762% of the abundance of oxygen atoms in the Solar System (Bao et al., 2016), compared to heavier and rarer isotopes ^{17}O (0.038%) and ^{18}O (0.2%). In general on Earth, the three isotopes of oxygen fractionate mass-dependently. The magnitude of mass-dependent fractionation can be can be quantified by comparing the ratio of ^{18}O or ^{17}O to ^{16}O in a sample to the ratio in a standard, through the equation:

$$\delta^x O = \left(\left(\frac{(^xR)_{sample}}{(^xR)_{standard}} \right) - 1 \right) \qquad \textit{(Eq. 1-1)}$$

where:

$$^xR = \left({}^xO / {}_{16}O \right) \qquad \textit{(Eq. 1-2)}$$

and x = 17 or 18.

For oxygen isotopes, the $\delta^{17}O$ and $\delta^{18}O$ are in units of parts per thousand (permil; ‰), and the standard isotope ratio is that of Vienna Standard Mean Ocean Water (VSMOW).

The mass-dependent behaviour of oxygen isotopes can be exploited by various geological applications. For example, in palaeoclimate studies, $\delta^{18}O$ in ice, seawater or carbonates is a proxy for a combination of ice volume and temperature because of mass-dependent fractionation processes acting in evaporation and precipitation,

and their temperature-dependence (Broecker and van Donk, 1970; Mix and Ruddiman, 1984; Shackleton, 1967).

Since most oxygen isotope fractionation processes on Earth are mass-dependent, most materials fall along the terrestrial fractionation line (TFL). Different definitions have been used by different authors, but in this thesis, the TFL is defined according to the relation:

$$\delta^{17}O = 0.528 \times \delta^{18}O \qquad \textit{(Eq. 1-3)}$$

The TFL is shown by the black dashed line in Figure 1-4. Mass-independent fractionation occurs when processes cause species to deviate from this relation, and the extent of mass-independent fractionation, $\Delta^{17}O$, is given by:

$$\Delta^{17}O = \delta^{17}O - 0.528 \times \delta^{18}O \qquad \textit{(Eq. 1-4)}$$

I have chosen to define the TFL and $\Delta^{17}O$ in most work presented here using the linear definition, and a slope of 0.528 (Eqs. 1-3 and 1-4), but for a review of definitions used in the literature, see Bao et al. (2016).

The only known source of O-MIF on Earth is in the reactions that form stratospheric ozone (R1.3, Section 1.3), which gains an oxygen isotope anomaly, $\Delta^{17}O$, of ~25-35‰ (Johnston and Thiemens, 1997; Krankowsky et al., 1995; 2000; 2007; Laemmerzahl et al., 2002; Mauersberger, 1987; Mauersberger et al., 2001; Thiemens and Heidenreich, 1983). This signal is then propagated through chemical reactions to other atmospheric species (Thiemens, 2006). CO_2 and H_2O_2, along with nitrate, sulphate and perchlorate aerosols in the atmosphere gain a positive $\Delta^{17}O$, diluted from the stratospheric ozone signal (e.g. Bao and Gu, 2004; Michalski et al., 2003; Savarino et al., 2000; Savarino and Thiemens, 1999; Yung et al., 1991). To conserve mass, atmospheric O_2 gains a negative $\Delta^{17}O$ (Luz and Barkan, 1999). The absolute magnitude of $\Delta^{17}O_{O2}$ in the modern atmosphere is very small (~-0.529) according to our definition in Equations 2-3 and 2-4, because the anomaly is spread over a large reservoir (Barkan and Luz, 2005; Blunier et al., 2002). Figure 1-4 shows

the existing observations of $\delta^{17}O$ and $\delta^{18}O$ for various atmospheric species (squares and circles) in relation to the TFL. Stratospheric ozone (dark blue, filled squares) has the largest $\delta^{17}O$ and $\delta^{18}O$ values, since this is the source of the mass-independent fractionation. While predominantly anthropogenically-produced, tropospheric ozone also has a large O-MIF. Additionally shown are anomalous isotopic compositions of species measured in rainwater ('×' symbols) and from dry deposition on the Earth's surface ('+' symbols).

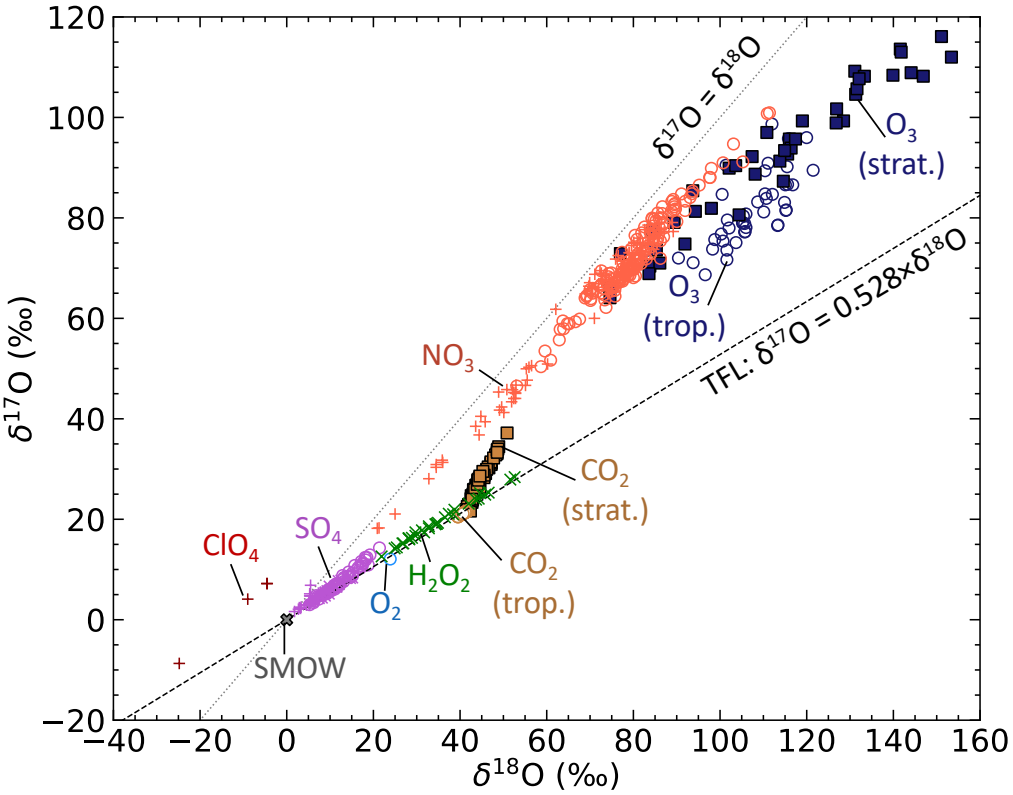

Figure 1-4: Oxygen isotope compositions of some atmospheric species, based on Figure 7 from Thiemens (2006). Stratospheric (filled squares, for O_3 and CO_2 only), tropospheric (unfilled circles), rainwater (crosses) and surface deposit (plus symbols) isotopic compositions are shown with colours for each species (Bao and Gu, 2004; Bao et al., 2001; Barkan and Luz, 2005; Geng et al., 2014; Jackson et al., 2010; Johnston and Thiemens, 1997; Krankowsky et al., 1995; 2000; 2007; Lämmerzahl et al.*, 2002; Lee and Thiemens, 2001; Liang et al., 2017; Michalski et al., 2004; 2005; Morin et al., 2009; Savarino and Thiemens, 1999; Savarino et al., 2007; 2013; Thiemens et al., 2014; Vicars and Savarino, 2014; Wiegel et al., 2013). Standard Mean Ocean Water (SMOW) has a composition at the origin, shown by the grey cross. For reference, the Terrestrial Fractionation Line and a line of gradient 1 are shown (black dashed and grey dotted lines respectively).*

In the following sections, I describe the current status of understanding on triple oxygen isotope measurements in the modern atmosphere, rainwater, deposited materials, and the geological record. I have two particular emphases in these sections: 1) a discussion of different oxygen isotope models applied to the modern and ancient atmosphere; and 2) a discussion of how O-MIF in the geological record can contribute towards an understanding of palaeo-atmospheres.

1.5.1 – How have oxygen isotope models aided understanding of $\Delta^{17}O$ in the modern Earth system?

Various modelling efforts have aimed to interpret the way in which the triple oxygen isotope anomaly is formed in stratospheric ozone and transferred to other atmospheric species and into species that are preserved in rocks. This section discusses some of the key atmospheric species which gain O-MIF signals.

1.5.1.1 – CO_2 and O_2

Atmospheric CO_2 gains a large, positive O-MIF value in the stratosphere, while O_2 consequently gains a negative $\Delta^{17}O$ value. The $\Delta^{17}O$ values of tropospheric CO_2 and O_2 are greatly influenced by atmospheric composition and fluxes of gases from Earth's surface, making preserved signals interesting proxies for palaeo-atmospheres. In this section I will discuss the factors that affect $\Delta^{17}O$ values of CO_2 and O_2 in the modern atmosphere, in order to better understand these influences for application to the past.

Some of the first modelling studies to examine the way in which the oxygen isotope anomaly is transferred from stratospheric ozone focussed on its propagation to atmospheric CO_2. Stratospheric CO_2 has a high $\Delta^{17}O$ value (Alexander et al., 2001; Boering et al., 2004; Lämmerzahl et al., 2002; Thiemens et al., 1995; Wiegel et al., 2013). Yung et al., (1991) and Yung et al. (1997) used a 1-D photochemical model including additional key species O and $O(^1D)$ (a photolysis product of O_3) to explore the atmospheric photochemistry pertaining to the relationships between these species. Initially, only ^{18}O and ^{16}O were incorporated into the model, but tracing of

the heavy isotopes led to their conclusion that the positive $\Delta^{17}O$ from ozone is transferred to CO_2 via the exchange reaction with $O(^1D)$, via the intermediate CO_3^* (see Figure 1-5a; Yung et al., 1991). With the inclusion of ^{17}O, Yung et al. (1997) investigated the sensitivity of model-predicted $\Delta^{17}O$ to initial fractionations, fractionation factors and reaction rates, in order to match experimental $\Delta^{17}O_{CO2}$ data from Wen and Thiemens (1993), carried out to advance understanding in the exchange of heavy isotopes between O_3 and CO_2.

In 2013, Wiegel et al. developed a kinetic photochemical model to simulate the $\Delta^{17}O$ of CO_2 under different conditions in the laboratory. In addition to the species included in the Yung et al. (1997) model, they included excited-state O_2 molecules $O_2(^1\Delta)$ and $O_2(^1\Sigma)$, and incorporated 19 core reactions (as well as isotopically-substituted reactions). They found that, at least for the laboratory studies, the $\Delta^{17}O$ of the CO_2 produced could be fully explained by the fractionation effects in the formation of ozone, and that no other fractionation effects, e.g. in ozone photolysis, were required to account for its magnitude. However, they did highlight sensitivities of stratospheric $\Delta^{17}O_{CO2}$ to temperature and mass-dependent fractionation effects. While stratospheric $\Delta^{17}O_{CO2}$ is high, measurements show that tropospheric $\Delta^{17}O_{CO2}$ is close to 0‰ (e.g. Liang et al., 2017; Thiemens et al., 2014). This is due to rapid isotope exchange with water, which has a $\Delta^{17}O$ value close to 0‰ in the troposphere. In detail, tropospheric $\Delta^{17}O_{CO2}$ can vary slightly on short timescales, due to, for example, the El Niño Southern Oscillation (ENSO; Thiemens et al., 2014), but these variations are generally smaller than the ones we will investigate in this thesis.

In addition to contributing towards an understanding of the propagation of O-MIF from O_3 to CO_2, oxygen isotope models have also constrained relative contributions of MIF and non-MIF sources to tropospheric O_2. Throughout the atmospheric column, O_2 has a small, negative $\Delta^{17}O$ (Luz et al., 1999; Thiemens et al., 1995). Yung et al. (1997) showed that a negative isotope anomaly is produced in the stratosphere as the result of mass balance as CO_2 becomes enriched via reaction with $O(^1D)$. The presence of CO_2 allows the heavier isotopes to be preferentially transferred from the

O_2 reservoir as O_3-O_x is produced and destroyed. This leaves the O_2 reservoir depleted in heavy isotopes (Figure 1-5a). However, since O_2 makes up 21% of the atmosphere, the magnitude of negative $\Delta^{17}O$ in O_2 is much smaller than the positive $\Delta^{17}O$ observed in the smaller O_3 reservoir (Blunier et al., 2002; Luz et al., 1999). Mixing from the stratosphere decreases the $\Delta^{17}O$ value of tropospheric O_2, which is also influenced by biologically-produced O_2 (Luz et al., 1999). The biological production of O_2 includes no inherent mass-independent fractionation, but it does fractionate oxygen isotopes mass-dependently (Guy et al., 1993). Due to slightly different $\delta^{17}O$-$\delta^{18}O$ slopes, this can produce an apparent mass-independent fractionation (e.g. Young et al., 2002). These are evident given measurement precision on the order of 10 parts per million (permeg), but are generally smaller than the permil observations that are the primary aim of this thesis.

Contributions of $\Delta^{17}O$ in tropospheric O_2 therefore come from both the mixing down of the negative anomalous stratospheric photochemical signal, and from mass-dependent effects that do not perfectly lie along the terrestrial fractionation line. Various authors have attempted to quantify the relative proportions of these two influences as follows.

Bao et al. (2008) estimated that 83% of the tropospheric $\Delta^{17}O$ value comes from the stratosphere, having calculated that the other 17% is a result of a slightly different fractionation slope for respiration. However, Young et al. (2014) use a 4-box model (with boxes for the stratosphere, troposphere, geosphere and hydrosphere/biosphere) to model the mixing ratios and oxygen isotope composition of O, $O(^1D)$, O_2, O_3 and CO_2 for the modern atmosphere. Their model incorporates 57 stratospheric reactions, as well as troposphere-stratosphere mixing, evapotranspiration, and respiration, to produce steady-state model atmospheres. Comparison of models run with and without evapotranspiration and respiration led them to conclude that a much lower proportion (33%) of the tropospheric $\Delta^{17}O$ originated in stratospheric photochemistry, with the remainder being the result of the apparent MIF due to mass-dependent biological processes with slightly different fractionation slopes.

Three factors that have been shown to affect the $\Delta^{17}O$ of tropospheric O_2 and/or CO_2 are the photosynthetic O_2 flux to the atmosphere (also referred to as the gross primary productivity, GPP), and the atmospheric concentrations of CO_2 and O_2 (Figure 1-5).

GPP affects the triple oxygen isotope composition of O_2 in the troposphere, because the flux of O_2 from photosynthesis in the biosphere has no mass-independent fractionations, though, as explained above, there may be small apparent mass-independent fractionations due to different fractionation slopes (Blunier et al., 2002; Luz et al., 1999; Young et al., 2014). This results in a dilution of the larger-magnitude negative O-MIF signal from the stratosphere as it mixes with biologically produced O_2 in the troposphere (see Figure 1-5b). Increased biological productivity would therefore act to reduce tropospheric $\Delta^{17}O_{O2}$ (Wing et al., 2013).

Luz et al (1999) demonstrated this using mass-balance calculations in a four-box model (with boxes for the stratosphere, troposphere, biosphere and hydrosphere). Through respiration, oxygen with a negative $\Delta^{17}O$ is removed from the atmosphere, and photosynthesis and evapotranspiration are a source of oxygen with no mass-independent signature (other than that caused by a difference in mass-dependent fractionation slope), resulting in a dilution of the stratospheric signal in the troposphere. They used their model to predict the global productivity of the biosphere over the last 82 kyr, from triple oxygen isotopes measured in gas-phase O_2 from ice cores. Blunier et al. (2002) built on this work by using a similar box model (with boxes for the stratosphere, troposphere, ocean biosphere and land biosphere) to deduce oxygen fluxes to the atmosphere from average measured $\Delta^{17}O_{O2}$ for the last 60 kyr. Values of $\Delta^{17}O$ from the geological record have high potential as a proxy for GPP further back in time (see e.g. review by Wing, 2013).

A similar observation was made for tropospheric CO_2. For example, Thiemens et al. (2014) investigated a correlation between $\Delta^{17}O_{CO2}$ and the intensity of the El Niño Southern Oscillation observed over a decade. A decrease in positive $\Delta^{17}O$ values of 0.06‰ (60 permeg) was coincident with an intense ENSO event, and various causal

mechanisms were discussed. It was concluded that the most likely mechanism behind the apparent ENSO-$\Delta^{17}O_{CO2}$ link is an ENSO-induced increase in biological activity, and therefore an increase in isotopic exchange between water and CO_2 (which takes place in plants). The water would take on the MIF signal (though presumably mass balance requires that this would be negligible, due to the comparatively enormous reservoir of water at the Earth's surface), and the CO_2 would gain a less anomalous isotope signal.

Along with GPP and other effects of the biosphere, various authors have investigated the sensitivity of tropospheric $\Delta^{17}O_{CO2}$ and, in particular, $\Delta^{17}O_{O2}$, to atmospheric levels of CO_2 and O_2. An increase of pCO_2 results in an increased sequestering of the heavier oxygen isotopes away from the O_2-O_x system and into the CO_2 reservoir (Figure 1-5a.2; Yung et al., 1997). As a result, the O_2 reservoir becomes increasingly depleted in ^{17}O and ^{18}O relative to ^{16}O, and so, all else equal, an increase in pCO_2 results in an increase in the negative magnitude of the $\Delta^{17}O_{O2}$. Conversely, an increase in pO_2 increases the rate of recombination of the photolysis products of ozone (O_2 and $O(^1D)/O$) back into ozone, relative to the rate of the reaction of product $O(^1D)$ with CO_2 instead (Figure 1-5a.3). This results in a decrease of the propagation of a large O-MIF out of the O_2-O_x system: O_2 becomes less depleted in heavy isotopes, and the $\Delta^{17}O_{O2}$ becomes less negative trending towards zero.

As Luz et al. (1999) and Blunier et al. (2002) estimated palaeo-primary productivity from ice core bubble $\Delta^{17}O_{O2}$, they acknowledged the influence of pCO_2 on the ultimate oxygen isotope composition of O_2. Since the ice cores yielded parallel estimates of pCO_2 over the timescale in question, this was accounted for in the models.

These relationships were further investigated by Young et al. (2014), who systematically investigated the dependence on GPP and pCO_2 of $\Delta^{17}O_{O2}$, at modern pO_2, using their four-box model. As detailed above, their treatment of stratospheric chemistry was significantly more detailed than that of Luz et al. (1999) and Blunier et al. (2002), and they explicitly included the additional species O, $O(^1D)$ and O_3.

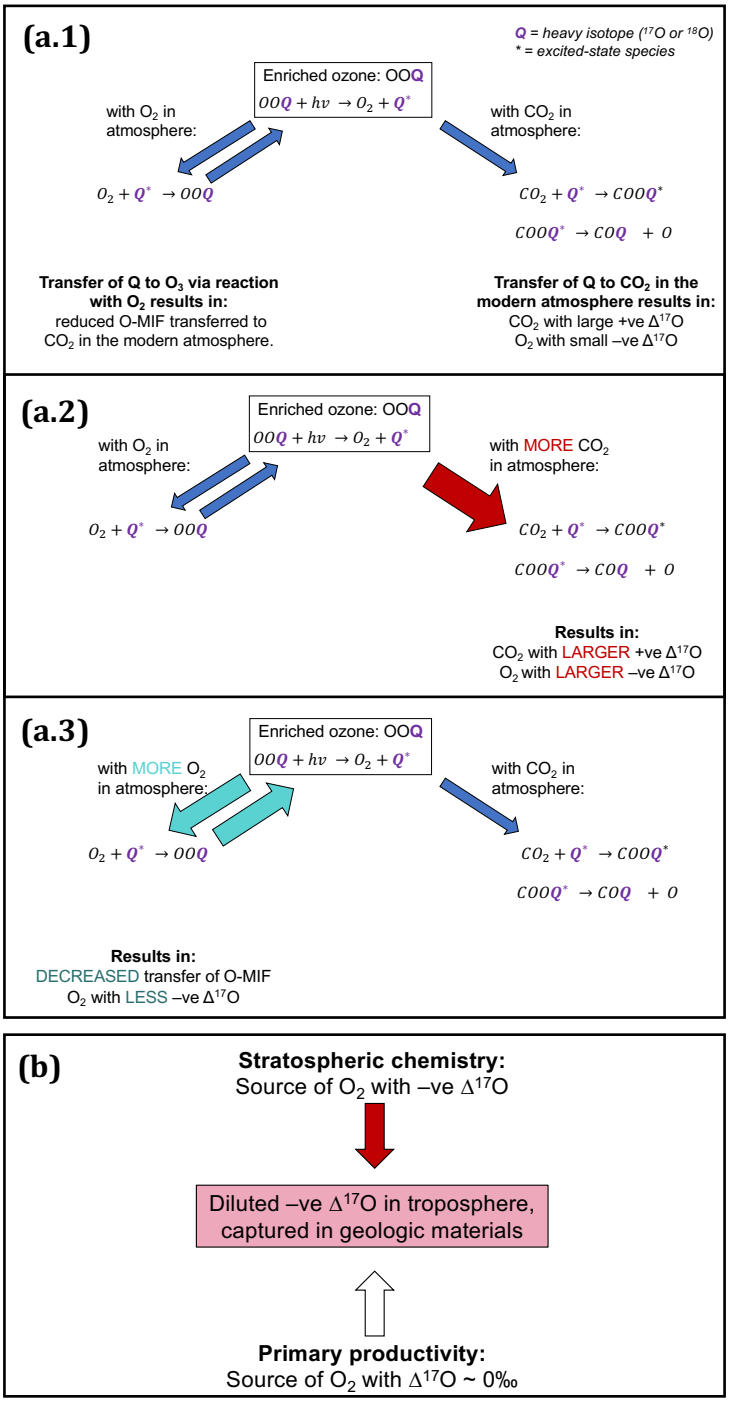

*Figure 1-5: Effects of pCO_2, pO_2 and GPP on the $\Delta^{17}O$ value of tropospheric O_2. **(a)** Panels a.1 to a.3 illustrate the way in which the transfer of heaver isotopes from ozone to CO_2 (leaving O_2 isotopically light) is affected by increased CO_2 concentrations (a.2), and increased O_2 concentrations (a.3). **(b)** Illustration of the effects of mixing of stratospheric O_2 with an oxygen isotope anomaly and biologically-produced O_2 on tropospheric O_2.*

They were able to predict $\delta^{18}O$ and $\delta^{17}O$ for each species as well as $\Delta^{17}O$. Their method of varying GPP was to vary the rates of photosynthesis and respiration in tandem, such that the O_2 concentration was not affected, but the circulation of O_2

through the system was changed. As well as commenting on potential explanations for specific deeper time cases (which I discuss further in Section 1.5.2), they demonstrated a strong and non-linear dependence of $\Delta^{17}O_{O2}$ on GPP and pCO_2. Time-dependent modelling also showed a dependence of $\Delta^{17}O_{O2}$ on net O_2 flux resulting from the balance between respiration and photosynthesis, which ultimately controlled pO_2 in a longer-term biogeochemical cycle. A drop in the net O_2 flux (and therefore pO_2) results in more negative $\Delta^{17}O$ values in tropospheric O_2, since the smaller reservoir enhances the signal. On the other hand, if pO_2 drops below a certain level, there may be insufficient ozone production to produce an observable anomaly (Crockford et al., 2018; Kasting and Donahue, 1980; Kasting et al., 1985; Segura et al., 2003; see also Chapter 3).

These relationships have been exploited for use in interpreting extremely negative $\Delta^{17}O$ in sulphates from the geological record, by invoking either very low primary productivity or very high pCO_2 as explanations (Bao et al., 2008; 2009; Cao and Bao, 2013; Crockford et al., 2018). Some of these applications will be discussed in Section 1.5.2, and explored using our model in Chapter 6. I will continue with a discussion of other atmospheric species which trap the positive O-MIF signal and can be transferred to the solid phase and deposited on Earth's surface.

1.5.1.2 – Nitrates, sulphates and perchlorates

Atmospheric nitrates (Michalski et al., 2003) and sulphates (Lee et al., 2001; Savarino et al., 2000) have been shown to inherit a positive oxygen isotope anomaly from ozone. In general, this is gained by the production of these species via oxidation by MIF-carrying oxidants, such as O_3 or H_2O_2 (Michalski et al., 2003; Savarino et al., 2000). Measurements and modelling have shown that the variation of the signals carried by these salts is due to variation in the relative importance of different oxidative pathways, since different oxidants carry different non-mass-dependent anomalies. The oxidative pathways themselves are affected by atmospheric conditions depending on concentrations of oxidants and reaction catalysts, and incoming solar radiation, which themselves may vary with season, geographic

location, and anthropogenic influence (e.g. Alexander et al., 2009b; McCabe et al., 2006; Morin et al., 2007, 2009; Savarino et al., 2007). Positive O-MIF can be detected not only in the molecules in the atmosphere but when they are dissolved in rainwater or removed from the atmosphere to the Earth's surface by dry deposition (Bao et al., 2000; Bao and Gu, 2004; Savarino and Thiemens, 1999). In this section, I describe some of the studies into sensitivities of the $\Delta^{17}O$ values of atmospheric and deposited salts to date, and explore the revelations brought about by oxygen isotope modelling of the Earth system.

Atmospheric nitrates, sulphates and perchlorates

Early measurements and modelling of the $\Delta^{17}O$ values of tropospheric nitrate showed a positive signal which varies seasonally due to the relative importance of oxidation by different pathways. Transfer of oxygen atoms from ozone can happen via oxidation of NO to produce NO_2, or subsequent oxidation of NO_2 to NO_3 (Michalski et al., 2003), though these oxidation pathways compete with others which impart no O-MIF.

Seasonal variation, particularly at the poles, has been investigated by various authors. Extremes in light and dark over the polar seasons has been suggested to affect the photochemical pathways producing nitrate at high latitudes. For example, Savarino et al. (2007) showed large atmospheric nitrate concentrations and O-MIF during the Antarctic winter compared to the rest of the year, suggesting that this could be due to the increased importance of the heterogeneous breakdown of N_2O_5, $ClONO_2$ and $BrONO_2$ to HNO_3 in the dark months, which are other pathways which transfer the large oxygen isotope anomaly from ozone effectively. Even for lower latitudes, large atmospheric $\Delta^{17}O_{NO3}$ at the ground-level shows that the oxidation of NO_2 by OH (which carries a negligible O-MIF signal) must be a relatively unimportant pathway, as it would produce nitrate with much lower $\Delta^{17}O$ (Morin et al., 2009). Variation of $\Delta^{17}O_{NO3}$ with aerosol particle size was suggested to support the importance of the heterogeneous pathways (especially N_2O_5 and $BrONO_2$ hydrolysis), even at low latitudes (Morin et al., 2009). Low ozone mixing ratios during Arctic ozone depletion events, due to polar photochemistry, were shown to

positively correlate with Arctic tropospheric $\Delta^{17}O_{NO3}$ over a springtime measurement campaign, which was interpreted to be due to variations in the oxidation pathways of the first step (from NO to NO_2) via O_3, RO_2 (peroxy radicals) and BrO (Morin et al., 2007).

Despite a dearth of stratospheric $\Delta^{17}O_{NO3}$ measurements, Lyons (2001) explored the potential atmospheric profile of the $\Delta^{17}O$ of NO_x species using a 1-D photochemical model. This model included several more species than the models described previously in this thesis, with 15 species (and their isotopic equivalents) involved in 70 reactions (rather than Yung et al. (1997)'s 6 species). This 1-D photochemical modelling approach allowed for predictions of the transfer of the MIF signal to a wider range of different molecules, rather than simply focussing on one or two key species. The model predicted large $\Delta^{17}O$ for NO_x (as well as ClO, $ClONO_2$ and HNO_3). It was validated for the modern atmosphere, as it predicted surface atmospheric $\Delta^{17}O_{HNO3}$ of 22‰, close to the measured value of 23‰ (Michalski and Thiemens, 2000). An interesting feature of the $\Delta^{17}O$ profile for the NO_x species NO and NO_2 is a peak in the stratosphere, and decrease with altitude above 30 km. This was explained by rapid exchange of NO_x and O (the latter of which has a very small $\Delta^{17}O$ due to exchange with O_2 in the upper atmosphere). While perhaps overestimating the fractionation factor for the MIF-forming reaction, this photochemical model was the first to predict $\Delta^{17}O$ variation with altitude in a range of O-bearing species, and something that we attempt to build on in Chapter 5.

The positive $\Delta^{17}O$ values measured in atmospheric sulphates were shown to be due to oxidation of S(IV) species (SO_2, $SO_2.H_2O$, HSO_3^- and SO_3^-) by O_3 and H_2O_2 (Lee et al., 2001), as opposed to mass-independent effects in the sulphate-producing reactions themselves (Savarino et al., 2000). Oxidation by these species tends to occur in the aqueous-phase, rather than gas-phase oxidation by OH, which is also an important oxidant but imparts no MIF signal, as most atmospheric OH is derived from H_2O which has a mass-dependent isotopic distribution (Lyons, 2001). An additional oxidation pathway is oxidation by O_2, which is catalysed by transition metal particles (Alexander et al., 2009a; Savarino et al., 2000, and references

therein). As with nitrate, the distinct isotopic fingerprints of each oxidation pathway have allowed atmospheric $\Delta^{17}O$ measurements to be used to better constrain the relative importance of sulphate formation pathways under a range of conditions.

Several authors have used a mass-balance approach to better understand the influence of different oxidants. Since Savarino et al. (2000) quantified that sulphate produced by aqueous-phase O_3 and H_2O_2 oxidation gains one and two oxygen atoms from the oxidant respectively, an estimate of product $\Delta^{17}O_{SO4}$ can be made with knowledge of both i) the triple oxygen isotopic composition of O_3 and H_2O_2, and ii) the relative importance of different oxidation pathways. The resulting isotopic composition of tropospheric (or deposited) sulphate can therefore be predicted by:

$$\Delta^{17}O_{SO4} = \sum \left(F_{ox} \times \Delta^{17}O_{ox}\right) \qquad \textit{(Eq. 1-5)}$$

Where F_{ox} is the fraction of $\Delta^{17}O_{SO4}$ from each oxidant, and *ox* represents each chosen oxidant (equation adapted from McCabe et al., 2006).

For example, Alexander et al. (2005) used a global 3-D model to predict the $\Delta^{17}O$ values of non-sea-salt sulphate, with the model tracing $\Delta^{17}O$ for sulphate produced by each oxidant, using assumed imparted $\Delta^{17}O$ values of 8.8‰, 0.9‰ and 0‰ for O_3, H_2O_2 and OH respectively (and defining $\Delta^{17}O = \delta^{17}O - \delta^{18}O^{0.52}$). They showed that aqueous-phase oxidation by ozone to sulphate, occurring on sea-salt aerosol particles, was an important source of atmospheric sulphate in the Marine Boundary Layer (MBL; the lowermost part of the atmosphere at which exchange with the ocean readily occurs) of the Indian Ocean, when sea-salt particle concentrations were high. Since oxidation by ozone tends to impart a higher O-MIF to product sulphate than H_2O_2 and OH, regions of measured high O-MIF suggest an important role for oxidation by O_3 in this part of the atmosphere. Since aqueous-phase oxidation by O_3 occurs only at pH > 6, and clouds tend to be more acidic, a key location for oxidation by O_3 is on alkaline sea-salt aerosol particles. When titration

by this source of alkalinity was included in the model, it reproduced observations of larger $\Delta^{17}O$ value with increased concentration of sea-salt aerosol.

MBL measurements in the subtropical region of the Atlantic Ocean showed variation in $\Delta^{17}O_{SO4}$ between sampling sites far from and close to land, as well as some variation between summer and winter measurements (Alexander et al., 2012). For the remote ocean sites, in contrast to those measured by Alexander et al. (2005), it was shown that oxidation by O_3 in clouds was an important pathway, and that low $\Delta^{17}O_{SO4}$ close to the Iberian Peninsula in summer was due to the increased importance of oxidation by anthropogenically-produced halogen species, which imparted a zero-$\Delta^{17}O$.

Seasonal variations of $\Delta^{17}O$ in atmospheric sulphate have been attributed to variations in the relative importance of aqueous-phase oxidation (prevalent during winter, leading to higher $\Delta^{17}O_{SO4}$) and gas-phase oxidation (prevalent during summer, resulting in less positive $\Delta^{17}O_{SO4}$). McCabe et al. (2006) used the mass-balance approach of Eq. 1-5 to predict the seasonal variation of Arctic sulphate aerosols, in which oxidation of SO_2 to sulphate was assumed to occur via O_3, H_2O_2 and OH only. Values for modern-day monthly F_{ox} for the three species came from the model of Feichter et al. (1996). Winter $\Delta^{17}O_{SO4}$ values were expected to be higher due to the expected increase in importance of oxidation by ozone as H_2O_2 and OH concentrations decrease due to decreased photolysis. Overestimates of model results compared to seasonal measurements, especially in the winter, therefore suggested the importance of a role of oxidation by O_2 during winter, catalysed by anthropogenically-produced transition metal particles.

Alexander et al. (2009a) explored the role of oxidation by O_2 further by including this pathway in their global chemical transport model. With a global contribution to sulphate production of 9-17% via this pathway, they reproduced the Arctic $\Delta^{17}O_{SO4}$ values published by McCabe et al. (2006). The role of O_2 oxidation was argued to be more important in the northern hemisphere than the southern hemisphere, due to larger concentrations of transition metal particles as a result of anthropogenic

activity and desert dust in the north. Geographically, it is also more important towards the poles compared to the tropics, due to limitations on other pathways at high latitudes as photolysis is reduced.

Observations and modelling of an atmospheric component in surface deposits and rainwater

The models described thus far in this section have been used to investigate the sensitivities of $\Delta^{17}O$ in sulphates and nitrates in the atmosphere to various factors, which have affected the relative importance of different oxidation pathways. However, large, positive $\Delta^{17}O$ are not only seen in the gas phase, but have been observed in salts of nitrates, sulphates and perchlorates deposited in soils, rainwater, groundwater, ice and evaporites (Bao et al., 2000; 2001; Bao and Gu, 2004; Michalski et al., 2004a). The presence of O-MIF in salts has therefore been interpreted to indicate at least a partial atmospheric origin, as explained in this section.

The high solubility of these salts (especially nitrate and perchlorate) means that the atmospheric signals are best preserved in the driest places on Earth (Bao et al., 2001), such as the Atacama Desert in northern Chile (e.g. Bao et al., 2001; Jackson et al., 2010; Michalski et al., 2003), the Mojave Desert in the south-west of the United States (e.g. Michalski et al., 2004a) and the Antarctic Dry Valleys (e.g. Bao et al., 2000; Bao and Marchant, 2006; Michalski et al., 2005). They can also be preserved in polar snowpits (e.g. Kunasek et al., 2008) and ice cores (e.g. Alexander et al., 2002; 2003; 2004; Kunasek et al., 2010). In fact, the large accumulation of nitrates with high $\Delta^{17}O$ puts a climatic constraint on the hyperarid core of the Atacama, with a model indicating that it has been arid for 2 million years (Michalski et al., 2004b).

Before the measurement of triple oxygen isotopes in deposited desert salts, Böhlke et al. (1997) argued for an atmospheric source of Atacama and Mojave nitrates and sulphates, from major sulphur and nitrogen isotope measurements, as well as large $\delta^{18}O$ values similar to those of atmospheric nitrates. Subsequently, $\Delta^{17}O_{NO3}$ measured in soils, water and ice records showed that the atmospheric signal was

propagated to the Earth's surface. Michalski et al. (2004a) used triple oxygen isotopes to quantify the atmospheric source of nitrates to Californian stream and soil systems, with applications for the effects of anthropogenic pollution. Michalski et al. (2004b) quantified atmospheric nitrate deposition rates, sources and timescales for the hyper-arid Atacama Desert. Antarctic nitrates were shown to be atmospheric in origin, and different atmospheric sources and pathways were compared (Michalski et al., 2005).

Even before Michalski et al.'s (2003) discovery of preserved $\Delta^{17}O$ in surficial nitrate deposits, Bao et al. (2001) were one of the first to show that anomalous oxygen isotope compositions can be recorded in surficial geological materials, as they measured positive $\Delta^{17}O$ values in sulphates in desert varnish in the Atacama. Comparison of these values with atmospheric sulphate $\Delta^{17}O$ led them to conclude that the sulphates were of at least partial atmospheric origin, and likely to have arisen by wet and dry deposition of sulphates from the atmosphere.

Perchlorate (ClO_4^-) is a salt with both natural and manmade sources (Dasgupta et al., 2005; Eriksen, 1983). It is a nonlabile oxyanion, so retains its isotopic signature well over time, but is very soluble and easily flushed away – even more so than nitrates and sulphates. The hyperarid regions of the Atacama Desert are therefore a good place to measure natural perchlorate as it is not flushed from the surface soil profiles, where it can be predominantly found in nitrate salt deposits. Bao & Gu (2004) measured and compared triple oxygen isotope signatures from both natural perchlorates from the Atacama Desert and manmade perchlorates. The former were found to have a positive $\Delta^{17}O$ value (mass-independent), while the latter had a mass-dependent signature, as shown in Figure 1-4. This not only had implications for the identification of natural or manmade perchlorate (of immediate societal importance when identifying the source of a groundwater pollutant), but implications for a better understanding of natural perchlorate formation mechanisms. Despite a lack of atmospheric perchlorate $\Delta^{17}O$ data, the positive, mass-independent anomaly implies that the natural perchlorate has a significant atmospheric component, and, more specifically, that approximately one of the four oxygen atoms in perchlorate

ultimately originates from ozone. This was used to suggest that one of the sinks for chlorine in the atmosphere could be oxidation by ozone to perchloric acid ($HClO_4$). Additional perchlorate triple oxygen isotope data from arid areas in the south-west U.S. were presented by Jackson et al. (2010), but its source(s), sensitivity to location and season, and an explanation for isotopic variance between wet and dry deposition have remained elusive.

Since the $\Delta^{17}O$ observations do point to at least a partial source of atmospheric perchlorate to natural perchlorate deposits, Catling et al. (2010) included chlorine species and reactions in their 1-D photochemical model (*Atmos*, the model used and developed in this thesis), in order to better constrain perchlorate formation pathways. They predicted mixing ratios of chlorine-bearing species and fluxes of perchlorate, to show that the relatively large concentrations in Atacama soils could be explained by oxidation of chlorine by O_3 followed by OH, after Simonaitis and Heicklen (1975), and tuned reaction rates of these understudied reactions to best match the observations.

Despite significant advances in the understanding of perchlorate formation that both triple oxygen isotope and photochemical modelling studies have afforded, the oxygen isotope composition of perchlorate and the processes by which it gains such compositions is much more poorly understood than for sulphate and nitrate. Further investigation in this field is of great interest, not only for a better understanding of the modern Earth's atmosphere, but also for that of Mars, since significant perchlorate concentrations were discovered in Martian soils by the NASA Phoenix Lander in 2007 (Kounaves et al., 2010).

Model interpretation of O-MIF in nitrates deposited at the Earth's surface

McCabe et al. (2007) used $\Delta^{17}O$ values from Antarctic surface and snowpit nitrates to analyse the relative importance of tropospheric and stratospheric chemistry on nitrate formation. Having found $BrONO_2$ hydrolysis to be an important source of atmospheric nitrate during ozone depletion events (Morin et al., 2007; see above), Morin et al., (2008) more specifically showed that the photolytic release of NO_x from

the snowpack, and subsequent oxidation by BrO leading to hydrolysis of $BrONO_2$ is important during the Arctic spring.

Arctic $\Delta^{17}O_{NO3}$ in snow also shows a seasonal variation. Kunasek et al. (2008) used a box model to predict seasonal variation in $\Delta^{17}O_{NO3}$ in a snowpit at Summit, Greenland. This used a mass-balance method and included 11 oxidation reactions of NO and NO_2 to HNO_3 and NO_3. Boundary conditions included monthly species concentrations, temperature, and atmospheric density. The $\Delta^{17}O$ values of ozone and other oxidants were assumed to be 35‰ and 0‰ respectively, and the $\Delta^{17}O$ values of NO_2 and nitrate were predicted. When run for a model timescale of a decade and compared to measurements from the snowpit, both the model results and measurements showed seasonal trends, with lower positive MIF values in summer, and higher values in winter. This, as for previous work, was attributed to an increase in the importance of oxidation by OH relative to O_3 in summer. In summer, greater photolysis results in a decrease in O_3 and increase in OH concentrations, resulting in a greater importance of the OH oxidation pathway.

However, there was a discrepancy between the predicted and measured values, whereby the predicted values were lower by 2-7‰ in summer. The reasons for this were discussed, and could be due to any of the following model assumptions: (1) polar $\Delta^{17}O_{OH}$ = 0‰ (whereas it may actually be slightly positive if OH is not in complete isotopic equilibrium with H_2O); (2) troposphere-stratosphere mixing is not included, but could increase in the summer; (3) reactions including halogens such as bromine are ignored, though may be important as explained above; (4) no transport of nitrate or oxidants from outside the local area. All four assumptions could partially explain the data-model discrepancy, though none can account for it individually. Better constraints on some of these assumptions could help in better understanding what $\Delta^{17}O$ in nitrates can indicate about the oxidative capacity of the atmosphere.

The aim of the study was to explore the potential of ice core measurements to offer information about the oxidative capacity of palaeo-atmospheres, and the

concentrations and relative importance of different oxidising species. The $\Delta^{17}O_{NO3}$ is certainly sensitive to the oxidising capacity of the atmosphere, but the variation at seasonal resolution is not well preserved in older records, and seasonal variation in nitrate accumulation rates could cause annual means to be misleading.

Alexander et al.'s (2009b) 3-D global chemical transport model of the $\Delta^{17}O$ value of modern atmospheric nitrate allowed for analysis of formation pathways at all latitudes, not only the poles and mid-latitudes. Comparison of model results to measurements for six sites of varying latitudes was made, including Summit. This allowed the inclusion of the effects of transport of atmospheric nitrate from lower latitudes, but there remained a discrepancy of 0-5‰ between higher summer measurements for this site compared to predictions, again potentially due to an absence of bromine chemistry in the model. They explored uncertainties including the value of tropospheric $\Delta^{17}O_{O3}$, and the probability of different ozone atoms being transferred to other species in reactions, which were limiting model reliability. The $\Delta^{17}O$ of nitrate was shown to be closely linked to the involvement of ozone in the oxidation of NO to NO_2 – more so than oxidation by ozone in later stages of NO_3 and HNO_3 production. The model also predicted large $\Delta^{17}O$ of nitrates at the poles compared to the tropics, and larger $\Delta^{17}O$ of polar nitrates during the winter compared to the summer.

Model interpretation of O-MIF in sulphates deposited at the Earth's surface

As for nitrates, positive MIF values measured in Quaternary ice core and soil sulphates deposited from the atmosphere are variable, and can therefore give information about the relative importance of different oxidants and formation pathways in the modern and the past. Various authors have used a mass-balance method, not only to interpret $\Delta^{17}O_{SO4}$ for the modern atmosphere, but also to predict $\Delta^{17}O$ of deposited sulphates from the past. This has been used for glacial-interglacial timescales as well as to interpret changes over the last 200 years, as follows.

Antarctic ice core sulphate $\Delta^{17}O$ values were higher for the Holocene and last interglacial compared to the last glacial (Alexander et al., 2002). This was attributed

to an increased importance of gas-phase (by OH) compared to aqueous-phase (by O_3) oxidation over the glacial periods compared to the interglacials (with oxidation by H_2O_2 assumed to be unimportant), due to variations in either the oxidative capacity of the atmosphere or cloud-processing efficiency. These conclusions were supported by complementary quadruple sulphur isotope data (Alexander et al., 2003).

On a more recent timescale, Greenland ice core increases in $\Delta^{17}O$ in sulphates and nitrates from 1692-1976 correlate with pre-industrial biomass burning in North America (Alexander et al., 2004). This was suggested to support evidence of changes in the role of O_3 as localised anthropogenic ozone concentrations increased.
On the other side of the globe, $\Delta^{17}O_{SO4}$ from an Antarctic ice core showed no significant change in $\Delta^{17}O$ since the mid-nineteenth Century (Kunasek et al., 2010). Kunasek et al. (2010) used a mass-balance to show that this lack of change was consistent with existing estimates of oxidation capacity changes, specifically those for O_3, H_2O_2 and OH oxidation, for the South Pole. Their mass-balance method was that used by McCabe et al. (2006; see Eq. 1-5), in which only oxidation by O_3, H_2O_2 and OH is considered. Again, the $\Delta^{17}O_{ox}$ values after Alexander et al. (2005) were assumed (Alexander et al., 2009a; McCabe et al., 2006). Values for modern F_{ox} came from the global model of Alexander et al. (2009b), and values for preindustrial F_{ox} from the existing estimates that were being tested. Since the model of Alexander et al. (2009) predicted a small contribution of sulphate production via oxidation by O_2 for this region in the modern, this pathway was neglected for the calculations. Similarly, oxidation of SO_2 by O_3 is only included in clouds rather than on sea salt aerosols.

Sofen et al., (2011) used the global chemical transport model (also used by Alexander et al., 2009; Kunasek et al., 2010) to consider the variations of different oxidant concentrations in the atmosphere that would be necessary to reproduce this observed ice core $\Delta^{17}O_{SO4}$ from both the Arctic and Antarctic (presented by Alexander et al., 2004; Kunasek et al., 2010), again considering changes over the last century and a half. They simulate the variations in oxidant concentrations that may

have occurred since preindustrial times, and find that, again using a mass-balance method to predict $\Delta^{17}O_{SO4}$, the model results are consistent with measurements from the polar ice cores. In addition to the methods of Kunasek et al. (2010), since they model global rather than purely Antarctic $\Delta^{17}O_{SO4}$, they include additional pathways of i) oxidation by O_2 catalysed by transition metals (Alexander et al., 2009; McCabe et al., 2006); and ii) oxidation by O_3 in both clouds and on sea salt aerosols, which offer different pH conditions (Alexander et al., 2005). Also, slightly different values of $\Delta^{17}O_{ox}$ are used (8.75‰ for O_3, 0.65‰ for H_2O_2, 0‰ for OH, and -0.09‰ for O_2). For the northern hemisphere, the results support Alexander et al.'s (2009) findings of an increased role of oxidation by O_2 due to the anthropogenic release of transition metals as catalysts. Further, anthropogenic cloud acidification contributes towards this by reducing the role of oxidation by O_3 despite increasing tropospheric concentrations. For the southern hemisphere, Kunasek et al.'s (2010) estimates of varying role of O_3, H_2O_2 and OH in SO_2 oxidation over the time period are supported.

Sofen et al. (2014) use the same mass-balance method, again coupled to the global chemical transport model, to predict $\Delta^{17}O_{SO4}$ (and $\Delta^{17}O_{NO3}$) in an Antarctic ice core (with measurements presented across the last 2400 years). Again focussing on the last 200 years, they use concurrent ice core proxy measurements to show that the changes in $\Delta^{17}O$ over this period are due to variations in the contributions of different oxidants as opposed to other factors. Using a Monte Carlo simulation with varying relative contributions of each oxidant (using F_{ox} values as in Sofen et al. (2011), apart from F_{O3}, which is varied between 6.25‰ and 8.75‰), they show that the oxidant changes supported by the modelling studies of Kunasek et al. (2010) and Sofen et al. (2011) are consistent with the observations, but that there are other plausible combinations of variations in the relative contributions of O_3, OH and H_2O_2 that could explain the changes. However, an increase in $\Delta^{17}O_{SO4}$ of 1.1‰ is observed in the early nineteenth Century, which is less plausibly explained by an increase in O_3 relative to OH. A decrease in halogen species concentrations (which can also provide an oxidation pathway for sulphate production, with a low $\Delta^{17}O$

contribution) could explain this, although constraints on concentrations for this time period are lacking.

The studies discussed above have highlighted some of the sensitivities of $\Delta^{17}O$ values of nitrates and sulphates to atmospheric conditions, and have shown that there are large variations globally and with season. The mass-balance model method (Eq. 1-5) has been used by various authors (Alexander et al., 2005; 2009; Kunasek et al., 2008; 2010; McCabe et al., 2006; Sofen et al., 2011) to consider the influence of different oxidants on atmospheric salts. These simple model calculations have been helpful in granting an understanding of the role of different oxidants. Their coupling to global chemical transport models, which predict the importance of different oxidation pathways, has allowed the consideration of different atmospheric conditions, such as the effects of varying cloud pH, and has allowed the prediction of $\Delta^{17}O$ values globally. In contrast, a 1-D photochemical model is less capable of predicting $\Delta^{17}O$ in different geographical areas (though parameterisations for, e.g. latitude, temperature, and rainfall can be made (see Chapters 2 and 4)). However, one of the strengths of a photochemical model in comparison is that it does not require assumptions for F_{ox} and $\Delta^{17}O_{ox}$ values, as the $\Delta^{17}O_{SO4}$ and $\Delta^{17}O_{NO3}$ (and their precursor oxidants) would be predicted from steady-state production and loss of sulphate and nitrate from the different reaction pathways, in a manner consistent with other model inputs and atmospheric species.

A note on fieldwork in the Atacama Desert

In November 2017, I was involved in fieldwork in the Atacama Desert in northern Chile, where we collected samples along a ~800 km transect from the hyperarid core of the desert in the north (22.3°S) to regions further south with marginally more annual rainfall (as far as 28.4°S; see Shen et al, 2021). We took samples from the surface as well as some at depths of up to 2m. One of the goals of the fieldwork was to measure the triple oxygen isotope compositions of nitrate and sulphate from these samples and to assess the variation of the resulting data with rainfall. Although not achieved during the course of this thesis, I hope to use the data to calibrate the

oxygen isotope model developed in Chapters 4, 5 and 6 for scenarios with varying rainfall.

1.5.2 – How have oxygen isotope models aided understanding of $\Delta^{17}O$ over geologic time?

1.5.2.1 - O-MIF data in the geological record?

The review in Section 1.5.1 showed that triple oxygen isotope measurements and modelling can inform us about the atmosphere today, and in recent palaeoclimate studies, particularly pertaining to the oxidising capacity of the atmosphere. However, oxygen isotope anomalies have been preserved in the geological record further back in time, with measurements from various intervals throughout the Phanerozoic and Proterozoic (see, e.g. Crockford et al., 2019). This longer-term oxygen isotope record is of particular interest for this thesis.

Most of the O-MIF data that we have from the geological record, at least from before ~2 Ma, is from sedimentary sulphates (Bao, 2015; Crockford et al., 2019). The red points on Figure 1-2 show $\Delta^{17}O$ values in the sulphates deposited over Earth history. In the modern and past 60 million years, there are many positive $\Delta^{17}O$ values for sulphates, which, as explained above, indicate that the sulphates have at least a partial atmospheric source, and have been produced via oxidation with O_3 or H_2O_2. Further back in time, the measured $\Delta^{17}O$ values for geological sulphates are negative. This is because atmospheric salts, including sulphate, are soluble and easily washed away, and palaeo-deserts are unlikely to be preserved in the long-term geological record. Ultimately, dissolved atmospheric sulphates will end up in the oceans, where there is a much larger reservoir of sulphate with no atmospheric signature, and any observable positive anomalous isotope composition is lost.

Sulphates in the geological record may instead have a negative $\Delta^{17}O$ value because oxygen is incorporated into sulphate molecules during oxidative weathering of pyrite (Bao et al., 2008; Bao, 2015). Since molecular oxygen has a small, negative $\Delta^{17}O$, some of this signal can be imparted to product sulphate. Like perchlorate,

sulphate is a stable tetrahedral molecule not liable to breakdown or exchange. It is considered a good archive because the high temperatures and acidity of fluids required to cause isotopic exchange with the fluid are likely to dissolve the sulphate itself (Bao, 2015). The oxygen atoms in sulphate are therefore considered a direct record of atmospheric O_2 $\Delta^{17}O$ for palaeo-atmospheres. However, this can be muted by intense biological sulphur cycling and is therefore considered a conservative tracer (Brunner et al., 2012; Crockford et al., 2019). In other words, the magnitude of a $\Delta^{17}O$ measurement can be reduced but not increased beyond the original signal by post-depositional processes.

Due to the difficulty of preservation of sulphates in general, a high-resolution record of triple oxygen isotope measurements for the whole of the Proterozoic and Phanerozoic is challenging to achieve, and the data is sparse. However, Figure 1-2 shows that non-zero $\Delta^{17}O$ values in sulphates have been observed throughout the Phanerozoic and Proterozoic, and the record is growing (e.g. Bao et al., 2008; 2009; Benn et al., 2015; Crockford et al., 2019; Peng et al., 2011; 2013; Warke et al., 2020a). Since mass-independent fractionation of oxygen isotopes on Earth occurs solely in the processes involved in ozone formation, no anomalous oxygen isotope signatures are expected to be observed before the Great Oxidation Event, when there was little free oxygen and therefore little ozone (Kasting and Donahue, 1980; Kasting et al., 1985; Segura et al., 2003). Values of $\Delta^{17}O$ since the GOE are primarily negative and fairly small, with a couple of episodes of particularly low $\Delta^{17}O$ values in the mid-Proterozoic (~1.4 Ga) and at the end of the Cryogenian period (~635 Ma) (Bao et al., 2008; 2009; Crockford et al., 2018). These two minima are of particular interest and will be discussed in further detail later in this section.

1.5.2.2 – How have MIF models helped us to understand these signals so far?

Various models have been developed in order to interpret $\Delta^{17}O$ values from the geological record in terms of atmospheric composition. Here I describe some of the models and the problems they have attempted to solve. To begin, the following

subsection is a review of the assumptions previous studies have made about the way in which the oxygen isotope signal is transferred from tropospheric O_2 to sulphate.

Sulphate as a record of $\Delta^{17}O$ in tropospheric O_2

Bao (2015) argues that sulphate is the best geologic "time capsule" to store palaeo-variations in the atmospheric $\Delta^{17}O$ of O_2. The extrapolation of sulphate $\Delta^{17}O$ to reproduce molecular oxygen $\Delta^{17}O$ requires an estimate of the proportion of oxygen atoms in sulphate that are derived from atmospheric O_2 as opposed to other oxidants with negligible $\Delta^{17}O$. However, this value is uncertain.

Estimates from experiments involving the tracing of ^{18}O range from 0 to 60%, (see e.g. reviews and references in Bao, 2015 and Kohl and Bao, 2011). Various estimates have been given by pyrite oxidation experiments. Those of Balci et al. (2007) suggested a contribution from O_2 of 8-15% of the oxygen atoms, which was not influenced by the presence of bacteria. These values, along with the relative magnitudes of modern seawater sulphates and tropospheric O_2, led Bao et al. (2008) to use a value of 10% ± 10% in their model. Crockford et al. (2018) and Planavsky et al. (2020) also used the estimates 8-15%, accounting for uncertainty by varying the value chosen between these limits with a uniform distribution in their Monte Carlo simulations. Bao et al. (2009) considered 10% and 25% as minimum and maximum values, the latter later supported by further abiotic pyrite oxidation investigations at various pH values, which resulted in a range of values between 21% and 29% (Kohl and Bao, 2011).

For the most part, the estimates above depend on the oxidation of sulphide minerals (e.g. pyrite) being an important mechanism in the formation of sulphates with anomalous O-MIF signatures. This has recently been questioned by Hemingway et al. (2020), who investigated a modern pyrite-oxidising system in the mountainous river systems of the Himalayas. They found that pyrite oxidation may occur by oxidants with a positive $\Delta^{17}O$, such as H_2O_2, and not necessarily by direct oxidation by O_2. However, acknowledging that geologic $\Delta^{17}O$ of sulphate is negative not

positive, they suggest that the negative O_2 signal may be incorporated via processes such as secondary sulphur recycling in the floodplain.

If, as they suggest may be the case, incorporation of O_2 into sulphate is not primarily via pyrite oxidation, the utility of the values given by the experiments above could be called into question. This is clearly something that needs further investigation. Because of this uncertainty, as well as secondary processes (e.g. involving microbes) acting to erase the $\Delta^{17}O$ signal in sulphate, it is considered most conservative to use the highest value for the proportion of oxygen atoms derived from atmospheric O_2 to extrapolate from sulphate $\Delta^{17}O$ to O_2 $\Delta^{17}O$, or to calculate a possible range with minimum and maximum values. This prevents an overestimate of the magnitude of palaeo-tropospheric $\Delta^{17}O_{02}$, and its invoking of extreme atmospheric conditions. However, to avoid the opposite problem, it is important to consider the depositional environment of the sulphates chosen, where possible identifying and using sulphates which have not had a chance to exchange fully with water and gain its negligible $\Delta^{17}O$ (Bao, 2015). From the data perspective, the most relevant piece of information may be the most negative $\Delta^{17}O$ value measured in a given environment.

$\Delta^{17}O$ and mid-Proterozoic atmospheres

As discussed in Section 1.5.1, the $\Delta^{17}O$ of tropospheric O_2 has been shown to be highly influenced by pCO_2, pO_2, and GPP. However, for ancient atmospheres, it is unclear how these three factors together may contribute towards the ultimate $\Delta^{17}O$ value recorded in a preserved sulphate.

Extremely low $\Delta^{17}O$ values were recorded in mid-Proterozoic (~1.4 Ga) sediments in the Sibley Basin in Ontario, Canada (Crockford et al., 2018). Crockford et al. (2018) used a Monte Carlo simulation, varying factors including pCO_2 and pO_2 across a range of values, to argue that low GPP was required to produce these signals. Specifically, they assume that pCO_2 was between 2 and 30 times modern levels, and conclude that, assuming the pO_2 was between 0.1-1% PAL or 1-10% PAL, GPP must have been either around 6% or 40% what it is today. They use a lower limit on pO_2 of 0.1% since this is the threshold value at which an ozone layer can form, according

to the model of Segura et al. (2003), although it has not been demonstrated what (if any) $\Delta^{17}O$ would be generated in an atmosphere with these O_2/O_3 concentrations. The 6% modern GPP value was preferred by the authors, since it seems to better fit with other proxies for biological cycling at that time. Other variables adjusted in the Monte Carlo simulation were the proportion of sulphate atoms that originate in tropospheric O_2 (varied uniformly between 8 and 15%; see above), the rate of troposphere-stratosphere exchange, the pO_2-pCO_2 ratio, the $\delta^{18}O$ value of CO_2, and the slope and intercept of the $\delta^{18}O$-$\Delta^{17}O$ line.

Planavsky et al. (2018) built on this work and proposed a maximum GPP of 3% that of modern, and pO_2 between 0.1% and 1.75% PAL. Later, Planavsky et al. (2020) used a similar Monte Carlo approach to constrain pO_2 during the mid-Proterozoic, using the same $\Delta^{17}O$ values from the mid-Proterozoic sulphates. These two studies improved upon that of Crockford et al. (2018), in that the Monte Carlo simulation better connected model variables that are correlated. In particular, the models run by Crockford et al. (2018) include no direct connection between pO_2 and primary productivity (although a correlation is seen in the results). In contrast, Planavsky et al. (2020) explicitly connect these parameters such that there are no model simulations with, for example, an enforced low GPP and inconsistently high pO_2. They conclude that mid-Proterozoic oxygen levels were below 1% PAL for some parts of the Proterozoic, since most combinations of pO_2, pCO_2 and primary productivity, which were consistent in terms of the Earth system and also explained the $\Delta^{17}O$ values, had low pO_2.

$\Delta^{17}O$ and the aftermath of a Snowball Earth event

Bao et al. (2008) reported $\Delta^{17}O$ values from sulphates over the last 750 million years, focussing on particular minimums in the early Cambrian, and at around 635 Ma. For the latter interval, $\Delta^{17}O$ values were low for a duration of up to one million years, and constitute the most negative values observed in the geological record (Bao et al., 2008, 2009; Killingsworth et al., 2013; see Figure 1-2). This was presented as potential evidence for very high pCO_2 for this interval, consistent with two existing hypotheses (Bao et al., 2008).

The first is the 'Snowball Earth' hypothesis. This is the theory that the Earth was globally glaciated for several million years (Hoffmann et al., 1998). The first lines of evidence for this were cap carbonates deposited directly above glacial diamictites (Kennedy et al., 1996), glacial signatures, such as dropstones and glacial tills at low palaeolatitudes (Schmidt and Williams, 1995), and negative carbon isotope excursions (Hoffmann et al., 1998; Kaufman et al., 1997; Knoll et al., 1995). As ice covered increasing low latitudes, the Earth's albedo increased, causing temperatures to drop further, and resulting in a positive feedback. The deglaciation is thought to have been triggered by a build-up of volcanic carbon dioxide, producing a greenhouse effect, which caused a runaway global warming as ice melted and albedo decreased again (Hoffmann et al., 1998). The pCO_2 estimated by Bao et al. (2008) from carbonate-associated sulphates from the cap carbonates could be CO_2 remaining from such high levels. The second hypothesis is the massive release of methane from clathrates following the Neoproterozoic glaciation (Kennedy et al., 1996). This methane, when oxidised, would cause high pCO_2, also consistent with the results of Bao et al. (2008).

In the following years, further triple oxygen isotope data was presented. Marinoan carbonate-associated sulphates from Svalbard were found to bear even lower $\Delta^{17}O_{SO4}$ values (Bao et al., 2009). If the one-dimensional model from Bao et al. (2008) is used, this corresponds to predicted pCO_2 concentrations of 12,500-80,000 ppm (~45-285 times preindustrial atmospheric levels, PAL) during the deposition of the carbonates. An alternative explanation presented is that a very low pO_2 could produce similar results, but only if the residence time of O_2 is long, which would require very reduced rates of biologic uptake and production. Either way, these results are presented as consistent with the 'Snowball Earth' hypothesis.

Variable $\Delta^{17}O_{SO4}$ values from two coeval sites in South China were also presented (Peng et al., 2011). Heterogeneity correlated to other geochemical proxies suggested that $\Delta^{17}O_{SO4}$ values were more negative in sediments formed near the palaeo-continents rather than in the open ocean, supporting the previous claims that $\Delta^{17}O_{SO4}$ values are a product of terrestrial oxidation of sulphides. An understanding

of the global distribution of highly negative $\Delta^{17}O_{SO4}$ values was further established by similar observations in Western Australia (Bao et al., 2012).

The proposed high-pCO_2 hypotheses were challenged by Sansjofre et al. (2011), who used paired carbon isotope data from cap carbonates in Brazil to give an upper limit on pCO_2, which was much lower than the values given by Bao et al. (2008; 2009), and was concluded inconsistent with the 'hard-snowball' (in which the atmosphere and ocean are isolated from one another by ice). The difference between the $\delta^{13}C$ for associated carbonate and organic carbon ($\Delta^{13}C_{carb\text{-}org}$) is a proxy for pCO_2, because it is dependent on the CO_2 concentration in the oceans, and therefore the atmosphere (Hayes et al., 1999). The low values found by Sansjofre et al. (2011) indicate low pCO_2, specifically 400 – 3200ppm (~1.5-11 PAL).

Sansjofre et al. (2011) argued that the triple oxygen isotope data presented by Bao et al. (2008) could be explained by either a lower pO_2 or a longer residence time of O_2 in the atmosphere. While Bao et al. (2008) use a pO_2 of 20%, Sansjofre et al. (2011) argue that evidence of low Ediacaran pO_2 renders a value more like 1% more appropriate; this gives a pCO_2 of around 600ppm (~2 PAL), within their prediction limits. Similarly, Young et al. (2014) find that reducing the GPP in their model reduces the pCO_2 required to reproduce the $\Delta^{17}O$ values from 20,000 ppm (~71 PAL) for modern GPP to less than 1000 ppm (~4 PAL) for lower O_2 inputs.

Cao and Bao (2013) used a four-box model (with boxes for the land, hydrosphere, troposphere and stratosphere) to investigate further whether alternative atmospheric conditions other than high pCO_2 (Bao et al., 2008; 2009) could produce the observed triple isotope values. The model produced solutions at steady state as well as allowing for the simulation of dynamically-changing $\Delta^{17}O_{O2}$ with various inputs. The latter allowed a time-dependent comparison of model results to observations. For this model, as opposed to that of Bao et al. (2008) and Sansjofre et al. (2011) an O_2 residence time did not need to be assumed. Out of the 'geologically reasonable' scenarios they modelled, they concluded that ultra-high pCO_2 concentrations were the most likely cause of the excursion. Low pO_2 was deemed

unlikely to play a key role because when they reduced the biological O_2 flux by 80%, the tropospheric $\Delta^{17}O_{O2}$ had a longer lasting and less negative excursion than observed in the rock record.

The crux of the debate is the interplay between the effects of pO_2, pCO_2 and primary productivity on the triple oxygen isotope signatures. Further work in constraining the factors affecting $\Delta^{17}O$ values in the rock record, particularly the importance of the influence of stratospheric chemistry, will be key in better understanding past atmospheres, such as at the end of the Marinoan glaciation.

$\Delta^{17}O$ in the Phanerozoic

As well as particularly low $\Delta^{17}O$ values at 635 Ma, Bao et al. (2008) also reported $\Delta^{17}O$ values throughout the Phanerozoic. They found particularly low values for the early Cambrian, which they interpreted as an indication of CO_2 levels more than ten times higher than in the modern atmosphere for this time period. The lowest measured $\Delta^{17}O$ values for the Phanerozoic to date are from the late Carboniferous/early Permian (Warke et al., 2020a), which we intend to probe in future work using the model developed in this thesis.

1.6 – $\Delta^{17}O$ as a promising proxy for palaeo-atmospheric composition

The discussion above shows that triple oxygen isotope signatures are a useful tool in investigating modern atmospheric processes, as well as probing palaeo-atmospheric composition on timescales ranging from the last 200 years to the last 2.45 billion years. In particular, it is a promising proxy for investigating the concentrations of O_2 that may have existed over Earth history. As a proxy that directly captures and preserves oxygen atoms from the atmosphere, it is strong compared to some other proposed atmospheric proxies such as redox-sensitive elements, or marine proxies which might tell a different story to that of the palaeo-atmosphere. Since the ozone-forming reaction is the only known terrestrial process

that produces O-MIF, the production of the signature is fairly well understood (Thiemens et al., 2012), and its utility as a diagnostic of atmospheric ozone chemistry is undisputed.

However, while the models described above have been useful in furthering the understanding of how O-MIF signals are transferred, affected by other factors, and preserved, the use of an oxygen isotope photochemical model is a useful direction for future research. Box models (e.g. Cao and Bao, 2013; Young et al., 2014) necessarily make assumptions regarding incoming light, concentrations of different species, and temperature, selecting one or two values representative of the whole atmospheric column. In contrast, a 1-D photochemical model incorporates atmospheric chemistry at different heights, thereby taking into account the concentrations of different species at each height and the resulting photolysis-driving UV fluxes that penetrate to different altitudes. This is particularly useful when considering the relationships between oxygen-bearing species, which are involved in processes that behave differently in the stratosphere and troposphere, and at different altitudes within these parts of the atmosphere. A photochemical model can also explore altitude-dependent temperature and pressure profiles, which can greatly affect the reaction rates of different species.

In this thesis, we therefore use and develop the 1-D photochemical model *Atmos* to include the three isotopes of oxygen (see Chapter 4). This model (or closely-related models) have been applied to the modern Earth, as well as early Earth atmospheres (e.g. Catling et al., 2010; Claire et al., 2014; Izon et al., 2019; Zerkle et al., 2012) and the atmospheres of other planets (e.g. Domagal-Goldman et al., 2014; Harman et al., 2018). This and similar photochemical models have been developed successfully to inform about the way in which sulphur MIF signals are propagated through the atmosphere and preserved (Claire et al., 2014; Pavlov and Kasting, 2002).

1.7 – Aims and thesis overview

Atmospheric composition, particularly in terms of oxygen levels over Earth history remains an interesting area of research, with considerable uncertainty. The aim of this thesis is to work towards a better constraining of atmospheric O_2 (and, to a lesser extent, pCO_2) for the second half of geological history.

Chapter 2 is an introduction to the 1-D photochemical model, *Atmos*, that we use and develop in the remainder of the thesis. Before developing, tuning and applying the oxygen isotope model, we undertake a systematic sensitivity study of the original model to the user-specified lower boundary conditions (Chapter 3). We find that the use of fixed flux boundary conditions for important redox species O_2 and CH_4 produces different results to previously-published models using fixed mixing ratio boundary conditions. This study provides potential constraints on pO_2 throughout Earth history, with a particular focus on the Proterozoic and Phanerozoic, since steady-state solutions are less prevalent and more unstable to perturbations in flux within certain pO_2 windows. The work in this chapter has been published in the journal *Earth and Planetary Science Letters*, as 'Gregory, B.S., Claire, M., and Rugheimer, S., 2021. *Photochemical modelling of atmospheric oxygen levels confirms two stable states.*'

The objective of the rest of the thesis is the development and application of the oxygen isotope model to predict $\Delta^{17}O$ that will exit the atmosphere for potential storage in geological materials under different atmospheric conditions. In Chapter 4, I describe the way in which the model was developed during this project to include the three isotopes of oxygen. Chapter 5 continues to describe the oxygen isotope model development, including the tuning of the model such that it better reproduces modern measurements. We include key processes, reactions and experimentally-determined fractionation factors. The sensitivity of model $\Delta^{17}O$ outputs to various parameters, such as rainfall, temperature and latitude, is also demonstrated.

Chapter 6 applies the oxygen isotope model developed in Chapters 4 and 5 to Proterozoic and Phanerozoic atmospheres, since O-MIF is only produced in atmospheres with an ozone layer, which did not exist before the GOE. We use the model to explore variation of oxygen isotope signals under various pO_2 and pCO_2 conditions outside those observed for the modern Earth, which can be compared to observations from the rock record. We particularly focus on some of the most negative $\Delta^{17}O$ observations from the mid-Proterozoic and the Cryogenian, discussed above, in order to contribute towards the community's discussion of how pO_2, pCO_2 and GPP may have affected preserved O-MIF.

Chapter 7 concludes the thesis, in which I will draw together the potential constraints that the three studies have provided in relation to pO_2 and pCO_2 over Earth history, and highlight areas for improvement and future study.

Chapter 2

Methods

For the work in this thesis we have used and built on the one-dimensional photochemical model *Atmos* (open source code available via https://github.com/VirtualPlanetaryLaboratory/atmos). Here, we describe the model and explain why it is a good tool for addressing the research questions presented.

2.1 – Introduction to the model *Atmos*

We use the 1-D photochemical model *Atmos*, which calculates the mixing ratios of included species in the atmosphere with altitude as determined by specific boundary conditions. Steady state solutions are obtained by running a time-dependent reverse Euler method solver to extremely long timesteps, which provides solutions for stiff numerical equations that are unconditionally convergent to those provided by Newton's method.

The model simulates a column through the atmosphere, from a lower boundary representing an altitude of 0 km (at the ground) to an upper boundary at the top of the atmosphere. The top of the atmosphere is dictated by the user-specified number of 0.5 km-thick layers or grid steps on the altitude grid, NZ. For the models presented here, NZ=160 for the flux-driven models described in Chapter 3, and NZ=200 for the oxygen isotope model described in Chapters 4, 5 and 6. This corresponds to an upper boundary at 80 km and 100 km respectively. The height of the tropopause can also be specified; in the models presented here, it is fixed at an altitude of 11 km.

The atmospheric density is determined through the assumption that the surface pressure is 1 bar.

At the lower boundary of the model, there are fluxes of gases into and out of the atmosphere, as well as deposition of particles. At the upper boundary, there is hydrogen escape to space (Zahnle et al., 2006), and fluxes of light at wavelengths 121.6 - 850 nm at roughly 2 nm resolution into the model atmosphere. Fluxes of gases across the boundaries are dictated by lower and upper boundary conditions, which are detailed further in Section 2.5. The model calculates the production and loss of chemical species involved in hundreds of kinetic and photochemical reactions. The model also includes the transport of long-lived species into and out of each grid step, via eddy and molecular diffusion, as well as parametrising process such as rain, particulate formation and fallout, and lightning.

Figure 2-1 shows a schematic of the model setup. The following subsections detail some of the ways in which the output steady state species mixing ratios are calculated.

2.2 – Reaction rates

For the models used in Chapter 3, 77 chemical species are produced and destroyed in each layer by 311 kinetic and 61 photolysis reactions. For the models in Chapters 4, 5 and 6, the addition of oxygen isotopes (and removal of some species, including chlorine-bearing species) results in 97 species involved in 784 kinetic and 148 photolysis reactions. The model templates used in this thesis include parameters relevant to the modern Earth and are calibrated to modern measurements. For a discussion of the sensitivity of the oxygen isotope model outputs to these parameters, see Chapter 5.

The rate at which a species, A, is produced, k_P, is:

$$k_P = \Sigma \kappa_r [C][D] \qquad \textit{(Eq. 2-1)}$$

where *[C]* and *[D]* are the number densities of reactant species *C* and *D*. The number density of a species is the number of molecules of that species per unit volume; in this thesis we use units of molecules cm^{-3}. The number density is equal to the mixing ratio of the species (unitless) multiplied by the density of the atmosphere (in units of molecules cm^{-3}). κ_r is the rate constant for reaction *r* (denoted J_r for photolysis reactions), and $\kappa_r[C][D]$ (or $\kappa_r[M][C][D]$ for three-body reactions, where [M] is the density of the atmosphere) is integrated over the number of reactions with species *A* as a product (Finlayson-Pitts and Pitts, 2000, p131).

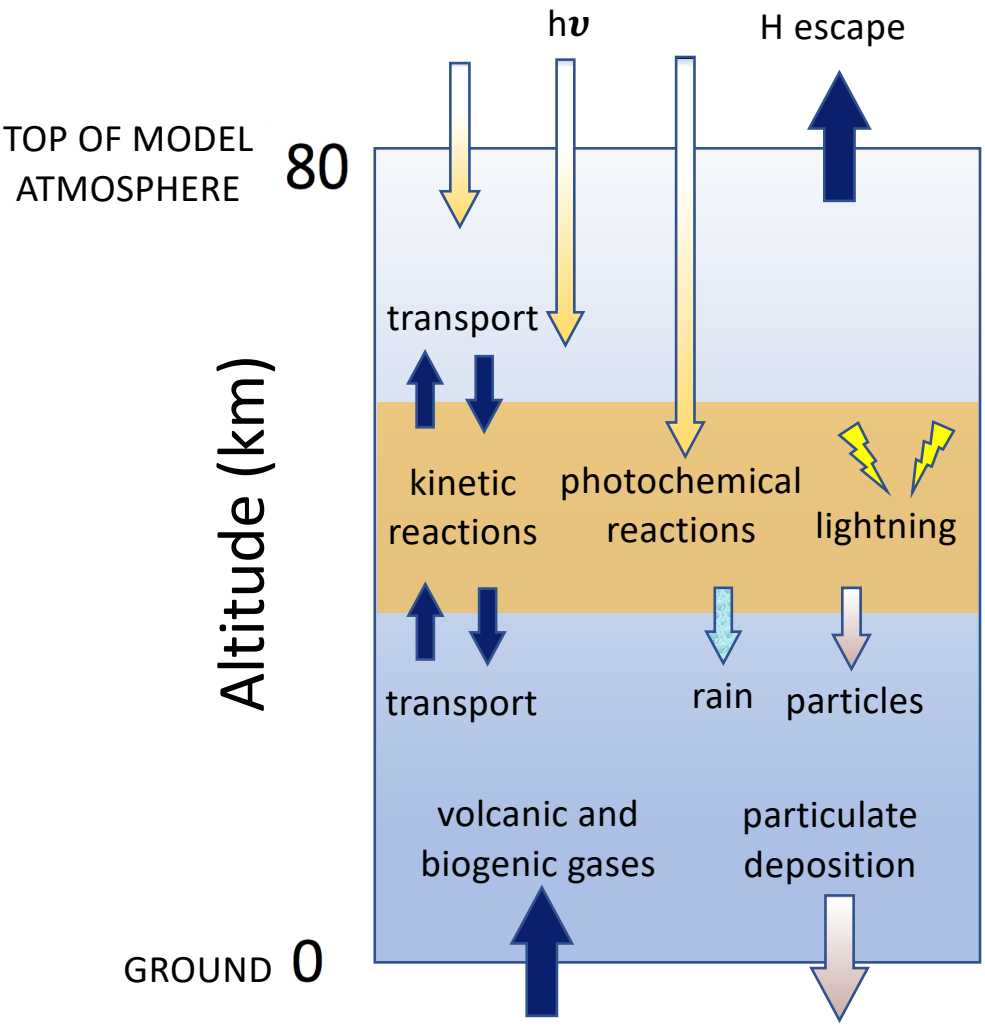

Figure 2-1: Setup of 1-D photochemical model. Yellow band represents one of NZ model grid steps, of thickness 0.5 km. See text for explanation of different processes incorporated.

The rate at which species *A* is destroyed, k_L is given by:

$$k_L = \Sigma \kappa_r [A][B] \qquad \textit{(Eq. 2-2)}$$

where κ_r is the rate constant of reaction *r*, and *[A]* is the number density of species *A*. Here, *[B]* is the number density of any species which reacts with A. κ_r*[A][B]* is integrated over the reactions for which species *A* is a reactant.

The rate constants come from recommendations from the JPL, NIST, KIDA and IUPAC databases (Atkinson et al., 2004; Burkholder et al., 2015; Manion et al., 2015; Wakelam et al., 2012). They are calculated for each reaction for each grid step (i.e. for each altitude), since the reactions are often dependent on temperature, pressure (in the case of three-body reactions), incoming light (in the case of photolysis reactions), or some combination of the three.

2.2.1 – Kinetic reaction rates

For two-body kinetic reactions, the rate constant (κ_r, in units of cm^3 $molecule^{-1}$ s^{-1}) is dependent on temperature (*T*) following the relation:

$$\kappa_r = A \left(\frac{T}{300}\right)^n e^{\left(-\frac{E}{RT}\right)} \qquad \textit{(Eq. 2-3)}$$

where *E* is the activation energy, *R* is the universal gas constant, and *A* and *n* are constants specific to each reaction, which have been experimentally or theoretically determined (Burkholder et al., 2015). The inclusion of the term $(T/300)^n$ accounts for a deviation from the Arrhenius relation with variation in *T* (Burkholder et al., 2015; Finlayson-Pitts and Pitts, 2000, p138).

Three-body reactions are pressure dependent, as they require the energy from a collision with a third body, *M*, in order to occur. In the modern atmosphere, *M* is usually N_2 or O_2. The rate constant for these reactions is:

$$\kappa_r = \left(k_0[M]/(1+\frac{k_0[M]}{k_\infty}\ )\right)0.6^{1/(1+(log\ (\frac{k_0[M]}{k_\infty})^2)} \qquad \textit{(Eq. 2-4)}$$

where [M] is the atmospheric density (molecules cm^{-3}), and k_0 and k_∞ (cm^6 $molecule^{-2}$ s^{-1}, and cm^3 $molecule^{-1}$ s^{-1}, respectively) are the low- and high-pressure-limiting rate constants, respectively, defined by:

$$k_0 = A_0\left(\frac{T}{300}\right)^{-n} e^{\left(\frac{-E_0}{RT}\right)} \qquad \textit{(Eq. 2-5)}$$

$$k_\infty = A_\infty\left(\frac{T}{300}\right)^{-m} e^{\left(\frac{-E_\infty}{RT}\right)} \qquad \textit{(Eq. 2-6)}$$

Here, A_0, A_∞, n, m, E_0 and E_∞ are constants theoretically or experimentally determined for each reaction (Burkholder et al., 2015).

2.2.2 – Photolysis reaction rates

Photolysis reactions involve the breakdown of molecules due to the absorption of energy from the Sun, which comes into the model atmosphere over the upper boundary.

The photolysis rate constant, J_r (units of s^{-1}), of a certain reaction is calculated as:

$$J_r = \sum_{\lambda=121.6}^{850} F(\lambda)\sigma(\lambda)\phi(\lambda) \qquad \textit{(Eq. 2-7)}$$

Here $F(\lambda)$ is the actinic flux incident at the altitude of the grid step, integrated over all directions (units: photons cm^{-2} s^{-1}). σ is the absorption cross-section for the species (units: cm^2 $molecule^{-1}$). ϕ is the quantum yield (units: molecules $photon^{-1}$).

2.2.2.1 – Actinic flux

At each altitude grid step, light at different wavelengths is absorbed, scattered or radiated by different species, which exist at different concentrations. The model uses the mixing ratios of each species at each grid step to calculate the resulting actinic flux over the wavelength spectrum. Figure 2-2a shows the incoming 'top of

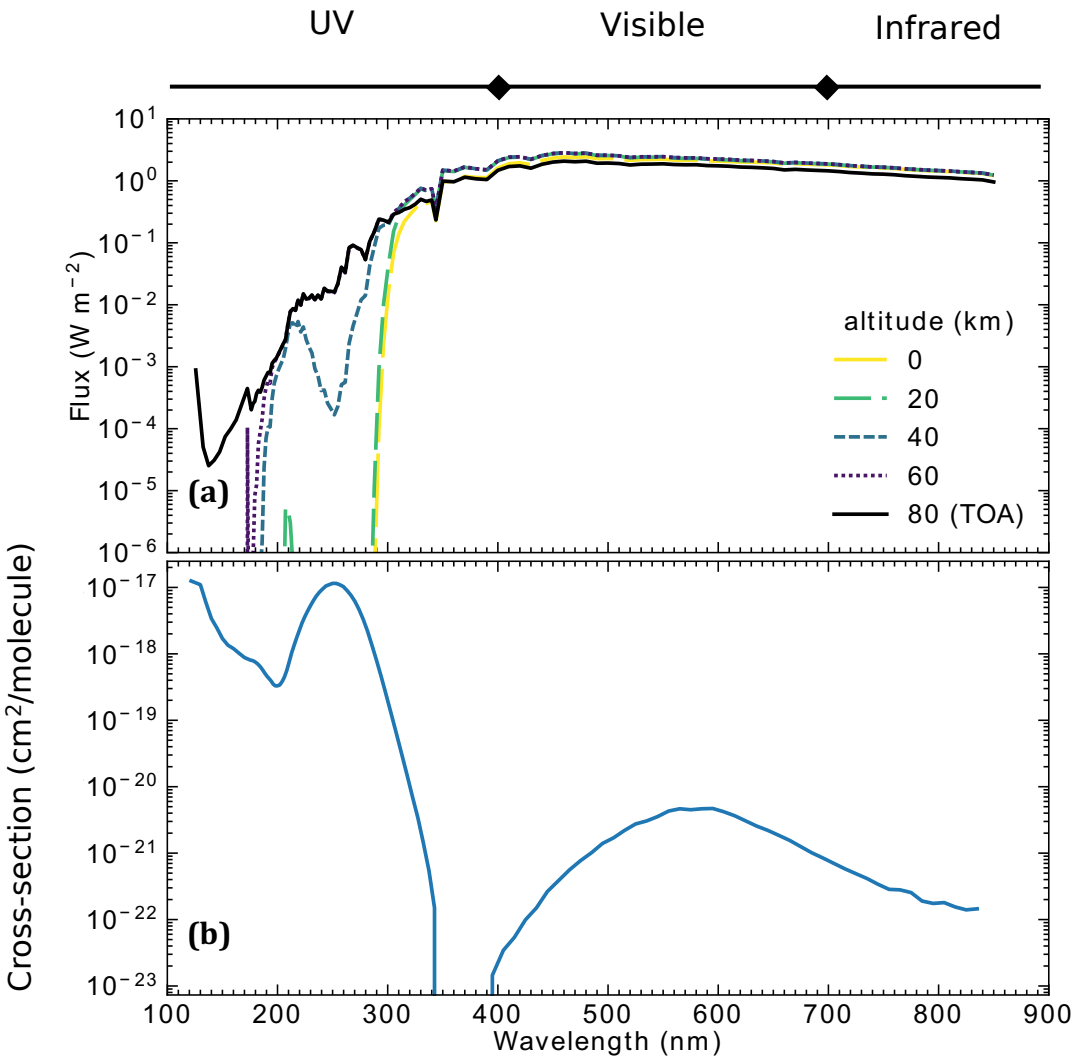

Figure 2-2: ***(a)*** *Fluxes of light of different wavelengths at different altitudes in the atmospheric column, for the 'Modern Earth+Cl' model used in Chapter 3. The incoming 'top of the atmosphere' (TOA) flux is shown in black.* ***(b)*** *TOA ozone absorption cross-section used in the model. Peak ozone absorption at 253 nm coincides with a dip in flux at lower altitudes in (a). Labels at the top of Figure (a) show wavelengths corresponding to different parts of the electromagnetic spectrum.*

the atmosphere' (TOA) flux (black line) for a modern atmosphere, across the model wavelength spectrum of 121.6-850 nm. Also shown are the fluxes at different altitudes, after the interactions with molecules in each grid step are taken into account. It can be seen that the actinic flux at UV wavelengths reduces with increasing path length (i.e. distance from the top of the atmosphere), and for this modern-like atmosphere, with high O_2 mixing ratios, almost all light is blocked at the ground-level within the harmful UV spectrum (for wavelengths shorter than 290

nm). The incident fluxes will be affected by the solar zenith angle chosen; for the model templates presented in this thesis, we use a zenith angle of 50°, and assume a diurnally-averaged flux (Catling et al., 2010; Claire et al., 2014; Guzmán-Marmolejo et al., 2013; Lyons, 2001; Zahnle et al., 2006). The surface albedo for these models is 0.25.

2.2.2.2 – Absorption cross-section

The absorption cross-section is a measure of the effectiveness of a species to absorb light at different wavelengths. Each species with a photolysis reaction is allocated an absorption cross-section. As an example, the absorption cross-section for O_3 used in the model is shown in Figure 2-2b. It can be seen that ozone is most effective at absorbing light with wavelengths of around 255 nm. The effective absorption of UV light by the ozone layer in a modern atmosphere is the reason for the absence of a ground-level UV flux seen in Figure 2-2a above.

2.2.2.3 – Quantum yield

The quantum yield for a photolysis reaction is a measure of how often the absorption of a photon causes photodissociation of the absorbed molecule, and is a fraction between 1 (for cases where every photon absorbed causes the molecule to break apart) and 0. The quantum yield may be dependent on wavelength.

2.2.3 – Temperature

Since many atmospheric reactions depend on temperature, a fixed temperature profile is specified. The profile used for the results presented in this thesis is shown in Figure 2-3a, and is a simplification of the measured temperature profile for the modern atmosphere (US Standard Atmosphere, 1976). The minimum point is the tropopause. There are maxima: i) at the surface, where the temperature is 288.15 K (or 15°C), due to the emission of infrared radiation after higher energy light has been absorbed by the Earth acting as a black body, and ii) the stratopause, where there is sufficient ozone to absorb high energy photons in the upper atmosphere. There is a linear temperature gradient in the troposphere of -6.5 K/km.

2.3 – Vertical transport of molecules

As well as production and loss of different species via reactions within each grid step, vertical transport of molecules between grid steps also contributes towards the calculation of resulting steady-state mixing ratios at different altitudes. This is dictated by eddy diffusion and molecular diffusion terms, which are parametrisations of 3-D transport processes for use within a 1-D model.

Eddy diffusion represents vertical mixing in the atmosphere, and affects all long-lived species in the model. The eddy diffusion terms vary with altitude, as shown in Figure 2-3b. The terms used in Chapters 4, 5 and 6 are from Massie and Hunten (1981). The resulting fluxes, F of species i, depend on the mixing ratio gradient of i, as:

$$F_i = -K[M]\frac{\partial f_i}{\partial z} \qquad \textit{(Eq. 2-8)}$$

where K is the eddy diffusion coefficient ($cm^2\ s^{-1}$), $[M]$ is the atmospheric density (molecules cm^{-3}), f_i is the volume mixing ratio of species i, and z is the altitude.

A molecular diffusion term is also implemented for the lightest species, H and H_2, only. The fluxes of these species between grid steps in the model are defined as:

$$F_i = [M]f_i \left(\frac{b_{i,air}}{[M]}\left(\frac{1}{H_{air}} - \frac{1}{H_i}\right)\right) \qquad (\textit{Eq. 2-9})$$

H_{air} and H_i are the scale heights of the air and species i, respectively, equal to $kT/m_{air}g$ and kT/m_ig, respectively (where k is Boltzmann's constant, T is the temperature, m_{air} and m_i are the average molecular mass of air and the molecular mass of species i, respectively, in grams, and g is the acceleration due to gravity). The subscript i indicates H or H_2. In *Atmos*, the binary diffusion coefficients, $b_{H,air}$ and $b_{H2,air}$, are $2.7\times10^{19}(T/200)^{0.75}$ and $1.4\times10^{19}(T/200)^{0.75}$, respectively (Marrero and Mason, 1972). Hydrogen escape can be calculated from this equation using values for $b_{i,air}$, $[M]$, f_i, T, H_{air} and H_i for the upper-most grid step.

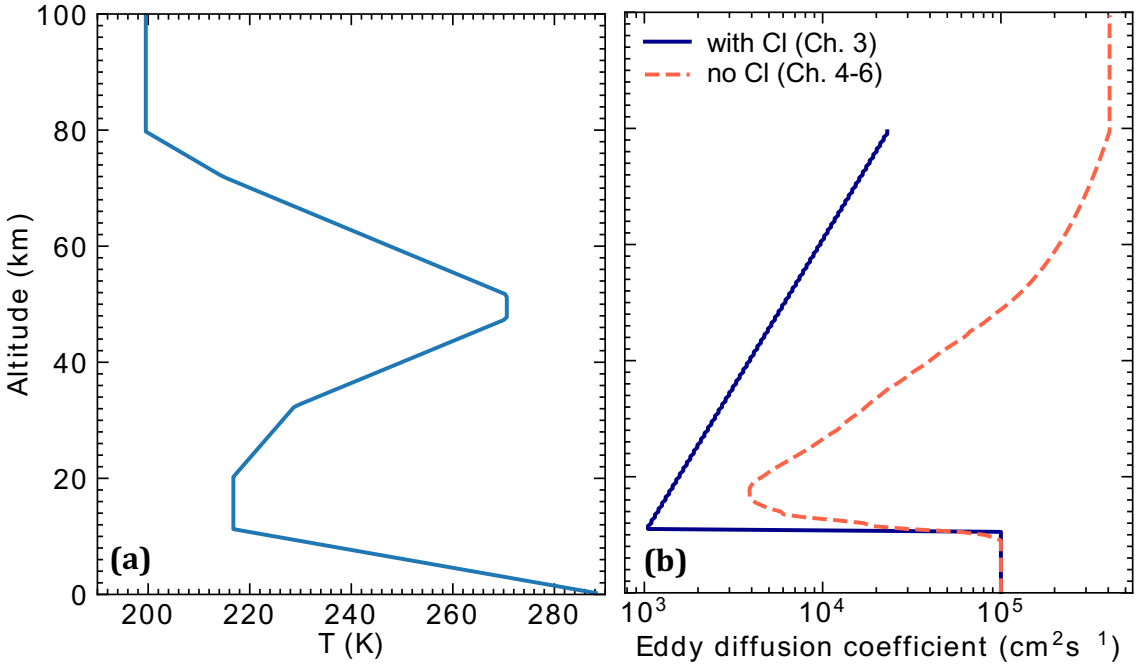

*Figure 2-3: **(a)** Temperature profile, and **(b)** eddy diffusion profiles for models presented in this thesis. All models presented here use the same T profile; the eddy diffusion profile differs between the models in Chapter 3 and Chapters 4–6.*

2.4 – Additional processes

2.4.1 – Lightning

The effects of lighting are included in the model troposphere, through the production and loss of certain species at rates equal to those of thermodynamic equilibrium at 3500 K (Kasting and Donahue, 1980 (who used T=2300 K); Claire, 2008). The species involved, and their reactions at thermodynamic equilibrium are:

$$\frac{1}{2}N_2 + \frac{1}{2}O_2 \leftrightarrow NO \qquad \textit{(Eq. 2-10)}$$

$$H_2O \leftrightarrow H_2 + \frac{1}{2}O_2 \qquad \textit{(Eq. 2-11)}$$

$$CO_2 \leftrightarrow CO + \frac{1}{2}O_2 \qquad \textit{(Eq. 2-12)}$$

$$\frac{1}{2}O_2 \leftrightarrow O \qquad \textit{(Eq. 2-13)}$$

2.4.2 – Rainout and H_2O

As with lightning, the inclusion of rainout of species only occurs in the model troposphere. The rate of removal of water vapour from the troposphere is calculated

following the method of Giorgi and Chameides (1985; e.g. Kasting, 1990), which results in an integrated removal of H_2O via rain (W_{H2O}) of $\sim 10^{17}$ molecules cm^{-2} s^{-1} ($\sim 3.3 \times 10^{-6}$ g cm^{-2} s^{-2}, the global average). Henry's law is used to calculate the dissolution of gases in the raindrops, which allows the removal of dissolved species to be calculated. Henry's law states that at equilibrium, the concentration of a species dissolved in liquid is proportional to the pressure of the species in the gas phase. For most species, the constant of proportionality the model uses is the species-particular Henry's law constant, which may be dependent on temperature. For some species, the model uses an 'effective Henry's constant' which is adapted to take into account aqueous chemistry within the raindrop. For the full derivation and further details of this parametrisation, see Giorgi and Chameides (1985).

The model assumes an infinite reservoir of water below the lower boundary, so the tropospheric mixing ratios of H_2O are reset after each timestep. They are reset to a profile equal to the relative humidity (following Manabe and Wetherald, 1967) multiplied by the saturation vapour pressure (dependent on T) at each altitude (see e.g. Catling and Kasting, 2017, pp.452-453).

2.4.3 – Particle formation and fallout

The model templates used for the work in this thesis include sulphate and S_8 aerosols as particle species, which are assigned condensation and fallout rates. S_8 aerosols do not form in oxygen-rich atmospheres, which are primarily explored within this thesis. The only source of sulphate aerosol in the model is the condensation of sulphuric acid, H_2SO_4, and the aerosol phase condenses and evaporates determined by the local H_2SO_4 saturation vapour pressure.

2.4.4 – Redox conservation

The model conserves redox, which requires that the sum of the redox states of gases moving in and out of the model atmosphere is zero. H_2O, N_2, CO_2 and SO_2 are considered to have a redox state of zero. Any additional O atoms increase the redox state by 1, and additional H atoms decrease it by 0.5 (Zahnle et al., 2006). The model

checks this by ensuring that the sources are equal to the sinks of each element (H, O, C, N, S, Cl).

2.5 – Boundary conditions

The (photo)chemistry within the model, including reaction rates, is fairly well-understood, so in general science using *Atmos* is conducted by varying boundary conditions and exploring resulting predictions. Each species is allocated upper and lower boundary conditions, which combine with the chemical, radiative, and transport schemes to define unique atmospheric profiles.

2.5.1 – Lower boundary conditions

There are four types of lower boundary condition used in *Atmos*. They are i) fixed mixing ratio; ii) fixed flux; iii) fixed deposition velocity; and iv) distributed flux with deposition velocity. A report of the effects of changing the type of boundary condition used for various major species is the basis of the work in Chapter 3. The following points describe each boundary condition.

i) Mixing ratio boundary conditions allow the user to specify the mixing ratio of a certain species in the lowermost grid step. The model is then free to vary fluxes of different species to produce an atmosphere that satisfies the boundary condition. In previous applications of *Atmos* and other photochemical models (e.g. Claire et al., 2014; Kasting and Donahue, 1980; Kasting et al., 1985; Segura et al., 2003; Zahnle et al., 2006), some major species including O_2 and CO_2 typically have mixing ratio boundary conditions, as they tend to produce models that converge to steady-state solutions more quickly.

ii) When a flux lower boundary condition is chosen, the flux of the species into the first model grid step is specified, and the model atmosphere responds by calculating the resulting mixing ratios of the different species. This is arguably a more intuitive approach to parametrising biological and volcanic

inputs of gases to the atmosphere than the mixing ratio boundary condition, and as such is proposed as a more appropriate type of boundary condition for O_2, CH_4, CO, H_2 and N_2O in Chapter 3 (Gregory et al., 2021).

iii) A third lower boundary condition is a deposition velocity boundary condition, in which a deposition velocity (V_{dep}, in cm s^{-1}) is specified, and the model calculates the resulting flux of the species out of the atmosphere over the lower boundary by multiplying the deposition velocity by the number density of the species in the lowermost grid step. This boundary condition can be considered as a parametrisation of the loss reactions or dissolution of species that do not have a major biological or volcanic flux at the Earth's surface.

iv) Finally, a distributed flux and deposition velocity boundary condition can be used, in which a deposition velocity is specified as above, and a flux boundary condition into the model is specified, but the flux of the species is distributed from the ground to a stipulated altitude, rather than just into the ground-level grid step. This distribution allows a flux of molecules into the atmosphere without those molecules causing the deposition flux, dependent on the mixing ratio in the first grid step, to increase dramatically and remove them immediately. In the standard model, the flux of SO_2 into the model atmosphere is distributed over the lowermost 20 km of the column, in order to simulate the effects of volcanic plumes, which can disperse SO_2 throughout the troposphere and lower stratosphere.

The boundary conditions and values chosen for i) the model template used in Chapter 3, and ii) the model template used in Chapters 4–6, are listed in Tables B-1 and B-2 in Appendix B. Other than those for O_2, CH_4, CO, H_2, N_2O and CO_2, for which further details are provided in the text of Chapters 3, 5 and 6, the boundary conditions are those used by Catling et al. (2010; after Segura et al. (2005)) and Domagal-Goldman et al. (2014), with only minor changes. The H_2S and SO_2 fluxes are from the 'modern low' values in Zahnle et al. (2006).

2.5.2 – Upper boundary conditions

Upper boundary conditions can also be specified in the model. For the standard model, most species have a constant effusion velocity upper boundary condition set to zero, stipulating that there should be no flux of the species into or out of the model atmosphere across the upper boundary. H and H_2 are treated differently, via a molecular diffusion term as mentioned above. To incorporate the effects of N_2 photolysis above the upper boundary, a fixed flux of the resulting atomic nitrogen (N) into the upper-most model grid step is specified. CO_2 photolysis above the upper boundary is accounted for through additional fluxes of CO and O over the upper boundary into the model atmosphere (e.g. Guzmán-Marmolejo et al., 2013).

2.6 – Model outputs

The model calculates mixing ratios for all long-lived species with altitude, using a first-order reverse Euler method. Timesteps are increased until there is no significant change in mixing ratio with a timestep of 10^{17} seconds (the same order of magnitude as the age of the Earth), at which point the model is considered to have converged to a steady-state solution. Here, we consider the model to have converged if there is no more than a 2% (and usually much smaller) change in mixing ratio across this timestep. Along with mixing ratios, other useful model outputs include fluxes of species between different grid steps and number densities of short-lived species (i.e. species whose mixing ratios are calculated from chemical production and loss only, with no vertical transport) with altitude.

2.7 – Justification of use of *Atmos* for an oxygen isotope model

The model *Atmos* is a good tool to investigate the interactions between oxygen, ozone, methane, carbon dioxide and other species under different conditions, as well as to develop as an oxygen isotope model. Firstly, the model includes a large number of atmospheric species and reactions, in order to closely simulate the interactions between different species. Other oxygen isotope models (e.g. Wiegel et

al., 2013; Young et al., 2014; Yung et al., 1997) include only major atmospheric species or important oxygen-bearing species. While production and loss processes via trace species are often less important in understanding the photochemistry of the O_x-O_2-CO_2 system, their inclusion in the model is critical in contributing towards a more complete picture of atmospheric chemistry. For example, HO_x, NO_x (included in all model results presented in this thesis) and ClO_x (included in the Chapter 3 model results) species and reactions are known to be important in catalysing the destruction of ozone. Reducing species such as H_2, CO and N_2O are also shown to be important in dictating, for example, oxygen mixing ratios under different fluxes (see Chapter 3). While adding complexity to the model, the vast suite of species that *Atmos* contains are a significant strength in terms of understanding the way in which different species interact in the atmosphere, under conditions which deviate from those of the modern Earth. This is enhanced with the inclusion of a suite of atmospheric processes included as subroutines in the model (see Section 2.4).

Secondly, many reaction rates are known to vary considerably with altitude due to dependences on temperature and pressure (and incident flux in the case of photolysis reactions). Some existing models (e.g. Young et al., 2014) calculate reaction rates assuming a single temperature, density and actinic flux for the whole stratosphere. In contrast, as a 1-D photochemical model, *Atmos* has an advantage over box models in that it is able to vary temperature, pressure and actinic flux with altitude, and therefore aids a better grasp of the variation of reaction rates with altitude. Furthermore, the atmospheric density and flux are calculated from the mixing ratios of the different species in each grid step in the model atmosphere, rather than being fixed, so are flexible for use in exploring a range of different atmospheric conditions. In addition, reaction rates are regularly and easily updated according to new theoretical and experimental results from the literature.

Another strength of *Atmos* is the option to couple the photochemical model with a climate model, which updates temperature, water vapour and pressure profiles according to the mixing ratios of the different species calculated by the photochemical model. The outputs can be fed back to the photochemical model to

update reaction rates accordingly, and this process can be iterated (for a similar and related model, see Segura et al. (2003)). While we focus only on the photochemical model and do not use this feature in the results presented here, coupling to the climate code in future work would be an interesting avenue. For example, the temperature structure of the atmosphere is likely to differ between low-O3 and high-O3 atmospheres, which may affect kinetic reaction rates in the stratosphere. However, use of the photochemical model alone still allows comparison with other photochemical models (e.g. Kasting and Donahue, 1980; Kasting et al. , 1985). Since inputs including the temperature, eddy diffusion and species concentration profiles, incoming stellar UV fluxes and boundary conditions can be easily changed, *Atmos* is flexible for application to other planets (e.g. Mars), as well as the early and modern Earth.

The utility of *Atmos* to the incorporation of multiple isotopes has already been shown in its ability to predict multiple sulphur isotope signatures (Claire et al., 2014). There, the model was applied to Archaean atmospheres, also proving its flexibility for use in deep time studies. As discussed further in Chapters 4 and 5, we incorporate oxygen isotopes in a different manner to that used for sulphur isotopes.

As a 1-D model, some atmospheric behaviour able to be captured by 2-D and 3-D models is not included here. However, we are able to parametrise some important processes (e.g. eddy diffusion allows 2-D and 3-D turbulent transport of species to be captured in a 1-D term) or make assumptions for others (e.g. choosing a mid-latitude zenith angle to average over the whole Earth; choosing volcanic fluxes averaged over the whole Earth). This is adequate because: 1) the complexity of the model is in the atmospheric column, and adding more dimensions would make the model slow, complicated, and difficult to calibrate, especially for non-modern-Earth cases; 2) uncertainties in e.g. continental formation in Earth's history would have to be accounted for.

Coupling of the photochemical model to a biogeochemical model (e.g. Bergman et al., 2004; Daines and Lenton, 2016) would be an interesting target for future work,

as further detailed in Chapter 3. The boundary conditions of *Atmos* currently parametrise ocean/land-atmosphere processes as fluxes of species, but this necessarily removes the ability for feedbacks with hydrospheric, biospheric and lithospheric systems to be included in the model. As explained in Chapter 3, we have made efforts to include some of these feedbacks by varying fluxes at the lower boundary, but future work is likely to involve the integration of *Atmos* with a biogeochemical model.

2.8 – Applications model to early Earth atmospheres

In Chapter 4, we develop the model to incorporate the three isotopes of oxygen. Calibration of the model is undertaken in Chapter 5 and the model is applied to palaeo-Earth atmospheres with various O_2-CO_2-CH_4 compositions in Chapter 6. The development of the oxygen isotope model is an overarching goal of this thesis, and the model that we develop and apply in Chapters 4–6 is flexible for use for other planetary atmospheres and the ancient Earth, as well as the modern Earth. However, it is only as reliable as the prediction of the bulk atmospheric chemistry. Chapter 3 therefore first focusses on the base model (without isotopes) and explores the results of a flux-driven model, in which O_2 and CH_4 fluxes are varied at the lower boundary as opposed to the commonly-used mixing ratio lower boundary condition. The results indicate that there could be some atmospheric oxygen levels that are unstable against perturbation and are unlikely to have occurred for long periods of time without unknown processes acting to increase the stability. This has implications for the oxygen levels that are likely to have existed over Earth history. We find that high-O_2 and trace-O_2 atmospheres appear stable, which indicates a lower limit for Proterozoic O_2 of around 1% of present atmospheric levels (PAL).

Chapter 3

Photochemical modelling of atmospheric oxygen levels confirms two stable states

Abstract

Various proxies and numerical models have been used to constrain O_2 levels over geological time, but considerable uncertainty remains. Previous investigations using 1-D photochemical models have predicted how O_3 concentrations vary with assumed ground-level O_2 concentrations, and indicate how the ozone layer might have developed over Earth history. These classic models have utilised the numerical simplification of fixed mixing ratio boundary conditions. Critically, this modelling assumption requires verification that predicted fluxes of biogenic and volcanic gases are realistic, but also that the resulting steady states are in fact stable equilibrium solutions against trivial changes in flux.

Here, we use a 1-D photochemical model with fixed flux boundary conditions to simulate the effects on O_3 and O_2 concentrations as O_2 (and CH_4) fluxes are systematically varied. Our results suggest that stable equilibrium solutions exist for trace- and high-O_2/O_3 cases, separated by a region of instability. In particular, the model produces few stable solutions with ground O_2 mixing ratios between 6×10^{-7} and 2×10^{-3} (3×10^{-6} and 1% of present atmospheric levels). A fully UV-shielding ozone layer only exists in the high-O_2 states. Our atmospheric modelling supports prior work suggesting a rapid bimodal transition between reducing and oxidising conditions, and proposes Proterozoic oxygen levels higher than some recent proxies suggest. We show that the boundary conditions of photochemical models matter, and should be chosen and explained with care.

The material in this chapter has been published as: Gregory, B.S., Claire, M. and Rugheimer, S., 2021. Photochemical modelling of atmospheric oxygen levels confirms two stable states. *Earth and Planetary Science Letters*, 561, 116818.

3.1 – Introduction

Improved constraints of atmospheric oxygen levels over Earth history are important for an enriched understanding of how life and Earth have co-evolved. As discussed in Section 1.1 of Chapter 1, various proxies have been used to estimate atmospheric oxygen levels over geological time. The disappearance of sulphur isotope mass-independent fractionation (S-MIF) in the geological record at 2.4-2.5 Ga (Bekker et al., 2004; Farquhar et al., 2000; Warke et al., 2020b) is considered strong evidence for the Great Oxidation Event (GOE). To explain this, models require the partial pressure of oxygen (pO_2, also referred to as the O_2 mixing ratio) at the surface to be less than 2.1×10^{-6} (10^{-5} times the present atmospheric level (PAL)) for the Archaean and more than 2.1×10^{-6} after the GOE (Pavlov and Kasting, 2002).

However, uncertainty remains regarding atmospheric O_2 levels since the GOE (see e.g. reviews by Farquhar et al. (2014); Kump (2008); Lyons et al. (2014)), in particular for the mid-Proterozoic, where palaeo-O_2 proxies yield differing constraints. Proxies for oxidative weathering and ocean oxygenation have classically led to pO_2 estimates between 2.1×10^{-3} and 0.084 (Canfield, 1998, 2005; Holland, 1994; Johnson et al., 2014; Lenton and Daines, 2017; Rye and Holland, 1998). The existence of an ozone layer, indicated by the presence of mass-independently fractionated oxygen isotopes (O-MIF) in sedimentary sulphates since the GOE (Crockford et al., 2019), is thought to require pO_2 exceeding 2.1×10^{-4} (Segura et al., 2003), while model interpretations of large, negative O-MIF from 1.4 Ga sulphates (Crockford et al., 2018) suggest an upper limit of 2.1×10^{-3} for this period (Planavsky et al., 2020). This upper limit is consistent with cerium anomalies from 1.87 Ga (Bellefroid et al., 2018) and a lack of fractionation of sedimentary chromium isotopes, interpreted to indicate pO_2 lower than 2.1×10^{-3} or even 2.1×10^{-4} for parts of the Proterozoic before 0.8 Ga (Cole et al., 2016; Frei et al., 2009;

Planavsky et al., 2014, 2018). However, the timing of the appearance of variable $\delta^{53}Cr$ (and its interpretation) in the geological record is debated, with some studies predicting much higher pO_2 between 0.8 and 1.1 Ga (Gilleaudeau et al., 2016) and even further back in the Mesoproterozoic (Canfield et al., 2018). Even for the Phanerozoic, where the continuous presence of animal life indicates relatively high oxygen levels, uncertainty remains (Krause et al., 2018). For the last 400 Myr, a continuous charcoal record suggests oxygen levels between 15% and 30% (Bergman et al., 2004; Glasspool and Scott, 2010; Glasspool et al., 2015).

Previous 1-D photochemical models (Kasting and Donahue, 1980; Kasting et al., 1985; Segura et al., 2003; Zahnle et al., 2006) have investigated potential palaeo-atmospheres by explicitly constructing models with a range of pO_2. These models utilised 'fixed mixing ratio' lower boundary conditions (LBCs) for O_2, in which the experimenter sets the pO_2 and the model is allowed to vary fluxes across the lower boundary and other species' concentrations to produce a steady-state solution which satisfies the given boundary conditions. In a brief summary overview, these previous studies (reproduced below) found that the ozone column density (the number of ozone molecules in an atmospheric column with a surface area of one square centimetre) initially increases as a power-law with pO_2, before saturating at higher O_2 concentrations (Figure 3-1: Extracted model results from suites using fixed mixing ratio lower boundary conditions for O_2. 3-1).

The results of these 1-D photochemical modelling studies have been simplified, parametrised, and incorporated into a number of Earth system evolution models, which include shorter-term biological and atmospheric feedbacks with longer-term planetary redox fluxes, such as volcanic degassing and hydrogen escape. Intriguingly, these models have predicted bimodal behaviour with respect to oxygen concentrations. For example, the 2-box model of Goldblatt et al. (2006) predicted two regions only: $pO_2 < 2.1\times10^{-6}$ and $pO_2 > 10^{-3}$. Similarly, the 3-box biogeochemical model of Laakso and Schrag (2017) found stable solutions with $pO_2 < 2.1\times10^{-8}$ and $pO_2 > 2.1\times10^{-4}$. Other biogeochemical models predict a 'GOE' in which O_2 mixing ratios change from 10^{-6} to 2×10^{-3} (Claire et al., 2006) or 10^{-2} (Alcott et al., 2019)

relatively quickly. While biological re-organisation to oxic conditions provides a positive feedback (Catling et al., 2007; Daines and Lenton, 2016), the primary driver captured is the development of an ozone layer which shields O_2 from photolysis (Claire et al., 2006; Goldblatt et al., 2006), as captured by parametrisations of 1-D photochemical models.

Here, we revise the classic photochemical modelling calculations which relate O_2 and O_3, by utilising 'fixed flux' LBCs for O_2 and other gases. The O_2 flux into the atmosphere is specified by the experimenter, and the model predicts the resulting mixing ratio profiles in equilibrium with the radiation field, kinetics, and other physical processes (e.g. lightning, particle formation, condensation). Flux boundary conditions represent a closer conceptual match to what real atmospheres do (e.g. fluxes vary and concentrations adjust), compared to the assumption that the planetary and biogenic fluxes somehow adjust in order to maintain fixed ground-level concentrations. First, we briefly introduce the 1-D photochemical model, *Atmos*. In Section 3.3, we use *Atmos* with fixed mixing ratio LBCs for O_2 to replicate previous results, but observe that these models predict potentially unrealistic fluxes. Our primary results comprise a systematic study of atmospheric chemistry resulting from variable O_2 and methane fluxes across the lower boundary. Specifically, we i) vary O_2 fluxes at several fixed CH_4:O_2 flux ratios (Section 3.4.1); ii) vary CH_4:O_2 flux ratios at several fixed O_2 fluxes (Section 3.4.2); and explore sensitivity to iii) oxidative weathering (Section 3.4.4) and iv) other important redox fluxes (Section 3.4.6).

Our investigation of 2067 flux-driven model atmospheres reveals a bimodal oxygen distribution similar to those observed in biogeochemical models, but one that arises entirely in the atmosphere itself. We explicitly demonstrate that some classic results are unstable equilibrium solutions (Section 3.4.3) and argue that many intermediate oxygen concentrations are photochemically unstable. In Section 3.5, we discuss implications for palaeo-O_2 constraints, provide suggestions for future work in both photochemical and biogeochemical modelling, and argue that the choice of

numerical methods used by 1-D photochemical models has implications for how the Earth system science community considers the evolution of atmospheric oxygen.

3.2 – Model description

We use the one-dimensional photochemical model *Atmos* described in Chapter 3. The 'ModernEarth+Cl' template utilised in this study (originally developed by Catling et al., 2010) incorporates 87 atmospheric species involved in 372 reactions, whose rates have been updated to follow recent recommendations from the JPL, NIST, and IUPAC gas kinetics databases (Atkinson et al., 2004; Burkholder et al., 2015; Manion et al., 2015; Appendix C). An altitude grid of 160 0.5 km layers gives a simulated atmosphere of height 80 km, with the tropopause set at 11 km, suitable for a mid-latitude profile. Each model presented here was run with modern eddy diffusion and temperature profiles (Figure 2-3), and the initial mixing ratios used as input were i) modern mixing ratios, for the first model run in a suite, or ii) the mixing ratios from the previous model output, for all other models in the suite. We analyse only steady-state solutions. The lower boundary of the model represents Earth's surface, across which we prescribe fluxes of volcanic and biogenic gases into the bottom-most model grid layer, in addition to gaseous, aqueous and particulate deposition out of the model atmosphere. LBCs are specified for each atmospheric species (see Section 2.5; Appendix B) and discussed further below.

3.3 – Results from fixed mixing ratio photochemical modelling

We used fixed mixing ratio LBCs for O_2 to compare outputs from *Atmos* to the results of previous studies (shown in Figure 3-1a). Kasting and Donahue (1980), Kasting et al. (1985) and Segura et al. (2003) used fixed flux or deposition velocity (specifying the removal rate from the atmosphere) LBCs for CH_4, H_2, CO and N_2O. The magnitudes of these fluxes were determined by predicted fluxes from a fixed mixing ratio LBC model simulating the modern Earth for these species (with the exception of Kasting and Donahue's (1980) H_2 and CO, which were allocated zero flux LBCs). Resulting negative (i.e. out of the atmosphere into the ocean) H_2 fluxes led Kasting et al. (1985) and Segura et al. (2003) to use deposition velocity and negative fixed

flux boundary conditions for H_2, respectively. Zahnle et al. (2006) used fixed mixing ratio LBCs for CH_4, and chose large positive fluxes of H_2 and CO. These (and all LBCs used in this study) are summarised in Table 3-1. We specify units of flux in 'photochemical units' or 'pu' (1 pu = 1 molecule cm^{-2} s^{-1} ~ 2.7×10^{-10} Tmol yr^{-1}).

Using *Atmos*, we produced suites of steady-state model atmospheres with O_2 ground-level mixing ratios varying between 2.1×10^{-11} and 0.42, choosing LBCs using the specific methods of the previous four studies. A fifth suite (hereafter referred to as Case 0; see Table 3-1) also incorporates fixed flux LBCs for CH_4, CO and N_2O equal to those computed by modern fixed mixing ratio calculations. Like the models of Kasting et al. (1985) and Segura et al. (2003), *Atmos* predicts a net flux of H_2 out of the atmosphere when run solely with modern fixed mixing ratio LBCs. This is physically unrealistic and numerically allows models significant leeway to mask redox imbalances by dumping hydrogen into the (assumed) ocean. We incorporated the predicted fluxes as fixed flux LBCs and tuned them, primarily by slightly reducing the larger (biogenic) CH_4 flux, to achieve an atmosphere predicting modern mixing ratios for the five species, but with a net flux of H_2 into the atmosphere within an order of magnitude of the modern volcanic flux (Aiuppa et al., 2011). A fixed mixing ratio LBC for preindustrial CO_2 (280 ppmv) was used. Allowing the model to compute CO_2 fluxes is justifiable here as CO_2 is redox-neutral, whereas O_2, CH_4, H_2, CO and N_2O are not (Zahnle et al., 2006).

The ozone column density increases with specified ground-level pO_2 but plateaus above a pO_2 of 10^{-2}, following a chemical pattern discussed in previous work (Figure 3-1a). Differences between our models for trace-O_2 concentrations are primarily due to the different choices of boundary conditions. Our results are very similar to those of previous models, with small changes due to updated kinetic rate coefficients, which is unsurprising given that *Atmos* shares a common code heritage. However, in what follows we discuss observations that led us to discover that some of the steady-state model atmospheres predicted by fixed mixing ratio LBCs exhibit behaviour of unstable equilibrium solutions.

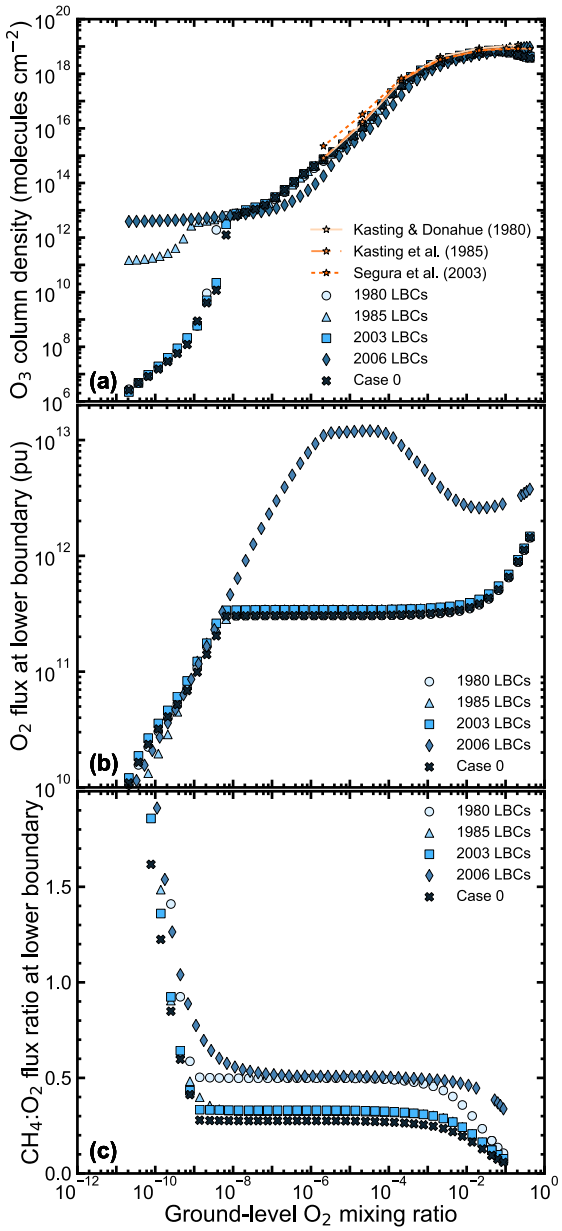

Figure 3-1: Extracted model results from suites using fixed mixing ratio lower boundary conditions for O_2.
Circles, triangles, squares and diamonds show results using Atmos with the same boundary conditions as previous authors. '1980 LBCs,' '1985 LBCs,' '2003 LBCs' and '2006 LBCs' refer to the boundary conditions used by Kasting and Donahue (1980), Kasting et al. (1985), Segura et al. (2003) and Zahnle et al. (2006), respectively. Crosses show Case 0 results, with fixed mixing ratio boundary conditions for O_2 and fixed flux boundary conditions for CH_4, H_2, CO and N_2O. For the boundary conditions used, see Table 4-1. ***(a)*** *Ozone column densities with user-specified ground-level O_2 mixing ratio. The results from previous studies are also shown (orange lines).* ***(b)*** *Predicted oxygen fluxes, and* ***(c)*** *predicted CH_4:O_2 flux ratios required to produce the fixed mixing ratio model atmospheres, plotted against user-specified O_2 mixing ratio.*

Table 3-1: Lower boundary conditions for the models described in this study.
Units of flux are in photochemical units (1 pu = 1 molecule cm^{-2} s^{-1} ~ 2.7×10^{-10} Tmol yr^{-1}). Abbreviations are as follows: LBCs: lower boundary conditions; DV: deposition velocity; MR: mixing ratio. For Case 4, (a), (b) and (c) indicate the model suites with 'modern low,' 'modern high' and 'Archaean high' reducing fluxes, respectively. Table is continued on next page.

Model	O_2	CH_4	CH_4:O_2 flux ratio	H_2	CO	N_2O	CO_2	Solar zenith angle
***Atmos* with Kasting and Donahue (1980) LBCs**	MR: Varying	Flux: 1.34×10^{11} pu	N/A	Flux: 0 pu	Flux: 0 pu	Flux: 4.71×10^{8} pu	MR: 2.57×10^{-4}	45◦
***Atmos* with Kasting et al. (1985) LBCs**	MR: Varying	Flux: 1.13×10^{11} pu	N/A	DV: 7.72×10^{-4} cm s^{-1}	Flux: 2.35×10^{11} pu	Flux: 4.21×10^{8} pu	MR: 3.4×10^{-4}	50◦
***Atmos* with Segura et al. (2003) LBCs**	MR: Varying	Flux: 1.13×10^{11} pu	N/A	Flux: -1.02×10^{10} pu	Flux: 2.35×10^{11} pu	Flux: 4.21×10^{8} pu	MR: 3.55×10^{-4}	45◦
***Atmos* with Zahnle et al. (2006) LBCs**	MR: Varying	MR: 10^{-4}	N/A	Flux: 3×10^{10} pu	Flux: 3×10^{9} pu	MR: 3.1×10^{-7}	MR: 0.01	50◦
Case 0	MR: Varying (2.1×10^{-11} – 0.42)	Flux: 8.4×10^{10} pu	N/A	Flux: 1.22×10^{8} pu	Flux: 2.65×10^{11} pu	Flux: 4.11×10^{8} pu	MR: 2.8×10^{-4}	50◦
Flux-driven modern model	Flux: 8.9×10^{11} pu	Flux: 8.4×10^{10} pu	0.094	Flux: 1.22×10^{8} pu	Flux: 2.65×10^{11} pu	Flux: 4.11×10^{8} pu	MR: 2.8×10^{-4}	50◦
Case 1	Flux: Varying (3×10^{10} - 4×10^{13} pu)	Flux: Varying	Varying: 0.094, 0.3, 0.45, 0.49	Flux: 1.22×10^{8} pu	Flux: 2.65×10^{11} pu	Flux: 4.11×10^{8} pu	MR: 2.8×10^{-4}	50◦

Table 3-1 (continued)

Model	O_2	CH_4	CH_4:O_2 flux ratio	H_2	CO	N_2O	CO_2	Solar zenith angle
Case 2	Flux: Varying (10^{11}, 3×10^{11}, 5×10^{11}, 10^{12}, 5×10^{12} pu)	Flux: Varying	Varying (0.1-0.5)	Flux: 1.22×10^{8} pu	Flux: 2.65×10^{11} pu	Flux: 4.11×10^{8} pu	MR: 2.8×10^{-4}	50◦
Case 3	Flux: Varying (6×10^{10} - 4×10^{13} pu), and DV (see Section 3.4)	Flux: Varying	0.094	Flux: 1.22×10^{8} pu	Flux: 2.65×10^{11} pu	Flux: 4.11×10^{8} pu	MR: 2.8×10^{-4}	50◦
Case 4	Flux: Varying (10^{9}-10^{12} pu)	Flux: Varying	(a): 0.16 (b): 0.16 (c): 0.15	Flux: (a): 2×10^{9} pu (b): 10^{10} pu (c): 3×10^{10} pu	Flux: (a): 2×10^{8} pu (b): 10^{9} pu (c): 3×10^{9} pu	Flux: (a): 4.1×10^{8} pu (b): 4.11×10^{8} pu (c): 4.11×10^{8} pu	MR: 2.8×10^{-4}	50◦
Case 5	Flux: Varying (10^{9} – 10^{12} pu)	Flux: Varying	0.094	Flux (3.4×10^{9}) and DV (2.5×10^{-4} cm s^{-1})	Flux (2.65×10^{11}) and DV (1.2×10^{-4} cm s^{-1})	Flux: 4.11×10^{8} pu	MR: 2.8×10^{-4}	50◦
Case 6	Flux: Varying (3×10^{10} – 4×10^{13} pu)	Flux: Varying	Varying (0.1-0.5)	MR: 5.3×10^{-7}	MR: 1.1×10^{-7}	MR: 3.1×10^{-7}	MR: 4×10^{-4}	45◦

3.3.1 – The restrictions of a fixed mixing ratio boundary condition

By construction, fixed mixing ratio LBCs enable the model to vary lower boundary fluxes to produce the user-specified concentration, but the required fluxes may not be physically realistic. Figure 3-1b shows the O_2 fluxes computed by the model to maintain the specified O_2 mixing ratio boundary conditions in Figure 3-1a. These fluxes (and others not shown) vary across the experiments, making the direct comparison of simulated atmospheres challenging, and are not necessarily representative of how a real biosphere would function. For example, Figure 3-1c shows that though the predicted CH_4:O_2 flux ratio is ~0.1 for most high-O_2 atmospheres, consistent with theoretical estimates and modern measurements, the CH_4:O_2 flux ratio varies significantly for moderate-O_2 atmospheres, and is greater than 0.5 for low-O_2 Archaean-like atmospheres, which exceeds the stoichiometric limit that life can extract from CO_2 and H_2O substrates. Model-computed imbalances in CO and H_2 fluxes into and out of the model (not shown) further complicate and occasionally mask potential non-physical behaviour in other species. A more intuitive approach is to simulate volcanism and biology as 'fluxes' to which the composition of the atmosphere adjusts, which motivates our use of fixed flux LBCs.

3.4 – Results from flux-driven photochemical modelling

We start with a 'flux-driven modern model,' which we construct as the best-fit model reproducing modern conditions using fixed flux LBCs for O_2, along with our 'Case 0' fixed flux LBCs for CH_4, H_2, CO and N_2O (Table 3-1). The model-predicted O_2 flux is 8.9×10^{11} pu, resulting in a CH_4:O_2 flux ratio of 0.094. While the modern gross O_2 production is much larger (~4×10^{13} pu), our O_2 flux ignores very short-term sources and sinks of atmospheric O_2, while capturing the seasonal imbalance between O_2 production and destruction as well as the most important components of the short/medium-term carbon cycle (Zahnle et al., 2006). Our methane flux (8.4×10^{10} pu) is similar to the estimated net modern methane flux to the atmosphere from natural sources, after a large proportion of the gross methane production flux has been oxidised in sediments (Schlesinger and Berhardt, 2013, p.434).

We produced suites of model atmospheres to explore a range of non-modern biologic flux conditions, primarily by changing the absolute O_2 flux and CH_4:O_2 flux ratio. We cover a parameter space designed to simulate a range of possible states of primary productivity, methane production, methanotrophy and sulphate reduction. Specifically, we varied the O_2 flux between ~0.01 to ~40 times that of the flux-driven modern model, which we conceptually identify with varying levels of primary productivity. We assigned the CH_4 flux at various flux ratios from 0.094 (the CH_4:O_2 flux ratio in the 'flux-driven modern model') to 0.5 (the stoichiometrically-balanced ratio). The former is representative of the modern Earth system, and the latter is a commonly-assumed simplification for the late-Archaean biosphere (Catling and Claire, 2005; Daines and Lenton, 2016). Intermediate CH_4:O_2 flux ratios might represent biospheres with increasing anaerobic oxidation of methane in sediments resulting from increasing sulphate concentrations (Catling et al., 2007; Daines and Lenton, 2016; Habicht et al., 2002).

3.4.1 – Case 1: Varying O_2 fluxes at fixed CH_4:O_2 ratios.

For a first test case, we varied O_2 flux between 10^{10} pu and 4×10^{13} pu. We produced 5 suites of up to 372 model atmospheres with O_2 fluxes between these values, with corresponding CH_4 fluxes set to maintain CH_4:O_2 flux ratios of 0.094, 0.3, 0.45 and 0.49. The model results, summarised in Figure 3-2, are strikingly different to those using fixed mixing ratio LBCs.

Model-predicted O_2 (Figure 3-2a) and CH_4 (Figure 3-2b) surface mixing ratios are shown with the O_2 flux as the independent variable. For CH_4:O_2 flux ratios of 0.094, 0.3 and 0.45, pO_2 remains low (less than 10^{-7}) until the O_2 flux reaches a critical value, at which point pO_2 jumps to a new value above 4×10^{-4} within a trivial flux range. Computed methane mixing ratios drop just before the jump in pO_2, supporting suggestions that a collapse of methane might be a prerequisite for the GOE (Claire et al., 2006; Warke et al., 2020b; Zahnle et al., 2006). Ozone column densities exhibit similar patterns to pO_2, with clusters of solutions at low and high column densities without intermediates (Figure 3-2c).

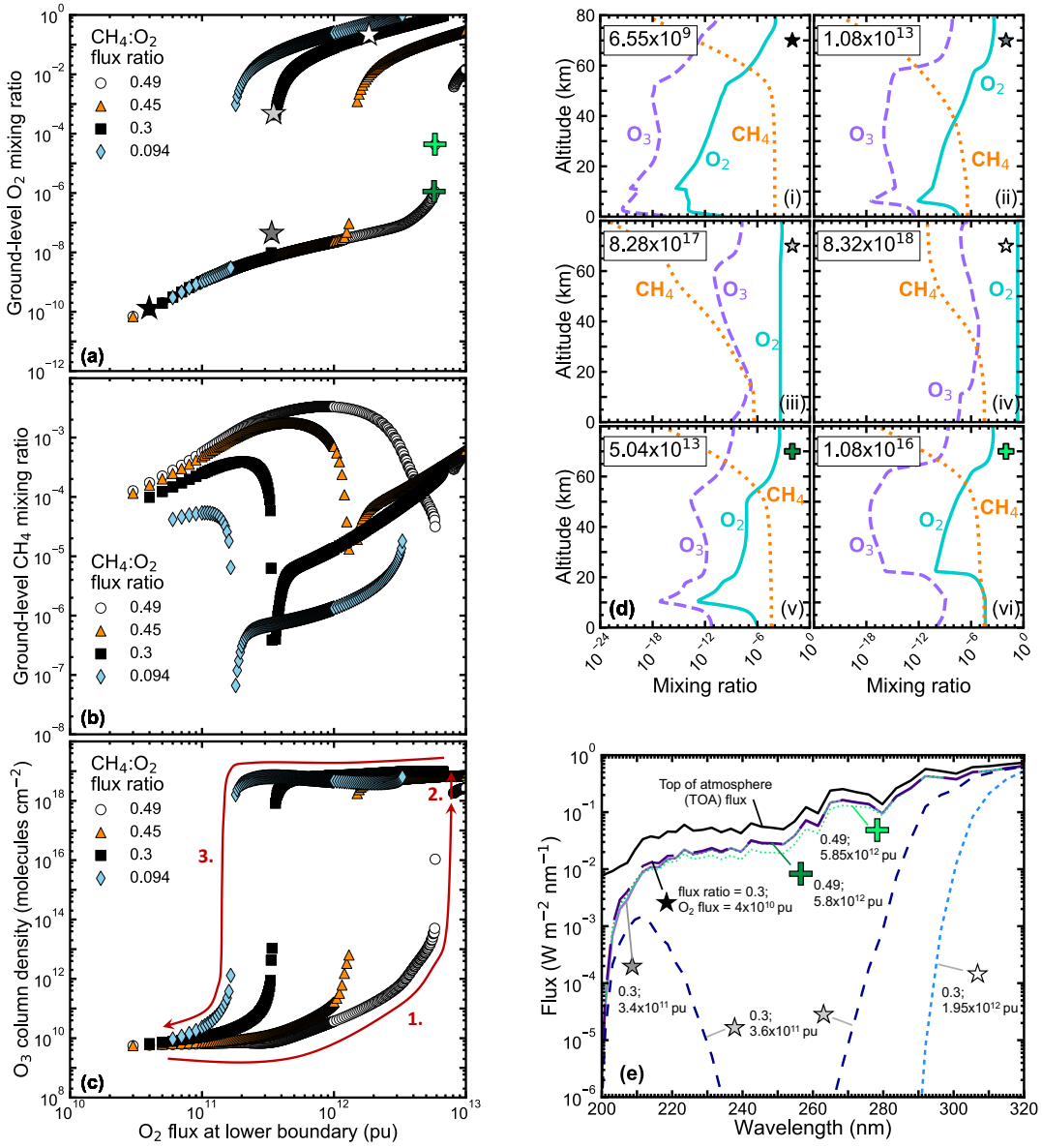

Figure 3-2: Case 1 model results.
(a) *Model-predicted ground-level O_2 mixing ratios with varying user-specified O_2 lower boundary flux, for different CH_4:O_2 flux ratios. Grey stars and green crosses indicate the O_2 lower boundary fluxes and mixing ratios of the six example model atmospheres examined in (d) and (e). Corresponding* ***(b)*** *model-predicted ground-level CH_4 mixing ratios, and* ***(c)*** *ozone column densities plotted against user-specified O_2 lower boundary flux. Red arrows on (c) illustrate the potential positive feedback discussed in Section 3.5.* ***(d)*** *O_2 (teal, solid lines), O_3 (purple, dashed lines) and CH_4 (orange, dotted lines) mixing ratio profiles for six example model solutions. Each panel refers to a model solution, indicated by a star or cross, on (a). Panels (i)-(ii) show two trace-O_2/trace-O_3 atmospheres with a CH_4:O_2 flux ratio of 0.3; panels (iii)-(iv) show two high-O_2/high-O_3 atmospheres, also with a CH_4:O_2 flux ratio of 0.3. Panels (v) and (vi) are for two atmospheres with a CH_4:O_2 flux ratio of 0.49. Ozone column densities are shown in the top left corners (units = molecules cm^{-2}).* ***(e)*** *UV ground flux with wavelength for the six example solutions shown on (a)/(d). The 'top of the atmosphere' (TOA) flux is also shown (black line). The labels for each model atmosphere refer first to the CH_4:O_2 flux ratio, and then to the O_2 flux across the lower boundary.*

When a CH_4:O_2 flux ratio of 0.5 was used (results not shown in Figure 3-2), the greater total flux of reductants (including H_2, CO and N_2O) than oxidants into the atmosphere resulted in a pO_2 always less than the CH_4 mixing ratio. For the 0.49 CH_4:O_2 flux ratio suite (Figure 3-2a-c), the O_2 flux was eventually increased sufficiently such that it exceeded the total reductant flux, despite co-increasing methane fluxes. For this suite, there are 'Archaean-like' solutions with O_2 concentrations up to 10^{-6} and one steady-state atmosphere with an O_2 mixing ratio of 4×10^{-5}, followed by a series of solutions with pO_2 exceeding 3×10^{-3} (1.5% PAL).

To summarise, our 1222 'Case 1' models predict that oxygen, methane and ozone levels exist in one of two states – trace-O_2/O_3 solutions, and high-O_2/O_3 solutions – separated by a 'gap' in which there is only one (very specific) solution for intermediate O_2 surface mixing ratios. To better understand, we explored the detailed altitude-dependent chemistry of models spanning these states.

3.4.1.1 – Two stable states of atmospheric chemistry?

We present mixing ratio profiles (Figure 3-2d) and ground-level UV fluxes (Figure 3-2e). Panels (i)–(iv) in Figure 3-2d show O_2, O_3 and CH_4 mixing ratio profiles for four atmospheres with O_2 fluxes from the 0.3 CH_4:O_2 ratio suite, illustrating how vertical distributions change as O_2 and CH_4 fluxes increase. Panels (v) and (vi) show profiles of two atmospheres with CH_4:O_2 flux ratios of 0.49, isolating our only model atmosphere with ground-level pO_2 between 10^{-6} and 10^{-4}. The corresponding fluxes of UV photons that pass through the entire atmosphere and reach the surface are shown in Figure 3-2e.

In the 'high-O_2/O_3' atmospheres (panels (iii) and (iv) in Figure 3-2d), O_2 is well-mixed and more abundant than methane. In panel (iii), a modern-like stratospheric ozone layer is emerging, which is fully developed by panel (iv). The significant ozone shielding results in increased methane mixing ratios and low UV fluxes at the surface, with modern-like behaviour where no photons shortward of ~290 nm reach the ground (Figure 3-2e). The other high-O_2 atmosphere (panel (iii) in Figure

3-2d) blocks substantial UV within the 200-320 nm range, but some photons at DNA-damaging wavelengths (200-220 nm) will reach the ground. This case is similar to the Segura et al. (2003) (fixed mixing ratio boundary condition) model of 2.1×10^{-3} for O_2, which was argued to be the tipping point at which ozone shielding significantly impacts ground UV fluxes.

The panel (v) atmosphere is similar to those in panels (i) and (ii), while panel (vi) shows an atmosphere with tropospheric O_2 and CH_4 mixing ratios both approximately 80 ppm – on the cusp of the reducing/oxic divide. However, there is not sufficient ozone to provide tropospheric UV shielding of O_2 (Figure 3-2e). While being a steady-state solution, it seems unlikely that this kind of atmosphere would be stable against small perturbations to the oxygen flux. The dearth of stable solutions between the trace-O_2 and high-O_2 attractors appears primarily due to positive feedbacks between increasing O_2 and O_3, which result in decreasing O_2 photolysis rates (Claire et al., 2006; Goldblatt et al., 2006). O_2 photolysis occurs only at wavelengths of 242 nm and below. The most abundant and effective absorbing molecule in the 200-300 nm wavelength range is O_3, with peak absorption at 240 nm. Increasing O_3 concentrations (Figure 3-2c) therefore shield O_2 in the lower atmosphere from photolytic destruction (Figure A-1, Appendix A), enabling O_2 concentrations to rise for a given flux. We explore this further in Section 3.4.3.

3.4.2 – Case 2: Varying CH_4:O_2 ratios at fixed O_2 fluxes

A second set of experiments designed to expand the parameter space of modelled fluxes investigates the reproducibility of our results under different conceptualisations of biogenic flux evolution. In the Case 2 suites, we fixed the absolute O_2 flux at five values (10^{11}, 3×10^{11}, 5×10^{11}, 10^{12} and 5×10^{12} pu), while decreasing the CH_4:O_2 flux ratio systematically from 0.5 to 0.1. These experiments might roughly capture the effects of increasingly sulphate-rich waters driving the locus of methane oxidation into sediments at a given primary productivity, but are admittedly a vast simplification of biospheric processes (Daines et al., 2017). The computed O_2 and CH_4 mixing ratios and corresponding O_3 column densities are

shown in Figure 3-3. As the CH_4:O_2 flux ratio is decreased from 0.5 to a critical value dependent on the absolute O_2 flux, an abrupt transition from reducing to oxidising atmospheres occurs (other than for an O_2 flux of 10^{11} pu, which is sufficiently low that this critical value is not reached for any CH_4:O_2 flux ratio less than 0.1). The Case

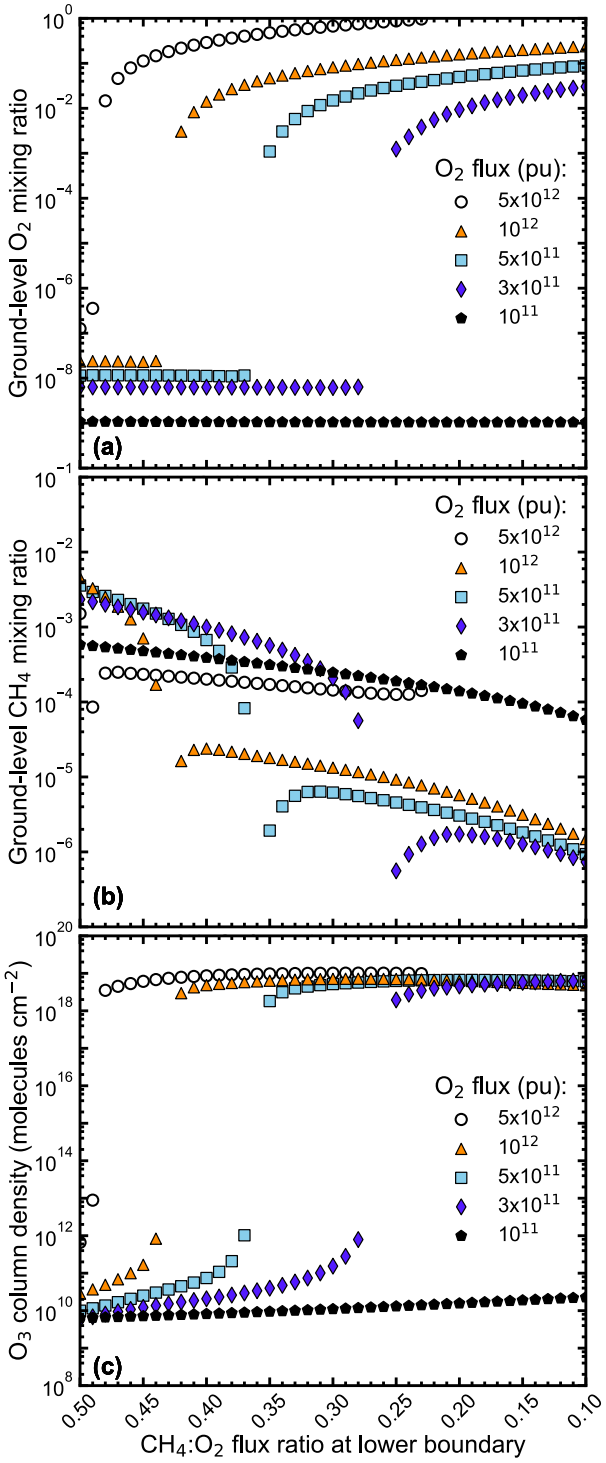

Figure 3-3: Case 2 model results. Model-predicted ***(a)*** *O_2 ground-level mixing ratios,* ***(b)*** *CH_4 ground-level mixing ratios, and* ***(c)*** *O_3 column densities of model atmospheres, with decreasing CH_4:O_2 ratio. Five O_2 flux cases are shown, with the magnitude of the O_2 fluxes indicated by the legend, in photochemical units (1 pu = 1 molecule cm^{-2} s^{-1}).*

2 experiments demonstrate a wider 'gap' in solutions than Case 1, with no predicted model atmospheres with O_2 mixing ratios between 4×10^{-7} and 10^{-3}.

3.4.3 – The photochemical (in)stability of atmospheres 'in the gap'

Atmospheres with O_2 mixing ratios between 4×10^{-7} and 4×10^{-4} are not produced in the flux-driven experiments described so far in this study, barring one case highlighted. By contrast, the identical numerical model utilising fixed mixing ratio boundary conditions produces results for all surface O_2 mixing ratios between 2.1×10^{-11} and 0.42 (Figure 3-1). As all results in this and previous efforts are steady-state equilibrium solutions, it should be possible, numerically speaking, to carefully specify fixed flux boundary conditions to reproduce model atmospheres with any ground-level O_2 mixing ratio, even within the 'gaps' identified in Cases 1 and 2. To explore this, we chose three of our Case 0 fixed mixing ratio LBC models, with pO_2

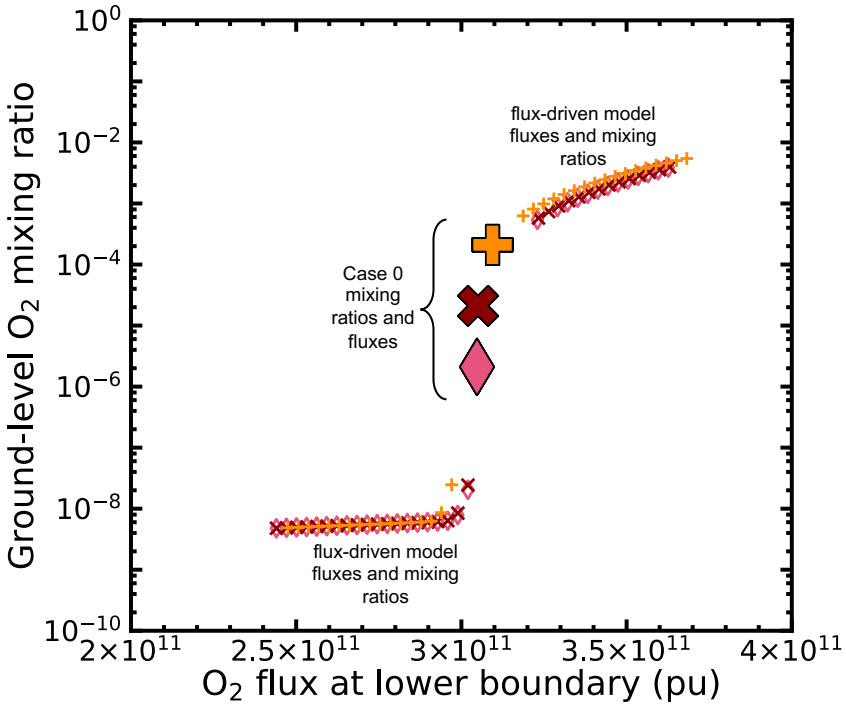

Figure 3-4: Model-predicted ground-level O_2 mixing ratios of model atmospheres with fixed flux boundary conditions for O_2, where the user-specified flux is equal to predicted fluxes from the fixed mixing ratio-driven models (Case 0).
Large, filled yellow plus, red cross and pink diamond indicate the three chosen O_2 surface mixing ratios (2.1×10^{-4}, 2.1×10^{-5} and 2.1×10^{-6}, respectively), and the O_2 fluxes required by the fixed mixing ratio-driven model to produce these atmospheres. Small yellow plus, red cross and open pink diamond symbols indicate O_2 mixing ratios of atmospheres produced when fluxes for each case are perturbed slightly. Note that the x axis has a linear scale.

values of 2.1×10^{-6}, 2.1×10^{-5} and 2.1×10^{-4}. We entered the predicted fluxes of O_2 and CH_4 (to 12 significant figures) as fixed flux boundary conditions and used the predicted species densities as initial values.

For each case, the flux-driven models did not converge when using the fluxes predicted by the fixed mixing ratio models. As fluxes were perturbed incrementally (at constant CH_4:O_2), no models converged until the O_2 fluxes were ~6%, ~6% and ~3% higher, or ~1%, ~1% and ~4% lower than Case 0, respectively (Figure 3-4). Subsequently, model solutions with $3\times10^{-8} < pO_2 < 5\times10^{-4}$ were not produced. Rounding our input fluxes to three significant figures for the 2.1×10^{-5} case to test for numerical precision issues made no significant difference to the results.

These tests supplement the preliminary conclusions from Cases 1 and 2, demonstrating that some steady-state model solutions computed using fixed O_2 mixing ratio LBCs between 4×10^{-7} and 5×10^{-4} are in fact unstable equilibrium solutions. They adjust to new solutions given trivial changes in lower boundary fluxes. This suggests, but does not fully prove, that fixed mixing ratio LBCs produce unstable equilibrium solutions in some (potentially large) regions of parameter space. A full stability analysis requires time-dependent computations beyond the scope of this effort, but will be forthcoming. Users of 1-D photochemical models (who must already carefully choose boundary conditions (e.g. Domagal-Goldman et al., 2014; Harman et al., 2018) are further cautioned to consider the stability of model results against small variations in flux, especially if using fixed mixing ratio boundary conditions.

3.4.4 – Case 3: Including negative feedbacks from oxidative weathering

Photochemical models to date have ignored a key negative feedback on oxygen fluxes at Earth's surface: as atmospheric O_2 concentrations build up, the removal rate via oxidative weathering increases. To test whether this could stabilise atmospheres with lower pO_2, we ran suites of models with the inclusion of deposition velocity boundary conditions that remove O_2 from the lower boundary

at a rate proportional to the O_2 mixing ratio. Numerically, this requires the photosynthetic O_2 flux to be delivered into the atmosphere at 0.5 km above the surface, but this has a negligible effect on the vertical profiles because large eddy diffusion coefficients rapidly mix near-surface layers.

Firstly, we defined the O_2 lower boundary flux as $F_{out} = V_{dep}[O_2]N_1$, where V_{dep} is the deposition velocity (cm s^{-1}), N_1 is the atmospheric density in the first grid step, and $[O_2]$ is the ground-level O_2 mixing ratio. In a second suite, we used $F_{out} = V_{dep}[O_2]^{0.5}N_1$, following pyrite oxidation kinetics experiments that show a half-power law relation (Johnson et al., 2019). We focus on pyrite rather than organic carbon oxidation (which we consider a redox-neutral part of the reversal of photosynthesis in our conceptualisation), but conveniently carbon oxidation rate laws are also approximately half-power in O_2 (e.g. Daines et al, 2017). We tuned values of V_{dep} to 5×10^{-9} cm s^{-1} and 2.3×10^{-9} cm s^{-1}, respectively, in order to reproduce the modern

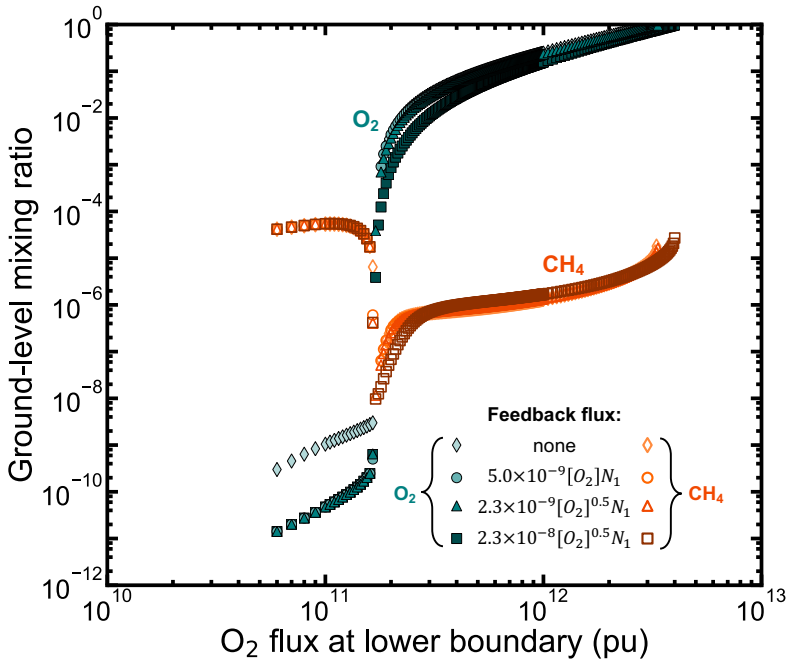

Figure 3-5: Case 3 model results.
Model results showing the effects of the inclusion of an oxidative weathering flux of O_2 out of the atmosphere (Case 3 results; circles, triangles and squares) compared to the Case 1 model atmospheres, for which there is no drawdown O_2 flux (diamonds). Model-predicted ground-level O_2 (filled, teal symbols) and CH_4 (open, orange symbols) mixing ratios are plotted against user-specified O_2 flux into the model atmosphere across the lower boundary. The ratio of the CH_4 flux to the upward (into-the-atmosphere) O_2 flux is 0.094 for each model suite (Table 3-1). The equation for the drawdown flux is shown in the legend, where $[O_2]$ is the mixing ratio of O_2 and N_1 is the number density of the atmosphere in the lowermost grid step.

oxidative weathering flux of ~2.6×10^{10} pu (Holland, 2002) and modern pO_2, when using the fixed-flux modern model. For a third suite, we increased V_{dep} by an order of magnitude for the half-power law case.

The results (Figure 3-5) reveal that the two-state behaviour observed in Cases 1 and 2 persists in the Case 3 suites, despite the inclusion of a negative feedback flux. Increasing V_{dep} by an order of magnitude produces several steady-state model atmospheres with O_2 mixing ratios between 10^{-6} and 10^{-3}, but they are not stable against trivial changes in flux.

3.4.5 – Confirmation of two stable states of atmospheric oxygen chemistry?

Figure 3-6 illustrates a key result of this work. Predicted O_2 ground mixing ratios are plotted against O_3 column densities for the 2067 flux-driven steady-state model solutions in Cases 1-3. Given the monotonic increase in O_3 column density with O_2 mixing ratio for the classic (Case 0) result, it previously appeared plausible to imagine that Earth's atmosphere could have existed in a wide range of stable mid-oxic states. In contrast, our flux-driven results suggest that, for a broad range of O_2 and CH_4 fluxes, the majority of solutions cluster in two locations, with limited stable solutions between.

The model atmospheres show a bimodal distribution, with 'high-' (mode of 0.1-0.2) and 'trace-' (mode of $1\text{-}2\times10^{-8}$) O_2 atmospheres (Figure 3-6, upper panel). With 'high-O_2' atmospheres defined as those with pO_2 above 2.1×10^{-6} and, as a conservative measure, discarding the atmospheres with O_2 concentrations greater than 0.30 (since these are unlikely to have existed for most of the Phanerozoic), 95% (2σ) of our model atmospheres have pO_2 greater than 5×10^{-3}, and 97.5% have pO_2 greater than 2×10^{-3} (~1% PAL). The results may be additionally conservative as the bulk of the solutions computed with lower than 1% PAL O_2 were from cases in which oxidative weathering was set one order of magnitude higher than presently constrained values. With 'trace-O_2' atmospheres defined as those with pO_2 less than

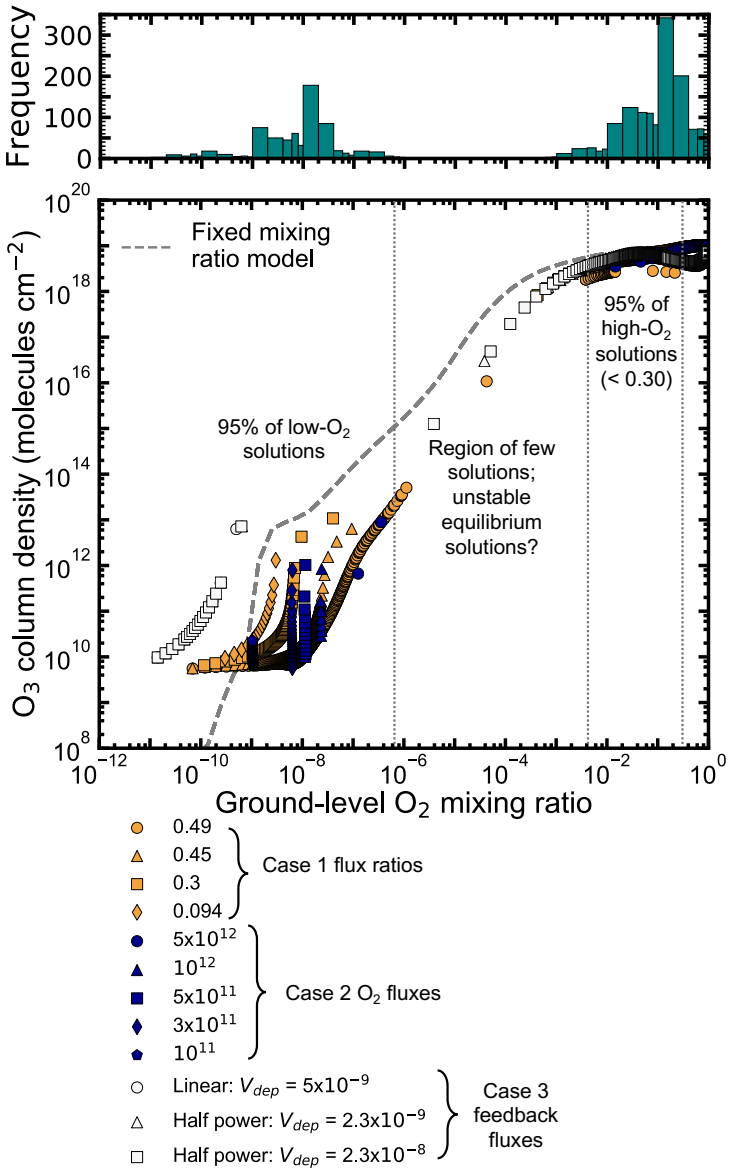

Figure 3-6: Summary of Cases 1-3 compared to the classic model.
Upper panel: histogram showing frequency of model atmospheres with different ground-level O_2 mixing ratios (Cases 1, 2 & 3). Lower panel: O_3 column density plotted against O_2 mixing ratio for all model atmospheres in Cases 1 (orange symbols), 2 (purple symbols), and 3 (white symbols), compared to the results from the fixed mixing ratio-driven model (Case 0; grey dashed line). Vertical dotted lines indicate the regions of O_2 mixing ratio space in which most of the model solutions lie.

2.1×10^{-3}, 95% of our model atmospheres have pO_2 less than 6×10^{-7}. While by no means a comprehensive statistical treatment, this supports previous studies (Claire et al., 2006; Daines and Lenton, 2016; Goldblatt et al., 2006; Laakso and Schrag, 2017), which concluded that there is a region of pO_2 parameter space spanning several orders of magnitude in which model atmospheric solutions are particularly sparse.

For Cases 1-3, the absolute fluxes of O_2 and CH_4 at which the atmospheres switch from reducing to oxic varies. Figure 3-7 normalises this by plotting against K_{oxy}, which is defined as the O_2 source flux divided by the stoichiometrically-balanced average fluxes of all reducing gases (Catling and Claire, 2005). Model atmospheres with K_{oxy} less than 1 are reducing, and those with K_{oxy} greater than 1 are oxic, suggesting that the ratio of total reductant to oxidant flux determines in which of the two states the atmosphere lies. It further illustrates the very narrow range in flux space for which intermediate solutions beyond our 95% confidence bounds exist. If any of these lower pO_2 solutions were to persist in the Earth system, they would require very strong (unspecified) negative feedbacks to maintain biologic fluxes in a tight window.

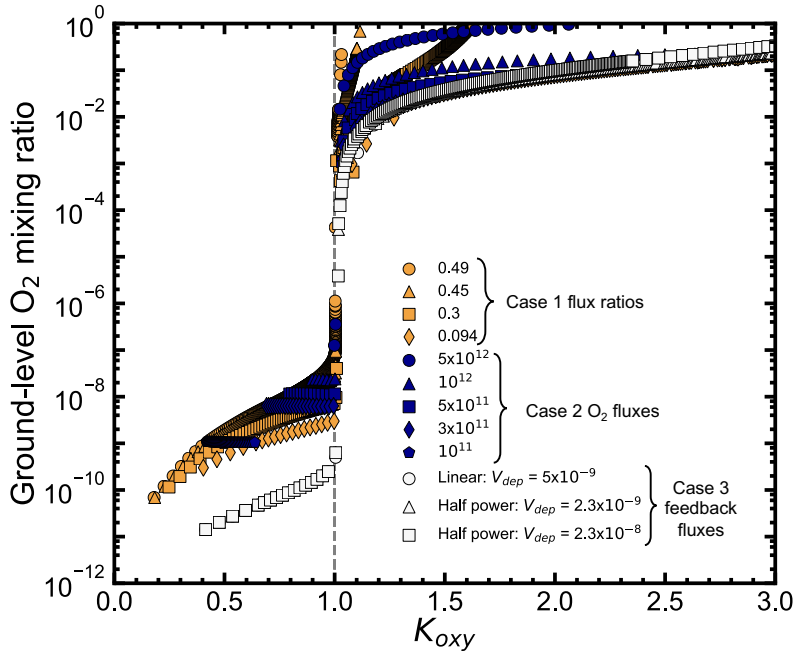

Figure 3-7: Model-predicted ground-level O_2 mixing ratios plotted against K_{oxy}, for all model atmospheres from Cases 1-3.
Model atmospheres with $K_{oxy} < 1$ are reducing, while those with $K_{oxy} > 1$ are oxidising.

3.4.6 – Exploring flux boundary conditions for other redox-relevant species

As a final set of tests, we examined the sensitivity of model output to the choice of boundary conditions for the reducing gases H_2 and CO. The H_2 flux has been shown to affect the pO_2 of steady-state model atmospheres (Laakso and Schrag, 2017). The

two-state behaviour described above persists despite changes in the magnitude of reducing fluxes, and further strengthens our conclusion that the user-specification of boundary conditions must be carefully considered, even for trace species.

3.4.6.1 – Case 4: Magnitudes of reducing fluxes

For a fourth test case, we varied the magnitude of the fluxes of H_2, CO, H_2S and SO_2 into the model atmosphere, using the 'modern low,' 'modern high' and 'Archaean high' values from Zahnle et al. (2006; Table 3-1). When we used the 'modern low' fluxes as fixed flux LBCs for a model with fixed mixing ratio (modern-like) boundary conditions for O_2, CH_4 and N_2O, the resulting mixing ratios for H_2 and CO were 7.7×10^{-7} and 2.5×10^{-8}, which are slightly higher and lower than modern estimates, respectively (Ehhalt et al., 2001). Using the computed N_2O flux and fixed CH_4:O_2 flux ratio of 0.16, we produced a model suite with varying O_2 flux. We repeated this method for the 'modern high' and 'Archaean high' fluxes.

For all three scenarios, a jump from reducing to oxic atmospheric solutions within a narrow flux range was observed (Figure 3-8). The 'gap' in O_2 mixing ratio solutions is slightly different to that produced in Cases 1-3, and again varies significantly over a range of O_2 fluxes. Regardless, the absolute magnitude of H_2 and CO fluxes (between end-member parametrisations) does not affect the overall two-state behaviour of the model atmospheres with varying user-specified O_2 flux.

3.4.6.2 – Case 5: Additional drawdown fluxes of reductants

Both H_2 and CO are consumed voraciously by microbes. We tested the model sensitivity to additional drawdown fluxes, by implementing a linear feedback flux equal to $V_{dep}[X]N_1$, where $[X]$ is the H_2 or CO mixing ratio. Following Zahnle et al. (2006), we chose deposition velocity values of 2.5×10^{-4} and 1.2×10^{-4} after Kharecha et al. (2005). We distributed the upward fluxes (from the flux-driven modern model) log-normally through the first 10 km of the atmosphere (Zahnle et al., 2006). Using the mixing ratio of CO in the flux-driven modern model, we calculated the resulting downward flux and adjusted the upward flux such that the net flux remained the

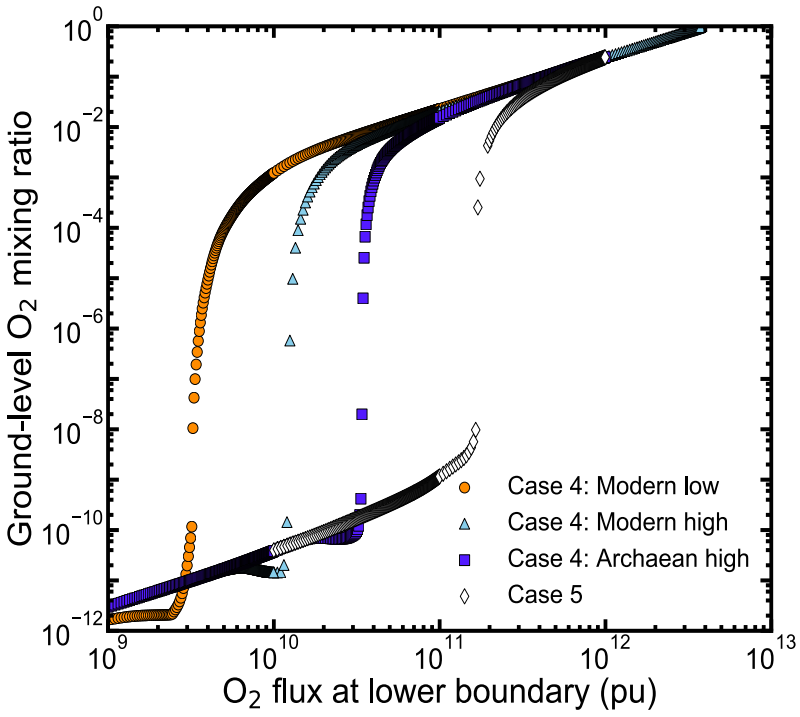

Figure 3-8: Cases 4 & 5 model results.
Model-predicted ground-level O_2 mixing ratios for model atmospheres, showing the effects of varying the fluxes of reducing species H_2, CO, H_2S and SO_2. Indigo squares, blue triangles and orange circles show the Case 4 results, for the 'Archaean high,' 'modern high' and 'modern low' magnitudes of fluxes from Zahnle et al. (2006), for H_2, CO, H_2S and SO_2, respectively. White diamonds show the Case 5 results, for which H_2 and CO are given additional deposition velocities (see Table 3-1).

same as for Cases 1-3. Using the same method for H_2 resulted in a net downward flux, so we increased the upward flux until the net H_2 flux was positive (i.e. into the atmosphere). The resulting CO and H_2 mixing ratios were fairly similar to the global measured averages (6.2×10^{-8} and 5.5×10^{-7}, respectively; Ehhalt et al., 2001). Using these combined flux and deposition velocity conditions for H_2 and CO, we reproduced a suite of models with varying O_2 flux, at a constant CH_4:O_2 flux ratio (0.094). The results (Case 5 on Figure 3-8) are our best attempt to properly model CO and H_2, and also display the two-state behaviour observed in Cases 1-3.

3.4.6.3 – Case 6: Mixing ratio boundary conditions for H_2 and CO – a cautionary tale

Using modern-like fixed mixing ratio LBCs for H_2, CO and N_2O produced results broadly similar to those described in previous subsections, in that there were

reducing and oxic model atmospheres, and a transition between them within a very narrow flux range. However, this model setup (preliminary work presented by Gregory et al. 2019) also produced a third cluster of 'very-low O_2' atmospheres ($7\times10^{-7} < pO_2 < 3\times10^{-5}$; not shown), occurring only inside the narrow transition flux range, and featuring considerable ozone, but not a fully protective ozone shield. In addition, the 'high-O_2' atmospheres only had minimum O_2 mixing ratios of 10^{-2}, considerably affecting the application of our model to palaeo-O_2 levels over Earth history.

This demonstrates that the fixed mixing ratio LBCs of some trace gases enables the same numerical issues (potentially unphysical fluxes across the lower boundary) as for the more dominant species. Our results from Cases 1-5 with fixed flux boundary conditions for H_2 and CO allowed us to determine that the original three-state behaviour was driven by instabilities in the model-predicted lower boundary fluxes of H_2 and CO, which the model was switching between net input and output depending on the CH_4:O_2 flux ratio. This emphasises our primary conclusion that any photochemical modelling effort must fully describe choices for boundary conditions, even for trace species, in order to allow reproducibility and assess reliability.

Having determined from Cases 4-6 that H_2 and CO flux boundary conditions produce rather different model atmospheres to mixing ratio LBCs, but that the magnitude of the fluxes, and the inclusion of negative feedback fluxes do not affect the primary result of pO_2 bistability, we focus our discussion on Cases 1-3. While a full exploration of appropriate H_2 and CO lower boundary fluxes is beyond the scope of this thesis, the 'flux-driven modern model' fluxes remain a good choice because of the better prediction of H_2 and CO ground-level mixing ratios, and their ease of comparison with previous 1-D photochemical modelling studies.

3.5 – Discussion

3.5.1 – Box models

Our results impact on previous work which predicts an abrupt shift from reducing to oxic atmospheres over an extremely narrow oxygen flux range (Alcott et al., 2019; Claire et al., 2006; Daines et al., 2017; Goldblatt et al., 2006; Laakso and Schrag, 2017). Despite extrapolating from the fixed-mixing ratio models we have called into question (e.g. Case 0), these box-model studies elucidated that flux-driven feedbacks within the Earth system drive a rapid transition between clusters of trace-O_2 and high-O_2 solutions, while passing through intermediates.

Model atmospheres with these 'intermediate' oxygen compositions have been produced by previous 1-D photochemical modelling efforts, but we have shown that some are unstable equilibrium solutions when explored in flux-driven photochemical models. Minuscule perturbations to lower boundary fluxes seemingly drive any intermediate 'solutions' towards attractors in high-O_2/O_3 or trace-O_2/O_3 regions of parameter space, due to positive feedbacks involving the formation of an optically thick ozone column (Claire et al., 2006; Goldblatt et al., 2006). While issues of kinetics remain to be determined, these atmospheric feedbacks will presumably occur much more rapidly than other biogeochemical feedbacks, which we predict would strongly amplify existing non-linear behaviour in box models, as well as potentially drive strong feedbacks on microbial ecology. A full exploration of the dynamics of photochemical (in)stability and kinetic timescales for transitions requires time-dependent atmospheric models beyond the scope of this thesis. Simultaneous incorporation of these short/medium-term atmospheric forcings into a long-term biogeochemical model with appropriate Earth system feedbacks would be an interesting target for future work.

3.5.2 – Proterozoic pO_2

The lower limit of the high-O_2/O_3 solutions has interesting applications as a potential constraint on Proterozoic pO_2. Palaeo-O_2 levels over Earth history

compatible with the regions of stability shown in this study are compared to proxy constraints in Figure 3-9. Though our model results comment only on the potential stability of palaeo-O_2 levels, as opposed to their temporal evolution, we have truncated our regions of stability to fit with the commonly-accepted temporal constraints associated with the presence of S-MIF, O-MIF and charcoal. Our results are consistent with the estimates of Proterozoic pO_2 given by the absence of redox-sensitive minerals in Proterozoic sediments (e.g. Johnson et al., 2014), evidence for surface ocean oxygenation (Lenton and Daines, 2017), and the presence of variable $\delta^{53}Cr$ since 1390 Ma (Canfield et al., 2018). They are also consistent with (but stronger than) the lower limit of 2.1×10^{-4} indicated by the presence of an ozone layer (Segura et al., 2003), as revealed by non-zero O-MIF. However, since this constraint arose from models using fixed mixing ratio boundary conditions, our

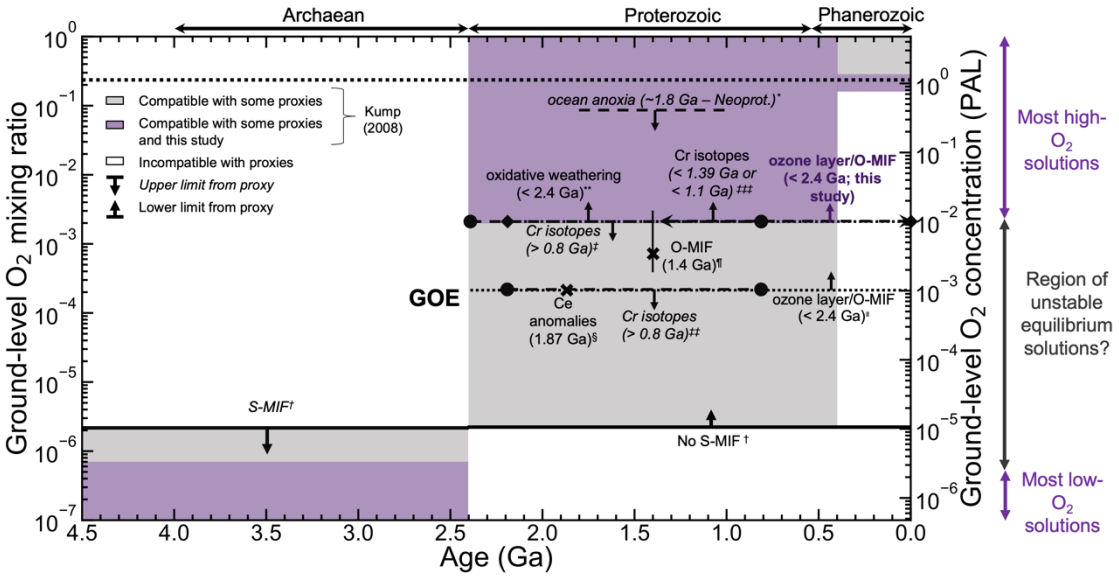

Figure 3-9: Summary of results from this study, in terms of palaeo-O_2 levels.
*Purple regions show the ground-level O_2 mixing ratios of most of our model solutions in the context of existing constraints for pO_2 over Earth history. Grey regions show O_2 mixing ratios compatible with some proxies, from the review by Kump (2008). In addition, existing upper limit constraints are shown with downward arrows and annotations in italics (*Canfield, 1998, 2005; †Farquhar et al., 2000; Pavlov & Kasting, 2002; ‡‡Planavsky et al., 2014 (dashed line with circle end markers); ‡Cole et al., 2016; Planavsky et al., 2018 (dashed line with circle end markers)). Existing lower limits are shown with upward arrows and annotations in regular text (‡‡‡Canfield et al., 2018; Gilleaudeau et al., 2016 (dashed line with arrow end markers); ‖ Crockford et al., 2018; Segura et al., 2003 (dotted line); **Holland, 1994; Rye and Holland, 1998 (dotted line with diamond end markers)). Existing constraints from single points in time are shown by crosses (§Bellefroid et al., 2018; ¶Planavsky et al., 2020 (vertical line shows 90% confidence interval)). The post-Devonian charcoal record constraints are well-established, so we trim our constraints (purple regions) to fit with this.*

results suggest a revision of the lower limit to 2×10^{-3}, as our flux-driven models produced very few solutions with both an ozone layer and pO_2 lower than this. Our results are inconsistent with arguments for low mid-Proterozoic pO_2 (e.g. Cole et al., 2016; Planavsky et al., 2014, 2020).

3.5.3 – Earth system feedbacks and switches between states

Our results also prompt comments on the reversibility of the switch between the trace-O_2/O_3 and high-O_2/O_3 states. After an oxic atmosphere is established, is it possible to reduce biospheric fluxes, through a primary productivity crash or ecological reorganisation, to sufficiently low levels (with $K_{oxy} < 1$) such that the ozone layer collapses and pO_2 falls by several orders of magnitude? The continuous existence of terrestrial eukaryotic life precludes this scenario for most of the Phanerozoic, while the presence of O-MIF (Crockford et al., 2019) after the GOE strongly argues against a return to the trace-O_2/O_3 state during the bulk of the Proterozoic. Apparently, feedbacks between atmospheric chemistry of ozone formation and biospheric oxygen production are quite strong.

Our model results suggest a previously undescribed stabilising feedback to prevent such reversibility. We have assumed that CH_4:O_2 flux ratios of 0.5 and 0.1 are representative of reducing biospheres and the modern biogeosystem, respectively. With this in mind, consider a reducing atmosphere supported by a putative low productivity late Archaean biosphere featuring a low O_2 flux and a CH_4:O_2 flux ratio of 0.49. Following this suite of models (along the arrow labelled (1) in Figure 3-2c), an increase in O_2 flux leads to a jump from the trace-O_2 to the oxic state, at an O_2 flux near 8.5×10^{12} pu in this example. In the resulting oxidising atmospheres, increased methane oxidation in sediments decreases the CH_4:O_2 ratio towards 0.1 (arrow labelled (2)). Subsequently, the decrease in O_2 flux necessary to plunge back into an anoxic world is far greater than for the higher CH_4:O_2 flux ratio values (arrow labelled (3)). This constitutes a hysteresis loop preventing small decreases in O_2 flux from reversing atmospheric oxidation. The sulphate-dependent transition to lower CH_4:O_2 ratios is therefore a positive Earth-system feedback that helps maintain an

oxic atmospheric state. In addition to time-dependent photochemical modelling, additional ecosystems modelling work is needed to consider this further, such as a study of the remineralisation dynamics and stability of sedimentary packages during the transition from Archaean-like CH_4:O_2 flux ratios of 0.5 to modern-like ratios below 0.1.

3.6 – Conclusions

In this study we have shown that photochemical models utilising fixed flux boundary conditions can contribute towards constraints on atmospheric oxygen over Earth history. Even with the inclusion of long-term negative feedback fluxes of O_2, atmospheric chemistry drives the atmosphere towards one of two states, between which there are few stable equilibrium solutions. Specifically, there is a dearth of stable atmospheric configurations with pO_2 between 6×10^{-7} and 2×10^{-3}. Our results support estimates of trace-O_2 levels in the Archaean and O_2 levels greater than 1% PAL during the Proterozoic and Phanerozoic. In Chapter 6, we will explore these constraints further with the use of a 1-D photochemical oxygen isotope model, which we develop in Chapter 5. However, principally this study highlights the importance of carefully prescribed and described boundary conditions in photochemical models.

Chapter 4

Triple oxygen isotope model development

We developed the 1-D photochemical model *Atmos* (described in Chapter 2; Catling et al., 2010; Claire et al., 2014) to include the three isotopes of oxygen. Here, we describe the implementation of the triple oxygen isotope model, including the assumptions made. We validate the model in Section 4.2, and explain its utility for addressing questions regarding the modern- and palaeo-Earth atmosphere in Section 4.3. Our triple oxygen isotope model is developed via a private repository (https://github.com/StAtmos/statmos), but will be included in future releases of *Atmos*, following publication of relevant thesis chapters.

4.1 – Development of the oxygen isotope model

We developed the model using similar assumptions to Pavlov and Kasting's (2002) and Claire et al.'s (2014) multiple sulphur isotope models, but slightly different methodology, as follows. The sulphur isotope models computed each individual minor isotope species in equilibrium with the major species after the steady-state solution was obtained, whereas we compute all isotopologue species and reactions self-consistently at each timestep within the main model code. The assumptions and boundary conditions described in this section are for an atmosphere in which no fractionations (mass-dependent (MDFs) or mass-independent (MIFs)) are imparted to atmospheric species, unless otherwise stated. For the effects of inclusion of MIFs and MDFs, see Chapters 5 and 6.

We took the existing template for *Atmos* that predicts a modern-like atmosphere, starting with a version that does not include chlorine-bearing species (which were

added by Catling et al., (2010)), since this version contains fewer species and is therefore simpler to develop as an initial model case. The original template incorporated 49 species involved in 229 reactions (37 of which were photolysis reactions). Of the 49 species, 32 contained at least one oxygen atom, and these were involved in 199 of the reactions.

4.1.1 – Adding new species and specifying initial mixing ratios

As outlined in Chapter 1, there are three isotopes of oxygen, with Solar System abundances 99.762% (^{16}O), 0.2% (^{18}O), and 0.038% (^{17}O) (Bao et al., 2016). For each oxygen-bearing species in the model, we added new species, specifying the oxygen isotope(s) for each one. For example, we replaced non-isotope-specific O_3 in the original model with three species: O_3, OOP and OOQ, where O, P and Q denote ^{16}O, ^{17}O and ^{18}O respectively throughout this thesis (Yung et al., 1997). We assume that species with more than one minor isotope (e.g. OPP, OPQ) would make up negligible proportions of the total species budget, and can therefore be neglected (Lyons, 2001; Pavlov and Kasting, 2002; Young et al., 2014).

Some existing oxygen isotope models differentiate between the same molecule but with different arrangements of the heavy and light oxygen isotope, in particular differentiating between asymmetric OOQ with a heavy atom at one end of the molecule, and symmetric OQO with a centrally-located heavy atom. It has been shown that the asymmetric isotopologues are more enriched in heavy isotopes than the symmetric isotopologues, due to different ozone formation rates for the different arrangements (Bhattacharya et al., 2008; Janssen, 2005). Furthermore, the different formation pathways have been shown to be temperature- and pressure-dependent (Bhattacharya et al., 2008; Guenther et al., 1999; Janssen, 2005; Wiegel et al., 2013). It has also been shown that asymmetric and symmetric ozone isotopomers have slightly different atmospheric lifetimes (e.g. Ndengué et al., 2014).

Some atmospheric nitrate formation models account for the different isotopomers. For example, Morin et al. (2009) calculate the contribution of O_3 oxidation of NO by

assuming an enrichment of asymmetric ozone with respect to bulk ozone, and assuming that this oxidation occurs by donation of one of the terminal oxygen atoms (Savarino et al., 2008). Alexander et al. (2009) explore model sensitivity to $\Delta^{17}O_{O3}$ value and oxidation mechanism, and find that the model best reproduces the data when tropospheric $\Delta^{17}O_{O3}$ is 35‰ and oxidation occurs only by the end-positioned oxygen atoms, and that the model is sensitive to these assumptions. Vicars and Savarino (2014) base their calculation of tropospheric ozone $\Delta^{17}O$, which contributed greatly to the existing tropospheric $\Delta^{17}O_{O3}$ dataset, on the assumption of transfer of predominantly terminal oxygen atoms from ozone in the formation of nitrate, and a greater O-MIF component in asymmetric ozone isotopomers.

Other oxygen isotope models also take into account the different isotopomers of ozone (e.g. Liang et al., 2006; Lyons, 2001; Michalski et al., 2014; Wiegel et al., 2013; Yung et al., 1997). However, these models tend to only track $\Delta^{17}O$ rather than $\delta^{17}O$ and $\delta^{18}O$ individually. Young et al. (2014) argue that this approach can overestimate $\Delta^{17}O$ relative to measurements.

Many existing oxygen isotope models focus only on the isotopic composition of bulk ozone, and do not account for isotopomerical differences (e.g. Alexander et al., 2004; Kunasek et al., 2008; Michalski et al., 2003; 2004; 2005; Morin et al., 2007; Young et al., 2014). While Morin et al. (2009) do differentiate between isotopologues, they find negligible difference to their nitrate isotope results between the two methods. Additionally, while other oxygen isotope models focussing on nitrate have found assumptions regarding the exact nature of the transfer of oxygen atoms from ozone to be helpful, we consider more species than nitrate. Many oxygen isotope models predicting the isotopic composition of sulphate have not taken this into account. For example, Sofen et al. (2011) assume a bulk ozone $\Delta^{17}O$ of 35‰, and that one sulphate oxygen atom comes from ozone, thereby assuming the contribution of $\Delta^{17}O$ from ozone to sulphate to be 35/4 = 8.75‰. However, their focus is on the change in $\Delta^{17}O_{SO4}$ value, over time, as opposed to the absolute value.

We follow the latter assumption in not differentiating between symmetric/asymmetric isotopomers of ozone, for the sake of simplicity at this stage.

Since we have several large oxygen-bearing species included in the model, the specification of ozone isotopomers ought to also include similar details for other molecules, which have not been so closely studied. Furthermore, we are interested in bulk ozone isotopic enrichment rather than the specific enrichment of different ozone isotopomers. However, since there is clear evidence for preferential ozone formation to certain isotopomers, as well as pressure- and temperature-dependencies of these enrichments, and this might affect the way in which the MIF signal is propagated to other atmospheric species (as has been shown for nitrate; Savarino et al., 2008), the inclusion of different isotopomers may be a good direction for future model development. However, we follow Young et al. (2014), who argue that the inclusion of mass-dependent as well as mass-independent fractionation effects is far more important than including detailed mechanisms of ozone MIF formation, given that the signal arises in only one reaction (see Chapter 5 for additional details).

One of the model inputs is initial mixing ratios with altitude for each of the long-lived species in the model. The model then adjusts these initial estimates to give an output steady-state solution, again in terms of mixing ratios with altitude for each species. We therefore added new initial mixing ratios for each additional species. In this process, we assumed that the concentrations of new minor species do not affect the concentrations of the major species (Pavlov and Kasting, 2002). Therefore, for simplicity, when choosing the initial mixing ratios, we keep those of the major isotopic species the same as the original non-specified species, but also add the minor species at the Solar System ratios. In effect, for species with one oxygen atom, we have 100.238% of the original abundance of the whole species, but this addition is negligible and does not affect the mixing ratios of non-oxygen-bearing species significantly.

For species with one oxygen atom (e.g. O, H_2O, NO, SO), the 'initial guess' mixing ratios are equal to the mixing ratio with altitude of the original species multiplied by the universal absolute isotope ratios for the minor species, ${}^{x}R_0$. ${}^{x}R_0 = {}^{x}O/{}^{16}O$, where x=17 or 18; ${}^{17}R_0$ is 0.00038 and ${}^{18}R_0$ is 0.002. For species with more than one

oxygen atom (e.g. H_2O_2, O_3, HO_2NO_2, N_2O_5), the initial mixing ratios chosen for the minor isotope species (MR_{min}) are equal to the mixing ratios of the original species (MR_{maj}) multiplied by ${}^{x}R_0$ and by the number of oxygen atoms, n_{oxy}. The rationale for this is explained in detail in Pavlov and Kasting (2002). To take H_2O_2 as an example, the possible combination of isotopologues is H_2O_2, H_2OP, H_2PO, H_2OQ and H_2QO, as there are two possible positions for the oxygen atoms (n_{oxy} = 2). The probability of choosing a molecule with one ^{17}O is therefore equal to the probability of having an ^{16}O atom in the first space (1, given our assumption) and a ^{17}O atom in the second space (0.00038), plus the probability of having a ^{17}O in the first space and a ^{16}O in the second space. The mixing ratio of the ^{17}O-bearing isotopologue is therefore:

$$MR_{H_2OP\ (inc.\ H_2PO)} = MR_{H_2O_2} \times \left(\left(1 \times {}^{17}R_0\right) + \left({}^{17}R_0 \times 1\right)\right) \qquad \textit{(Eq. 4-1)}$$

More generally, then:

$$MR_{min} = MR_{maj} \times n_{oxy} \times {}^{x}R_0 \qquad \textit{(Eq. 4-2)}$$

Since we do not treat isotopologues with the minor isotopes in different positions as different species (including O_3, as discussed above), the increased abundances of minor isotopologues with multiple oxygen atoms must be taken into account in the specification of mixing ratios.

4.1.2 - Boundary conditions

As in the original model, each new species was allocated boundary conditions. The way in which boundary conditions for the triple oxygen isotope model are chosen is summarised in Table 4-1, and as follows. See Section 2.5 and Chapter 3 for a more comprehensive account of the four different types of lower boundary used in *Atmos*.

i) For species with mixing ratio boundary conditions, we kept the mixing ratio of the major isotopologue (only containing ^{16}O atoms) the same as the mixing ratio of non-isotope-specified species in the original model, despite the

addition of the minor isotopic species. As with the 'initial guess' mixing ratios (see above), for the minor isotopologues, the mixing ratio boundary condition was set equal to the major isotopologue mixing ratio multiplied by ${}^{x}R_0n_{oxy}$. For example, for O_2 in the standard modern model atmosphere, the $^{16}O^{16}O$ mixing ratio is 0.21 (the same as O_2 in the original model). For OP, the mixing ratio at the lower boundary was set to '0.21 × 0.00038 × 2,' and for OQ, '0.21 × 0.002 × 2.'

ii) For each flux-driven boundary condition, we kept the specified fluxes the same for the major isotopologues as with the original model, and multiplied those fluxes by ${}^{x}R_0n_{oxy}$. For the standard model, there are no species with this boundary condition, but our flux-driven experiments from Chapter 3 show that it is worthwhile running experiments with this type of boundary condition, as we do in Chapters 5 and 6.

iii) For species with deposition velocity boundary conditions, the minor isotopologues have the same value for V_{dep} as the major isotopologues, because we assume that the major and minor isotopologues of a certain species are as 'sticky' and reactive at the Earth's surface as each other. In other words, we assume that there is no oxygen isotope fractionation due to processes at the surface, at least in the standard isotope model. The absolute flux of molecules out of the atmosphere will differ between the major and minor isotopologues, because the flux is a product of the number density and V_{dep}. Since the number densities of the minor isotopologues should be equal to that of the major isotopologue multiplied by ${}^{x}R_0n_{oxy}$ (see above), the resulting flux of molecules out of the atmosphere over the lower boundary should be equal to that of the major isotopologue multiplied by ${}^{x}R_0n_{oxy}$.

iv) Finally, with a combined distributed flux and deposition velocity boundary condition, the total distributed flux of the minor species is calculated as with the flux boundary condition, and the deposition velocity is kept the same (as above). The height, H, over which the flux is distributed is the same for each

isotopologue, since the standard model does not incorporate fractionations that could occur in processes in the injection of volcanic and biogenic gases into the model. For example, SOP and SOQ have the same deposition velocity as SO_2 (though the absolute fluxes out of the atmosphere scale with the number densities), but the fluxes that are distributed within the first 20 km of the atmosphere have been multiplied by ${}^{x}R_0$ and n_{oxy}.

Since the standard modern model atmosphere only uses upper boundary conditions for atomic nitrogen (Section 2.5.2), no upper boundary conditions need to be adjusted for the oxygen isotope model.

4.1.3 – Reaction rates for reactions involving minor isotopologues

As discussed in Section 2.2, one primary model input is the rates of kinetic and photochemical reactions that produce and destroy the species in the atmosphere. For each reaction that involves an oxygen-bearing species, the reaction is replaced by multiple reactions with the different isotopologues. For reactions where all oxygen-bearing reactants only contain the major isotope ^{16}O, the reaction rate remains the same as in the original model. For reactions involving minor isotopologues, we follow the same assumptions as Pavlov and Kasting (2002), as follows:

4.1.3.1 – Kinetic reaction rates

We assume that reactions involving two or more P- or Q-bearing species do not occur, e.g.

$$\mathrm{P} + \mathrm{Q} \rightarrow \mathrm{PQ}$$

$$\mathrm{PH} + \mathrm{HOP} \rightarrow \mathrm{H_2}\ \mathrm{P} + \mathrm{OP}$$

Table 4-1: Summary of boundary conditions for minor isotopologues, where MR is the mixing ratio (with subscripts min=minor isotopologue, maj=major isotopologue, or the species name), n_{oxy} is the number of oxygen atoms in the molecule, and ${}^{x}R_0$ is the universal isotope ratio (${}^{17}R_0$=0.00038, ${}^{18}R_0$=0.002). The last column shows the O-bearing species with the boundary condition in the standard model (major species name only).

Lower boundary condition	**Relation to major isotopologue boundary condition**	**Example**	**Species**
i) Mixing ratio	$MR_{min} = MR_{maj} \times {}^{x}R_0 \times n_{ox}$	$MR_{OP} = MR_{O_2} \times 0.00038 \times 2$ $MR_{OQ} = MR_{O_2} \times 0.002 \times 2$	O_2, CO, N_2O, CO_2
ii) Flux	$F_{min} = F_{maj} \times {}^{x}R_0 \times n_{ox}$	$F_{OP} = F_{O_2} \times 0.00038 \times 2$ $F_{OQ} = F_{O_2} \times 0.002 \times 2$ (NB. Not in standard model.)	None in standard model; see Chapter 5.
iii) Deposition velocity	$V_{dep\_min} = V_{dep\_maj}$ Resulting in $F_{out} = V_{dep} \times MR_0 \times [M]_0$ Where F_{out} is the resulting flux out of the atmosphere, and MR_0 and $[M]_0$ are the mixing ratio and atmospheric density at the ground respectively.	$V_{dep\_OOP} = V_{dep\_O_3}$ $V_{dep\_OOQ} = V_{dep\_O_3}$ Resulting in $F_{out\_OOP} = F_{out\_O_3} \times 0.00038 \times 3$ $F_{out\_OOQ} = F_{out\_O_3} \times 0.002 \times 3$ (since $MR_{min} = MR_{maj} \times {}^{x}R_0 \times n_{ox}$)	O, H_2O, OH, HO_2, H_2O_2, HCO, H_2CO, NO, NO_2, HNO, SO, H_2SO_4, HSO, SO_3, OCS, O_3, HNO_3, NO_3, HO_2NO_2, N_2O_5, SO_4^{AER}
iv) Distributed flux & deposition velocity	$F_{min} = F_{maj} \times {}^{x}R_0 \times n_{ox}$ $V_{dep\_min} = V_{dep\_maj}$ $H_{min} = H_{maj}$	$F_{SOP} = F_{SO_2} \times 0.00038 \times 2$ $F_{SOQ} = F_{SO_2} \times 0.002 \times 2$ $V_{dep\_SOP} = V_{dep\_SO_2}$; $H_{SOP} = H_{SO_2}$ $V_{dep\_SOQ} = V_{dep\_SO_2}$; $H_{SOQ} = H_{SO_2}$	SO_2

This is consistent with our earlier assumption that no molecules with more than one minor isotope exist, since these would otherwise be produced. This simplification is acceptable because the proportions of minor isotopic species are sufficiently low that the resulting reaction rates would be negligible. For kinetic reactions with only one product pathway, such as:

$$O + OOP \rightarrow O_2 + OP$$
$$O + NQ + M \rightarrow NOQ + M$$

the reaction rate remains the same as for the original reaction (Lyons, 2001; Pavlov and Kasting, 2002). In Chapter 5, we develop the model to include mass-dependent fractionations via rate dependencies on the reduced mass of the isotopologues in all two-body and three-body reactions (e.g. Liang et al., 2007; Young et al., 2014), which allows the model to simulate important processes in the atmosphere.

4.1.3.2 – Branching ratios

If the addition of different isotopologues results in more than one combination of products, e.g.

$$HCP + O_2 \rightarrow CO + HOP \text{ or}$$
$$\rightarrow CP + HO_2$$
$$O + NOQ \rightarrow NO + OQ \text{ or}$$
$$\rightarrow NQ + O_2,$$

the reactions are allocated a 'branching ratio,' such that the total of the branching ratios of the different pathways is equal to one. The branching ratios can be chosen using one of two methods.

A first option is that the branching ratio can be calculated statistically, as 1 divided by the number of oxygen atom 'positions' that a ^{17}O or ^{18}O could fall into (i.e. $1/(n_{oxy,R1} + n_{oxy,R2})$). For example, for the reaction:

$$HCO + O_2 \rightarrow CO + HO_2$$

three oxygen atoms are involved. When the reactants are instead HCP and O_2, the products could be either CO + HOP or CP + HO_2. Since two of the three oxygen atoms involved in this reaction are in the HO_2 molecule, the probabilities of the minor isotope ending up in the HO_2 and CO are ⅔ and ⅓ respectively. When the reactants are CO + HOP, the same two product pathways again have probabilities of ⅔ and ⅓. This whole method will then be copied for the Q-bearing isotopologues, which will be treated in the same way.

The second option involves more careful thought about the pathways that are more likely to occur in terms of chemical kinetics. To continue to use the reaction HCO + O_2 → CO + HO_2 as an example, chemically-speaking, it seems more probable that the reactant O_2 will attract the H from HCO, leaving the CO as a product, as opposed to the carbon atom and one of the O atoms from O_2 swapping places. The intuition of this particular example has supporting evidence from theoretical work (Hsu et al., 1996), which has shown that the most likely pathway for the reaction involves the attachment of the O_2 molecule to the carbon atom, followed by the joining of the H atom to the far end of the oxygen molecule, and the breaking of the second C-O bond. In this case, the two O atoms in the product HO_2 will be the same two O atoms from the O_2 reactant.

Therefore, this second method of selecting branching ratios involves elimination of the branches that are chemically unlikely to occur, and redistribution of the statistical probability of other branches (such that they still sum to 1). For most cases, including the example in the previous paragraph, this will mean there is only one pathway remaining, which gains a branching ratio of 1, such that the rate is the same as the original reaction. For others, where for example, there are three products, and one is unlikely to be significant, the probability of each pathway can be calculated as with Method 1. An example of this kind of situation is the reaction:

$$O + HO_2NO_2 \rightarrow OH + NO_2 + O_2$$

Using Method 1, for reactants P + HO_2NO_2, there are five oxygen atom 'positions', so the probability of products PH + NO_2 + O_2, OH + NOP + O_2, and OH + NO_2 + OP are ⅕,

⅖ and ⅖ respectively. The same statistical distribution would hold if the reactants were O + HO_2NOP. However, using Method 2, it could be argued that the reaction is most likely to occur by the abstraction of the H by the single O atom, alongside the breakdown of the rest of the molecule to NO_2 and O_2, as opposed to any other combination of mechanisms. For reactants P + HO_2NO_2 therefore, it can be assumed that the products will always be PH + NO_2 + O_2, and that the other combinations of branches are negligible. On the other hand, for reactants O + HO_2NOP, the branch to PH + NO_2 + O_2 is unlikely to occur. Because we do not specify the position of the minor isotope in the initial HO_2NO_2 molecule, and there are two oxygen atom 'positions' in each of the products NO_2 and O_2, the branches to products NOP + O_2 and NO_2 + OP are half as likely as the major isotopologue reaction.

In these cases, the branching ratios to the products may therefore be different depending on where the minor isotope in the reactants is located. In the case of:

$$HCO + O_2 \rightarrow CO + HO_2$$

our previous discussion would suggest that the reaction HCP + O_2 could be assumed to always result in CP + HO_2, and the reactants HCO + OP would always result in CO + HOP. However, for the reaction:

$$O + HO_2 \rightarrow OH + O_2$$

which Sridharan et al. (1985) shows proceeds by O-abstraction from the HO_2 molecule, the possible pathways would be as follows:

O + HO_2 → OH + O_2, rate k
P + HO_2 → OH + OP, rate k (with branch to PH + O_2 assumed negligible)
O + HOP → PH + O_2, rate ½k (because one of the two oxygen atoms in HO_2 remains attached to the H as OH)
O + HOP → OH + OP, rate ½k (because one of the two oxygen atoms in HO_2 joins the O to form O_2)

If the reaction were treated using Method 1, the pathways would be:

$O + HO_2 \rightarrow OH + O_2$, rate k

$P + HO_2 \rightarrow OH + OP$, rate $\frac{2}{3}k$

$P + HO_2 \rightarrow PH + O_2$, rate $\frac{1}{3}k$

$O + HOP \rightarrow OH + OP$, rate $\frac{2}{3}k$

$O + HOP \rightarrow PH + O_2$, rate $\frac{1}{3}k$

For each method, the total of the rates of the pathways of two specific reactants is equal to the rate of the original reaction, but the rates of each pathway differ to some extent. Note that the P and Q species are being treated exactly the same – produced and destroyed in reactions with the same rate constants and branching ratios.

We chose to use the second method in the development of the oxygen isotope model, in order to achieve a model atmosphere with reaction rates as representative of the actual atmosphere as possible. Where there was not sufficient evidence found in the literature to suggest that one pathway was more probable than another, we used Method 1. For an investigation of the model sensitivity to this assumption, see Section 5.4.3 of Chapter 5.

4.1.3.3 – Reaction rates of isotopic 'twins'

We followed the method of Pavlov and Kasting (2002), also used by Claire et al. (2014), by doubling rates in the case of a self-reaction between a major and minor isotopologue of the same molecule (e.g. OH + PH, O + Q). This was used to ensure mass conservation in the sulphur isotope models. To illustrate the necessity of this method, consider the three-body reactions:

$$O + O\ (+ M) \rightarrow O_2\ (+ M) \qquad \text{R4.1}$$

$$O + Q\ (+ M) \rightarrow OQ\ (+ M) \qquad \text{R4.2}$$

Through reaction R4.1, O_2 is produced at rate: $k_1[O][O]$, which can be normalised to $k_{4.1}{\times}1{\times}1$ or simply $k_{4.1}$ (by neglecting the absolute concentration of $[O]$), where $k_{4.1}$ is the rate constant for reaction R4.1. Meanwhile, OQ is produced at rate $k_{4.2}[O][Q]$, which can be normalised to $k_{4.2}{\times}1{\times}0.002$ or $0.002k_{4.2}$, where $k_{4.2}$ is the rate constant

for reaction R4.2. If $k_{4.1}$=$k_{4.2}$, OQ would be produced at 0.002 times the rate of O_2. However, as outlined in Section 4.1.1, the OQ concentration should be 0.004 times that of O_2, because there are two oxygen atoms in the molecule; the sinks of OQ will then be 0.004 times those of O_2. At steady state, the rate constant $k_{4.2}$ must therefore be twice that of $k_{4.1}$ to conserve mass balance. For two-body reactions, this is done by multiplying the A in Eq. 2-3 by two. For three-body reactions, the rate is doubled by doubling both the A_0 and the A_∞ values, prior to combination.

4.1.3.4 – Photolysis reactions

All the photolysis reactions in *Atmos* involve the breakdown of a molecule by light into two or more molecules, or the excitation of a molecule into a higher energy state. For these reactions, there may be more than one pathway for products, but there is only one reactant, so we assume that probabilities of different pathways occurring is based on the number of spaces for oxygen atoms in each molecule, as in Method 1. For example, for the reaction $SO_3 + h\nu \rightarrow SO_2 + O$, the photolysis of SOOP is likely to produce SOP + O two thirds of the time, and SO_2 and P one third of the time.

We also assume here that the photolysis cross-sections of minor isotopologues are the same as those of the major isotopologues. Work with the photolysis of SO_2 (e.g. Endo et al., 2015) has shown that this is not necessarily an adequate assumption for multiple sulphur isotopes, but, since our aim at this stage is to develop an oxygen isotope model with no fractionations initially, the isotopically-substituted species must behave in the same way as the major isotopologues, so this assumption is both convenient and acceptable here. Additionally, oxygen MIF has been studied for decades and has only been found to be generated through one reaction under atmospheric conditions, which is the formation (rather than the photolysis) of ozone (e.g. Wiegel et al., 2013).

4.1.4 – Other considerations

As well as modifying reaction rates and initial densities, inclusion of the three isotopes necessitated incorporation into other various model subroutines.

4.1.4.1 – Rainout and H_2O

Firstly, since H_2O in the model is reset for the troposphere (see Section 2.4.2), the same is required for H_2P and H_2Q (which were set to $MR_{H2O}{}^{x}R_0$). This simplification is based on the assumption of an infinite reservoir of water, which, in relation to atmospheric concentrations, the oceans constitute. Since the mass of the oceans is so large, the isotopic composition of oceanic H_2O is only negligibly affected by atmospheric fractionation processes and photosynthetic production (Young et al., 2014). Secondly, the minor isotopic species were given the same Henry's law coefficients as the corresponding major isotopic species, since differing coefficients would cause fractionations. The different isotopologues rain out of the atmosphere with a different number of molecules per second, but this is due to the differences in mixing ratio in the troposphere.

4.1.4.2 – Treatment of particle species

In the isotope model, the sulphate aerosol has three isotopologues - SO_4^{AER}, $SOOOP^{AER}$, and $SOOOQ^{AER}$. All sulphate isotopologues have the same fallout rate and rate of production through sulphuric acid. Again, this means that, since the concentrations of the isotopologues depend on the mixing ratios, which should be related via the fractionation factors, the absolute rates of condensation and deposition will be different and proportional to ${}^{x}R_0 n_{oxy}$.

4.1.4.3 – Lightning

In the isotope code, the rates at which the major isotopologues of species involved in the lightning parametrisation are produced and destroyed differs slightly to the rates dictating the minor isotopologues. As an example, N_2 and O_2 are destroyed with rate constant $k_{lightning}$, and NO is produced as a result. Since "half" an O_2 molecule is required to produce a NO molecule, O_2 is destroyed at rate

½($k_{lightning}$[M][O_2]), where [M] is the atmospheric density, with NO produced at twice that rate. Please note that N_2 is treated as an inert gas, whose mixing ratio is calculated as that required, once the mixing ratios of major species are accounted for, to produce a 1 bar atmosphere. Its loss in this reaction is therefore not calculated explicitly (eg. Claire et al., 2014).

However, lightning could break down an OP molecule to either NP or NO. The rate of OP destruction is therefore ½($k_{lightning}$[M][OP]), as above, but the rates of NP and NO production will also be ½($k_{lightning}$[M][OP]), assuming that the two branches are equally likely to occur. Similar branching assumptions were made for the other thermal equilibrium reactions.

4.1.4.4 – CO_2 photolysis above the upper boundary

In the triple oxygen isotope code, as well as additional CO and O flowing into the uppermost grid step to simulate CO_2 photolysis above the upper boundary, the products of COP and COQ photolysis (CP + O, CO + P, CQ + O, CO + Q) are also added. The rates of each set of products is set to half that of the major isotopologues, since there are two branches for each minor isotopologue, and each of the two branches is equally likely to occur.

4.2 – Validation of the oxygen isotope model

In order to ensure that the developed isotope model is applicable for use in modelling experiments, model validation must occur. As explained by Claire et al. (2014) and Pavlov and Kasting (2002), the model, without the inclusion of user-specified fractionations, should produce mixing ratios of oxygen-bearing atmospheric species with mass-dependent and mass-independent fractionations equal to zero throughout the atmosphere. This means that any fractionations in subsequent results should be due only to simulated fractionations representative of the atmospheric system being modelled rather than artificial fractionations. To that end, we examined the MDF and MIF produced by the model for all species, for a modern Earth-like atmosphere.

4.2.1 – Mass-dependent fractionations in the baseline model

Figure 4-1 shows the $\delta^{17}O$ and $\delta^{18}O$ with altitude for all oxygen-bearing species in the oxygen isotope model. The species are ordered in the plot by largest cumulative fractionation (integrated over altitude).

For each species with altitude, the $\delta^{17}O$ and $\delta^{18}O$ are the same, meaning that the isotopologues containing P and Q are being treated in exactly the same way. However, there are mass-dependent fractionations, despite none being purposefully introduced into the code. The largest fractionation is in the short-lived trace species OCS_2, with a peak fractionation of ~15‰ in the lower mesosphere. Most other species have maximum fractionations of magnitudes up to ±5‰. O_3, O_2 and CO_2 are all important atmospheric species in this area of study, and also have the smallest cumulative fractionations. O_3 has fractionations of no more than 0.1‰ for most of the atmosphere, but has a maximum of 1‰ near the upper boundary. O_2 and CO_2 have negligible fractionations throughout the atmosphere, apart from altitudes of 80 km and above, where a small negative fractionation is introduced in O_2 near the upper boundary.

Even larger mass-dependent fractionations produced earlier in the development of this code were reduced by ensuring that the method outlined in Section 4.1 was followed exactly with no mistakes. Reaction rates were checked, ensuring that reactions involving twin isotopic species were doubled, and the isotopologues were treated the same in all subroutines. Currently, despite significant efforts to identify the source, it is not clear why there are mass-dependent fractionations in the baseline model. Something in the model means that ^{16}O is being treated slightly differently to ^{17}O and ^{18}O. The following subsection details some of the possible sources of the fractionations.

4.2.1.1 – Possible sources of fractionations

An obvious potential source of the fractionations would be a mistake in a reaction rate. Since there are almost 1000 reactions in the isotope model, it is plausible that

a mistake could have been included and propagated through other reactions to affect the mixing ratios of several species. However, in addition to checking the reaction rate tables thoroughly, we have developed python scripts to plot reaction rates and rate constants, and calculate integrated rates and rate constants with altitude, in order to better visualise any problems, and these have shown nothing out of the ordinary. Particle deposition and rainfall rates were checked in output files to ensure that all isotopologue species were treated in the same way. Branching ratios were checked in order to ensure that the total of the rates of multiple branches with isotopic species was equal to that of the original reaction rate.

We tested the removal of the Q-bearing species, to investigate whether fractionations were reduced in a model with only ^{16}O and ^{17}O. For this model atmosphere, the mass-dependent fractionations were greatly reduced (with a maximum of 2.5‰ in OCS), but had a very similar shape to the fractionations for the model atmosphere with all three isotope species. This shows that i) the source of the fractionations is independent of the model template used, and therefore likely to be due to an error in the wider model code as opposed to in the introduction of isotope species; ii) the fractionations are exacerbated by the inclusion of a third isotope species. This latter point hints at the possibility that some of the assumptions we have made in the isotope model are adding to these fractionations.

For example, we have assumed that molecules with multiple heavy oxygen atoms make up negligible proportions of the total mixing ratios, and have thus ignored them. However, this means that there is a slightly greater sink and source for species containing only ^{16}O atoms. For example, in the reaction:

R4.3) $O + O_2 \rightarrow O_3$
R4.4) $P + O_2 \rightarrow OOP$
R4.5) $O + OP \rightarrow OOP$
R4.6) $Q + O2 \rightarrow OOQ$
R4.7) $O + OQ \rightarrow OOQ$,

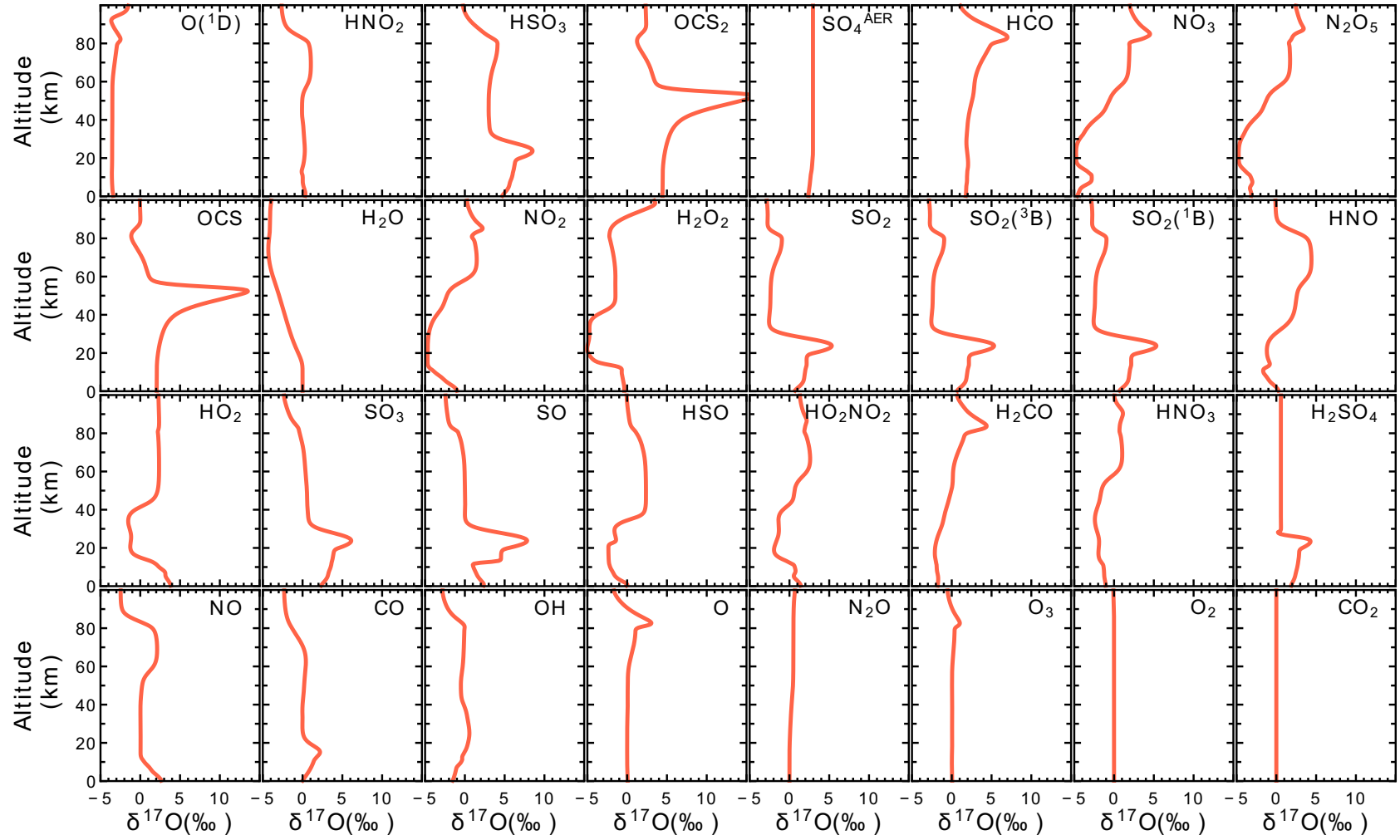

Figure 4-1: $\delta^{17}O$ with altitude for all oxygen-bearing species in the oxygen isotope model, for a case with no user-specified fractionations. The species are ordered in the plot (left to right, and top row to bottom row) by largest cumulative fractionation (integrated over altitude). For all species in this case, the $\delta^{17}O$ values are equal to the $\delta^{18}O$ values. Some artificial non-zero $\delta^{17}O$ values are produced. For this model case, the $\delta^{18}O$ profiles for each species (not shown) are identical.

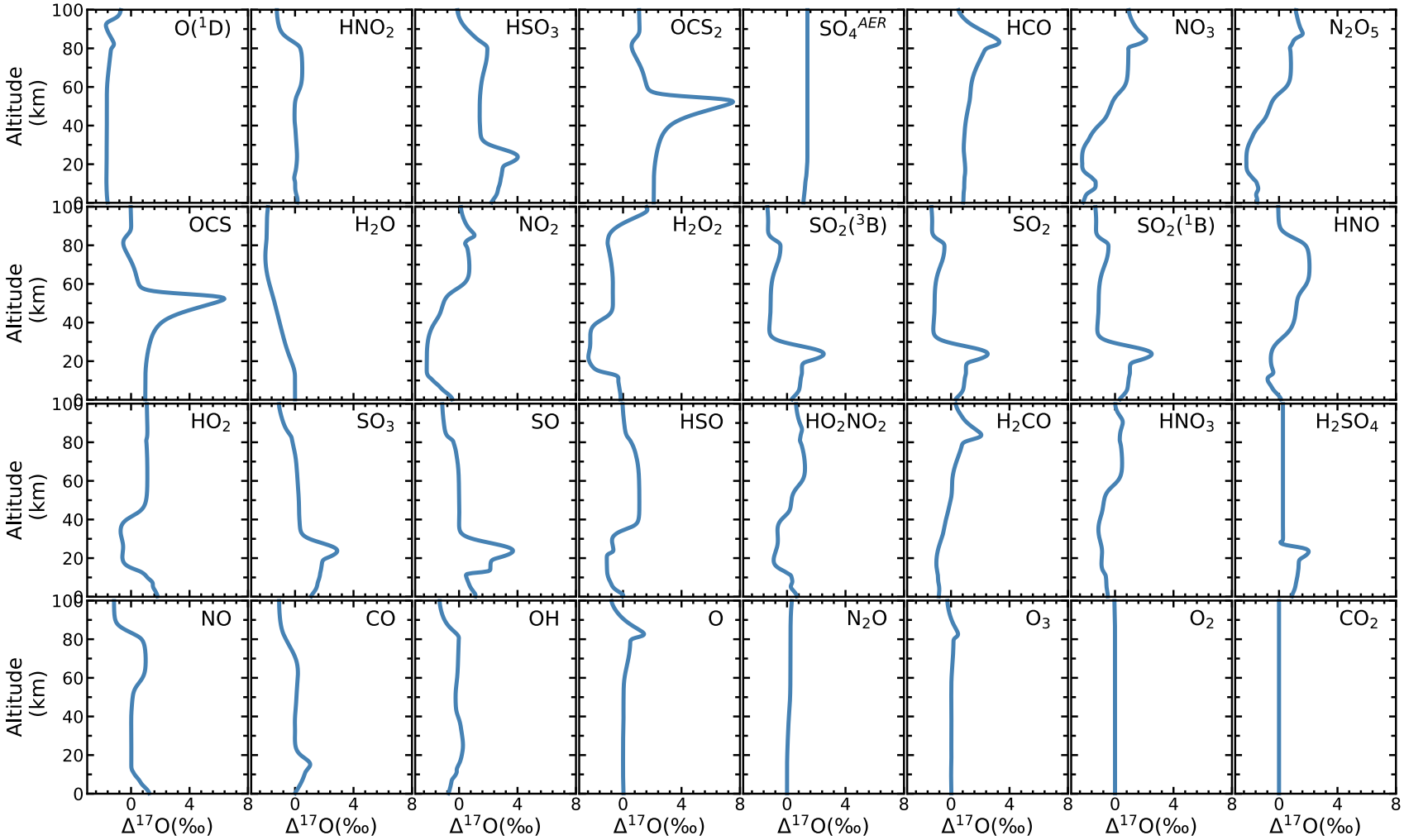

Figure 4-2: $\Delta^{17}O$ values with altitude for all oxygen-bearing species in the oxygen isotope model, with $\Delta^{17}O = \delta^{17}O - 0.528 \times \delta^{18}O$, for a case with no user-specified fractionations. The profiles are close to zero for most species, but there are some artificial fractionations introduced. The species are ordered in the plot (left to right, and top row to bottom row) by largest cumulative $\Delta^{17}O$ (integrated over altitude).

O_2 is destroyed by R4.3, R4.4 and R4.6 (all with rate constant *k*), whereas OP and OQ are only destroyed by R4.5 and R4.7, respectively (also with rate constant *k*). However, if we allowed for multiply-substituted species, each isotopic 'version' of O_2 is destroyed by three reactions, with the addition of:

R4.8) P + OP → OPP
R4.9) O + PP → OPP
R4.10) P + PP → PPP
R4.11) Q + OQ → OQQ
R4.12) O + QQ → OQQ
R4.13) Q + QQ → QQQ
R4.14) O + PQ → OPQ
R4.15) P + OQ → OPQ
R4.16) Q + OP → OPQ
R4.17) P + PQ → PPQ
R4.18) Q + PP → PPQ
R4.19) P + QQ → PQQ
R4.20) Q + PQ → PQQ

These sources of error have in previous work (e.g. Claire et al., 2014; Lyons, 2001; Pavlov and Kasting, 2002; Young et al., 2014) been assumed to be negligible, but it is possible that these small fractionations could accumulate, especially as there are several species that contains several oxygen atoms, in which this effect would be intensified. In fact, Wiegel et al. (2013), find that there is a difference of 2-3‰ for their species of interest (CO_2 and $O(^1D)$) between cases with and without the inclusion of doubly-substituted species and reactions. Their model involved 20 non-substituted reactions, so it was considerably simpler for them to include doubly-substituted reactions than it would be to include them in our model (with more than 300 non-substituted reactions). However, they also found that the inclusion of triply-substituted species and reactions made little difference on top of this. The inclusion of doubly-substituted species, without the added complication of adding

triply-substituted species might therefore be a helpful and feasible aim for development of *Atmos*.

Alternatively, the fractionation may be due to our assumption in which we set the mixing ratios of the major isotopic species to the initial mixing ratios of the species, and added the ^{17}O- and ^{18}O- substituted species mixing ratios on top of these (see Section 4.1.1). However, further investigation of these two potential sources of error is beyond the scope of this thesis at the present time.

4.2.2 – Mass-independent fractionations

4.2.2.1 – $\Delta^{17}O$ in the baseline model

As mentioned above, the $\delta^{17}O$ and $\delta^{18}O$ are the same in this model for all species, since we have not yet included mass-dependent fractionations to tune it to predict the modern atmosphere. This means that, despite the non-zero artificial fractionations in ^{17}O and ^{18}O, the model is not artificially producing fractionations between the two heavy isotopes. However, because of the non-zero $\delta^{17}O$ and $\delta^{18}O$ values and their relationship to $\Delta^{17}O$, the $\Delta^{17}O$ values are also non-zero. This can be seen in Figure 4-2, in which the $\Delta^{17}O$ values of the different species are plotted with altitude. Ideally, the $\Delta^{17}O$ values would be $0 \pm \sim 5\times10^{-5}$ ‰, which reflects the Fortran machine error for 8-bit precision floating-point numbers, and is on the same order of magnitude as that of Claire et al.'s (2014) multiple sulphur isotope model. The maximum $\Delta^{17}O$ value is ~7.5‰ for OCS_2, since the greatest $\delta^{17}O$ and $\delta^{18}O$ were 15‰ for this species and altitude. For most species, the $\Delta^{17}O$ values are $0 \pm \sim 2$ ‰. Again, the smallest artificial fractionations are for O_3, O_2 and CO_2, which is useful, as these are key species of interest for Chapters 5 and 6. For these species in particular, this error is small compared to the mass-dependent fractionations that we will introduce in Chapter 5, but we must bear in mind that this error remains.

This model is therefore suitable within specified error for predicting mass-independent fractionations in atmospheric species, as we can be confident that, at least for a modern-like atmosphere, only small mass-independent fractionations are

being produced. Despite the fractionations, the uncertainty for key species O_3, O_2 and CO_2 is very low for $\delta^{17}O$, $\delta^{18}O$ and $\Delta^{17}O$.

For the baseline model shown in Figures 4-1 and 4-2, CO_2 is treated as a long-lived species rather than an inert species. This is an important change to make to the model, since CO_2 is thought to have an important role in the propagation of large oxygen isotope anomalies through the atmosphere (see Chapter 1). There is very little difference between the $\Delta^{17}O$ values predicted by the baseline model with and without this change. This model has therefore also been validated for use in predicting mass-independent fractionations, and treatment of CO_2 as a long-lived rather than inert species will be used in all future models.

4.3 – Utility of the oxygen isotope model

The baseline model can be used to predict the magnitudes of $\Delta^{17}O$ values for all species at all altitudes in the model, within error. However, further work must be done to reduce the artificial mass-dependent (and resulting apparent mass-independent) fractionations in the three-isotope model, to allow for more meaningful comparison between the isotopic compositions of some species and observations from the literature. However, since the artificial fractionations of several of our particular species of interest (CO_2, O_2, and O_3) are small, we can compare $\delta^{17}O$, $\delta^{18}O$ and $\Delta^{17}O$ values to observations, bearing in mind this small potential for error.

For Chapters 5 and 6, we consider how best to account for the uncertainty due to artificial fractionations in our model results. One option is to subtract the artificial $\delta^{17}O_{art}$, $\delta^{18}O_{art}$ and $\Delta^{17}O_{art}$ (with 0‰ for the latter), calculated for a parallel model with no user-introduced fractionations but with otherwise identical conditions, from the model-produced values, to obtain only the non-artificial fractionations. A second option, and the one we have adopted for Chapters 5 and 6, is to subtract the artificial $\delta^{17}O_{art}$ and $\delta^{18}O_{art}$ from the model-produced $\delta^{17}O$ and $\delta^{18}O$ values, before calculating the $\Delta^{17}O$ values, as follows:

$$\Delta^{17}O_{corrected} = \left(\delta^{17}O_{model} - \delta^{17}O_{art}\right) - 0.528 \times \left(\delta^{18}O_{model} - \delta^{18}O_{art}\right) \quad \textit{(Eq. 4-3)}$$

4.3.1 – Calibration of the oxygen isotope model

In Chapter 5, we take the baseline model described here, and further develop it to better reproduce the modern atmosphere. In particular, we consider boundary conditions of major species, include important isotope exchange reactions, and incorporate reactions known to impart mass-independent and mass-dependent oxygen isotope fractionations. We use 18 model cases to demonstrate how each of the features affects the δ^{17}O, δ^{18}O and Δ^{17}O of various atmospheric species, and compare model outputs to triple oxygen isotope data from the literature in order to fine-tune the model for further application.

4.3.2 – Applications of the oxygen isotope model to early Earth atmospheres

In Chapter 6, we systematically model the response of the atmosphere in terms of output Δ^{17}O in various species under different O_2/CO_2 concentrations and ratios, as it has been suggested that low productivity and/or high pCO_2 might be the cause of incidences of very negative Δ^{17}O in the geological record (Bao et al., 2008; 2009; Cao and Bao, 2013; Crockford et al., 2018; Planavsky et al., 2020; Young et al., 2014). We also carry out flux-driven modelling in order to investigate whether the non-zero Δ^{17}O measured in the geological record of the Proterozoic (e.g. review by Crockford et al. (2019)) could have been produced by Chapter 3's trace-O_2 atmospheres.

Chapter 5

Predicting $\Delta^{17}O$ profiles for modern atmospheric species using a 1-D photochemical model

Abstract

In Chapter 1 we outlined the potential for a 1-D photochemical oxygen isotope model for interpreting $\Delta^{17}O$ in the geological record in terms of palaeo-atmospheric composition. Here, we continue to develop the model described in Chapters 2 and 4, in order to better predict triple oxygen isotope compositions of key species in the modern atmosphere. We show the effects and importance of the inclusion of i) large-magnitude fixed flux (with deposition velocity) lower boundary conditions for O_2 and CO_2; ii) mass-dependent fractionations; and iii) various isotope exchange reactions between CO_2, $O(^1D)$, O and O_2, which were not included in the models presented in Chapter 4. We test the sensitivity of $\delta^{18}O$ and $\Delta^{17}O$ (for CO_2, O_2, H_2O, NO_3, SO_4, O_3, H_2O_2, HNO_3 and H_2SO_4) to environmental factors including rainfall, temperature, latitude and the isotopic composition of local water vapour, demonstrating that our model achieves spreads in triple oxygen isotope space similar to observations. In particular, the trends in our model results are in the same direction as those seen in global nitrate observations. We then show that the model case that best reproduces modern observations (other than for sulphate) includes isotopologue-specific mass-independent fractionation factors which are pressure- and temperature-dependent. This is the model case we will utilise in Chapter 6.

This chapter is in preparation as a journal article with the author list: B. Gregory, M. Claire, S. Rugheimer.

5.1 – Introduction

The deviation of $\delta^{17}O$ from the Terrestrial Fractionation Line (TFL) for a given $\delta^{18}O$, denoted by $\Delta^{17}O$, has in recent years been shown to be a useful proxy for various atmospheric processes. Since the only known source of mass-independent fractionation of oxygen isotopes (O-MIF) is in the formation of stratospheric ozone via the Chapman reactions (see Chapter 1, Section 1.3), $\Delta^{17}O$ values measured in other atmospheric species and geological materials can offer information about the transfer of such signals in the atmosphere.

Many atmospheric species, including CO_2, $O(^1D)$, H_2O_2, SO_4, NO_3 and ClO_4 have been shown to have inherited a large, positive oxygen isotope anomaly from stratospheric ozone through chemical reactions (e.g. review by Thiemens, 2006; Thiemens et al., 1995b). It has long been understood, through the use of both box and 1-D photochemical models, that the transfer of O-MIF from stratospheric ozone to stratospheric CO_2 is by the oxygen isotope exchange between CO_2 and $O(^1D)$ (the latter being a photolysis product of enriched O_3), via the short-lived, excited-state intermediate CO_3* (Yung et al., 1997; see Figure 1-5a). The use of various oxygen isotope models since then has identified potential pathways through which the anomaly is transferred to other aforementioned species (e.g. Alexander et al., 2009b; Lyons, 2001; Michalski et al., 2004b). Some of the first predictions of $\Delta^{17}O$ values in a large number (15) of oxygen-bearing species throughout the atmospheric column were made by a photochemical model (Lyons, 2001). Many of these species interact with the Earth's surface and are removed from the atmosphere. Sulphate (SO_4), nitrate (NO_3) and perchlorate salts can be removed from the atmosphere through wet and dry deposition, and preserved in sufficiently arid conditions. Non-zero $\Delta^{17}O$ observations for these salts in Atacama and Mojave Desert soils (e.g. Bao et al., 2001; Bao and Gu, 2004; Jackson et al., 2010; Michalski et al., 2003; 2004a; 2004b), in the Antarctic Dry Valleys (e.g. Bao et al., 2000; Bao and Marchant, 2006; Michalski et al., 2005), and in snow pits and ice cores (e.g. Alexander et al., 2002; 2003; Geng et al., 2014; Kunasek et al., 2008; 2010) have revealed at least a partial atmospheric component.

To maintain isotopic mass-balance, atmospheric O_2 gains a negative $\Delta^{17}O$ value, which is small in magnitude because the modern atmospheric oxygen reservoir is large (Bender et al., 1994). The tropospheric O_2 $\Delta^{17}O$ value is a result of mixing of the stratospheric signal and primary productivity (Luz et al., 1999; see Figure 1-5b). Primary productivity is a source of mass-dependently fractionated oxygen, which is compounded by the mass-dependent effects of respiration. The latter preferentially draws isotopically-light O_2 out of the atmosphere. However, the slope of the $\delta^{17}O$ against $\delta^{18}O$ values is slightly different for respiration compared to other processes, which results in an additional apparent mass-independent fractionation (e.g. Nagel et al., 2001; Young et al., 2014).

Here, we continue to develop the 1-D photochemical model, *Atmos*, in its inclusion of the three isotopes of oxygen. This enables prediction of $\Delta^{17}O$ profiles with altitude for 32 oxygen-bearing species, as well as $\Delta^{17}O$ of species removed from the atmosphere and deposited on the Earth's surface through wet and dry deposition. In Section 5.2, we briefly re-introduce the oxygen isotope model we developed in Chapter 4. In Section 5.3, we introduce some important factors which affect the triple oxygen isotope composition of oxygen-bearing atmospheric species and discuss options for incorporating them into our oxygen isotope photochemical model. We outline the test cases we carry out to determine both the sensitivity of the model to these factors and their role in improving the model to better simulate modern oxygen isotope measurements. Specifically, our first test cases (Cases 0-6) develop the model to imitate important processes such as large biological fluxes of O_2 and CO_2, isotope exchange between CO_2 and $O(^1D)$, and mass-dependent fractionations (MDFs). We also test the sensitivity to an assumption we made in Chapter 4 about the branching ratios of atmospheric reactions. Our second set of test cases (Cases 7-12) use Case 6 as a base model and demonstrate the effects of the variation of globally-heterogeneous environmental factors. Our third set of test cases (Cases 13-17) is intended to show how adjustment of fractionation factors and inclusion of additional isotope exchange reactions build on the simpler base model of Case 6 to better reproduce modern observations. The results are presented in Section 5.4, where the model output is compared to existing model and observed

$\Delta^{17}O$ values. This comparison allows us to use these test cases to calibrate the model for use in the modern atmosphere, focussing on nine species in particular (CO_2, O_2, H_2O, NO_3, SO_4, O_3, H_2O_2, HNO_3 and H_2SO_4). Section 5.5 presents Case 17 as the model case that best reproduces modern atmospheric measurements and therefore the model case we will use in Chapter 6. We also discuss some areas for future work for further development and calibration of the model.

5.2 – Model description

For details of model development and assumptions made, see in Chapter 4. The resulting oxygen isotope model includes 97 species involved in 932 reactions (including 21 new reactions added in this chapter). The model includes the same parametrisations of atmospheric processes (e.g. lightning, H escape) as that in Chapters 2–4. Here, as in Chapter 4, the model atmosphere is split into 200 grid steps with the change in altitude between each grid step equal to 0.5 km. Chlorine species have been neglected for simplicity. As described previously, each model atmosphere is a steady state solution.

To begin, we must ensure that we are consistent with the use of the definition of $\Delta^{17}O$. There has been much debate about the most appropriate definition for $\Delta^{17}O$ (see, e.g. review by Bao et al., 2016), as different mass-dependent processes can fractionate oxygen isotopes with slightly different $\delta^{17}O$-$\delta^{18}O$ slopes. In addition, some workers use a linear definition, while others use a natural logarithmic definition. We choose to use the definition:

$$\Delta^{17}O = \delta^{17}O - 0.528\ \delta^{18}O \qquad \textit{(Eq. 5-1)}$$

where:

$$\delta\ ^{x}O = \left(\left(\frac{^{x}R_{species}}{^{x}R_{standard}}\right) - 1\right) \qquad \textit{(Eq. 5-2)}$$

and:

$$^{x}R = \frac{^{x}O}{^{16}O} \qquad \textit{(Eq. 5-3)}$$

and x is 17 or 18. Therefore, in our comparison of model results with published data and models, we ensured that, if our sources used a differing definition, we recalculated $\Delta^{17}O$ using Equation 5-1.

As outlined in Section 4.3, small artificial fractionations are accounted for in the models presented here by subtracting $\delta^{17}O_{art}$ and $\delta^{18}O_{art}$ from the model-produced $\delta^{17}O$ and $\delta^{18}O$ values before calculating $\Delta^{17}O$.

5.3 – Factors affecting triple oxygen isotope compositions of atmospheric species

The stratospherically-derived mass-independent fractionation produced in the formation of ozone is an important component of the resulting triple oxygen isotope composition of atmospheric species. However, in addition, the magnitude of biological fluxes and various mass-dependent fractionations affect $\Delta^{17}O$, $\delta^{17}O$ and $\delta^{18}O$ values. Oxygen isotope exchange reactions can be important in transferring MIF between species, and environmental factors, such as rainfall, temperature and latitude also appear to play a role. In this chapter, we perform a series of experiments to test the sensitivity of the model to these factors, and use the experiments to hone the model to reproduce modern observations. The results will be presented in Section 5.4, but in this section we give an overview of the experiments, discussing the importance of some of these major factors and how they are tested and/or implemented in our model.

A synopsis of the test cases we will run can be found in Tables 5-1, 5-2, 5-3 and 5-4, with Table 5-1 giving an overview. In Cases 0-6, we gradually develop a base model (Case 6), which includes some of the important processes determining oxygen isotope compositions of atmospheric species (Table 5-1). We incrementally incorporate these major processes, showing how they affect the $\Delta^{17}O$ profiles of some major species, meanwhile demonstrating that our assumptions regarding lower boundary conditions (LBCs) and reaction branching ratios are acceptable. In

particular, this involves examining the sensitivity of a model with a single source of O-MIF to boundary conditions, branching ratios of reactions, the inclusion of a reaction implementing isotope exchange between CO_2 and $O(^1D)/O$, and the inclusion of MDFs. Further details of the incorporation of MDFs are summarised in Table 5-2. We then use the resulting Case 6 as a base model against which model atmospheres with varying rainfall, temperature, latitude, H_2O vapour isotopic composition, vertical mixing and tropopause height are compared (Table 5-3), in order to assess whether our model can reproduce spreads of values observed in atmospheric and geologic measurements globally. Subsequently, we examine the effect of varying the O-MIF source in ozone formation (Case 13; Table 5-4) and finally tune the model by adjusting one of the fractionation factors and including some additional isotope exchange reactions (Cases 14-17).

The following subsections detail some of the factors that can influence $\delta^{17}O$, $\delta^{18}O$ and $\Delta^{17}O$ values of atmospheric species, which we consider in this thesis.

5.3.1 – Mass-independent fractionation in ozone formation

Ozone forms via a three-body, pressure-dependent reaction between O and O_2 (Chapter 1, Section 1.3). In this thesis, we do not differentiate between asymmetric and symmetric ozone isotopologues (i.e. between molecules with the heavy isotope positioned either terminally or centrally). We choose to do this for simplicity, because we are only concerned with the bulk ozone $\Delta^{17}O$, and because the inclusion of mass-dependent fractionation effects appears to be more important (Young et al., 2014). In our reaction network therefore, the ozone-forming reactions are:

$$^{16}O + {}^{16}O_2 + M \rightarrow {}^{16}O_3 + M \quad \text{[R5.1a]}$$

$$^{16}O + {}^{16}O^{17}O + M \rightarrow {}^{16}O^{16}O^{17}O + M \quad \text{[R5.1b]}$$

$$^{17}O + {}^{16}O_2 + M \rightarrow {}^{16}O^{16}O^{17}O + M \quad \text{[R5.1c]}$$

$$^{16}O + {}^{16}O^{18}O + M \rightarrow {}^{16}O^{16}O^{18}O + M \quad \text{[R5.1d]}$$

$$^{18}O + {}^{16}O_2 + M \rightarrow {}^{16}O^{16}O^{18}O + M \quad \text{[R5.1e]}$$

Table 5-1: Overview of test cases presented in this chapter, with details of the factors varied for each. Abbreviations used are as follows: LBCs (lower boundary conditions); α_{MIF} (mass-independent fractionation factor); MDFs (mass-dependent fractionations); BRs (branching ratios); pu (photochemical units, 1 pu = 1 molecule cm^{-2} s^{-1}); DV (deposition velocity); MR (mixing ratio).

Case No.	**Factor(s) examining**	**Results in Fig.:**	**LBCs for O_2, CH_4, H_2, CO, N_2O & CO_2**	**Exchange reactions included**	**α_{MIF}**	**MDFs included**	**Reaction BRs**
0	α_{MIF}, LBCs	5-2	Fixed flux for: O_2 (9.5×10^{11} pu) CH_4 (10^{11} pu) H_2 (2.38×10^{9} pu) CO (3.15×10^{11} pu) N_2O (1.06×10^{9} pu) CO_2 (10^{9} pu & DV = 5.94×10^{-5} cm s^{-1})	-	1.065	None	Method 2
1	LBCs	5-2	MR for: O_2 (0.21) CH_4 (1.8×10^{-6}) H_2 (5.3×10^{-7}) CO (1.1×10^{-7}) N_2O (3.1×10^{-7}) CO_2 (2.8×10^{-4})	-	1.065	None	Method 2
2	LBCs	5-2 (& 5-3)	Fixed flux for: O_2 (4×10^{13} pu & DV = 7.56×10^{-6} cm s^{-1}) CH_4 (10^{11} pu) H_2 (2.38×10^{9} pu) CO (3.15×10^{11} pu) N_2O (1.06×10^{9} pu) CO_2 (2.2×10^{13} pu & DV = 3.2×10^{-3} cm s^{-1})	-	1.065	None	Method 2

Table 5-1 cont.

Case No.	Factor(s) examining	Results in Fig.:	LBCs for O_2, CH_4, H_2, CO, N_2O & CO_2	Exchange reactions included	α_{MIF}	MDFs included	Reaction BRs
3a	Reaction BRs	5-3	Fixed flux; additional DV for O_2 & CO_2 (as Case 2)	$O(^1D) + O_2 \rightarrow O + O_2$ (through Method 1 BR assumption)	1.065	None	Method 1
3b	Exchange reactions	5-3	Fixed flux; additional DV for O_2 & CO_2 (as Case 2)	$CO_2 + O(^1D) \rightarrow CO_2 + O$	1.065	None	Methods 1 (3bi) & 2 (3bii)
4	MDFs	-	Fixed flux; additional DV for O_2 & CO_2 (as Case 2)	$CO_2 + O(^1D) \rightarrow CO_2 + O$	1.065	O_2 fluxes in and out. See Table 5-2)	Method 2
5	MDFs	5-4 (5c only)	Fixed flux; additional DV for O_2 & CO_2 (as Case 2)	$CO_2 + O(^1D) \rightarrow CO_2 + O$	1.065	O_2 fluxes in and out; CO_2. See Table 5-2.	Method 2
6	MDFs	5-4, 5-5 (& 5-6, 5-7, 5-8, 5-11)	Fixed flux; additional DV f or O_2 & CO_2 (as Case 2)	$CO_2 + O(^1D) \rightarrow CO_2 + O$	1.065	O_2 fluxes in and out; CO_2 fluxes in; all 2- and 3-body reactions. See Table 5-2.	Method 2
7-12	Environme-ntal factors (see Table 5-3)	5-6 – 5-11	Fixed flux; additional DV for O_2 & CO_2 (as Case 2)	$CO_2 + O(^1D) \rightarrow CO_2 + O$	1.065	O_2 fluxes in and out; CO_2 fluxes in; all 2- and 3-body reactions (as Case 6)	Method 2

Table 5-1 cont.

Case No.	Factor(s) examining	Results in Fig.:	LBCs for O_2, CH_4, H_2, CO, N_2O & CO_2	Exchange reactions included	α_{MIF}	MDFs included	Reaction BRs
13	α_{MIF}	5-12, 5-13, 5-14 (13d only)	Fixed flux; additional DV for O_2 & CO_2 (as Case 2)	$CO_2 + O(^1D) \rightarrow CO_2 + O$	See Table 5-4	As Case 6	Method 2
14	MDFs	5-14, 5-15	Fixed flux; additional DV for O_2 & CO_2 (as Case 2)	$CO_2 + O(^1D) \rightarrow CO_2 + O$	Varying, T- and P-dependent (as Case 13d; see Table 5-4)	Adjustment to MDF in CO_2 flux in (see Table 5-2).	Method 2
15	Exchange reactions	5-15	Fixed flux; additional DV for O_2 & CO_2 (as Case 2)	$CO_2 + O(^1D) \rightarrow CO_2 + O$ $O(^1D) + O_2 \rightarrow O + O_2$	As Case 13d	As Case 14	Method 2
16	Exchange reactions	5-15, 5-16	Fixed flux; additional DV for O_2 & CO_2 (as Case 2)	$CO_2 + O(^1D) \rightarrow CO_2 + O$ $O(^1D) + O_2 \rightarrow O + O_2$ $O + O_2 \rightarrow O + O_2$	As Case 13d	As Case 14	Method 2
17	Exchange reactions	5-16	Fixed flux; additional DV for O_2 & CO_2 (as Case 2)	$CO_2 + O(^1D) \rightarrow CO_2 + O$ $O(^1D) + O_2 \rightarrow O + O_2$ $O + O_2 \rightarrow O + O_2$ $O_2 + CO_2 \rightarrow O_2 + CO_2$	As Case 13d	As Case 14	Method 2

Table 5-2: Summary of mass-dependent fractionations (MDFs) included in Cases 4-6. $^{17}R_0$ and $^{18}R_0$ are the universal isotope ratios of ^{17}O and ^{18}O relative to ^{16}O, respectively, and n_{oxy} is the number of oxygen atoms in the molecule.

Case No.	Description	Details of MDFs
4	MDF in O_2 fluxes in and out of atmosphere	OP flux in = O_2 flux × $^{17}R_0$ × n_{oxy} × $1.00525^{0.52}$ OQ flux in = O_2 flux × $^{18}R_0$ × n_{oxy} × 1.00525 OP DV = O_2 DV × $1/1.0182^{0.5149}$ OQ DV = O_2 DV ×1/1.0182
5a	MDF in H_2O-CO_2 isotope exchange reaction	O_2 fluxes in and out as in Case 4. MDF in CO_2-H_2O exchange reactions (rates adapted from Young et al. (2014)), for i) whole troposphere; ii) lowermost grid step.
5b	MDF in CO_2 fluxes in and out of atmosphere	O_2 fluxes in and out as in Case 4. COP flux in = CO_2 flux × $^{17}R_0$ × n_{oxy} × $1.041^{0.528}$ × $1.0182^{0.5149}$ COQ flux in = CO_2 flux × $^{18}R_0$ × n_{oxy} × 1.041 × 1.0182 (See Eqs. 5-4 and 5-5.) COP DV = CO_2 DV × $1/1.041^{0.528}$ × $1/1.0182^{0.5149}$ COQ DV = CO_2 DV × 1/1.041 × 1/1.0182
5c	MDF in CO_2 fluxes *into* atmosphere only	O_2 fluxes in and out as in Case 4. COP flux in = CO_2 flux × $^{17}R_0$ × n_{oxy} × $1.041^{0.528}$ × $1.0182^{0.5149}$ COQ flux in = CO_2 flux × $^{18}R_0$ × n_{oxy} × 1.041 × 1.0182 (See Eqs. 5-4 and 5-5.) No fractionation in CO_2 fluxes out of atmosphere.
6	MDFs in all two- and three-body reactions	O_2 fluxes in and out as in Case 4. CO_2 fluxes in as in Case 5c. Fractionations incorporated into reaction rates (see Eqs. 5-6 and 5-7).
14	Adjusted MDF for CO_2 flux into atmosphere	O_2 fluxes in and out as in Case 4. COP flux in = CO_2 flux × $^{17}R_0$ × n_{oxy} × $1.041^{0.523}$ COQ flux in = CO_2 flux × $^{18}R_0$ × n_{oxy} × 1.041 Fractionations incorporated into reaction rates (see Eqs. 5-10 and 5-11).

Table 5-3: Summary of chosen parameter space explored in sensitivity tests of Cases 7-12.

Case no.	Factor	Base model value	Min. value	Max. value	No. of models
7	Rainfall	Default (global average)	10^{-9} × default	10 × default	10
8	Temperature	Default (from US Standard Atmosphere, 1976)	Base model profile – 20 K (throughout whole profile); see Fig. 5-1.	Base model profile + 20 K (throughout whole profile); see Fig. 5-1.	6
9	Solar zenith angle (dependent on latitude)	50° (i.e. midlatitude	45° (i.e. low latitude)	80° (i.e. high latitude)	4
10	H_2O isotopic composition (w/o (10a) and w/ (10b) adjusted CO_2 flux MDFs	$\Delta^{17}O$ = 0‰ $\delta^{18}O$ = 0‰ $\Delta^{17}O$ = 0‰	$\Delta^{17}O$ = -15.84‰ $\delta^{18}O$ = -30‰ $\Delta^{17}O$ = 0‰	$\Delta^{17}O$ = 0‰ $\delta^{18}O$ = 0‰ $\Delta^{17}O$ = 0‰	4
11	Eddy diffusion profile (parametrising vertical transport)	Default	0.1 × default (throughout whole profile)	10 × default (throughout whole profile)	2
12	Tropospheric height	11 km	9 km (i.e. polar)	17 km (i.e. tropical)	2

Table 5-4: Fractionation factors (α_{MIF}) of reactions R5.1b-R5.1e used in Cases 13b-13d. Pressure (P) in Torr. Please note that the max. value in the T profile is 288 K.

Reaction	**α_{MIF} and justification/reference**			
	Case 13a	**Case 13b**	**Case 13c**	**Case 13d**
R5.1b: O + OP → OOP	α_{MIF} = 1.065 Young et al. (2014) Increased to 1.07, 1.08, 1.09, 1.1.	α_{MIF} = 1.17 Mauersberger et al. (1999). Average of α_{MIF} used by Wiegel et al. (2013); also used by Michalski et al., (2004a).	α_{MIF} = 1.17 + 2.07×10^{-5} (T – 300 K) Wiegel et al. (2013) assume T-dependence is the same as O + OQ in Janssen et al. (2003).	$\alpha_{MIF} = 0.5\left(1.3543 + \frac{0.97167 - 1.3543}{1 + \left(\frac{P}{3576.2}\right)^{-0.68094}} + 0.99\right) + 2.07 \times 10^{-5}\ (\mathrm{T} - 300\ \mathrm{K})$ Average of P-dependent asymmetric rate and non-P-dependent symmetric rate (Wiegel et al., 2013).
R5.1c: P + O_2 → OOP	α_{MIF} = 1.065 Young et al. (2014) Increased to 1.07, 1.08, 1.09, 1.1.	α_{MIF} = 1.03 Mauersberger et al. (1999); Wiegel et al. (2013); also used by Michalski et al. (2004a).	α_{MIF} = 1.03 + 7.82x10^{-4} (T – 300 K) Wiegel et al. (2013)	α_{MIF} = 1.03 + 7.82x10^{-4} (T – 300 K) Wiegel et al. (2013) assume no P-dependence (after Guenther *et al.*, 1999).
R5.1d: O + OQ → OOQ	α_{MIF} = 1.065 Young et al. (2014) Increased to 1.07, 1.08, 1.09, 1.1.	α_{MIF} = 1.246 Janssen et al. (2003); Mauersberger et al. (1999). (Michalski et al., 2004a, use 1.27).	α_{MIF} = 1.246 + 2.07x10^{-5} (T – 300 K) Janssen et al. (2003); in Wiegel et al. (2013)	$\alpha_{MIF} = 0.5\left(1.4538 + \frac{1.0092 - 1.4538}{1 + \left(\frac{P}{3010.6}\right)^{-0.69388}} + 1.08\right) + 2.07 \times 10^{-5}\ (\mathrm{T} - 300\ \mathrm{K})$ Average of P-dependent asymmetric rate and non-P-dependent symmetric rate (Wiegel et al., 2013).
R5.1e: Q + O_2 → OOQ	α_{MIF} = 1.065 Young et al. (2014) Increased to 1.07, 1.08, 1.09, 1.1.	α_{MIF} = 0.92 Janssen et al. (2003); Wiegel et al. (2013). (Michalski et al., 2004a use 0.93).	α_{MIF} = 0.92 + 1.03x10^{-3} (T – 300 K) Janssen et al. (2003); Wiegel et al. (2013)	α_{MIF} = 0.92 + 1.03×10^{-3} (T – 300 K) Wiegel et al. (2013) assume no P-dependence (after Guenther et al., 1999).

(from reaction R1.3 in Section 1.3).

These reactions fractionate oxygen isotopes mass-independently. This can be built into the model by including fractionation factors in the reaction rates. A fractionation factor (α_{MIF}) of 1.065 was chosen by Young et al. (2014) for the rates of reactions R5.1b-R5.1e relative to that of reaction R5.1a in their model. In other words, the isotopically-substituted reaction rates are 65% faster than reaction R5.1a. Since the same α_{MIF} value is used for reactions involving ^{17}O- and ^{18}O-bearing species (i.e. for R5.1b-R5.1e), a mass-independent fractionation results. Young et al. (2014) chose 1.065 as the fractionation factor because it reproduced observed atmospheric oxygen isotope compositions for ozone.

We begin our experiments by including only the mass-independent fractionation producing high $\delta^{17}O$ and $\delta^{18}O$ in stratospheric ozone, also using a fractionation factor of 1.065 for R5.1b-R5.1e. For Cases 0-3, this is the only source of fractionation in the model. This initial test is important as it isolates the effects on $\Delta^{17}O$ of the introduction of a single fractionation source in the atmospheric system. For simplicity, we also use this α_{MIF} value for Cases 4-12 as we examine the effects of varying other factors (see below). In Case 13a, we explore the effects of varying the magnitude of α_{MIF} from 1.065, choosing 1.1 as an arbitrary maximum value.

However, the fractionation factors have also been determined via empirical measurement. It was discovered through experiments that α_{MIF} in fact differs between reactions depending on the isotopologues involved (Anderson et al., 1997; Mauersberger et al., 1999; Sehested et al., 1998). The results of Mauersberger et al. (1999) suggested that the reactions involving ^{16}O and either OP or OQ were more likely to occur than reactions involving ^{16}O and $^{16}O^{16}O$ or P/Q and $^{16}O^{16}O$. Janssen et al. (2001) developed this argument by demonstrating that when a ^{16}O atom collides with OQ, the rate of formation of OOQ (the asymmetric molecule) is greater than that of OQO (the symmetric molecule). Therefore, in Case 13b, we include different fractionation factors for reactions R5.1b-R5.1e (Column 3 in Table 5-4). We use rates adapted from Wiegel et al. (2013), with adjustments since they differentiate

between reactions producing symmetric and asymmetric isotopologues, whereas we do not. Since Janssen et al. (2003) and Mauersberger et al. (1999) give combined rates for R5.1b and R5.1d, where Wiegel et al. (2013) specify between asymmetric and symmetric isotopologues, we use the rates of the former two authors for Case 13b.

Experiments have also displayed a temperature- and pressure-dependence of α_{MIF} for each reaction, which are incorporated into the model of Wiegel et al. (2013). The temperature-dependence was measured by Janssen et al. (2003) for the ^{18}O-substituted reactions; we use their formulations, along with those assumed by Wiegel et al. (2013) for the ^{17}O-substituted reactions, for our model in Case 13c (Column 4 in Table 5-4). The fractionation factor increases with increasing T (temperature in Kelvin). Note that, for most model runs presented in this thesis, the maximum temperature in the atmospheric profile is 288 K at the ground, so the rates for each altitude in Case 13c are lower than those for Case 13b.

We attempt to investigate the pressure-dependence of α_{MIF} (e.g. Guenther et al., 1999) using the terms adopted by Wiegel et al. (2013) and given in Table 5-4. (Column 5; Case 13d) It is assumed that the only pressure-dependent fractionation factor is that of the branches of R5.1b and R5.1d which produce the asymmetric isotopologue (Guenther et al., 1999; Wiegel et al., 2013). Since we do not differentiate in Case 13 between symmetric and asymmetric isotopologues of ozone, we adapt the latter authors' pressure-dependent fractionation factors such that we use an average of the P-dependent asymmetric-isotopologue-producing term and the non-P-dependent asymmetric-isotopologue-producing term. We include T-dependent factors, as in Case 13c, for all four reactions. For the Case 13 experiments, we keep all other factors the same as in the Case 6 base model (Table 5-1).

These processes are likely to be important in predicting the oxygen isotope compositions of atmospheric species. While Wiegel et al. (2013) choose a single temperature and pressure representative of the whole atmosphere for each model run, we vary temperature and pressure with altitude in the atmospheric column, so

our incorporation of these factors will allow variation of the fractionations in the ozone-formation reactions with altitude.

5.3.2 – Lower boundary conditions

One of our main conclusions from the study of lower boundary conditions in Chapter 3 was that it is important to carefully prescribe and describe LBCs in photochemical models. We showed that for an exploration of LBCs for different O_2 levels, it was helpful and intuitive to allocate flux-driven LBCs to O_2 and CH_4, representative of various magnitudes of biological flux. We also concluded that it is more appropriate to choose flux boundary conditions for the trace reducing species H_2, CO and N_2O. While *Atmos* has utilised mixing ratio boundary conditions for these species for a number of years to reproduce the modern Earth atmosphere, use of alternative boundary conditions is important for the varying-O_2 flux cases we run in Chapter 6. Furthermore, boundary conditions involving fluxes of key species into and/or out of the atmosphere are more useful for our applications of an oxygen isotope code than boundary conditions that hold mixing ratios fixed. This is because we intend to predict $\Delta^{17}O$ of oxygen-bearing species (such as O_2 and CO_2) at the ground-level, rather than prescribing them by fixing a mixing ratio as an input.

We therefore choose to use flux-driven boundary conditions for O_2, CH_4, H_2, CO and N_2O, with or without an additional drawdown flux specified by a deposition velocity (see Chapter 2) for O_2. For Case 0, we choose a fixed flux lower boundary condition for O_2, similar to that used in Cases 1 and 2 of Chapter 3, equal to the flux predicted by the model for a modern O_2 mixing ratio of 0.21. Flux boundary conditions are also given to CH_4, CO and N_2O, equal to the predicted fluxes for the models with mixing ratio boundary conditions for these species. The CH_4, CO and N_2O fluxes required are 1.43×10^{11} pu (where 1 pu = 1 molecule cm^{-2} s^{-1}), 3.15×10^{11} pu and 1.06×10^{9} pu, respectively. The predicted flux for H_2 is negative (into the ocean from the atmosphere), so we reduce the CH_4 flux to 10^{11} pu such that the H_2 flux becomes positive (2.38×10^{9} pu), and use this (see Chapter 3 for a similar approach). These fluxes differ slightly from those chosen for the modern atmosphere in Chapter 3 for

two reasons. Firstly, the model presented here is marginally more oxidising, because of our assumption that the mixing ratio of the purely ^{16}O-bearing species is equal to the original mixing ratio of the species, so the total mixing ratio for a particular species has been increased by the additional mixing ratios of the P- and Q-bearing species. Secondly, this model does not include chlorine-bearing molecules, which will result in some variations in the dynamics of oxidising and reducing species in the atmosphere.

For the models in Chapter 3, CO_2 had a fixed mixing ratio boundary condition, set to the pre-industrial modern value of 2.8×10^{-4}. For Case 0, since as with O_2, we want to predict rather than prescribe the $\Delta^{17}O$ values of CO_2 in the atmosphere, we use a boundary condition in which both a distributed flux and a deposition velocity are specified. Assuming that a significant proportion of the modern CO_2 flux to the atmosphere is biological rather than volcanic, we distribute the flux of CO_2 into the model atmosphere over the first grid step only (equal to 500m). With a fixed mixing ratio boundary condition, the predicted flux is into the ocean from the atmosphere. Rather than using either a flux boundary condition with a negative value or a deposition velocity only, both of which are numerically imperfect options, we choose a small flux into the atmosphere (10^9 pu) across the first 500m and a large deposition velocity (5.94×10^{-5} cm s^{-1}), such that the preindustrial CO_2 mixing ratio is predicted as a result. To test the sensitivity of the model to the choice of LBC type, we compare Case 0 to a case in which O_2, CH_4, CO, H_2, N_2O and CO_2 are given fixed mixing ratio boundary conditions (equal to modern Earth mixing ratio values (Table 5-1); Case 1).

However, it has been shown that the tropospheric $\Delta^{17}O$ of O_2 is influenced by both stratospheric $\Delta^{17}O$, which is negative due to the mass-balance in ozone formation (Yung et al., 1997), and photosynthetic O_2, which is mass-dependently fractionated (Luz et al., 1999; Young et al., 2014). For Case 0, as in Chapter 3, we use an O_2 flux of magnitude $\sim10^{12}$ pu to reproduce annually-averaged inputs. For our purposes earlier in this thesis, the parametrisation of large, short-term O_2 fluxes into and out of the atmosphere as a combination of smaller fluxes was acceptable, since they

cancelled out on the timescales in which we were interested. Here however, the gross flux of O_2 into the atmosphere from photosynthesis (gross primary productivity, GPP) is important, because it has an influence on the $\Delta^{17}O$ of tropospheric O_2. O_2 is pumped into the atmosphere mass-dependently, but is removed with an isotopic ratio related to the isotopic composition of the atmosphere. Primary productivity therefore acts to dilute the mass-independently-fractionated composition of atmospheric O_2 (Figure 1-5b). Since the modern gross O_2 production is $\sim 4\times10^{13}$ pu (Zahnle et al., 2006), an order of magnitude greater than the annually-averaged O_2 flux used for Case 0, it follows that the latter should produce $\Delta^{17}O$ values roughly ten times too big.

For an additional case (Case 2), we therefore increased the O_2 flux over the lower boundary into the model to 4×10^{13} pu, which was entered into the first 500m of the atmosphere. Coupling to a (tuned) deposition velocity boundary condition of 7.56×10^{-6} cm s^{-1} maintained a modern O_2 mixing ratio of 0.21. OP and OQ fluxes into the model for this case were kept at ratios of 7.6×10^{-4} and 4×10^{-3} relative to O_2, respectively, in order to introduce no mass-independent or mass-dependent fractionations at this stage. These fluxes into and out of the model are much larger than those we used for Chapter 3, but this is acceptable, since the purpose here is different. In Chapter 3, we used a feedback flux related to concentration via a half-power law to simulate longer-term oxidative weathering (Johnson et al., 2019), but since here the overwhelming sink of O_2 is short-term respiration, we use a linearly-related feedback flux instead. To ensure that the lower boundary fluxes of trace species CH_4, H_2, CO and N_2O were still valid for predicting modern mixing ratios of these gases, we repeated the steps noted above, by setting the boundary conditions back to modern mixing ratios for these species, and individually changing them to flux boundary conditions using the predicted fluxes. As it happened, the predicted fluxes were the same as those for Case 0, so these are also used for the Case 2 models, and all other cases presented in this chapter.

For CO_2, the modern fluxes on short timescales are also much larger than the net CO_2 fluxes used in Case 0. Similar to O_2, CO_2 entering the atmosphere has no mass-

independently fractionated component, whereas CO_2 removed from the atmosphere has an oxygen isotope composition dependent on atmospheric $\Delta^{17}O_{CO2}$, so a larger CO_2 flux will act to dilute the $\Delta^{17}O$ values. For Case 0, we use a boundary condition allowing for a distributed flux of CO_2 into the atmosphere and a deposition flux out of the atmosphere, with values chosen only to reproduce the net flux out of the atmosphere (with a small token flux into the atmosphere for numerical reasons). However, the gross CO_2 flux into the atmosphere consists of volcanic and biogenic fluxes, is much larger and is balanced by a large flux of CO_2 out of the atmosphere into the oceans through dissolution and photosynthesis.

For Case 2, we choose a CO_2 flux of 2.2×10^{13} pu, because this is the rate of CO_2 effusion from the oceans used by Young et al. (2014) in their oxygen isotope model. The averaged volcanic CO_2 flux into the atmosphere is much smaller, with estimates from 1.5×10^{10} pu (used in the Young et al. (2014) model) to 3×10^{10} pu (Zahnle et al., 2006). Since the volcanic flux is negligible compared to the oceanic flux, we assume this is contained within our estimate of flux to the atmosphere. Having set the CO_2 flux, we varied the deposition velocity such that the modern preindustrial CO_2 mixing ratio of 2.8×10^{-4} was produced. The deposition velocity required was 3.2×10^{-3} cm s^{-1}. The ground-level number density in this case is 7×10^{15} molecules cm^{-3}, which results in a flux out of the atmosphere of 2.24×10^{13} pu. The $\delta^{17}O$ and $\delta^{18}O$ values of the fluxes of CO_2 into and out of the atmosphere are zero, achieved by imposing into-the-atmosphere fluxes of COP and COQ at the isotopic ratios of 0.00076 and 0.004 (as with O_2), and using the same V_{dep} value for all three isotopologues.

The large-magnitude biological O_2 and CO_2 fluxes of Case 2 are important, so will be included for all models in Cases 2-17 of this chapter (Table 5-1).

5.3.3 – Atmospheric kinetic reactions

The steady-state atmospheric chemistry of the model output is dependent on the hundreds of reactions which are included in the model atmosphere. It is therefore

important that the reaction network and rates are representative of the chemistry of the atmosphere.

Firstly, as discussed in Section 4.1.3 of Chapter 4, there are two methods that can be used when considering incorporating reactions involving heavy oxygen isotopologues. The oxygen isotope model presented in Chapter 4 used 'Method 2,' in which only the product isotopologues that are most likely to be formed from a certain set of isotopically-substituted reactants are included, while others are removed. In 'Method 1,' the branching ratios of possible reactants are dependent only on the number of oxygen isotope positions, and therefore the simple statistical likelihood of a heavy isotope ending up in one of those positions. Method 1 has been used by previous authors (e.g. Lyons, 2001; Young et al., 2014; Yung et al., 1997), so we considered it worthwhile to produce a model atmosphere using Method 1, to examine the effect on $\Delta^{17}O$ profiles of this assumption (Case 3a).

Secondly, having compared the reactions in the oxygen isotope model of Young et al. (2014) to our reactions table, we noticed that the former included isotopic exchange reactions in the quenching of $O(^1D)$ by CO_2 ($CO_2 + O(^1D) \rightarrow CO_2 + O$ and isotopic equivalents; R916-R924 in reaction Table C-1 in Appendix C). These are not present in our original model developed in Chapter 4. This reaction is actually very important, as it parametrises the reaction $CO_2 + O(^1D) \rightarrow CO_3^* \rightarrow CO_2 + O$, which has been shown to be key in the transfer of the MIF signal to stratospheric CO_2 (Yung et al., 1991; 1997), and which involves isotopic scrambling (Burkholder et al., 2015, and references therein). To understand the importance of the inclusion of these reactions in the model, we compare the model with and without the reactions R916-R924 (Table C-1, Appendix C). We use rate constants from the JPL Evaluation Number 18 (Burkholder et al., 2015), which is the same as used by Wiegel et al. (2013), though they use the rate constant for 298 K only for their model.

To explore these concepts, we compare two model atmospheres using Methods 1 and 2, without the $CO_2/O(^1D)$ isotope exchange reaction (Cases 2 and 3a, respectively), to two using Methods 1 and 2, but with the additional reaction (Cases

3bi and 3bii, respectively). For Cases 4-17, we choose the Method 2 branching ratios and include the isotope exchange reaction.

There are several other oxygen isotope exchange reactions which have been included in the reaction networks of other models. We include three exchange reactions in Cases 15-17 after incorporation of the mass-dependent fractionations (Cases 4-6) and the more complex mass-independent fractionations in ozone formation (Case 13). This is because the way they are incorporated into models differs between authors and is a little more uncertain. We therefore decide to demonstrate that their inclusion allows our model to better reproduce atmospheric measurements once the other factors have been taken into account. The three groups of reactions are as follows.

The exchange reaction $O(^1D) + O_2 \rightarrow O + O_2$ is included in the model of Wiegel et al. (2013), and we reintroduce it for Case 15. In all models in Cases 0-14 (except Cases 3a and 3bi, with Method 1 branching ratios), this reaction is included only as a quenching reaction. Inclusion of an isotope exchange reaction involves the addition of four further reactions, and the reduction of rates such that the total rate for a set of reactants remains the same, as follows (see R96-104, Table C-1, Appendix C):

R5.2) $O(^1D) + O_2 \rightarrow O + O_2$, rate k

R5.3) $O(^1D) + OP \rightarrow O + OP$, rate k,

changed to R5.2a) $O(^1D) + OP \rightarrow O + OP$, rate ⅔ k, and

R5.2b) $O(^1D) + OP \rightarrow P + O_2$, rate ⅓ k

R5.4) $P(^1D) + O_2 \rightarrow P + O_2$, rate k,

changed to R5.3a) $P(^1D) + O_2 \rightarrow P + O_2$, rate ⅓ k, and

R5.3b) $P(^1D) + O_2 \rightarrow O + OP$, rate ⅔ k

R5.5) $O(^1D) + OQ \rightarrow O + OQ$, rate k,

changed to R5.4a) $O(^1D) + OQ \rightarrow O + OQ$, rate ⅔ k, and

R5.4b) $O(^1D) + OQ \rightarrow Q + O_2$, rate ⅓ k

R5.6) $Q(^1D) + O_2 \rightarrow Q + O_2$, rate k,

changed to R5.5a) $Q(^1D) + O_2 \rightarrow Q + O2$, rate ⅓ k, and

R5.5b) $Q(^1D) + O_2 \rightarrow O + OQ$, rate ⅔ k

Another isotopic exchange reaction that involves isotopic redistribution between O and O_2, as discussed by Michalski et al. (2004b), Wiegel et al. (2013), Young et al. (2014) and Yung et al. (1997) is exchange between O and O_2, via the following reactions (R925-928, Table C-1, Appendix C):

R5.7a) $P + O_2 \rightarrow O + OP$

R5.7b) $O + OP \rightarrow P + O_2$

R5.7c) $Q + O_2 \rightarrow O + OQ$

R5.7d) $O + OQ \rightarrow Q + O_2$

These reactions are important because they are fast compared to the formation rate of ozone (Michalski et al., 2004b), so dictate the isotopic composition of the O and O_2 that form ozone. They also impart a mass-dependent fractionation, since the forward and backward reactions occur at different rates, and vary between the isotopologue products according to temperature, as measured by Kaye and Strobel (1983).

Michalski et al. (2004b) use a box model rather than a comprehensive reaction scheme, so use only the equilibrium rate constants for P (equal to $\frac{rate\ of\ 5.7a}{rate\ of\ 5.7b}$) and Q (equal to $\frac{rate\ of\ 5.7c}{rate\ of\ 5.7d}$). Young et al. (2014) use a fixed non-T-dependent rate constant of 2×10^{-16} $cm^3\ s^{-1}$ for these reactions, taken from that for the reaction $O_2(^1\Delta) + O$ from Sander et al. (2006). In the model of Young et al. (2014), the rate constants of R5.7a-R5.7d differ only due to mass-dependent effects (later described in Section 5.3.4; Case 6) and the statistical likelihood of a heavy isotope ending up in a certain position. Wiegel et al. (2013) use the reaction rate as measured by Fleurat-Lessard et al. (2003, which is also used by Früchtl et al. (2015)), along with the equilibrium rate constants from Kaye and Strobel (1983).

We follow Wiegel et al. (2013) in our incorporation of the rates and equilibrium rate constants from Fleurat-Lessard et al. (2003) and Kaye and Strobel (1983) respectively, for Case 16 (Table C-1, Appendix C).

Finally, we noted that Wiegel et al. (2013) include quenching and exchange reactions via:

$O_2(^1\Sigma) + CO_2 \rightarrow O_2(^1\Delta) + CO_2$, rate coefficient = 4.1×10^{-13} cm^3 s^{-1}
$O_2(^1\Delta) + CO_2 \rightarrow O_2 + CO_2$, rate coefficient < 2×10^{-20} cm^3 s^{-1}

and isotopic equivalents, which involve excited-state O_2 molecule species $O_2(^1\Sigma)$ and $O_2(^1\Delta)$. We do not include the excited-state O_2 molecules in the model at present, but consider the parameterisation of these reactions in our model, by including isotopic exchange during a fictitious reaction between O_2 and CO_2 (R929-932, Table C-1, Appendix C):

R5.8a) $OP + CO_2 \rightarrow O_2 + COP$
R5.8b) $O_2 + COP \rightarrow OP + CO_2$
R5.8c) $OQ + CO_2 \rightarrow O_2 + COQ$
R5.8d) $O_2 + COQ \rightarrow OQ + CO_2$

We justify this given that Wiegel et al. (2013) also include isotopic exchange between O_2 and $O_2(^1\Sigma)/O_2(^1\Delta)$. To incorporate this in our model, we take the lowest of the two rate constants (2×10^{-20} cm^3 s^{-1}), and divide this by the number density ratio of $O_2(^1\Delta)$ to O_2 in the upper atmosphere, which is roughly 10^{-8} (Yankovsky and Manuilova, 2006) to approximate a rate constant for our new reactions. We divide this rate by two to account for isotopic branching ratios assuming statistical equilibrium – a first branch has the same products and reactants, and is not included in our reaction table, while the second branch is for the exchange reactions. This results in a low rate constant of 10^{-28} cm^3 s^{-1} for R5.8a-5.8d. Normally, reaction rates this slow would have little effect on model photochemistry, but the number densities of reactants O_2 and CO_2 are large.

5.3.4 – Mass-dependent fractionations

While the magnitude of $\Delta^{17}O$ is our main concern, we model the effects of the incorporation of mass-dependent fractionations for two main reasons. Firstly, we want to attempt to simulate $\delta^{17}O$ and $\delta^{18}O$ of different species as well as $\Delta^{17}O$ (despite the inherent error due to artificial fractionations produced – see Section 4.2 of Chapter 4). Secondly, there are various mass-dependent processes that occur in the Earth system that nevertheless produce an apparent mass-independent fractionation if they have a different $\delta^{17}O$-$\delta^{18}O$ slope (see e.g. Bao 2016; Young et al., 2002; 2014).

While unable to incorporate all possible mass-dependent effects, we attempt to include some of the more important ones for the O_3-CO_2-O_2 system. The test cases are summarised in Table 5-2.

5.3.4.1 – MDF in O_2 fluxes

Young et al. (2014) argued from their oxygen isotope model that only around a third of the $\Delta^{17}O$ of tropospheric O_2 results from stratospheric chemistry (i.e. the mass balance resulting from the enrichment of ozone, CO_2 and $O(^1D)$ through the ozone formation reaction and subsequent reactions), with the remainder being a result of mass-dependent processes with a slightly different fractionation slope. We therefore incorporated the mass-dependent fractionations for O_2 by i) varying the O_2, OP and OQ fluxes into the model, such that the $\delta^{17}O$ and $\delta^{18}O$ of O_2 are non-zero; ii) adjusting the deposition velocities of O_2, OP and OQ such that a fractionation is imparted as the isotopologues are removed from the atmosphere.

Following Young et al. (2014), we incorporate a mass-dependent fractionation in oxygen isotopes due to photosynthesis with enriched source water by multiplying the source of OQ at the lower boundary by 1.00525, and the source of OP by $1.00525^{0.52}$. Note that this assumes that all oxygen flowing into the model is from photosynthesis, which is an adequate assumption, given that we are simulating gross primary productivity, which is the largest source of oxygen on short timescales.

Respiration preferentially removes lighter isotopes from the atmosphere. Again, following the model of Young et al. (2014), we account for this by multiplying the deposition velocity of OQ by 1/1.0182 to impart an 18.2‰ fractionation in ^{18}O, and multiplying the deposition velocity of OP by $1/1.0182^{0.5149}$.

5.3.4.2 – MDF in CO_2 fluxes

Measurements of ground-level atmospheric CO_2 indicate $20.45‰ \leq \delta^{17}O \leq 21.74‰$ and $39.49‰ \leq \delta^{18}O \leq 41.84‰$ (Thiemens et al., 2014). Young et al. (2014) model this by including CO_2-H_2O exchange reactions, which account for fractionations between tropospheric CO_2 and water at the surface, including those involving processes in leaves. Exchange between CO_2 and H_2O is rapid, so they assume $\delta^{17}O$, $\delta^{18}O$ and $\Delta^{17}O$ values of 0‰ for CO_2 flowing into the model. They include no fractionations in (or even concentration-dependence on) the rate of photosynthesis drawing CO_2 out of the atmosphere.

We explore two potential methods of incorporating accurate fractionations in the CO_2-H_2O system. Firstly, we try a method similar to that of Young et al. (2014). We keep fluxes of CO_2 in and out of the model at the same isotopic ratios as the standard, VSMOW. We include the exchange reactions using a rate based on Young et al.'s (2014) model, but lower, since they include the number density of H_2O in their rate constant. We run cases i) with the reactions for the troposphere only (Case 5ai); and ii) with the reactions for the lowermost grid step only (Case 5aii). We try both options since our model is different in set-up to that of Young et al (2014). While they use a box model with troposphere and hydrosphere boxes, we are using a full 1-D photochemical model. Since CO_2-H_2O exchange is a process that happens predominantly at the surface, catalysed by the biosphere, we consider it important to test the sensitivity to the vertical extent of the effects of these exchange reactions.

Secondly, we implement the fractionations in CO_2 by instead adjusting the fluxes of CO_2 into and out of the model atmosphere. We use the following relation for the CO_2 flux into the atmosphere:

$$\text{COP flux} = CO_2 \text{ flux} \times {}^{17}R_0 \times n_{oxy} \times \alpha_{\text{exch.}}{}^{\beta} \times \alpha_{\text{evap.}}{}^{0.52} \quad \textit{(Eq. 5-4)}$$

$$\text{COQ flux} = CO_2 \text{ flux} \times {}^{18}R_0 \times n_{oxy} \times \alpha_{\text{exch.}} \times \alpha_{\text{evap.}} \quad \textit{(Eq. 5-5)}$$

where ${}^{x}R_0$ is the standard isotopic ratio of heavy isotope ${}^{x}O$ to ${}^{16}O$ (i.e. ${}^{17}R_0 = 0.00038$ and ${}^{18}R_0 = 0.002$) and n_{oxy} is the number of oxygen atoms (i.e. 2 for CO_2; see Chapter 4). The $\alpha_{\text{exch.}}$ and $\alpha_{\text{evap.}}$ terms are the mass-dependent fractionation factors for the CO_2 flux due to CO_2-H_2O exchange and evapotranspiration, respectively, while β is a constant that governs the fractionation due to exchange in COP, and the exponent for evapotranspiration is 0.52, after Young et al. (2014). We use values of 1.041 and 1.00525 for $\alpha_{\text{exch.}}$ and $\alpha_{\text{evap.}}$, respectively, following Young et al. (2014). We assume a β value of 0.528 (Young et al., 2014), but Hofmann et al., (2012) find a β value of 0.522, and Barkan and Luz (2012) and Liang et al. (2017) use 0.5229, so there is some uncertainty. In one of our final test cases (Case 14), we experiment with the $\alpha_{\text{evap.}}$ and β values in order to tune the model to better reproduce modern observations.

Though Young et al. (2014) included no fractionation in CO_2 for photosynthesis, we test the effects of including a mass-dependent fractionation in the drawdown flux, which would act to preferentially remove the lighter isotopes. We incorporate a fractionation such that COQ was removed at a rate $\frac{1}{1.041} \times \frac{1}{1.0182}$ times as quickly as CO_2, and COP was removed at a rate $\frac{1}{1.041^{0.528}} \times \frac{1}{1.0182^{0.5149}}$ as quickly as CO_2. This effectively doubles the fractionation incorporated in the upward flux, and is similar to the way in which the exchange reactions in Young et al.'s (2014) model destroy CO_2, COP and COQ at different rates (while simultaneously forming them at different rates).

5.3.4.3 – MDFs in two-body and three-body reactions

To incorporate some of the mass-dependent fractionations that occur in other oxygen-bearing species via reactions, we follow the method of Young et al. (2014), who include a mass-dependent fractionation factor (α_{MDF}) due to collision frequencies of different isotopologues, while ignoring the effects of reactions

between molecules that are vibrationally-excited and zero-point energy differences. We adopt their method and assumptions as follows.

For each two-body and three-body reaction in our reaction network, we multiply the reaction rate by a factor, α_{MDF}, dependent on the masses of the molecules of the reactants via:

$$\alpha_{MDF} = \sqrt{\frac{\mu}{\mu'}} \qquad \textit{(Eq. 5-6)}$$

Where μ' is the reduced mass of the two reactants, with molecular masses m_1 and m_2, respectively, related by:

$$\mu' = \frac{m_1 m_2}{m_1 + m_2} \qquad \textit{(Eq. 5-7)}$$

and μ is the reduced mass of the isotopologues of the two reactants containing only ^{16}O (rather than heavier isotopes). Since α_{MDF} is therefore unity for the reactions containing only the lightest isotope, we only include α_{MDF} for the reactions involving isotopologues containing ^{17}O and ^{18}O. We round the molecular masses (m_1 and m_2) to integer numbers. For all other reactions therefore, the value of α_{MDF} is less than 1, since larger molecules move more slowly and are less likely to collide.

For Case 6, these fractionations are included in combination with the $CO_2/O(^1D)$ isotope exchange reaction (Case 3b), and MDFs in O_2 fluxes (Case 4) and the upward CO_2 flux (Case 5c).

5.3.5 – Environmental factors

Triple oxygen isotope measurements from atmospheric and deposited species show spreads in the data for different species, due to differences in source locations globally and/or seasonal variations (Figure 1-4; e.g. Thiemens et al., 2014). We therefore explore the sensitivity of our model to several environmental factors, to investigate whether it reproduces some of the spread of the observational data. The factors we focus on are rainfall, temperature, latitude, the isotopic composition of tropospheric water vapour, vertical transport and tropopause height.

We use Case 6 as a 'base model,' from which to vary the aforementioned factors, for comparison. To summarise, Case 6 incorporates a fractionation factor of 1.065 for all four isotopically-substituted O_3-forming reactions. Mass-dependent fractionations are incorporated in O_2 fluxes in and out of the model atmosphere over the lower boundary, in the CO_2 flux into the model atmosphere, and as collision velocity fractionations in each two-body and three-body reaction. The branching ratios of Method 2 are used, with the inclusion of the $CO_2/O(^1D)$ exchange reactions R916-R924.

Table 5-3 is a synopsis of the values used by the base model for various parameters explored in this section. The base model uses *Atmos'* default rainfall level for Earth (see Section 2.4.2) and default eddy diffusion profile (without Cl; see Figure 2-3b), to parametrise vertical transport, and is run with a solar zenith angle of 50° to simulate a mid-latitude location. The tropospheric H_2O $\delta^{17}O$ and $\delta^{18}O$, which are hardcoded in the model, are set to 0‰, as they also are for Cases 0-6. The tropospheric height is set to 11 km, and the temperature profile is that of the modern atmosphere (US Standard Atmosphere, 1976), with a surface temperature of 288.15 K (15°C).

The base model does not perfectly match all the data (see Case 6 results), partly because it does not include the isotopologue-specific mass-independent fractionation factors (see Case 13) or several important isotope exchange reactions (see Cases 14-17). However, these omissions allow us to focus on the effects of environmental variables on a simpler system with a single mass-independent fractionation source. While the absolute oxygen isotope ratios might not match the published measurements due to these omissions, this study is nevertheless useful in investigating the sensitivities of the model to changes in the chosen factors.

5.3.5.1 – Rainfall

It has been shown that $\Delta^{17}O$ in various species varies with rainfall. Areas of particular interest for the measurement of high $\Delta^{17}O$ in nitrates, sulphates and

perchlorates include some of the driest places on Earth, including the Atacama Desert in northern Chile and the Antarctic Dry Valleys. These locations are conducive to the preservation of high O-MIF, since the isotopically-anomalous atmospheric salts are less easily leached away (e.g. Bao, 2015; Michalski et al., 2004a) or reworked by biological and other processes (e.g. Bao et al., 2001). Drier atmospheric columns can also dictate species' formation pathways and influence the initial $\Delta^{17}O$ values in these areas, by varying the relative importance of different oxidants (e.g. Catling et al., 2010) and their isotopic composition (e.g. Lee et al., 2001; Michalski et al., 2003; Savarino et al., 2000). For example, dry polar air can reduce isotopic exchange between isotopically 'normal' tropospheric H_2O and the oxidant OH, which is then able to impart a non-zero oxygen isotope anomaly (Morin et al., 2007). Effects on oxidative pathways over glacial-interglacial timescales have also been studied (e.g. Alexander et al., 2003).

We therefore investigate the sensitivity of the model to rainfall by varying the rainfall rate by several orders of magnitude. The default rainfall rate in the model, used in the base model and all other results presented thus far, is representative of the average annual rainfall rate on Earth. For Case 7, we increase the rate by an order of magnitude, and decrease it by nine orders of magnitude (essentially to nothing).

5.3.5.2 – Temperature profile

The global surface temperatures are wide-ranging, and it is possible that some of the scatter in the observed oxygen isotope compositions of atmospheric and surface-deposited species reflects temperature variations, which also occur in the same geographical location with seasonal variation. We therefore explore the sensitivity of the model results to variations in temperature. We carry out these experiments by adding or subtracting several Kelvin from the original temperature profile, such that the shape of the profile is the same for each case, but shifted in temperature space. We run 7 models (Case 8), using the original temperature profile

and the temperature profile ±5 K, ±10 K and ±20 K (see Figure 5-1 for the temperature profiles used). It would be interesting to explore the effects of only varying the surface temperature, or the tropospheric temperatures, as these are the ones most likely to undergo the largest temperature variations globally, but this is beyond the scope of this work. Since most of the model reactions involve temperature dependence, the bulk chemistry of the entire atmosphere is perturbed by these temperature variations.

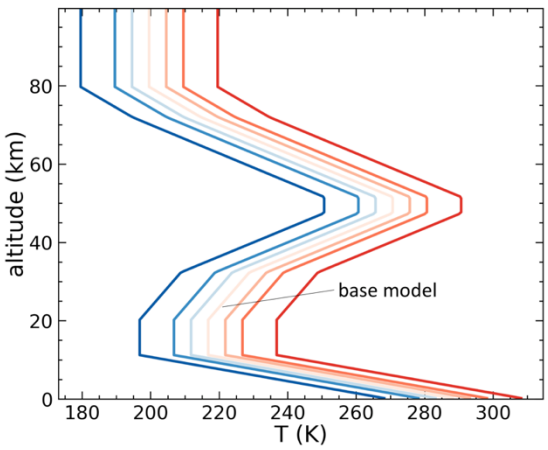

Figure 5-1: Temperature profiles used for the models in Case 8. Red colours show profile temperatures increasing from the base model; blue colours show temperatures decreasing from the base model.

5.3.5.3 – Case 9: Latitude

The latitude in the model is important since it dictates the diurnally-averaged incoming flux of solar light, as well as the column density through which the radiation passes. Both of these factors drive photolysis reaction rates, which critically influence the formation of ozone and therefore the production of O-MIF. The measured data shown in Figure 1-4 (and figures in this chapter) are from a range of latitudes, with some trends seen in oxygen isotope composition with latitude (see e.g. Figure 5-9).

The model uses an insolation-weighted average solar zenith angle as an input, which is 50° for all model results presented so far in this chapter (and for most model results presented in Chapter 3), simulating a mid-latitude atmosphere (arguably an average representative for the globe). Lower and higher zenith angles can be used to simulate lower and higher latitudes respectively. We vary solar zenith angle from 45° to 80° (representative of tropical and polar latitudes, respectively; Hartmann, 1994), with additional sensitivity tests for zenith angles of 50°, 60° and 70°.

5.3.5.4 – Isotopic composition of H_2O

It has been shown that the isotopic composition of water vapour can vary substantially globally. One factor affecting this is movement of atmospheric parcels over the continents. As water vapour rises over landmasses, it becomes depleted in heavier isotopes, as these are preferentially removed by rainfall as the air mass rises and cools. This results in negative $\delta^{18}O$ and $\delta^{17}O$ values relative to VSMOW. Investigating the sensitivity of the model output to the isotopic composition of water vapour is important because it has been shown to affect that of carbon dioxide, as CO_2-H_2O exchange in the troposphere is an important process acting to dilute the stratospheric MIF signal in tropospheric CO_2.

Our base model atmosphere (and all model atmospheres presented in Cases 0-9) are programmed such that the H_2O, H_2P and H_2Q mixing ratios are reset after every timestep, in order to account for an assumed 'infinite' source of water from the oceans, which is a much larger reservoir for H_2O than the atmosphere. The mixing ratios are set such that $\delta^{17}O = \delta^{18}O = 0‰$. (Note that this (somewhat artificially) results in $\Delta^{17}O = 0‰$.) For Case 10, we test the sensitivity of $\Delta^{17}O$ and $\delta^{18}O$ of atmospheric species to the tropospheric isotope composition of H_2O.

The isotopic composition of water vapour, according to the $\delta^{17}O$-$\delta^{18}O$ plot of atmospheric species in the review by Thiemens (2006), shows that water vapour falls along the terrestrial fractionation line and has $\delta^{18}O$ ranging from 0-30‰. For a first test (Case 10a), we choose a $\delta^{18}O$ value in the middle of this field (-17.4‰) which is also the average summer $\delta^{18}O$ measured by Welp et al. (2008). In order to maintain a $\Delta^{17}O$ value of 0‰ for the troposphere, we choose a $\delta^{17}O$ value of 0.528 × -17.4‰ (-9.1872‰).

The isotope exchange between H_2O and CO_2 is a process which we attempt to include in our model (see Case 5). Of the two options discussed in Section 5.3.4.2, we choose to do this by including fractionations in the CO_2 flux into the model atmosphere for Cases 5c-10a. However, the alternative method of Young et al. (2014), who incorporate this relationship through the addition of atmospheric reactions

between CO_2 and H_2O, has the advantage of a clear relationship between the isotopic compositions of H_2O and CO_2. A change in the former therefore results in a change in the latter, which will not occur using the method of Case 10a, as we have not included this link.

Recall that the fractionation we included for the flux of CO_2 into the model atmosphere (Eqs. 5-4 and 5-5) was incorporated by multiplying the flux of CO_2 by the universal ratio of the isotopic species, a fractionation factor ($\alpha_{\text{exch.}}$) of 1.041 (representing the fractionation of CO_2 from H_2O) and a fractionation factor of 1.00525 (for evapotranspiration). So far, our model has assumed that the H_2O $\delta^{18}O$ is 0‰, and so $\alpha_{\text{exch.}}$ produces the same, positive fractionation in CO_2, which is then compounded by the evapotranspiration fractionation. However, if the H_2O $\delta^{18}O$ is less than 0‰, this must be taken into account in the fractionation of the fluxes, and the term becomes:

$$\alpha_{exch.} = \left(\frac{\delta^{18}O_{H2O}}{1000}\right) + 1.041 \qquad (Eq.\ 5\text{-}8)$$

This should act to reduce the $\delta^{18}O$ and also $\delta^{17}O$, as the fractionation factor for ^{17}O becomes:

$$\alpha_{exch.}{}^{\beta} = \left(\left(\frac{\delta^{17}O_{H2O}}{1000}\right) + 1.041\right)^{0.528} \qquad (Eq.\ 5\text{-}9)$$

Therefore, for each model run, we change the H_2O isotopic composition and, for consistency, the fractionation of the CO_2 fluxes into the model atmosphere, in order to account for the same fractionation (41‰) from a different initial H_2O isotopic composition.

5.3.5.5 – Eddy diffusion coefficient profile

As mentioned in Chapter 2 (Section 2.3), vertical transport of molecules in the model is parametrised by eddy diffusion coefficients, which vary with altitude. The eddy

diffusion coefficient is high in the troposphere and low in the lower stratosphere, increasing again with altitude in the stratosphere (Figure 2-3b).

We vary the eddy diffusion profile to assess whether a change in vertical transport affects the vertical distribution of O-MIF in the atmospheric column. While such changes in vertical transport are not necessarily realistic representations of the Earth system, they are nevertheless useful in understanding the effects of transport of molecules on the ultimate $\Delta^{17}O$ of different species, and may capture some of the variation in vertical transport globally, due to, e.g. increased tropospheric mixing at low latitudes. We therefore vary the eddy diffusion profiles from an order of magnitude lower than in the base model to an order of magnitude higher (Case 11). We multiply the eddy diffusion coefficient at all altitudes by the chosen factor.

5.3.5.6 – Tropopause height

We note that some authors define a tropopause at an altitude other than the 11 km that we use in our model (e.g. Wiegel et al., 2013). In general, the tropopause occurs at a lower altitude at the poles and a higher altitude at the equator. We therefore test the effects of changing the tropopause height in the model from 9 km (representative of the poles) to 17 km (representative of the tropics) for Case 12.

5.4 – Results

In this section, we present our model results and compare the output oxygen isotope compositions of various species to those of existing models and observational data. We examine $\Delta^{17}O$ profiles of key species at a range of altitudes. For Cases 7-12, we also compare $\delta^{18}O$ and $\Delta^{17}O$ values from deposited species, including sulphates and nitrates. We present the results in order of case number. Firstly, we show the effects of introducing a mass-independent fractionation factor of 1.065 into the ozone-forming reactions (Case 0). We secondly demonstrate the sensitivity of the model to LBCs, reaction branching ratios, $CO_2/O(^1D)$ exchange and MDFs (Cases 1-6). The third group of cases presented determines the effects of environmental factors. The

more detailed tests regarding α_{MIF} are presented as a fourth group (Case 13). Finally, we demonstrate that a final test case (Case 17) reproduces modern observations fairly well, having tuned one of the α_{MDF} values (Case 14) and included further isotope exchange processes (Cases 15-17).

5.4.1 – Case 0: Effect of a mass-independent fractionation in the reaction forming stratospheric ozone

We initially assess the effect of including a single mass-independent fractionation in the ozone-formation reaction (α_{MIF} = 1.065 for R5.1b-R5.1e). Figure 5-2 shows the $\Delta^{17}O$ profiles for selected species for Case 0 (teal lines), which utilises fixed flux lower boundary conditions for O_2, CH_4, CO, H_2 and N_2O, and a fixed distributed flux with deposition velocity LBC for CO_2. The Case 0 results are compared to values from existing models and data, which are shown as symbols. The mass-independent fractionation in the ozone-forming reaction results in a large, positive $\Delta^{17}O$ value for ozone of 26‰, which is uniform throughout the whole atmospheric column, consistent with observations. Sulphate and nitrate aerosol inherit a large $\Delta^{17}O$, which peaks in the stratosphere and is lower in the troposphere, lying within the range of tropospheric observations. In comparison to measurements showing negligible $\Delta^{17}O_{CO2}$ in the modern troposphere (e.g. Thiemens et al., 2014), our Case 0 model values are much larger, as carbon dioxide gains a uniform positive $\Delta^{17}O$ of 2-2.5‰. While positive as expected, the $\Delta^{17}O_{CO2}$ profile does not show the observed increase in $\Delta^{17}O$ in the stratosphere. In conserving mass balance, O_2 gains a negative $\Delta^{17}O$ of -4‰ in the model. O_2 in the modern atmosphere does have a negative MIF signal, but the magnitude is roughly ten times smaller than predicted here. Atomic oxygen (not shown) behaves similarly in the model, with fairly large negative $\Delta^{17}O$ values throughout the atmospheric column, but only when O_2 has flux boundary conditions. With fixed flux boundary conditions, N_2O has a small positive $\Delta^{17}O$ and CO has a very small negative $\Delta^{17}O$ (not shown).

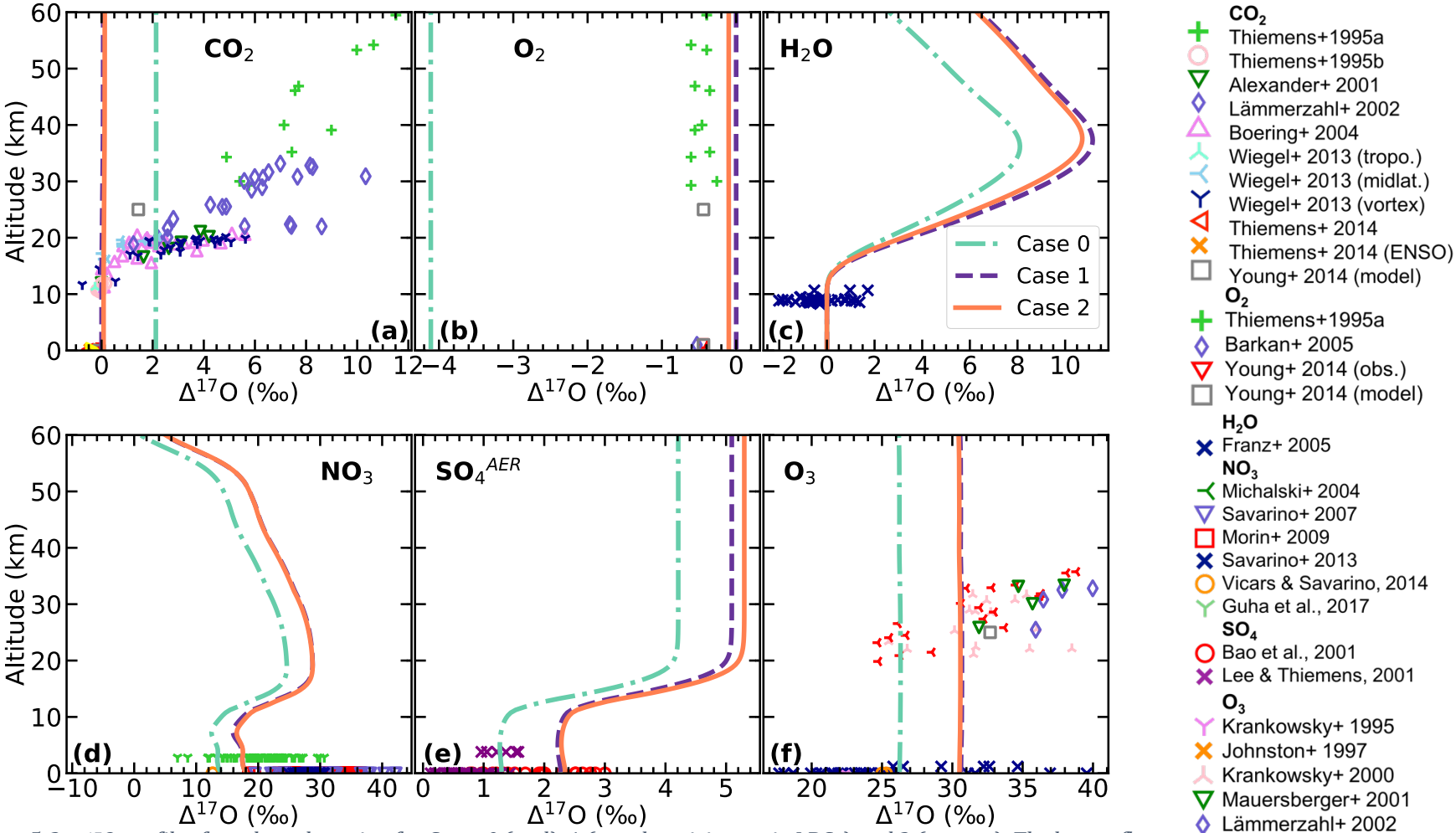

Figure 5-2: $\Delta^{17}O$ profiles for selected species, for Cases 0 (teal), 1 (purple; mixing ratio LBCs) and 2 (orange). The larger fluxes of O_2 and CO_2 in and out of the model atmosphere for Case 2 compared to Case 0 result in a decrease in the magnitude of $\Delta^{17}O$. For comparison, some observed $\Delta^{17}O$ values from the literature are shown (see key to right of plot for references).

H_2O, H_2P and H_2Q (water vapour) mixing ratios are initially set in the model such that the $\delta^{17}O$ and $\delta^{18}O$ are equal to 0‰ (see Section 4.1.4), so $\Delta^{17}O$ in the troposphere is also 0‰; stratospheric water vapour on the other hand has a large $\Delta^{17}O$, peaking at an altitude of 35-40 km. Related species OH, HO_2 and H_2O_2 also have small $\Delta^{17}O$ in the troposphere, and large, positive $\Delta^{17}O$ values in the stratosphere (not shown).

The inclusion of a single MIF in ozone formation has allowed the model to predict some of the general trends of atmospheric $\Delta^{17}O$, but comparison with observations shows that this falls short of fully reproducing real $\Delta^{17}O$ profiles. In the following sections, our exploration of the model sensitivity to some of the other factors described in Section 5.3 will help to highlight ways in which inclusion or improvement of the model treatment of these factors might better reproduce the modern $\Delta^{17}O$ profiles.

5.4.2 – Cases 1 and 2: Lower boundary conditions

Inclusion of a mass-independent fractionation in the ozone-forming reactions results in large, non-zero O-MIF in some atmospheric species (Case 0). On Figure 5-2, these results are compared to the results of a case with mixing ratio boundary conditions for O_2, CH_4, H_2, CO, N_2O and CO_2 (Case 1), which indicates the sensitivity of the model to the choice of type of boundary condition. As for Case 0, the inclusion of the mass-independent fractionation results in large $\Delta^{17}O$ values for O_3 and stratospheric NO_3, SO_4 and H_2O. However, with mixing ratio boundary conditions, $\Delta^{17}O$ for O_2 and CO_2 are 0‰ throughout the whole atmospheric column, which is not unexpected, as oxygen isotope composition is prescribed at the lower boundary for these species.

For Case 0, the $\Delta^{17}O$ values for O_2 and CO_2 are negative and positive, respectively, but with magnitudes too large compared to tropospheric measurements. Figure 5-2 also shows the results of Case 2, in which large fluxes of O_2 and CO_2 into and out of the atmosphere over the lower boundary are chosen. As a result, the magnitudes of

both the $\Delta^{17}O_{O2}$ and $\Delta^{17}O_{CO2}$ decrease. The $\Delta^{17}O$ for CO_2 becomes ~0‰ in the troposphere, with a negligible increase in the stratosphere and upper atmosphere. The absolute oxygen $\Delta^{17}O$ values decrease to ~-0.1‰. While these profiles do not perfectly match the observational data, the inclusion of gross fluxes of O_2 and CO_2 both into and out of the atmosphere is clearly important in the accurate prediction of modern atmospheric $\Delta^{17}O$, at least for O_2 and CO_2. The remainder of the cases described in this chapter use the 'Case 2' LBCs, allowing large fluxes into and out of the atmosphere for these two species, with only minor changes in magnitude to incorporate mass-dependent fractionations, and these LBCs are used in our final model (Case 17).

5.4.3 – Case 3: Reactions and rates

5.4.3.1 – Case 3a: Choice of branching ratios

Figure 5-3 shows the $\Delta^{17}O$ profiles of selected species with the Method 2 (solid purple lines) and Method 1 (solid teal lines) branching ratios, to indicate the sensitivity of the model to the branching ratios of the atmospheric reactions (Case 3a). The choice of method does not affect the atmospheric $\Delta^{17}O$ profiles of O_2 or CO_2, but there is a noticeable effect for some other species. For Method 2, O_3 (and O and $O(^1D)$, not shown) have fairly uniform $\Delta^{17}O$ values throughout the atmospheric column, whereas under the Method 1 assumption, there is a minimum at an altitude of ~50 km (around the stratopause), with a maximum decrease in $\Delta^{17}O$ of ~2‰, ~6‰ and ~1.5‰ respectively. This inflection is also seen in the profiles of HNO_3 (not shown) and NO_3, which are known to inherit an anomalous oxygen isotope signature from ozone. The magnitude of the $\Delta^{17}O$ values in the atmospheric profiles of H_2O and SO_4 is also reduced somewhat using Method 1. The decrease in $\Delta^{17}O$ value in species with a large, positive oxygen isotope anomaly results in a slight decrease in the magnitude of $\Delta^{17}O_{O2}$, of less than 0.1‰, to conserve mass balance.

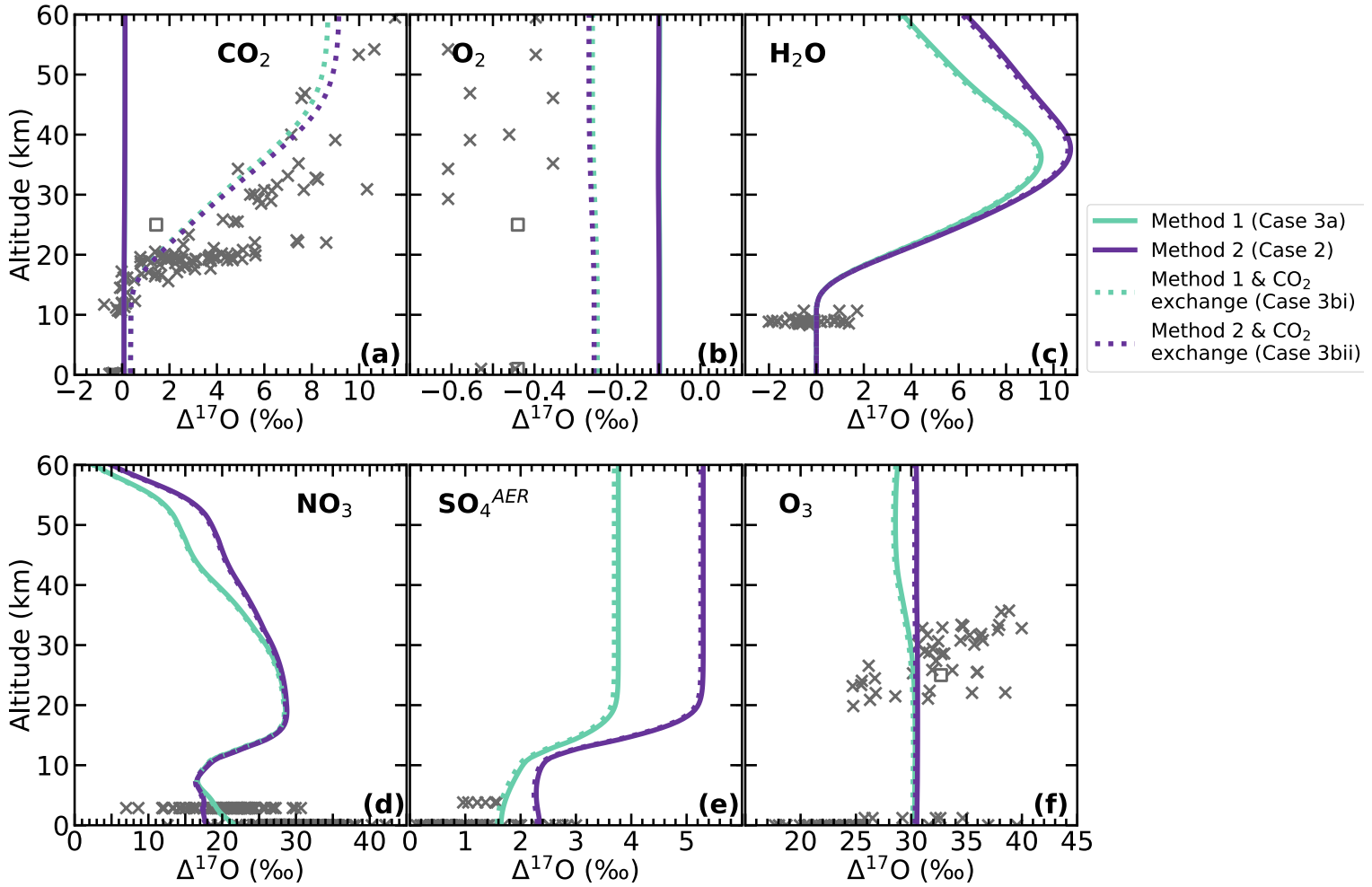

Figure 5-3: Δ¹⁷O profiles for selected species for Case 3. Results from models run using Method 1 (teal) and Method 2 (purple) for the branching ratios of the reactions are shown (Case 3a and Case 2, respectively). The dotted lines show models in which the exchange reactions R916-R924 have been included (Case 3b). Grey crosses show observations (see Figure 5-2 for references), and grey squares show model predictions from Young et al. (2014).

Having isolated the effects of a couple of reactions included in Method 1 but not Method 2, and considered likely to cause the inflection in the O_x species, we found that the simulated addition of isotopic exchange in the $O(^1D)$ quenching reaction $O(^1D) + O_2 \rightarrow O + O_2$ accounts for all of the change in $O(^1D)$, O and O_3 between the two methods (not shown in figure; see Figure 5-15 for results of similar experiment (Case 15)). For Method 2, we assume that this is purely a quenching rather than an isotope exchange reaction, whereas Wiegel et al. (2013) include isotope exchange between O_2 and $O/O(^1D)$ via this mechanism, as in Method 1.

This reaction also accounts for some of the differences in the $\Delta^{17}O$ profiles between Methods 1 and 2 for NO_3, H_2O and SO_4. We will consider the remaining minor differences between the methods for these species a possible source of uncertainty for predicting nitrate and sulphate oxygen isotope compositions, but overall the similarities in the profiles should instead be a reason for confidence that our branching ratio assumptions using Method 2 are acceptable and not producing wildly different results to the statistical treatment. We therefore use Method 2 for our final model (Case 17), and test the sensitivity to inclusion of the isotope exchange reaction again in Case 15, incorporating it into the final model (Case 17).

5.4.3.2 – Case 3b: Inclusion of the isotope exchange reaction $CO_2 + O(^1D) \rightarrow CO_2 + O$

Model results comparing the inclusion and exclusion of the reaction $CO_2 + O(^1D) \rightarrow CO_2 + O$ (and its equivalents with substituted P and Q) are shown in Figure 5-3 by dotted lines, for models with Method 1 (teal) and Method 2 (purple) branching ratios.

For both Methods 1 and 2, the inclusion of the exchange reactions produces a more negative $\Delta^{17}O$ for O_2 throughout the whole atmospheric profile, with a reduction at the ground-level from -0.1‰ to -0.25-0.3‰, which is closer to the measured and model values (Barkan and Luz, 2005; Young et al., 2014). The other species that this particularly affects is CO_2, which develops a pronounced tropospheric-stratospheric

difference in its $\Delta^{17}O$ profile with the inclusion of the exchange reactions, as observed (Alexander et al., 2001; Boering et al., 2004; Lämmerzahl et al., 2002; Thiemens et al., 1995a; 1995b; Wiegel et al., 2013).

As shown by Yung et al. (1997), this exchange reaction is critical for the transfer of the large positive MIF from ozone to CO_2, through $O(^1D)$, which is a product of ozone photolysis. This explains the large increase in $\Delta^{17}O$ in stratospheric CO_2. The inclusion of the exchange reactions does not seem to affect the $\Delta^{17}O$ of $O(^1D)$ greatly (not shown), but the $\Delta^{17}O_{O2}$ profiles suggest that a considerable part of the mass-balance is maintained by the increase in the magnitude of the negative MIF in O_2. There are also slight decreases in MIF in ozone and O (not shown) as a result of the inclusion of the exchange reactions. With an added sink for heavy $O(^1D)$ in the form of these reactions, the rate at which $O(^1D)$ recombines (through O) with O_2 to produce O_3 decreases, thereby decreasing the $\Delta^{17}O$ of ozone slightly. The lack of exchange with CO_2 also keeps the heavier isotopes within the O_2-O_x system, whereas when there is a route out of the system for the heavier isotopes, this leads to a depletion in O_2 with respect to the heavier isotopes.

However, another result of the inclusion of the exchange reactions is the slight increase of tropospheric $\Delta^{17}O_{CO2}$, which moves further from the tropospheric measurements (Thiemens et al., 2014), which show a slight negative MIF according to our definition of $\Delta^{17}O$. Nevertheless, the improvement of the entire atmospheric profile, as well as the inclusion of these reactions by other authors (Wiegel et al., 2013; Young et al., 2014; Yung et al., 1997) highlight these as important reactions for the final model.

The results of this case are encouraging, since one of the effects we investigate in Chapter 6 is that of varying pCO_2/pO_2 on $\Delta^{17}O$, which are related by the rate at which the exchange reaction occurs (Young et al., 2014; Yung et al., 1997). It is helpful to know that the inclusion of this reaction increases the $\Delta^{17}O$ of stratospheric CO_2 and decreases the $\Delta^{17}O$ of ground-level O_2, as expected, which stands us in good stead for sensitivities of the right order when pCO_2/pO_2 is varied.

5.4.4 – Cases 4, 5 and 6: Mass-dependent fractionations

Here we present the results of including mass-dependent fractionations in i) O_2 fluxes in and out of the model atmosphere; ii) CO_2 sources and sinks; and iii) two- and three-body reactions, simulating kinetic effects.

Incorporating the combination of the ~5.25‰ and 18.2‰ fractionations (of ^{18}O relative to ^{16}O) from photosynthesis and respiration, respectively, for the O_2 fluxes in and out of the model atmosphere, respectively, results in a $\delta^{18}O$ of ground-level O_2 of 22.6‰, close to observations (Case 4; results not shown, but very similar to Cases 5c and 6 in Figure 5-4b for O_2). Even though no further mass-independent fractionations have been added to the model, the differing $\delta^{17}O$-$\delta^{18}O$ slopes for the mass-dependent photosynthesis and respiration processes produce a more negative $\Delta^{17}O$ in O_2 than is observed for Case 3b (compare Case 5c, which is similar to Case 4 (Figure 5-4b), to Case 3b (Figure 5-3b)). The inclusion of photosynthesis alone allows the model to approach the observed value, while the inclusion of both processes overshoots and produces a $\Delta^{17}O$ more negative that those observed (Barkan and Luz, 2005; Young et al., 2014).

The Case 4 atmospheres have ground-level $\delta^{17}O$ and $\delta^{18}O$ of zero for CO_2, while measurements indicate values of ~21‰ and ~40‰, respectively. Cases 5ai and 5aii, in which MDFs are incorporated into tropospheric CO_2 via exchange reactions with H_2O, after Young et al. (2014), produce atmospheres with vastly isotopically light tropospheric CO_2 (results not shown). This happens because, in our model, there is an infinite source of H_2O with the isotopic composition of VSMOW, so isotopically light H_2O is constantly replenished and able to exchange with CO_2, decimating the concentrations of heavier COP and COQ. Using exactly the same method as Young et al. (2014) is therefore not the best approach for this factor.

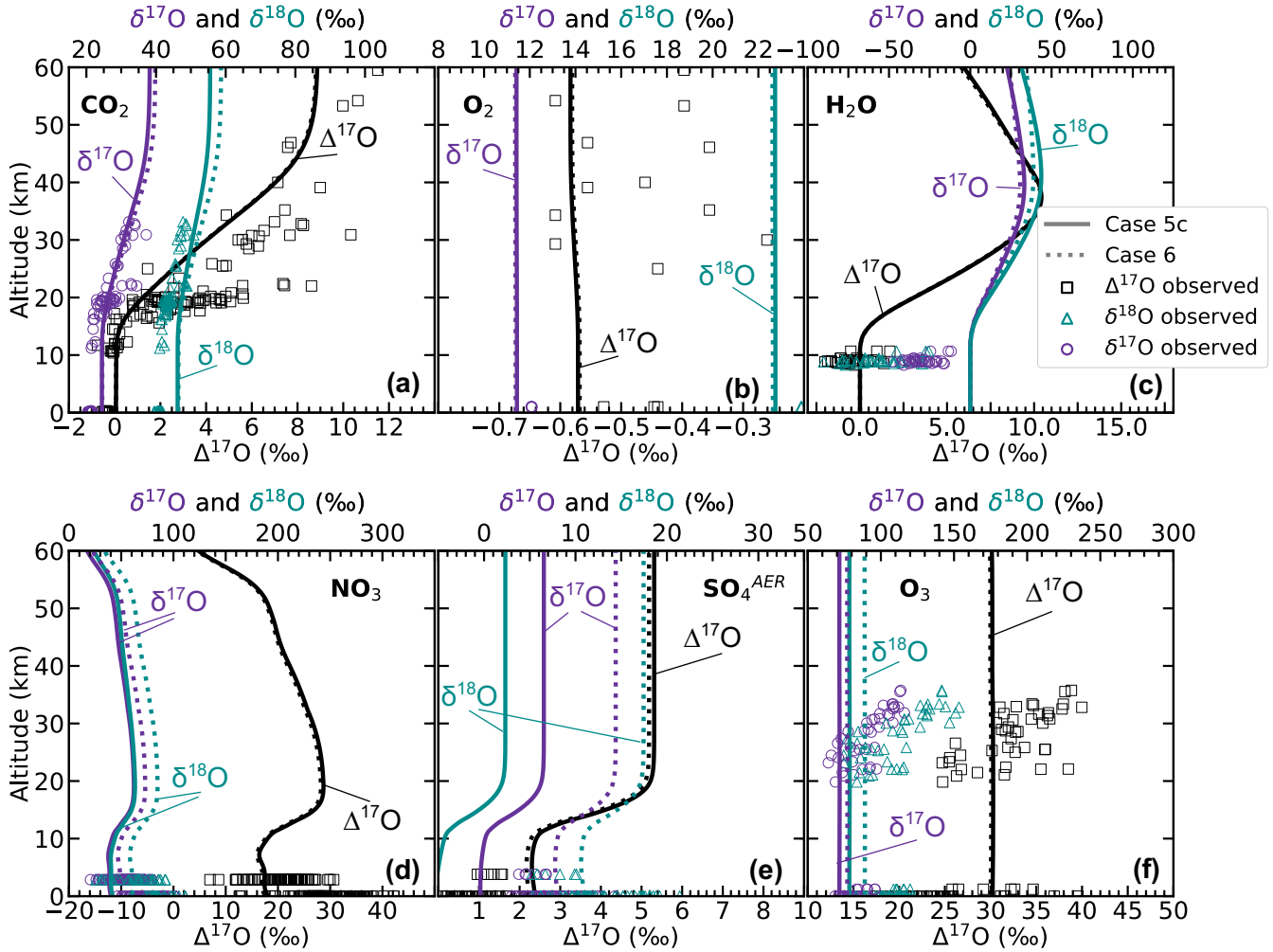

Figure 5-4: Profiles of model $\delta^{17}O$ (purple), $\delta^{18}O$ (teal) and $\Delta^{17}O$ (black) values for selected atmospheric species for Cases 5c (solid line) and 6 (dotted line). Note the fractionations in O_2 and CO_2 for both cases due to the inclusion of mass-dependently fractionated fluxes of these species, compared to Case 3b. O_2 fractionations for Case 4, not shown here, are similar to those of Cases 5c and 6. Comparison of the Case 5c and Case 6 profiles highlights the effects of fractionations due to varying collision velocities between isotopologues (included in the latter). Note the different axes for $\delta^{17}O/\delta^{18}O$ and $\Delta^{17}O$ values, respectively.

The inclusion of MDFs in CO_2 fluxes both in and out of the model atmosphere (Case 5b) results in $\delta^{17}O$ and $\delta^{18}O$ values which are too large compared to atmospheric measurements of CO_2 (results not shown). For the remaining cases described in this chapter, we therefore follow Young et al. (2014) and neglect any fractionations in the drawdown of CO_2 from the atmosphere, instead only including fractionations in the upward flux of CO_2 (Case 5c; Figure 5-4).

Figure 5-4 shows that the inclusion of mass-dependent fractionations in all two-body and three-body reactions (Case 6, compared to Case 5c) produces a noticeable effect on the $\delta^{17}O$ and $\delta^{18}O$ of all species. For some species (e.g. O_3, CO_2, HNO_3, SO_4 and H_2SO_4, as well as H_2O_2 and H_2CO, not shown), $\delta^{18}O$ is reduced in magnitude. This is a particularly stark effect for sulphate, nitrate and ozone, which are heavy molecules, so the resulting fractionations are larger and the $\delta^{17}O$ and $\delta^{18}O$ are significantly reduced. However, for other species (e.g. OH, HO_2 (not shown), O_2), $\delta^{18}O$ increases with the addition of the Case 6 fractionations. The $\Delta^{17}O$ profiles, both with and without these fractionations (Figure 5-4), show that the effect on $\Delta^{17}O$ is very small, as expected.

One thing to note is that, for Case 6, the SO_4 and H_2SO_4 $\delta^{17}O$ and $\delta^{18}O$ values are much lower than measurements suggest (e.g. Bao et al., 2001; Lee et al., 2001; Michalski et al., 2004b), reaching negative values. This could be because the only sinks of H_2SO_4 in the model are the formation of particulate SO_4 aerosol and rain, and the only sinks of SO_4 aerosol are particle fallout and rain, and none of these processes currently includes an MDF. As a result, light isotopes are concentrated in these species, since the heavier isotopes are involved in reactions less frequently. It may therefore be worth investigating the inclusion of mass-dependent effects in the wet and dry deposition of these species. It would also be instructive to include additional sulphate-forming reactions in the model, since there are other production pathways via heterogeneous oxidation of SO_2 involving MIF-carrying O_3 and OH (Savarino et al.er, 2000) that we have not included.

Figure 5-5 summarises the Case 6 ground-level atmospheric results in $\delta^{18}O$-$\Delta^{17}O$ space for 8 key species, compared to atmospheric measurements. In general, the model $\Delta^{17}O$ values match the measurements fairly well, though the $\delta^{18}O$ values are not quite the same.

5.4.5 – Cases 7-12: Sensitivity of model $\delta^{17}O$, $\delta^{18}O$ and $\Delta^{17}O$ to environmental factors

With some important components incorporated in the oxygen isotope model, Case 6 matches the existing $\Delta^{17}O$ measurements fairly well. However, for NO_3/HNO_3, SO_4/H_2SO_4 and O_3, the spread of data points from existing literature shows that various factors acting in the Earth system can induce a spread in $\Delta^{17}O$ and $\delta^{18}O$ values (Figure 5-5; Figure 1-4). Here, we show how rainfall, temperature, latitude,

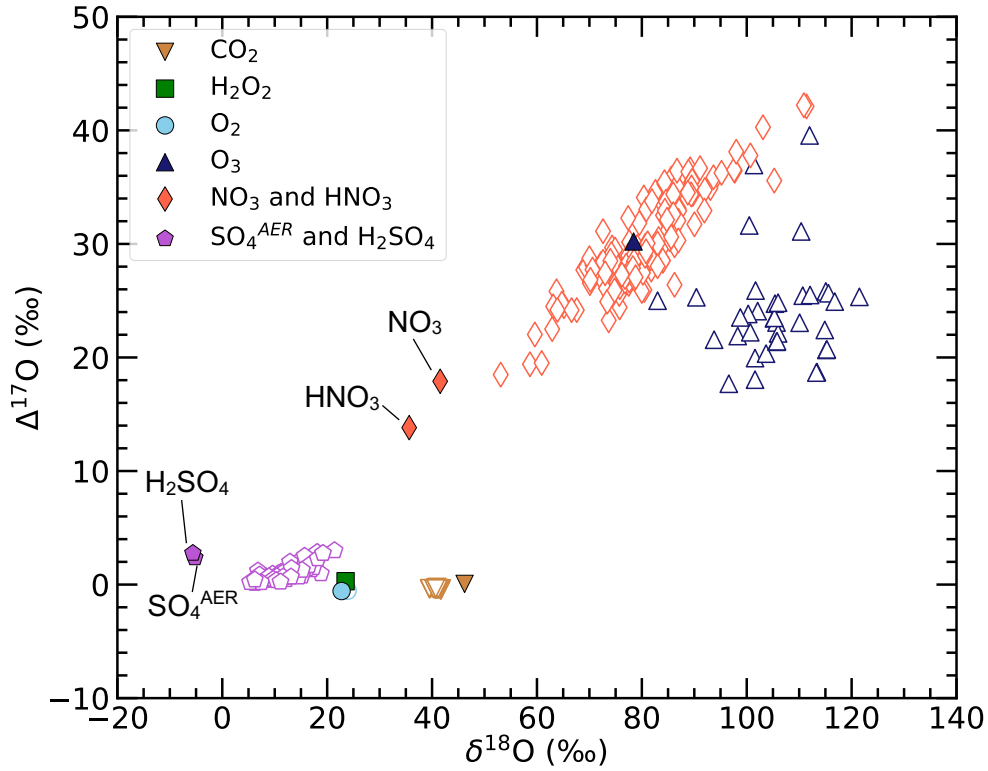

Figure 5-5: Ground-level model atmosphere $\delta^{18}O$ and $\Delta^{17}O$ (filled symbols) compared to ground-level atmospheric measurements (unfilled symbols) for selected species. Please note that atmospheric measurements for O_2 and H_2O_2 are hidden behind model predictions.

the isotopic composition of tropospheric water vapour, vertical transport and tropospheric height affect our triple oxygen isotope model output and contribute to the spread of existing measurements in $\delta^{18}O$-$\Delta^{17}O$ space. The results of these sensitivity tests are shown in Figures 5-6 – 5-11, with comparison to the base model (Case 6; Table 5-1; Table 5-3). Further improvements are made to better tune the base model to modern measurements later in this chapter (Sections 5.4.7 and 5.4.8), but at this stage our results nevertheless indicate the way in which the oxygen isotope ratios of atmospheric and deposited species can be affected by environmental variables.

Figure 5-6 shows the spread of atmospheric $\Delta^{17}O$ variation with altitude for each factor (Cases 7–10). Figures 5-7 and 5-8 show the way in which each factor affects the position of several chosen species on a plot of $\delta^{18}O$ against $\Delta^{17}O$, for dry and wet deposition, respectively. Here, we define dry deposition as the flux of species flowing over the lower boundary out of the model atmosphere. Wet deposition is the removal of the species via dissolution in rainwater. It is therefore expected that some combination of the two types of deposition results in the isotopic composition of species measured at the surface (e.g. on or in soils). Figure 5-9 focusses on nitrate (HNO_3) in particular, comparing the trends seen within Cases 7–9 more closely with trends in the existing data. The results of Case 11 are shown in Figure 5-11.

5.4.5.1 – Case 7: Investigating sensitivity to rainfall

The variation in rainfall (between 10 times and 10^{-9} times the average modern rainfall rate) affects the $\Delta^{17}O$ profiles of CO_2, O_3, H_2O and stratospheric NO_3 very little (Figure 5-6, blue shading). However, the magnitude of the $\Delta^{17}O$ values for O_2 and tropospheric NO_3 and SO_4 decrease with increasing rainfall. Figure 5-7 shows that the $\delta^{18}O/\Delta^{17}O$ values of CO_2 are little affected by the rainfall rate, but trends are seen for HNO_3, SO_4, H_2SO_4 and H_2O_2, with increasing $\delta^{18}O$ and $\Delta^{17}O$ values with decreasing rainfall (Figures 5-7 and 5-8). This trend is only significant to rainfall levels of 0.01% of the base model rainfall rate. Rates lower than this are so small that further decreases have little further effect. Figure 5-9a compares this trend for nitrate with

the trends in the data. The $\Delta^{17}O$ of deposited nitrate salts in the Mojave Desert have lower $\delta^{18}O$ and $\Delta^{17}O$ values than those from the drier Atacama Desert and Antarctic Dry Valleys (source locations not shown on Figure 5-9). Our data show the same trend of decreasing O-MIF with increasing rainfall, but our sensitivity test does not capture the large spread of observed values. In order to match observations, it may be that a combination of variations in rainfall and other geographic factors (e.g. temperature and latitude) in combination are required.

5.4.5.2 – Case 8: Investigating sensitivity to the temperature profile

The red shading on Figure 5-6 shows the space that the $\Delta^{17}O$ profiles cover with the modelled variations in temperature profile (up to ±20 K at all altitudes). $O(^1D)$, O (not shown) and O_3 are very little affected by temperature variations, except at altitudes above 70 km (not shown). The $\Delta^{17}O$ of tropospheric CO_2 is relatively unaffected, while in the stratosphere lower temperatures result in higher $\Delta^{17}O$, matching the observations slightly better. For O_2, temperature has little effect on $\Delta^{17}O$ profiles, apart from for the highest temperature, which results in a decrease of $\Delta^{17}O$ to more negative values by 0.05‰, accounting for most of the spread seen in Figure 5-6 for O_2.

Large $\Delta^{17}O$ in stratospheric water vapour between the stratopause and ~11 km at low temperatures contributes towards the high $\Delta^{17}O$ in stratospheric SO_4, but there is little variation in tropospheric $\Delta^{17}O_{SO4}$, especially at the surface, although $\Delta^{17}O$ is slightly higher for higher temperatures. The opposite is the case for tropospheric $\Delta^{17}O_{NO3}$, where some of the spread of the measured ground-level atmospheric measurements seems to be captured by high-T low-$\Delta^{17}O$ and low-T high-$\Delta^{17}O$ models. In the stratosphere, the peak of $\Delta^{17}O_{NO3}$ is higher in magnitude and altitude for higher temperatures, resembling the ozone mixing ratio curve.

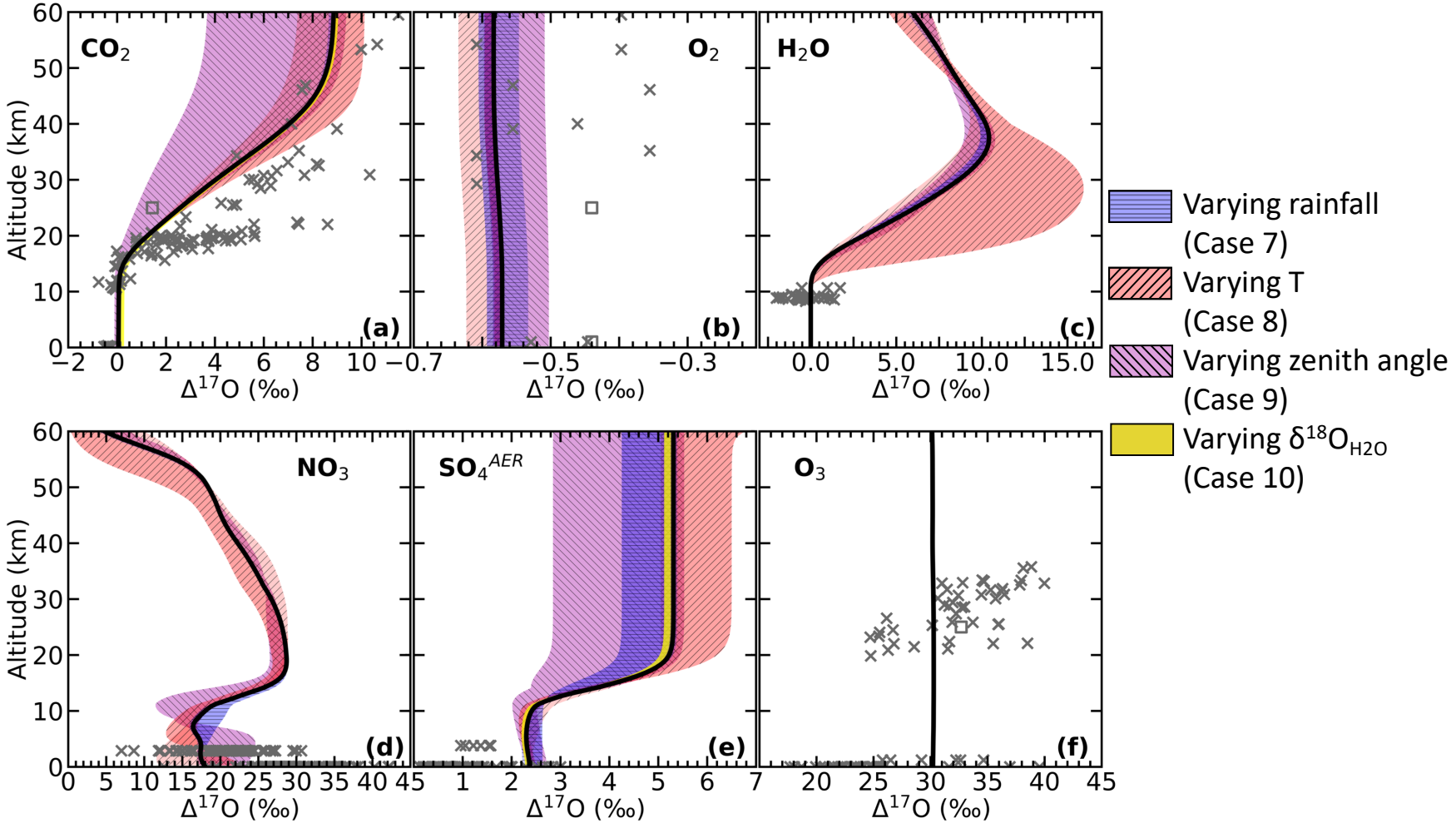

Figure 5-6: $\Delta^{17}O$ space covered by $\Delta^{17}O$ profiles when the environmental parameters are varied. Blue, red, purple and orange shaded areas show the range of $\Delta^{17}O$ profiles produced when the rainfall (Case 7), temperature (Case 8), zenith angle (Case 9) and tropospheric $\delta^{18}O$ of water vapour (Case 10b) are varied, respectively. Black solid line shows the base model profile (Case 6). Existing experimental (crosses) and model (squares) data are shown as grey points.

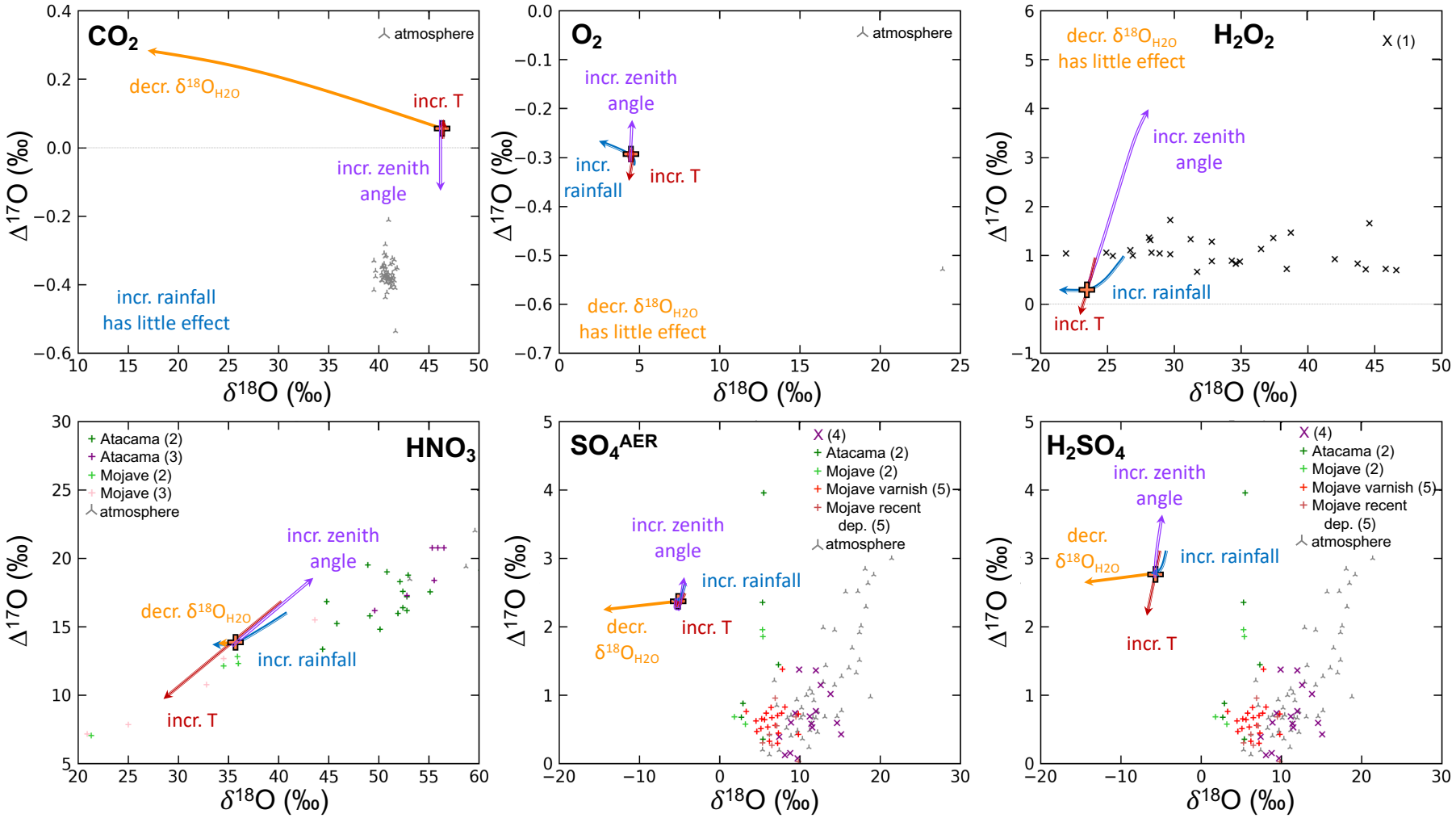

Figure 5-7: Effects on oxygen isotopic composition of species as they are removed from the atmosphere across the lower boundary of varying rainfall (Case 7), temperature (Case 8), zenith angle (Case 9) and $\delta^{18}O_{H2O}$ (Case 10b). Orange crosses show isotope composition of species removed from the atmosphere for the base model (Case 6). Coloured arrows show the effects of varying each parameter. Arrow heads signify increasing zenith angle, temperature or rainfall rate, or decreasing $\delta^{18}O_{H2O}$. Observations are shown as points: 'x' symbols show rainwater measurements (references: (1) Savarino & Thiemens, 1999; (4) Lee & Thiemens, 2001); '+' symbols show measurements from surface deposits (references: (2) Michalski et al., 2004b; (3) Jackson et al., 2010; (5) Bao et al., 2001); triangular points show atmospheric measurements).

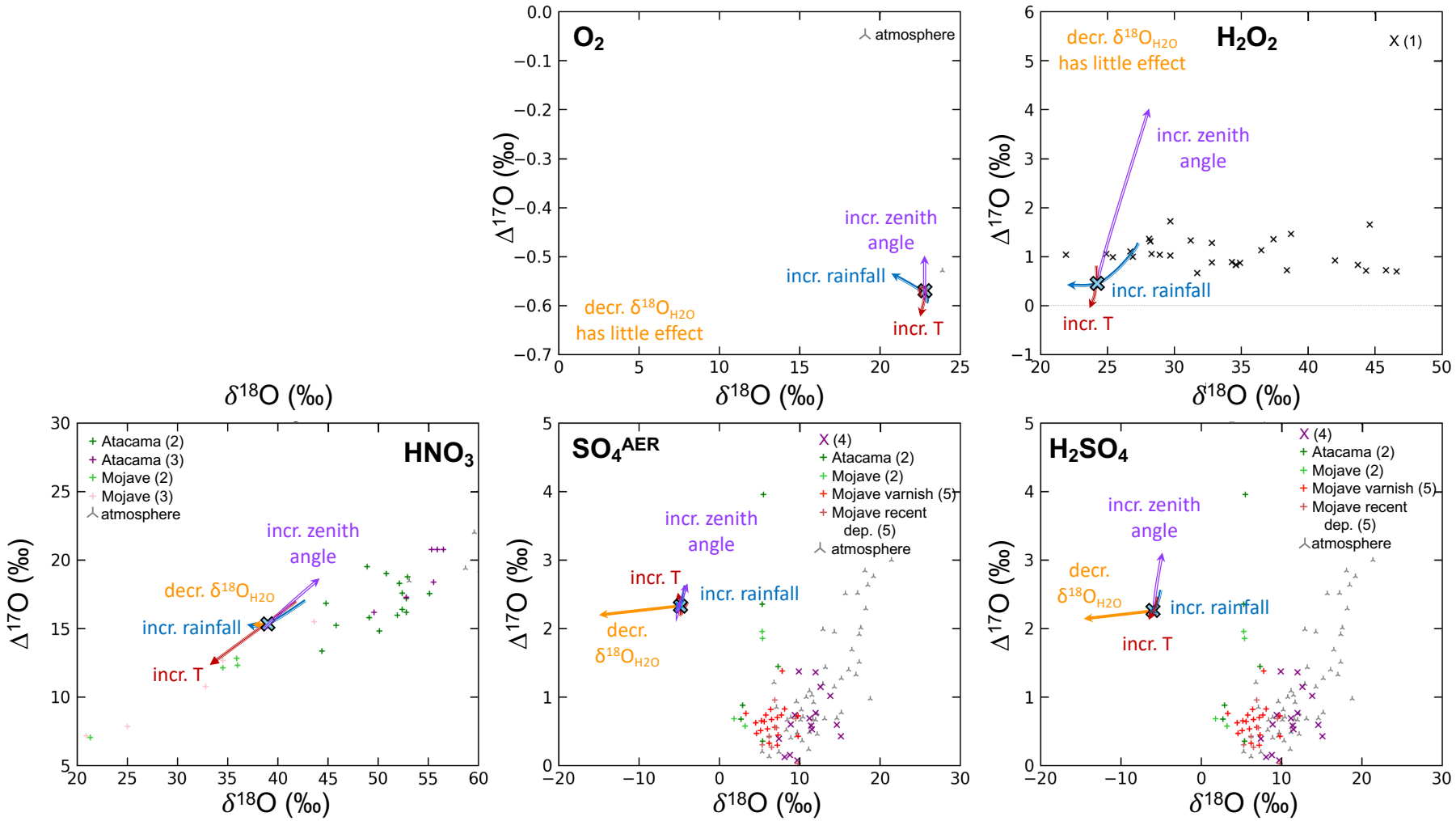

Figure 5-8: Effects on oxygen isotopic composition of species dissolved in rainwater of varying rainfall (Case 7), temperature (Case 8), zenith angle (Case 9) and $\delta^{18}O_{H2O}$ (Case 10b). Blue crosses show isotope composition of species removed from the atmosphere for the base model (Case 6). Coloured arrows show the effects of varying each parameter. Arrow heads signify increasing zenith angle, temperature or rainfall rate, or decreasing $\delta^{18}O_{H2O}$. Observations are shown as points: 'x' symbols show rainwater measurements (references: (1) Savarino & Thiemens, 1999; (4) Lee & Thiemens, 2001); '+' symbols show measurements from surface deposits (references: (2) Michalski et al., 2004b; (3) Jackson et al., 2010; (5) Bao et al., 2001); triangular points show atmospheric measurements).

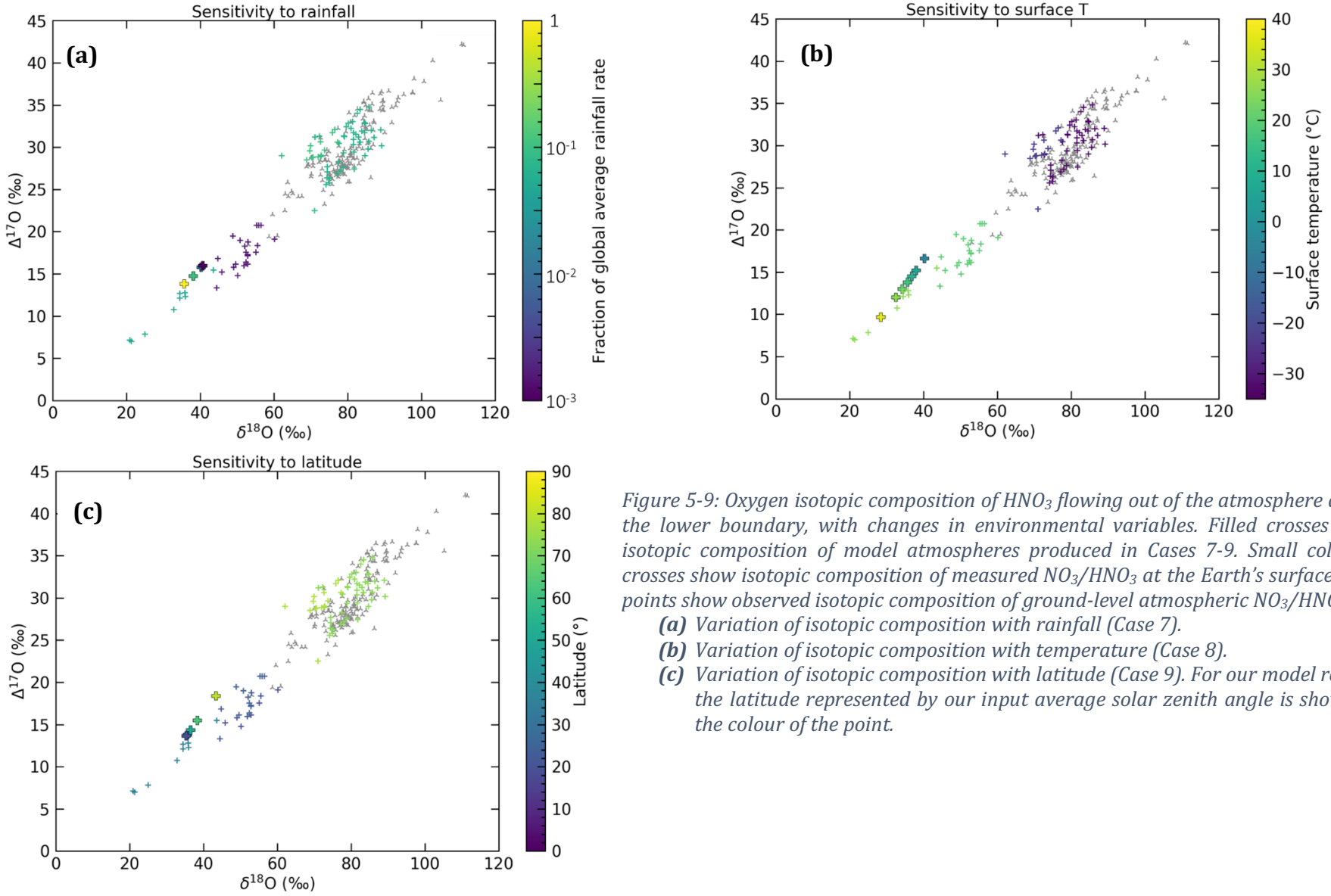

Figure 5-9: Oxygen isotopic composition of HNO_3 flowing out of the atmosphere across the lower boundary, with changes in environmental variables. Filled crosses show isotopic composition of model atmospheres produced in Cases 7-9. Small coloured crosses show isotopic composition of measured NO_3/HNO_3 at the Earth's surface. Grey points show observed isotopic composition of ground-level atmospheric NO_3/HNO_3.

- ***(a)*** *Variation of isotopic composition with rainfall (Case 7).*
- ***(b)*** *Variation of isotopic composition with temperature (Case 8).*
- ***(c)*** *Variation of isotopic composition with latitude (Case 9). For our model results, the latitude represented by our input average solar zenith angle is shown by the colour of the point.*

Figures 5-7 and 5-8 show the model results as they plot in $\delta^{18}O$-$\Delta^{17}O$ space. Temperature affects the O_3 from dry deposition very little. The $\delta^{18}O$ values of O_2, H_2O_2, HO_2 (not shown) and CO_2 are not affected greatly by temperature, but there is a positive correlation between T and $\Delta^{17}O_{CO2}$, and a negative correlation between T and $\Delta^{17}O_{HO2}$ (not shown) and T and $\Delta^{17}O_{H2O2}$. For the latter, the lowest temperatures appear to match the mid-latitude rainwater isotope measurements best (Savarino and Thiemens, 1999). The $\delta^{18}O_{SO4}$ and $\delta^{18}O_{H2SO4}$ values are still too low compared to the measurements, but the model results demonstrate an increase in $\Delta^{17}O$ (and a small increase in $\delta^{18}O$) with decreasing temperature. This pattern is seen more obviously in the nitrate data, which fit along the slope of the observed points. Figure 5-9b shows that this pattern is also seen in the measurements, as nitrates from colder polar environments have higher $\Delta^{17}O$ and $\delta^{18}O$ than those from warmer climates.

The very small effect on $\Delta^{17}O_{O3}$ and $\Delta^{17}O_{O2}$ (apart from at the highest temperatures for the latter) seems unexpected, given such a large range of temperatures, as do the relatively small ranges in isotopic composition in these sensitivity tests compared to the measured data. One might expect that temperature would have a larger effect, since it affects so many reactions in the model. However, the mass-independent fractionation in the ozone-forming reaction is temperature-dependent (Janssen et al., 2003), so the inclusion of this temperature-dependence (in Case 13) may enable the model to capture more of the global variation.

5.4.5.3 – Case 9: Investigating the sensitivity to latitude

Figure 5-10 shows the solar incoming radiation and the resulting ground-level UV fluxes with wavelength for models with varying zenith angle, varied to examine changes in latitude. All five model atmospheres block harmful UV radiation with wavelengths between 200 and 290 nm, and show similar curves in ground-level fluxes with wavelength. However, atmospheres with higher zenith angles (representative of higher-latitude atmospheric columns) provide slightly more shielding than atmospheres with lower zenith angles. This can particularly be seen

in the difference between the 80° case and the other models for wavelengths between 300 and 320 nm.

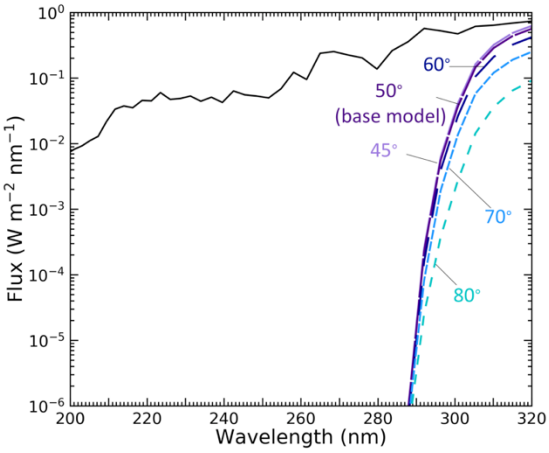

Figure 5-10: Ground UV fluxes for the model atmospheres in Case 9. Labels show zenith angle used for model run. Black line shows the incoming 'top of the atmosphere' fluxes at each wavelength, which does not change with zenith angle.

This variation in incoming solar flux throughout the atmosphere affects the oxygen isotope compositions of some of the species. In the stratosphere, an increase in latitude results in a decrease in the magnitude of O-MIF for the selected species (other than O_3, which remains unchanged). The stratospheric effect on NO_3 is small (see Figure 5-6), but towards the surface the magnitude of $\Delta^{17}O$ increases with latitude, which is seen in Figures 5-7 and 5-8. Figures 5-7 and 5-8 also show that the $\delta^{18}O$ values of O_2 and CO_2 are little affected by the changes in latitude, while $\Delta^{17}O_{CO2}$ decreases to negative values and $\Delta^{17}O_{O2}$ increases to less negative values. For H_2O_2 and SO_4, the case with a zenith angle of 80° is an extreme case with $\delta^{18}O$ and $\Delta^{17}O$ values much higher than the other points (although this cannot be seen on Figures 5-7 and 5-8). It is also distinctive because of the different shapes of profiles that this case produces in SO_4, H_2O_2 and H_2O (not highlighted in Figure 5-6). Since the photolysis rates at the highest altitudes are likely to be fairly different to those further towards the equator, it is not unexpected that the profiles for this model run do not follow the same shape as the others.

Our results show trends in $\Delta^{17}O$ and $\delta^{18}O$ for some species with changes in zenith angle. Figure 5-9c shows the results for NO_3 in particular. The same trend of increasing $\delta^{18}O$ and $\Delta^{17}O$ with increasing latitude is observed. Our results cover a large range of oxygen isotope compositions along this trend, yet do not account for the whole spread of data points. Part of this discrepancy could be that, in the Earth system, changes in latitude are not the only factor affecting atmospheric chemistry. With a change in latitude may come a change in temperature or tropospheric height,

which may act to compound the effects on $\Delta^{17}O$ and $\delta^{18}O$. Here however, our effort is to isolate the effects that individual factors have on the oxygen isotope composition of different species. We speculate (though beyond the scope of this thesis) that if combined, the effects of latitude, rainfall and temperature, as well as $\delta^{18}O_{H2O}$, would magnify and account for variations in the data, and intend to explore this in future work.

5.4.5.4 – Case 10: Investigating sensitivity to the isotopic composition of H_2O

The isotopic composition of H_2O is affected when tropospheric $\delta^{17}O_{H2O}$ and $\delta^{18}O_{H2O}$ values of -9.1872‰ and -17.4‰, respectively, are set (Case 10a; not shown in figure). The $\delta^{18}O$ values decrease, not only in the troposphere, but throughout the atmospheric column. The profiles of OH, HO_2 and H_2O_2 (which are closely-related to H_2O), and H_2SO_4 and SO_4 are also affected. The latter two species are only produced by one reaction with reactant H_2O, so their $\delta^{18}O$ profiles are highly influenced by the change implemented here. Despite the effects on $\delta^{18}O$ and $\delta^{17}O$, the $\Delta^{17}O$ profiles are negligibly affected.

For Case 10b, with the adaptation to the $\alpha_{exch.}$ value to simulate CO_2-H_2O exchange in the CO_2 fluxes (Eqs. 5-8 and 5-9), the variation of H_2O isotopic composition by 30‰ produces an identical shift in $\delta^{18}O$ values in tropospheric CO_2, with smaller shifts in the $\delta^{18}O$ of SO_4 and NO_3 (Figures 5-7 and 5-8). However, it has very little effect on the $\Delta^{17}O_{CO2}$ profile (Figure 5-6), though the higher H_2O $\delta^{18}O$ and $\delta^{17}O$ values result in marginally lower $\Delta^{17}O$ values. Tropospheric CO_2 measured in La Jolla, California (Thiemens et al., 2014) exhibited $\delta^{18}O$ values of around 40‰, which, for Case 10b, correspond to a tropospheric H_2O $\delta^{18}O$ value of between 0 and -10‰. It is possible that this is close to the isotopic composition of water vapour at this site, since it is close to the Pacific Ocean and coastal areas tend to have higher $\delta^{18}O_{H2O}$. However, further work of comparison of tropospheric $\delta^{18}O_{CO2}$ and $\delta^{18}O_{H2O}$ ought to be done to test the correlation that the model predicts, and therefore authenticate the way in which we have linked the CO_2 into-the-atmosphere flux with the chosen H_2O isotopic composition.

5.4.5.5 – Case 11: Investigating sensitivity to eddy diffusion coefficient profile

The results of the eddy diffusion profile sensitivity test are shown in Figure 5-11. Higher eddy diffusion causes the isotopically 'normal' tropospheric H_2O signal to propagate further into the stratosphere, compared to the base model or the low eddy diffusion case. This reduces the magnitude of $\Delta^{17}O_{H2O}$ higher in the atmosphere. It also affects the $\Delta^{17}O$ of SO_4, but in this species it battles with the effect of an increased stratospheric signal into the troposphere, resulting in higher tropospheric $\Delta^{17}O$ with faster vertical transport.

The vertical profiles of O_2, O_3 and CO_2 become more uniform with respect to $\Delta^{17}O$ with increased eddy diffusion coefficient, because any peaks and minima in $\Delta^{17}O$ are ironed out by increased mixing. For O_2, the tropospheric $\Delta^{17}O$ decreases by more than 0.1‰ with a tenfold increase in eddy diffusion coefficient. For CO_2, a decreased eddy diffusion coefficient increases the troposphere-stratosphere difference in $\Delta^{17}O_{CO2}$. This is an effect also observed in the model of Yung et al. (1997), who tested the sensitivity of the $\Delta^{17}O_{CO2}$ profile to a twofold variation in vertical transport in their 1-D model.

5.4.5.6 – Case 12: Investigating the sensitivity to tropopause height

The $\Delta^{17}O$ profiles (not shown) show that the change in tropospheric height has a negligible effect on most species, other than H_2O and SO_4. The former is affected because the troposphere, in which the $\Delta^{17}O$ is held at a constant 0‰, extends further into the atmosphere, resulting in smaller $\Delta^{17}O$ in the stratosphere. This affects the latter, as $\Delta^{17}O_{SO4}$ is closely dependent on $\Delta^{17}O_{H2O}$. No other species have been affected by this change.

This may seem unusual, as it might be assumed that the height of the tropopause would have more of an effect on lots of species. After all, the physics and chemistry of the troposphere are very different to that of the stratosphere. However, in reality this is due to additional differences, especially temperature structure differences, which we have kept the same for the three Case 12 models. In fact, the only

difference that a change in the model tropospheric height has is that of the vertical extent of the zero O-MIF H_2O profile, and the altitude over which rainfall occurs. It therefore makes sense that the only species affected are H_2O and the closely-related SO_4. Therefore, in order to better test the sensitivity to tropopause height, future tests should co-vary this with self-consistent temperature and eddy diffusion profiles.

Our experiments in Cases 7-12 have shown that our model is sensitive to changes in rainfall, temperature, latitude, $\delta^{18}O_{H2O}$ and vertical transport in a way expected from global oxygen isotope observations. However, a key target for future work would be to expand beyond 'one-at-a-time' analysis and investigate simultaneous co-variation of these effects in a Monte-Carlo scheme.

5.4.6 – Case 13: Variation of α_{MIF}

Thus far, we have used a value for α_{MIF} of 1.065, from Young et al. (2014). Here, we present the sensitivity of the model results to the choice of value for α_{MIF}, and the inclusion of variation of the fractionation factors between isotopologues, with or without additional temperature- and pressure-dependencies.

5.4.6.1 – Case 13a: Varying magnitude of α_{MIF}

The grey shading in Figure 5-12 shows the range in $\Delta^{17}O$ value with altitude resulting from an increase in α_{MIF} value from 1.065 to 1.1 (Case 13a). As expected, the magnitude of the O-MIF signal, whether positive or negative, increases with increased fractionation factor. An increase in α_{MIF} of 35‰ produces an increase in $\Delta^{17}O_{O3}$ of 16.5‰, and a decrease in $\Delta^{17}O_{O2}$ of 0.055‰. From these results in comparison to atmospheric ozone measurements, fractionation factors greater than 1.09 seem to be too large to predict the right magnitudes of $\Delta^{17}O_{O3}$ (at least for this case, when the same α_{MIF} is used for both P-bearing and Q-bearing species at all altitudes).

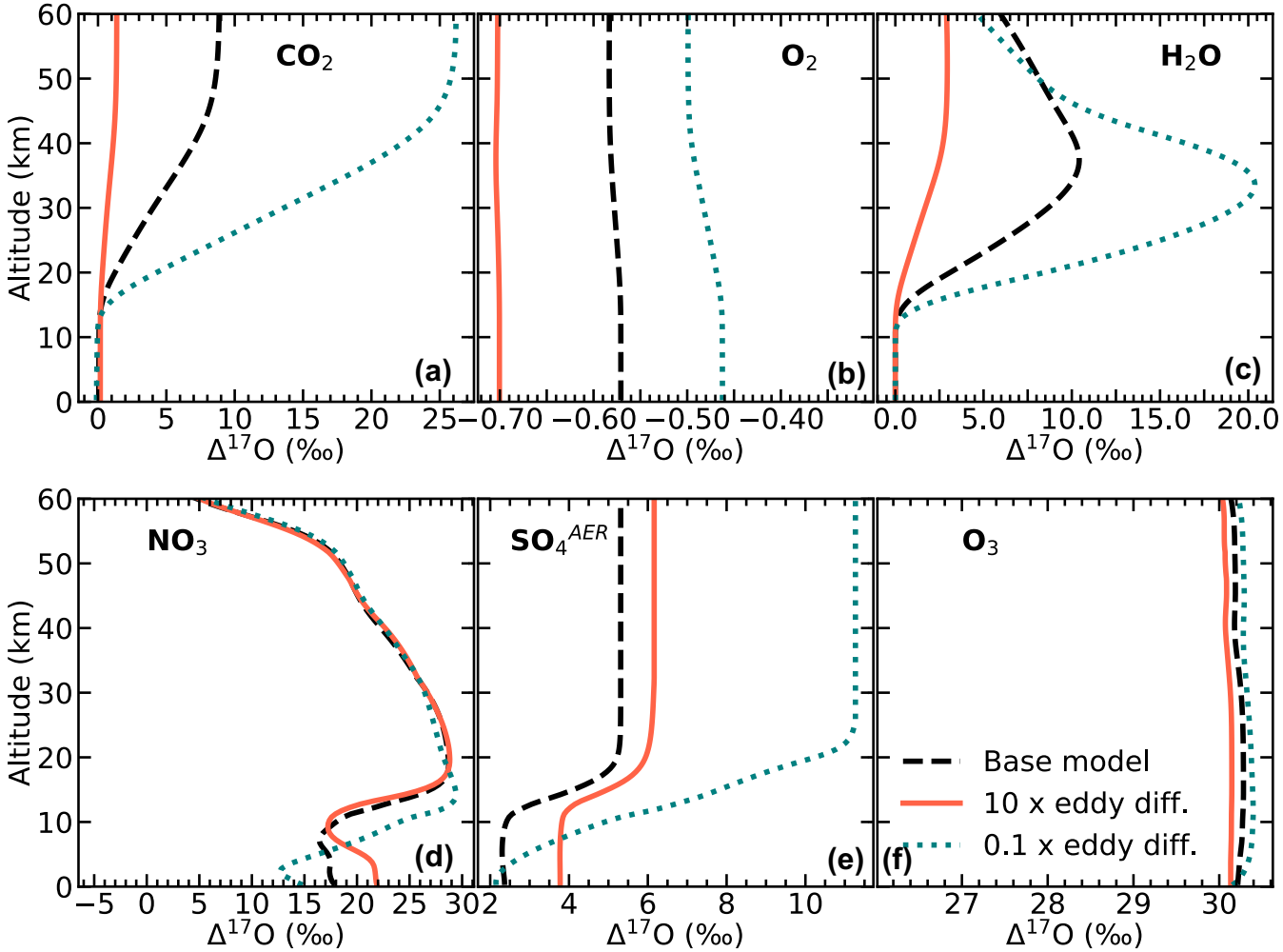

Figure 5-11: Profiles of $\Delta^{17}O$, $\delta^{17}O$ and $\delta^{18}O$ for Case 11, including i) the base model (Case 6; black dashed line); ii) a case with the eddy diffusion greater by a factor of 10 (orange solid line); iii) a case with the eddy diffusion coefficient smaller by a factor of 10 (teal dotted line).

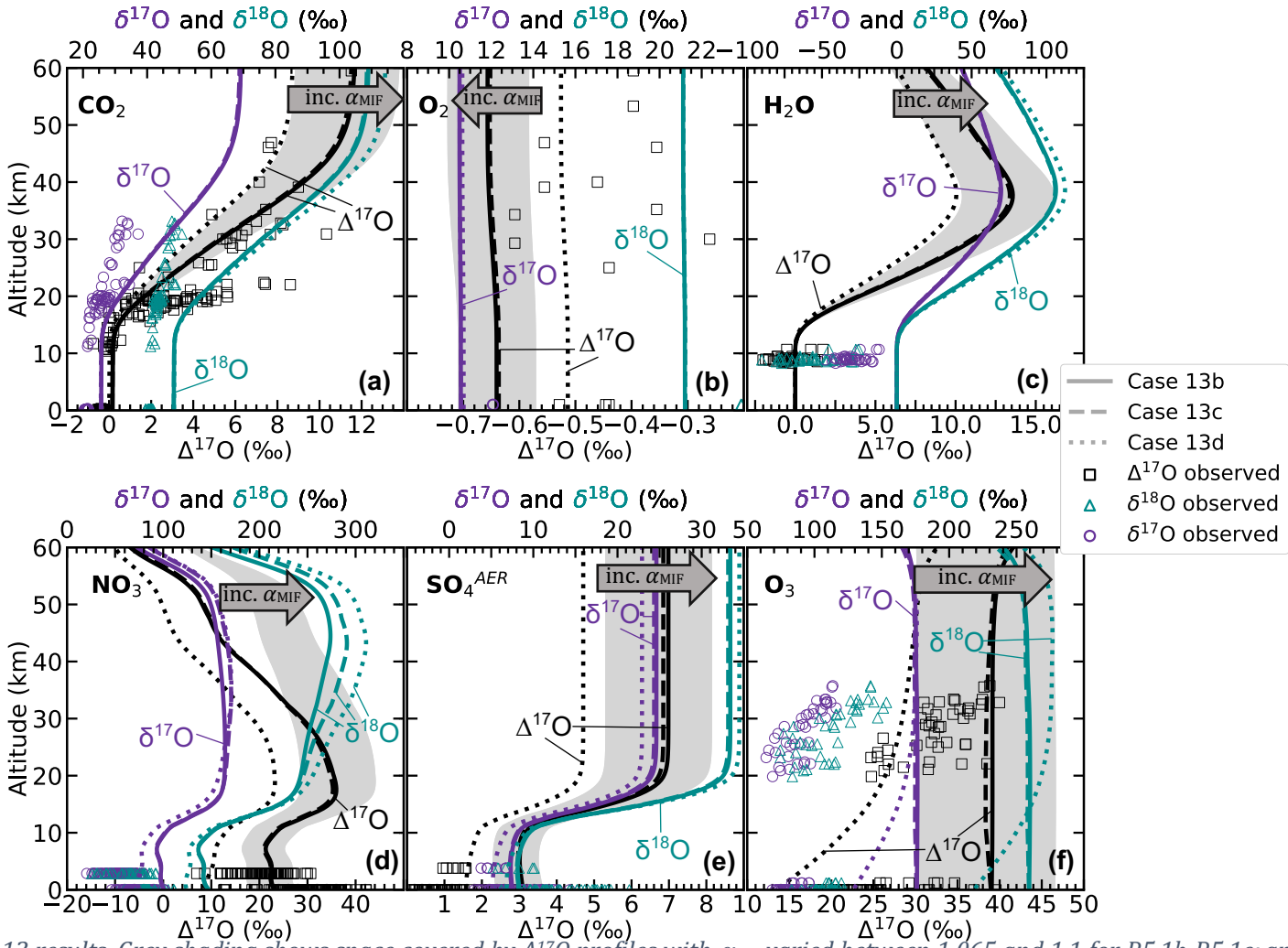

Figure 5-12: Case 13 results. Grey shading shows space covered by $\Delta^{17}O$ profiles with α_{MIF} varied between 1.065 and 1.1 for R5.1b-R5.1e; grey arrow shows direction of increasing α_{MIF} (Case 13a). Lines show profiles of $\delta^{17}O$, $\delta^{18}O$ and $\Delta^{17}O$ for selected species, for Case 13b-13d models, in which α_{MIF} is varied for each of the four isotopically-substituted ozone-forming reactions. Note the different scales for the upper and lower x axes.

5.4.6.2 – Case 13b: Initial incorporation of variation of α_{MIF} between different ozone-isotopologue-forming reactions

The large measured fractionation factors, varying between the four ozone-forming reactions (Case 13b; Table 5-4), compared to the fractionation factor of 1.065 from Young et al. (2014; Cases 0-12), result in large $\delta^{17}O$ and $\delta^{18}O$ throughout the atmospheric column for O, O_3 (Figure 5-12) and $O(^1D)$ (not shown). There are large enrichments in $\delta^{17}O$ and $\delta^{18}O$ for many other species, including OH, HO_2, H_2O_2 (not shown), H_2O, N-bearing species and SO_x species, especially in the stratosphere. However, in many cases, the model now overestimates $\delta^{17}O$ and $\delta^{18}O$ compared to atmospheric measurements.

Since the magnitude of the α_{MIF} values on average has increased compared to those in previous cases, the $\Delta^{17}O$ in the atmospheric profiles is also greater. $\Delta^{17}O_{O3}$ for the troposphere and stratosphere has increased by almost 10‰, predicting $\Delta^{17}O$ values at the upper limit of the observations. This results in $\Delta^{17}O_{O(1D)}$ of a similar magnitude and large negative $\Delta^{17}O_O$ values (not shown). Stratospheric CO_2, H_2O and H_2O_2 (not shown) $\Delta^{17}O$ values increase, as do $\Delta^{17}O_{SO4}$ values throughout the whole atmospheric column, with ground-level predictions now at the upper end of the field of measurements for the latter. $\Delta^{17}O_{NO3}$ values in the troposphere and lower stratosphere also increase. The magnitude of the negative $\Delta^{17}O_{O2}$ values is increased slightly, though by less than 0.1‰.

While the $\Delta^{17}O$ values in general continue to fit fairly well with the atmospheric measurements, the $\delta^{17}O$ and $\delta^{18}O$ values of the species are quite different, with larger fractionations than observed for many species. Since our primary aim is to reproduce and predict $\Delta^{17}O$ rather than $\delta^{17}O$ and $\delta^{18}O$, this is of secondary importance, but it is possible that i) the fractionation factors are too large or; ii) other fractionation factors involved in the production and destruction of ozone are required. Since the fractionation factors have been measured and used for the last twenty years (Janssen et al., 2003; Mauersberger et al., 1999; Wiegel et al., 2013), it is unlikely that the former is the problem. We show later in this chapter (Cases 15-

17) that exchange reactions acting to reduce the large MDFs caused by our inclusion of these big fractionation factors should be incorporated.

5.4.6.3 – Case 13c: Investigating the T-dependence of α_{MIF}

The $\delta^{17}O$ and $\delta^{18}O$ profiles (not shown) for most species are not greatly affected by the addition of α_{MIF} temperature-dependence compared to Case 13b. However, $\delta^{17}O$ and $\delta^{18}O$ for O increase at the percent level, with a peak around the tropopause and lower stratosphere. Since this is the coolest point in the atmospheric profile (apart from at altitudes greater than 70 km), and the strongest temperature-dependencies are for reactions R5.1c and R5.1e where heavy isotopes of O are the reactants, this difference can be explained by significantly slower rates of P and Q consumption relative to O-consumption in R5.1b and R5.1d, compared to Case 13b.

The difference that the temperature-dependent term makes to $\Delta^{17}O$ profiles is also not large, but can be seen in Figure 5-12. The most obvious differences in $\Delta^{17}O$ between Cases 13b and 13c are in the upper troposphere and lower stratosphere (and at the top of the model atmosphere above ~70 km, not shown), where the temperatures are much cooler than 300 K. At temperatures closer to 300 K, the differences are greatly reduced.

Here, we therefore show that the temperature-dependence has little effect on model $\Delta^{17}O$ profiles. However, since there has been shown to be a temperature-dependence in the O-MIF-producing reaction, and our model is capable of varying reaction rates with altitude in a temperature-dependent manner, we will implement this in our final model, along with the variable α_{MIF} values introduced for Case 13b.

5.4.6.4 – Case 13d: Investigating the pressure-dependence of α_{MIF}

Figure 5-13 shows the fractionations imparted to ozone by the variation of the rates of our reactions R5.1b and R5.1d with pressure (in Pa) for the range of pressures in our vertical column, in order to better visualise what the relationship between pressure (and therefore altitude) and α_{MIF} look like for Case 13d. At low pressures, higher in the atmosphere, α_{MIF} approaches the value used in Case 13b. At higher

pressures, lower in the atmosphere, the fractionation factor decreases. As a result, the fractionations generated in Case 13d in general are lower than those produced in Cases 13b and 13c.

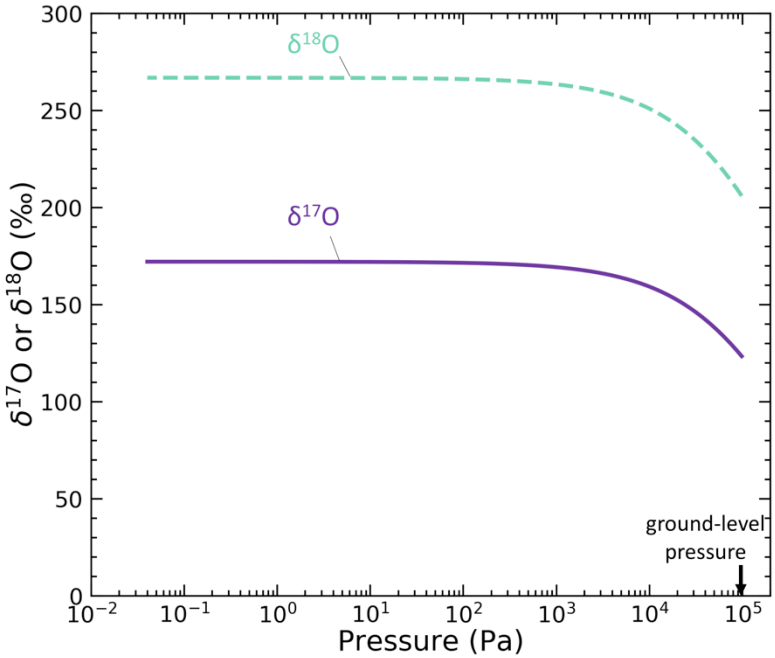

Figure 5-13: Relationship between pressure and fractionation factor in ^{17}O and ^{18}O for the pressure-dependent Case 13d.

The profiles of isotopic composition with altitude show that the pressure-dependence causes a greater variation in $\delta^{17}O$, $\delta^{18}O$ and $\Delta^{17}O$ for ozone with altitude than in Cases 13b and 13c (Figure 5-12). Higher pressure nearer the Earth's surface results in lower values than higher in the atmosphere. This results in a decrease in the difference in the $\Delta^{17}O$ values of ozone throughout the atmospheric column, especially lower in the atmosphere. The $\Delta^{17}O$ profile increases by more than 0.1‰ for O_2 and decreases by nearly 3‰ in stratospheric CO_2. There are also large decreases in $\Delta^{17}O$ throughout the atmospheric column for NO_3 and SO_4.

The addition of pressure-dependence improves the model predictions to some extent. It satisfies the expectation (e.g. Lyons, 2001) and constraints from measurements that stratospheric $\Delta^{17}O_{O3}$ should be higher than tropospheric $\Delta^{17}O_{O3}$, and reproduces stratospheric ozone measurements fairly well. Tropospheric $\Delta^{17}O$

predictions for O_2, SO_4 and, to a lesser extent, CO_2 move closer to the ground-level measurements, as do predictions for tropospheric $\delta^{17}O_{SO4}$ and $\delta^{17}O_{NO3}$. However, the model underestimates tropospheric $\Delta^{17}O_{O3}$ and $\Delta^{17}O_{NO3}$. It continues to underestimate $\delta^{17}O_{O2}$ and $\delta^{18}O_{O2}$ and continues to overestimate $\delta^{17}O_{O3}$ and $\delta^{18}O_{O3}$ throughout the atmospheric column, and tropospheric $\delta^{17}O_{CO2}$ and $\delta^{18}O_{CO2}$.

Drawing the results from Cases 13a-13d together, we have shown that including the experimentally-determined fractionation factors in our final model is important as they allow a more detailed simulation of the modern atmosphere and enable the model to reproduce stratospheric $\Delta^{17}O_{O3}$ and atmospheric $\Delta^{17}O_{O2}$ well. However, further tuning and development of the model from Case 13d is required to better match the existing data. In particular:

i) For CO_2, the $\delta^{17}O$ and $\delta^{18}O$ values seem to be too high by around 5‰, compared to the data, throughout the atmospheric column. The tropospheric $\Delta^{17}O$ values are also slightly higher in the model.

ii) Inclusion of the T- and P-dependence of the α_{MIF} values seems to be important, since the rates are supported by evidence in the literature, and inclusion of them improves the simulation of $\Delta^{17}O_{O2}$ and stratospheric $\Delta^{17}O_{O3}$, as well as $\delta^{17}O_{NO3}$ and $\delta^{18}O_{NO3}$ to a lesser extent. However, without the pressure-dependent terms, the model does a better job at predicting tropospheric $\Delta^{17}O_{NO3}$, whereas with them the predictions are at the lower end of the observations.

iii) Stratospheric $\Delta^{17}O_{O3}$ is well-predicted by the model, but tropospheric $\Delta^{17}O_{O3}$ is much lower than observations. In all cases, $\delta^{17}O_{O3}$ and $\delta^{18}O_{O3}$ predictions are higher than observations.

We therefore present the results of a few last additions to the model, whose inclusion allow the model to better reproduce modern measurements.

5.4.7 – Case 14: Tuning fractionations in CO_2 flux

For Case 13d, the $\delta^{17}O$ and $\delta^{18}O$ values are higher than observations throughout the atmospheric profile by several permil. This can be accounted for, as shown in Case 10, by a variation in the isotopic composition of the source water. A variation in $\delta^{18}O_{H2O}$ results in a model variation in $\delta^{18}O_{CO2}$ by around the same amount, according to our assumptions. The difference is therefore not greater than our uncertainty in the effects of isotopic composition of water on that of CO_2. If the observations (shown as points on Figure 5-12a) were from the same location, it might be feasible to find an average $\delta^{18}O_{H2O}$ for the local region and adjust the model to incorporate this. However, the observational CO_2 isotope data for the troposphere and lower stratosphere is from a wide range of locations globally (Liang et al., 2017; Thiemens et al., 2014; Wiegel et al., 2013), where a wide range in isotopic composition of source water would be expected. Furthermore, Young et al. (2014) estimate the global average source water oxygen isotope composition as 5.25‰, which is what we have thus far included in the model to account for global isotopic variations.

Nevertheless, despite the use of the global average, we continue to overestimate both $\delta^{17}O$ and $\delta^{18}O$, and $\Delta^{17}O$ to a lesser extent. The isotopic composition of tropospheric CO_2 is highly sensitive to the isotopic composition of the lower boundary CO_2 flux, so for Case 14 we therefore adjust the COP and COQ fluxes such that they reproduce the observations from the literature. We neglect the $\alpha_{evap.}^{0.52}$ and $\alpha_{evap.}$ terms in Eqs. 5-4 and 5-5 and use a value for β of 0.523 (rather than 0.528) for respiration in Eq. 5-4, which is within the range measured or used in existing literature for this process, such that the COP and COQ fluxes are:

$$\text{COP flux} = CO_2 \text{ flux} \times {}^{17}R_0 \times n_{oxy} \times 1.041^{0.523} \qquad \textit{(Eq. 5-10)}$$

$$\text{COQ flux} = CO_2 \text{ flux} \times {}^{18}R_0 \times n_{oxy} \times 1.041 \qquad \textit{(Eq. 5-11)}$$

This better reproduces the tropospheric observations (Case 14; see Figure 5-14). The adjustment of β for the CO_2 boundary flux slightly decreases the resultant $\Delta^{17}O$

such that the model values lie at the upper end of the ground-level observations. The $\delta^{17}O$, $\delta^{18}O$ and $\Delta^{17}O$ values of the other selected species are not affected by this change.

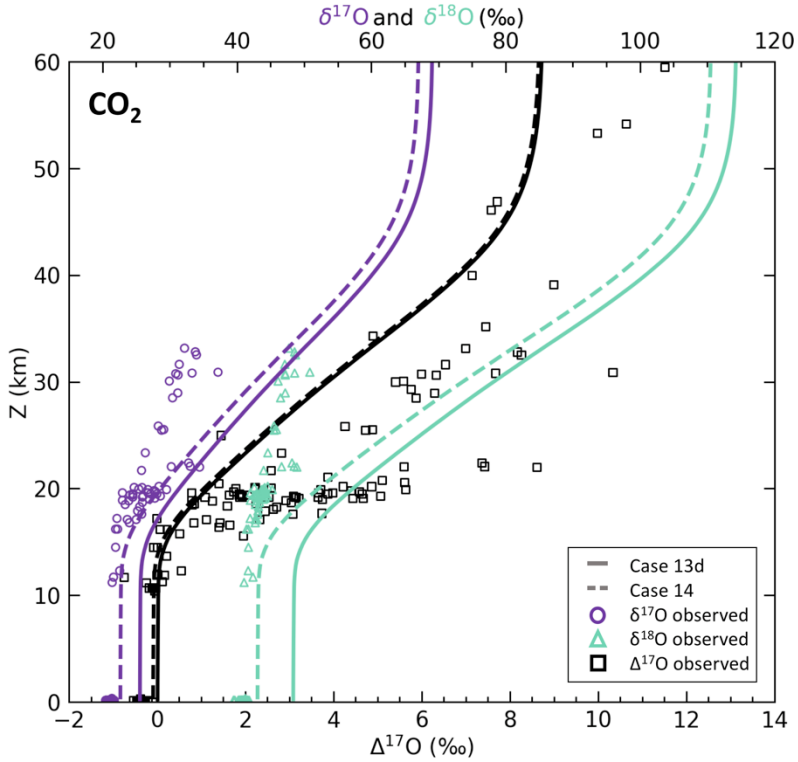

Figure 5-14: $\delta^{17}O$, $\delta^{18}O$ and $\Delta^{17}O$ profiles of CO_2 for Cases 13d and 14. The difference between the cases is a slight change in the COP and COQ fluxes.

5.4.8 – Cases 15-17: Tuning through exchange reactions

As we noted in Section 5.4.3, there is a slight difference between the model-predicted atmospheres using Methods 1 and 2 for the branching ratios of the reactions, predominantly due to the lack of exchange in the reaction $O(^1D) + O_2 \rightarrow O + O_2$ and its isotopic equivalents with Method 2. The model with isotopic exchange included for this reaction (Case 15) is shown by the dashed line in Figure 5-15, with comparison to Case 14. As noted for Case 3a, isotopic exchange via this reaction reduces $\Delta^{17}O_{O3}$ by a few permil in the stratosphere, which affects stratospheric H_2O, CO_2 and NO_3 in the same way. The magnitude of the $\Delta^{17}O$ values of O_2 throughout the whole atmospheric column is decreased by less than 0.1‰.

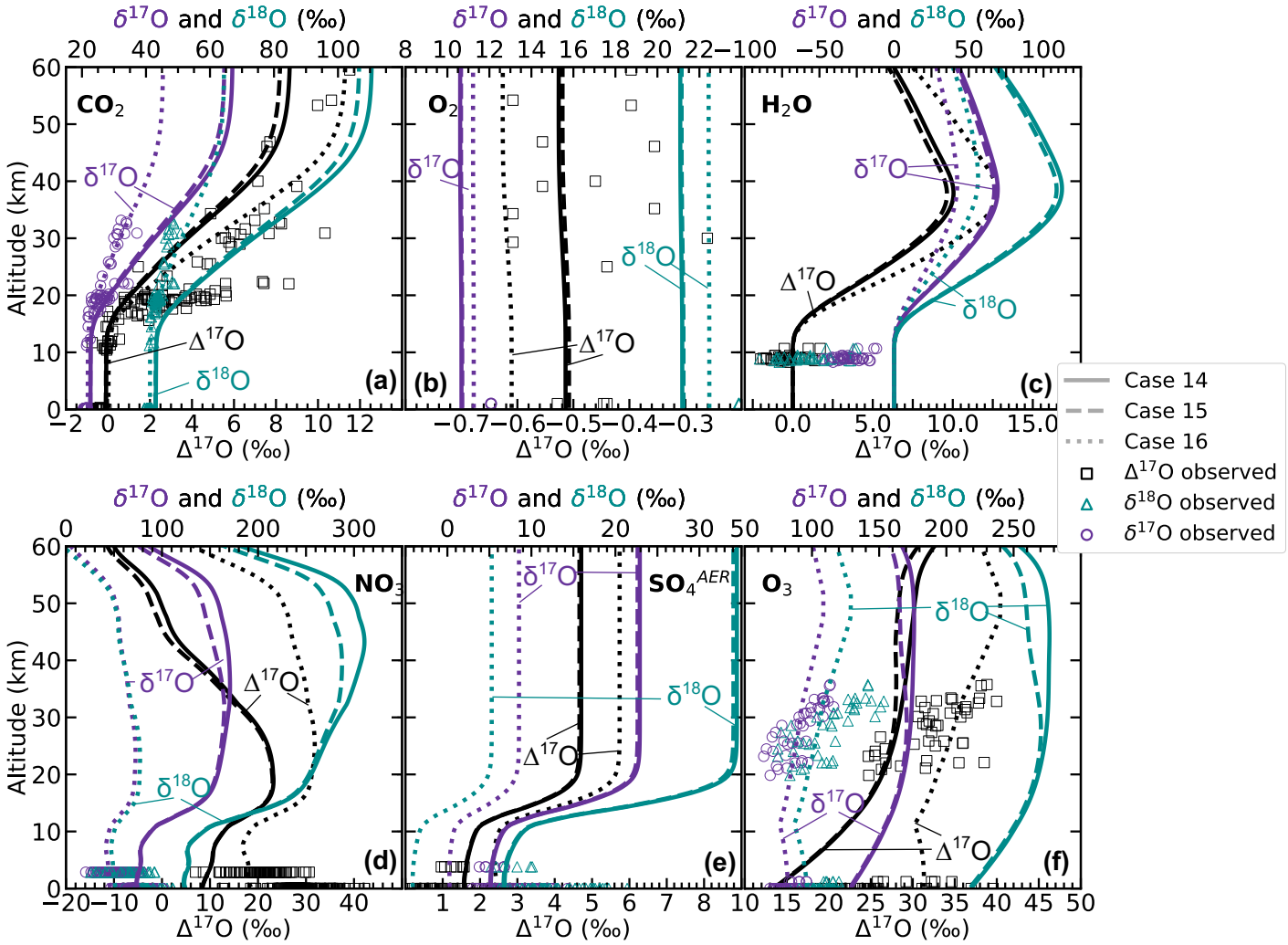

Figure 5-15: Profiles of $\delta^{17}O$, $\delta^{18}O$ and $\Delta^{17}O$ for selected species for Cases 14, 15 and 16. Case 15 includes isotope exchange via isotopically-substituted reactions of $O(^1D) + O_2 \rightarrow O + O_2$, and Case 16 includes additional exchange through isotopically-substituted reactions of $O + O_2 \rightarrow O + O_2$.

Inclusion of the isotope exchange reaction between atomic oxygen and O_2 (Case 16; Figure 5-15) has a bigger effect, allowing our model to match ozone $\delta^{17}O$, $\delta^{18}O$ and $\Delta^{17}O$ measurements much more closely in the troposphere and stratosphere. The $\delta^{17}O$, $\delta^{18}O$ and $\Delta^{17}O$ profiles for O_3, O_2 and CO_2 (the species we are particularly interested in for our work in Chapter 6) are also predicted well by this model. For O_2, the $\delta^{17}O$ and $\delta^{18}O$ values become slightly less negative, resulting in $\Delta^{17}O$ values at the lower end of atmospheric observations; for CO_2, the stratospheric profiles of $\delta^{17}O$ and $\delta^{18}O$ steepen (showing less change in $\delta^{x}O$ with a change in altitude), while the opposite is true of stratospheric $\Delta^{17}O_{CO2}$. Potential slight improvements to the Case 16 model to better match observations would be a small reduction in the $\Delta^{17}O$ of ground-level CO_2 and a small increase in the $\Delta^{17}O$ of ground-level O_2.

In order to address these two areas for improvement, we include isotope exchange reactions between O_2 and CO_2 (Case 17), as a way of incorporating the effects of exchange reactions between CO_2 and excited-state oxygen species (Wiegel et al., 2013). Figure 5-16 shows the results of the inclusion of these reactions on CO_2 and O_2 oxygen isotope profiles. For CO_2, the values of $\delta^{17}O$, $\delta^{18}O$ and $\Delta^{17}O$ decrease slightly, while the $\delta^{17}O$, $\delta^{18}O$ and $\Delta^{17}O$ values for O_2 increase slightly. For CO_2, the predictions fit the observations just as well as in Case 16, but the inclusion of the O_2/CO_2 reactions improves the predictions for O_2. There is little change to the oxygen isotope compositions of H_2O, NO_3, SO_4 and O_3 (not shown). We therefore demonstrate that this exchange process improves the model prediction of atmospheric measurements, and include it in our final model.

5.5 – New 'base model' description for Chapter 6

In Chapter 6, we explore the effects on $\Delta^{17}O$ signatures of variations in pCO_2 and pO_2. There, we use as a new 'base model' the Case 17 model developed in this chapter and shown in Figure 5-16. To summarise, as well as the reactions and features described for Case 6, we choose to include pressure- and temperature-dependent mass-independent fractionation factors for the ozone-forming reactions (as added for Case 13), the COP and COQ fluxes adapted for Case 14, and the exchange

reactions included for Cases 15-17. We choose to use these features because they are justified by the literature, and predict $\Delta^{17}O$ values with altitude that reproduce observations, for the most part. Further discussion of some of the assumptions made will be done in Chapter 6, particularly regarding the inclusion of the O_2/CO_2 exchange reactions.

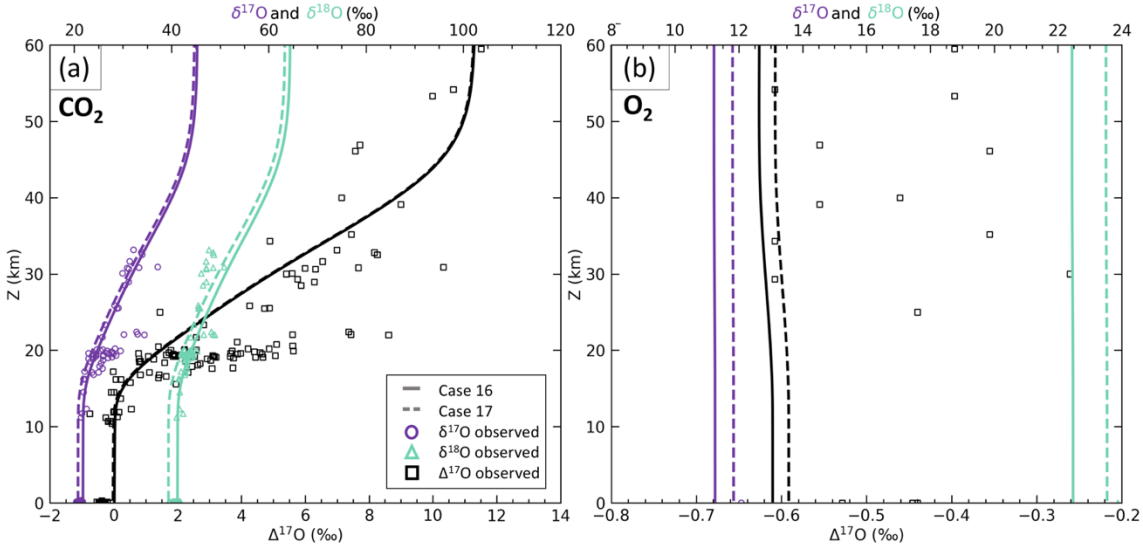

*Figure 5-16: $\delta^{17}O$, $\delta^{18}O$ and $\Delta^{17}O$ profiles for **(a)** CO_2 and **(b)** O_2 for Cases 16 and 17. Case 17 includes the exchange reactions for $O_2 + CO_2 \rightarrow O_2 + CO_2$.*

5.5.1 – A note on sulphate predictions

Atmospheric sulphate is not predicted particularly well by the model, since ground-level $\Delta^{17}O$ is overestimated and $\delta^{17}O$ and $\delta^{18}O$ are underestimated compared to observations. One reason for the poor predictions of tropospheric sulphate could be the lack of some sulphate-producing reactions. Currently, the only source of sulphate in the model is condensation of H_2SO_4, which is only formed by the reaction of SO_3 with H_2O. The production of sulphate via heterogeneous oxidation by isotopically-anomalous O_3 and H_2O_2 are neglected. This might explain the underestimation of $\delta^{17}O$ and $\delta^{18}O$, but does not necessarily explain the overestimation of $\Delta^{17}O$ by the model. Inclusion of these reactions will be important for the accurate prediction of triple oxygen isotopes in atmospheric sulphates, which has applications for both the modern and past atmospheres. However, in

Chapter 6 we are primarily interested in the oxygen isotope compositions of CO_2 and O_2. The sulphate we predominantly consider in Chapter 6 is sedimentary sulphate that incorporates the atmospheric O_2 signal via oxidative weathering, as opposed to the sulphate particles that form directly in the atmosphere and are considered in this chapter, so we will leave the improvement of the prediction of the latter for future work.

5.5.2 – A note on model uncertainties

Model uncertainties come from several sources. While atmospheric reaction rates are fairly well constrained, there remains some uncertainty (see, e.g. quantified uncertainty in data tables of Burkholder et al. (2015)). As discussed in this chapter, some uncertainty has been introduced when we have included features in the model, e.g. in the isotopic composition of CO_2 fluxes into the atmosphere, and in the relationship between $\delta^{18}O_{CO2}$ and $\delta^{18}O_{H2O}$. As well as investigating the effects of co-variation of environmental variables, as suggested at the end of Section 5.4.5, it would be instructive in future work to use a Monte-Carlo approach to investigate the combined uncertainty of our assumptions.

5.6 – Conclusions

Here, we have developed the initial oxygen isotope photochemical model described in Chapter 4, to better reproduce modern measurements of atmospheric and deposited species. We have shown the model's dependence on a wide range of simulated processes, which demonstrates that our parametrisation of the processes and our assumptions are acceptable and result in a model atmosphere producing output close to triple oxygen isotope atmospheric observations. We have also shown the sensitivity of the model to environmental variables, demonstrating that our model output varies with rainfall, temperature, latitude, $\delta^{18}O_{H2O}$ and vertical mixing as expected. We will use the final model presented here (Case 17) as a new 'base model' for our varying-pO_2/pCO_2 model suites in Chapter 6, with applications to early-Earth atmospheres.

Chapter 6

Model-predicted $\Delta^{17}O$ of atmospheric O_2 at various pO_2 and pCO_2, and implications for $\Delta^{17}O$ of sulphate in the geological record

Abstract

The $\Delta^{17}O$ value of tropospheric O_2 can be preserved in sulphates in the geological record, and its magnitude is affected by pCO_2, pO_2 and gross primary productivity (GPP). Here, we use the 1-D oxygen isotope photochemical model developed in Chapters 4 and 5 of this thesis, to investigate the sensitivity of the $\Delta^{17}O$ values of key species to these factors, with a particular focus on the negative O-MIF signal in O_2. We find that the model-predicted $\Delta^{17}O_{O2}$ values decrease as expected with increasing pCO_2 or decreasing pO_2/GPP. We use model results with coupled variations in pCO_2 and pO_2/GPP to consider specific minima in observed $\Delta^{17}O_{SO4}$ during the Cryogenian period and in the mid-Proterozoic, in terms of palaeo-atmospheric composition.

This chapter is in preparation as a journal article with the author list: B Gregory, M. Claire, S. Rugheimer.

6.1 – Introduction

The triple oxygen isotope composition of tropospheric oxygen ($\Delta^{17}O_{O2}$) has been shown to be influenced by several factors. A mass-independent fractionation is imparted to stratospheric O_2 when ozone is formed, which, through troposphere-stratosphere mixing can affect the $\Delta^{17}O$ value of O_2 lower in the atmosphere (Luz et al., 1999). This effect has been shown to be exacerbated by an increase in

atmospheric CO_2, since CO_2 can inherit the large, positive $\Delta^{17}O$ from ozone formation through the photolysis product $O(^1D)$, leaving the O_x-O_2 system relatively more depleted in $\Delta^{17}O$ (Yung et al., 1997; Figure 1-5a).

However, the observed $\Delta^{17}O$ value of tropospheric O_2 is also influenced by mass-dependent processes at the Earth's surface. Biological respiration consumes oxygen while oxygenic photosynthesis replaces it with mass-dependently fractionated O_2. Despite the absence of mass-independent fractionation in these processes, small differences in the fractionation slope can produce a non-zero $\Delta^{17}O$, depending on the chosen definition of $\Delta^{17}O$ with respect to $\delta^{17}O$ and $\delta^{18}O$. This can contribute significantly to observed non-zero $\Delta^{17}O$ values in tropospheric O_2 (Young et al., 2014).

It has therefore been shown that the primary three factors influencing the $\Delta^{17}O$ value of tropospheric O_2 are gross primary productivity (GPP), pCO_2 and pO_2 (illustrated in Figure 1-5). All else being equal, an increased GPP acts to dilute the stratospheric non-zero $\Delta^{17}O$ signal in tropospheric O_2 (although mass-dependent O_2 fluxes may impart a small non-zero $\Delta^{17}O$ value on tropospheric O_2; Blunier et al., 2002; Luz et al., 1999; Young et al., 2014). An increase in pCO_2 increases the rate at which isotopically-heavy $O(^1D)$ from ozone photolysis exchanges with CO_2, leaving the O_2 and O_3 reservoir increasingly depleted in heavy isotopes, so acts to increase the magnitude of the negative atmospheric $\Delta^{17}O_{O2}$ (Yung et al., 2002). An increase in pO_2, all else being equal, would increase the rate of $O(^1D)$ and O recombination with O_2 to produce O_3, allowing for less removal of heavy isotopes from the O_x-O_2 network. This results in a less negative tropospheric $\Delta^{17}O_{O2}$.

Tropospheric $\Delta^{17}O_{O2}$ can be captured in sulphate through oxidative weathering of sulphides, and preserved stably in the geological record (e.g. Bao, 2015). Observations of particularly negative $\Delta^{17}O$ values in geological sulphate have been observed for certain intervals over the Phanerozoic and Proterozoic, and presented as a proxy for atmospheric composition. Please note that, while our model predicts positive $\Delta^{17}O$ values for sulphates produced in the atmosphere via our kinetic

reaction network (presented in Chapter 5 and in Figures 6-2e and 6-5e), it is the sulphates that inherit the negative $\Delta^{17}O$ values of O_2 in which we are most interested in this chapter. The isotopic composition of these sulphates is not directly predicted by our model, but can be calculated from that of O_2.

Bao et al. (2008) observed particularly negative $\Delta^{17}O$ in carbonate associated sulphates (CAS) in cap carbonates deposited above glacial diamictites linked to the proposed Marinoan Snowball Earth. They interpreted the large negative $\Delta^{17}O$ values as evidence for large atmospheric pCO_2, caused by an accumulation of volcanic CO_2 throughout the Snowball Earth period, which acted as a negative feedback to warm the Earth and reverse the glaciation (Hoffmann et al., 1998; Pierrehumbert, 2004). Another sedimentary succession of particular interest is that of the Sibley Basin in Canada, where particularly low $\Delta^{17}O$ in sulphates have been interpreted by Crockford et al. (2018) and Planavsky et al. (2020) as evidence for low primary productivity and low atmospheric O_2 respectively, for at least some parts of the Proterozoic. In addition, Crockford et al. (2019) synthesised $\Delta^{17}O_{SO4}$ records for the last 3 Gyr, and used these, along with estimates of pCO_2 and pO_2 to predict GPP since the record began, with a particular focus on the Proterozoic. As discussed in Chapter 1, many of these interpretations arise from significant extrapolations from simple models of atmospheric chemistry of oxygen isotopes.

Here, we systematically vary pCO_2 and pO_2/GPP in our 1-D oxygen isotope photochemical model to predict the $\Delta^{17}O$ values of atmospheric species, particularly focussing on O_2, with some attention to CO_2 and O_3.

6.2 – Methods

We use the oxygen isotope photochemical model developed for this thesis, as described in Chapters 4 and 5. The model includes 97 species involved in 932 reactions, including isotopically-substituted oxygen-bearing species (Tables B-2 and C-1 in Appendices B and C, respectively), and all model runs presented are steady-state solutions.

The model inputs and boundary conditions are described in Section 5.5 (Case 17). O_2 and CO_2 have large incoming and outgoing fluxes across the lower boundary, representative of short-timescale GPP. Flux boundary conditions are given for H_2, CO and N_2O, as described in Section 5.3.2 and Table 5-1 (Case 2 onwards). Mass-dependent fractionations are incorporated in the model through i) the fluxes of O_2 into and out of the model atmosphere; ii) the flux of CO_2 into the model atmosphere; and iii) via all two-body and three-body reactions. For the latter, the reaction rates are adjusted to account for different collisional frequencies between reactants with different isotopes. A mass-independent fractionation in the reactions that form atmospheric ozone is included, which is temperature-, pressure-, and product isotopologue-dependent. Rapid isotopic exchange reactions between $O(^1D)/O$ and CO_2, $O(^1D)/O$ and O_2, and O_2 and CO_2 are included as described in Chapter 5.

6.3 – Results

We use the model to investigate the way in which the $\Delta^{17}O$ values of six key species (CO_2, O_2, H_2O, NO_3, SO_4 and O_3, with a particular focus on O_2 and CO_2) are affected by changes in pCO_2 and pO_2/GPP. First, the model outputs are examined with respect to independent changes in pCO_2, and then pO_2, while keeping all others fixed. We continue by exploring the effects of coupled changes in pCO_2 and pO_2.

6.3.1 – Case 1: Increasing pCO_2 results

We assess the effects on the model output $\Delta^{17}O$ of atmospheric species by incrementally increasing the lower boundary flux of CO_2. The deposition velocity (the first-order rate constant which controls CO_2 removal from the atmosphere) is held constant at the value used in the base model (see Chapter 5), in order to allow CO_2 to build up in the atmosphere to greater mixing ratios. We choose to increase pCO_2 through a flux boundary condition rather than a mixing ratio boundary condition, to allow the ground level CO_2, COP and COQ mixing ratios and therefore the isotopic composition of CO_2 to vary freely. For Case 1, the boundary conditions for all other species are the same as for the base model.

In their box models, Crockford et al. (2018) and Planavsky et al. (2018) vary pCO_2 between 2 and 30 times, and 2 and 100 times pre-anthropogenic levels respectively, while Planavsky et al. (2020) vary pCO_2 between 0 and 500 times the present atmospheric level, to simulate a mid-Proterozoic atmosphere. As an initial test, we vary the flux of CO_2 between 1 and 50 times the base model value (2.2×10^{13} pu). The results are shown in Figures 6-1 and 6-2.

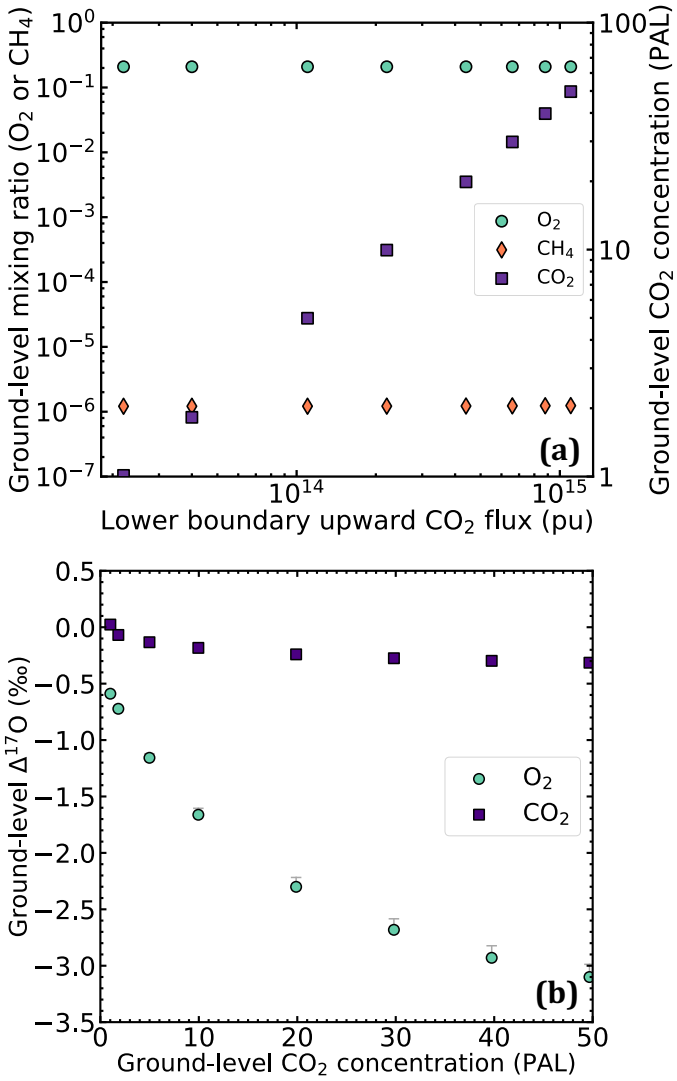

Figure 6-1: Results for Case 1 models. ***(a)*** *Predicted ground-level mixing ratios of O_2 and CH_4 (left-hand axis) and ground-level CO_2 concentration in PAL (right-hand axis) with lower boundary CO_2 flux, for model atmospheres with increasing CO_2 flux.* ***(b)*** *Predicted ground-level $\Delta^{17}O$ values for O_2 (teal) and CO_2 (purple) plotted against predicted ground-level CO_2 concentration, for the model atmospheres with increasing CO_2 flux. Grey bars show values before correction for artificial fractionation is applied. If no grey bar is visible, the uncertainty is smaller than the size of the point.*

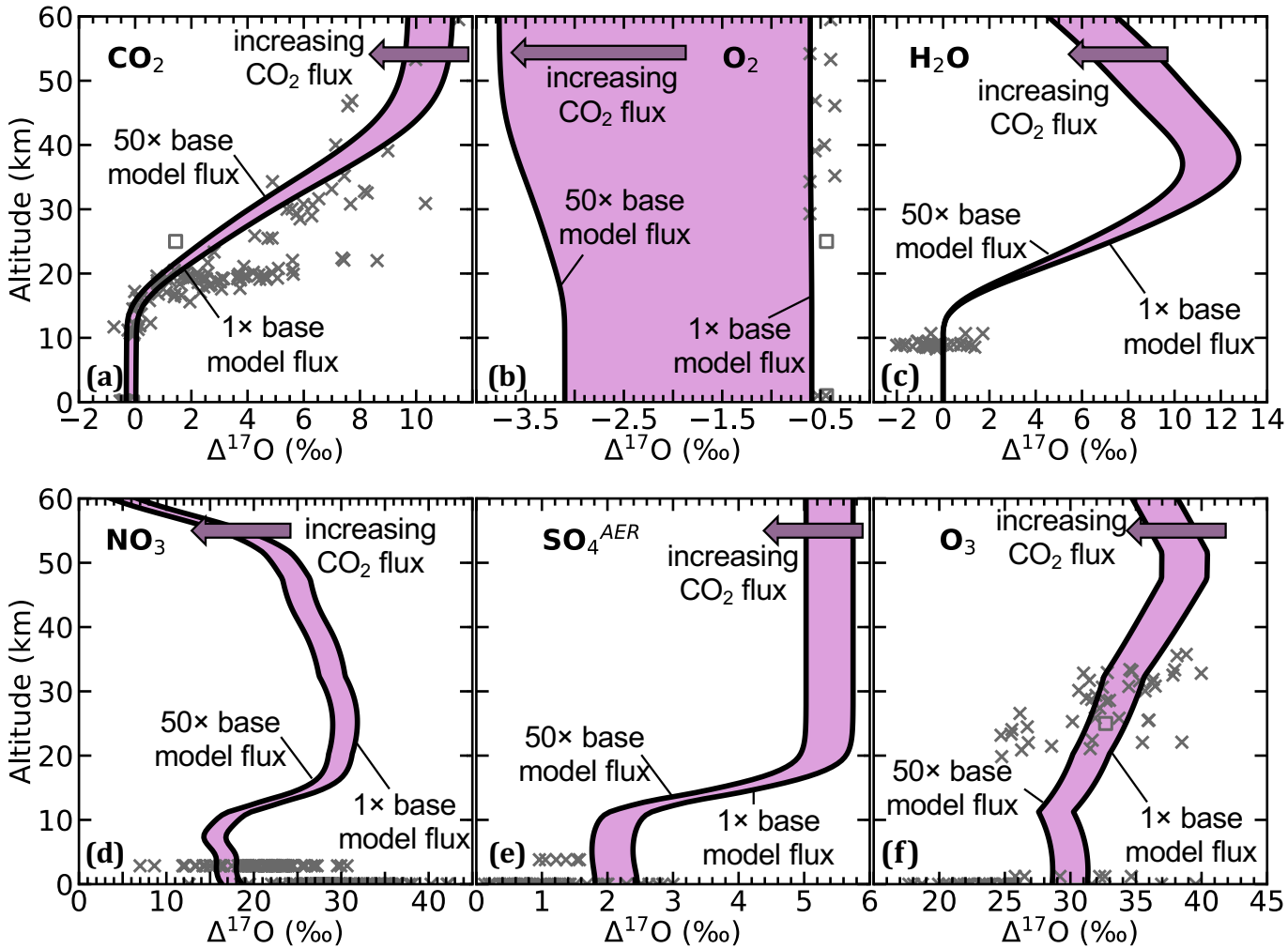

Figure 6-2: $\Delta^{17}O$ profiles of selected species with increasing pCO_2, which increases from 1 PAL to ~50 PAL as the upward CO_2 flux is increased fiftyfold. Purple shading shows variation of $\Delta^{17}O$ with altitude between the smallest (1 PAL CO_2; right-most line) and largest (50 PAL CO_2; left-most line) CO_2 flux cases. Grey points show observations (crosses) and existing model predictions (squares) for the modern atmosphere (1 PAL CO_2; see Figure 5-2 for references).

The purple squares in Figure 6-1a show that our fifty-fold increase in CO_2 flux results in model atmospheres with CO_2 mixing ratios of 2.8×10^{-4} to 1.39×10^{-2}, which simulates approximately 1 to 50 times the 'pre-anthropogenic level' (defined as 2.8×10^{-4} with Crockford et al., 2018; see also Chapters 3 and 5). Figure 6-1a also shows that the O_2 (teal circles) and CH_4 (orange diamonds) mixing ratios remain relatively unchanged by the increase in CO_2 flux, so any variation in $\Delta^{17}O$ value is likely to be due to the increase in pCO_2 rather than other factors.

Figure 6-1b shows the $\Delta^{17}O$ values of ground-level CO_2 and O_2 for the models with increasing ground-level CO_2 mixing ratio. Here, $\Delta^{17}O$ values are plotted against model-predicted CO_2 mixing ratios rather than CO_2 flux, because we have demonstrated above that increasing CO_2 flux is an adequate way to vary pCO_2 that does not affect other major species. The results show that $\Delta^{17}O_{O2}$ values (teal circles) become more negative with increasing pCO_2, as expected, and $\Delta^{17}O_{CO2}$ values (purple squares) decrease to negative values with increasing pCO_2. The effects of an increase in pCO_2 are most clearly seen in the $\Delta^{17}O$ value of tropospheric O_2. Since the tropospheric O_2 isotopic composition is the one captured in sulphates and preserved in the geological record, these are the values we are most interested in. For a discussion of how $\Delta^{17}O$ values of O_2 correspond to magnitudes of sulphate $\Delta^{17}O$ in the geological record under these conditions, see Case 4 (Section 6.3.4).

Figure 6-2 shows the $\Delta^{17}O$ profiles with altitude of several selected atmospheric species, for the different CO_2 fluxes. As observed in Figure 6-1b, the $\Delta^{17}O_{O2}$ values at all altitudes become increasingly negative (signifying a greater mass-independent fractionation) with increasing pCO_2 (Figure 6-2b). As mentioned in Section 6.1, this can be explained by an increased transfer of heavier oxygen isotopes from the O_x-O_2 system to CO_2. This is consistent with the model results showing decreased $\Delta^{17}O$ for O_3 at all altitudes (Figure 6-2f). The decrease in $\Delta^{17}O$ for CO_2 (Figures 6-1 and 6-2) is a result of both the decrease in $\Delta^{17}O_{O_3}$ and an increase in the size of the CO_2 reservoir across which the anomaly is spread. This effect is particularly large in the stratosphere for CO_2 and O_2. This could be because the rate of $O(^1D)/O$ exchange with CO_2 (shown to be important in dictating $\Delta^{17}O_{CO2}$ in Chapter 5, and known to be

key in the transfer of the oxygen isotope anomaly from O_3 to CO_2) peaks with ozone concentrations in the stratosphere. Indeed, Figure 6-2 reveals a decrease of $\Delta^{17}O$ value at all altitudes for *all* species shown. In addition, exchange with H_2O in the troposphere (parametrised by mass-dependent fractionations in the lower boundary conditions of CO_2, COP and COQ; see Chapter 5) acts to quickly dilute non-zero $\Delta^{17}O$ from the tropospheric CO_2 reservoir. Sulphate, nitrate and stratospheric H_2O $\Delta^{17}O$ values also decrease with increasing pCO_2. It is clear that CO_2 plays a major role in transferring oxygen isotope anomalies to other atmospheric species.

Our results follow a similar overall trend to previous studies, but predict lower magnitudes of $\Delta^{17}O_{O2}$ for a given increase in pCO_2 than Bao et al. (2008) and Young et al. (2014). In the following subsection, we discuss the results in Figures 6-1 and 6-2 in comparison with these two previous studies, considering different formulations of boundary conditions, model sophistication and inclusion (or lack thereof) of isotope exchange reactions.

6.3.1.1 – Comparison with previous models varying pCO_2

Figure 6-3 shows a comparison of our model results with varying pCO_2 to those of Bao et al. (2008; solid teal line), who used a photochemical model to predict tropospheric $\Delta^{17}O_{O2}$ with varying pCO_2. Note that, in order to allow for comparison, the definition of $\Delta^{17}O$ (for the teal points in this figure only) has been changed to $\Delta^{17}O = \delta'^{17}O - 0.52\times\delta'^{18}O$ (where $\delta'^{x}O = \ln({}^{x}R_{species}/{}^{x}R_{standard})$; Definition 1). Bao et al. (2008) describe a linear correlation between pCO_2 and $\Delta^{17}O_{O2}$, except for high-pCO_2 cases where this relationship weakens slightly. This is supported by a linear relationship shown in ice core data (Blunier et al., 2002; Luz et al., 1999), although the pCO_2 range for the data is much smaller (190-281 ppmv) than the extrapolation by Bao et al. (2008). They attribute the slight departure from the linear negative correlation at high pCO_2 to a negative feedback, as the shuttling of heavier oxygen isotopes from O_3 by $O(^1D)$ and CO_2 results in a decreased $\Delta^{17}O$ value of the ozone formed. Our $\Delta^{17}O_{O2}$ values for pCO_2 between 1 and 10 PAL are similar to those of Bao et al. (2008), but our model atmospheres show no linear relationship. Instead,

the effect of pCO_2 on $\Delta^{17}O$ decreases as pCO_2 increases past 10 PAL, rendering our $\Delta^{17}O$ values less negative than theirs for the same pCO_2. The effect of the negative feedback described by Bao et al. (2008) appears therefore to be stronger in our model.

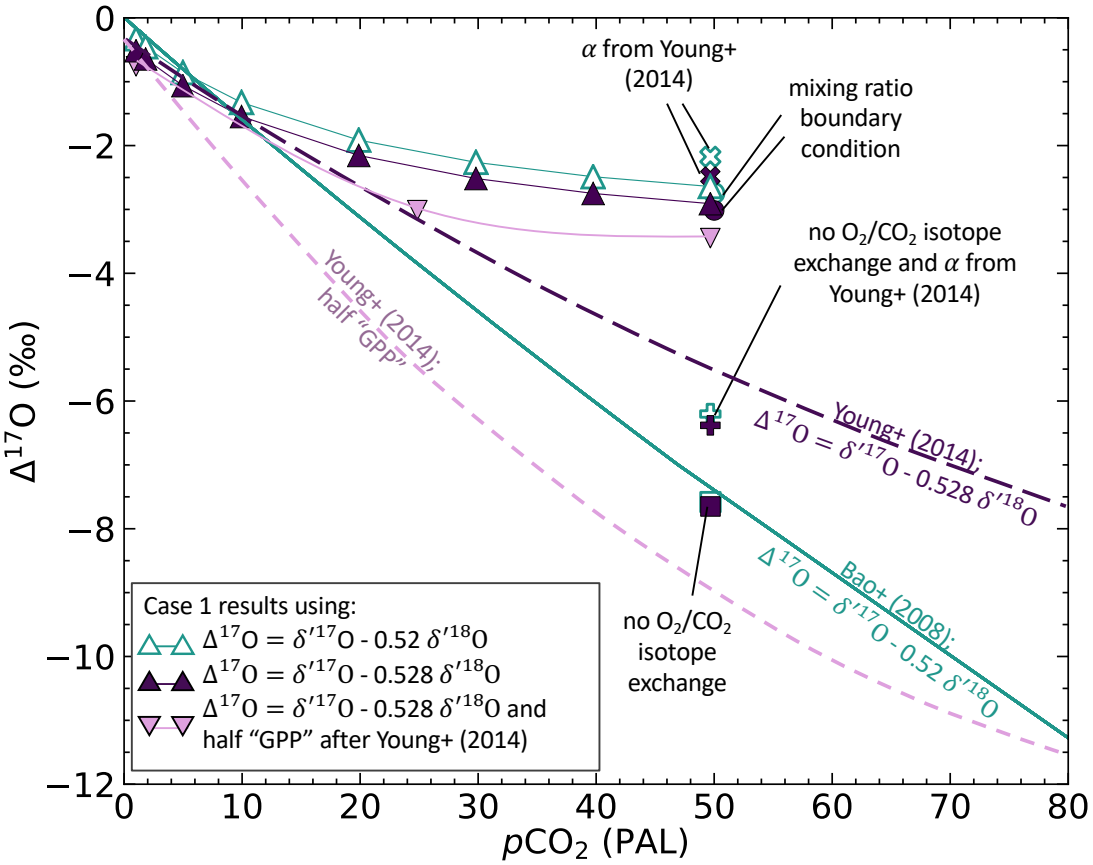

Figure 6-3: Comparison of Case 1 models to existing models. Points show model-predicted $\Delta^{17}O$ values of ground-level O_2, with model-predicted ground-level pCO_2. Teal, unfilled symbols show our model results plotted using the definition $\Delta^{17}O = \delta'^{17}O - 0.52\times\delta'^{18}O$ to allow comparison to the oxygen isotope model of Bao et al. *(2008; teal solid line). Dark purple, filled symbols show our model results plotted using the definition $\Delta^{17}O = \delta'^{17}O - 0.528\times\delta'^{18}O$ to enable comparison to the model of Young* et al. *(2014; dark purple, dashed line). Upward-pointing triangles show our results from Case 1, for cases with increasing pCO_2. Circles show $\Delta^{17}O_{O2}$ value of a model atmosphere using a fixed mixing ratio lower boundary condition of 50 PAL for CO_2. Squares show results of model atmospheres with no isotope exchange between O_2 and CO_2. Crosses show results using fractionation factors for the ozone formation reactions from Young* et al. *(2014; 1.065 for all four reactions forming heavy ozone isotopologues) rather than the P-, T- and isotopologue-dependent fractionation factors (Section 5.3.1). 'Plus' symbols show results for a case with no O_2/CO_2 exchange and the Young* et al. *fractionation factors. Pale purple downward-pointing triangles show model results with half the upward O_2 flux and half the deposition velocity, to simulate what Young* et al. *(2014) call "50% GPP."*

Young et al. (2014) use their 4-box model to demonstrate a similar non-linear relationship between pCO_2 and $\Delta^{17}O$, for various GPP, although also predict lower negative $\Delta^{17}O_{O2}$ for a given pCO_2 (dark purple dashed line on Figure 6-3). Note that Young et al. (2014) use a definition for $\Delta^{17}O$ of $\delta'^{17}O - 0.528 \times \delta'^{18}O$ (Definition 2), and the dark purple, filled symbols on Figure 6-3 show our results according to this definition for comparison. With increasing pCO_2, the increase in the magnitude of $\Delta^{17}O_{O2}$ decreases, compared to the more linear results of Bao et al. (2008). Again, our model results agree well with those of Young et al. (2014) for low pCO_2 (10 PAL and less), but are less negative than the published model results for higher pCO_2.

There are several possible reasons for the shallowing of the negative pCO_2-$\Delta^{17}O$ gradient with increasing pCO_2. Firstly, variations in pCO_2 could affect the mixing ratios of other major species in the atmosphere. However, Figure 6-1a shows that O_2 and CH_4 concentrations are not significantly affected by the increase in pCO_2. Also, the concentrations of ozone increase by only 0.5% between the 1 and 50 PAL CO_2 models, so the change in $\Delta^{17}O$ is not due to a change in the rate of ozone formation. Secondly, we noted that the way in which pCO_2 was varied was by adjusting the upward lower boundary flux only, rather than the deposition velocity which dictates the downward flux across the lower boundary. However, it would be expected that the increased cycling of CO_2 into and out of the atmosphere that this causes would actually act to remove isotopically anomalous CO_2 from the atmosphere and replace it with CO_2 with no stratospheric isotope anomaly. This would exacerbate the removal of heavy isotopes from the system and drive down the $\Delta^{17}O$ values of CO_2, O_3 and O_2, rather than causing them to level off. However, in order to show that the boundary conditions were not the cause of the discrepancy, we produced a single model atmosphere with a mixing ratio lower boundary condition stipulating a ground-level CO_2 concentration of 50 PAL (teal, unshaded and dark purple, shaded circles for Definitions 1 and 2 respectively, on Figure 6-3). This did not greatly affect the $\Delta^{17}O_{O_2}$ value.

Thirdly, we considered the rates of isotope exchange reactions $O(^1D) + CO_2 \rightarrow O + CO_2$ and $O_2 + CO_2 \rightarrow O_2 + CO_2$ and their isotopic equivalents, and their variation with

pCO_2. These reaction rates increase linearly with pCO_2. As the importance of the former reaction increases, the isotope anomaly is increasingly quickly transferred from ozone to carbon dioxide, but the increase in rate of the second reaction acts as a negative feedback to bring some of the heavy isotopes back into O_2. The O_2/CO_2 isotope exchange reactions are not included in the reactions of Bao et al. (2008) or Young et al. (2014). In fact, they are fictitious reactions that we included (Section 5.3.3; Section 5.4.7) to parametrise the measured isotope exchange between CO_2 and excited-state O_2 species $O_2(^1\Sigma)$ and $O_2(^1\Delta)$ (after Wiegel et al., 2013). To test whether this negative feedback could explain the decreasing gradient of the pCO_2-$\Delta^{17}O$ slope in our results, we produced a model atmosphere with the O_2/CO_2 exchange reaction rate set to zero (squares on Figure 6-3). Neglecting the exchange produces atmospheres close to the results of Bao et al. (2008) in pCO_2-$\Delta^{17}O$ space. It therefore seems that this is likely to be a reason for the difference between our results and those of Bao et al. (2008).

As discussed in Chapter 5, we chose the rate for this reaction by dividing the JPL-18 recommended $O_2(^1\Delta)/CO_2$ reaction rate constant by the O_2:$O_2(^1\Delta)$ concentration ratio, and then adjusting to best fit the $\Delta^{17}O$ profile data. While reasonable to first order, it is therefore possible that the exchange reaction rate used here is too fast, and requires revisiting. The best solution would be to include $O_2(^1\Sigma)$ and $O_2(^1\Delta)$ in the isotope model, since they are involved in some important reactions. Development of *Atmos* during the course of the work in this thesis has incorporated these species and associated reactions (Burkholder et al, 2015; Wiegel et al., 2013) into some modern Earth model templates (not shown), and predicts mixing ratios close to measurements (Yankovsky & Manuilova, 2006). Inclusion of isotopic equivalents for excited-state O_2 via the methods outlined in Chapter 4 will be a priority in future work.

However, without the O_2/CO_2 isotope exchange, our model now produces more negative $\Delta^{17}O_{O2}$ at high pCO_2 than Young et al. (2014). We considered other potential differences between our model and that of Young et al. (2014). Firstly, the latter use 1.065 as a fixed fractionation factor in the ozone formation reaction for all four

heavy-isotopologue reactions at all altitudes, whereas we (like Bao et al., 2008) adopt experimentally-determined and altitude-variable fractionation factors. To assess the effect of this difference, we produced two model atmospheres with fifty times the upward lower boundary CO_2 flux as the base model, but using the same α values (1.065 with no P- or T-dependence). One model atmosphere included the O_2/CO_2 isotope exchange reactions (crosses on Figure 6-3), and the other did not ('plus' symbols on Figure 6-3). The model atmospheres using the Young et al. (2014) fractionation factors had less negative $\Delta^{17}O$ for ground-level O_2 than those using the base model fractionation factors. Perhaps unsurprisingly, the model without O_2/CO_2 exchange and with Young et al.'s (2014) fractionation factors matches their model the best, differing by only 0.8‰ in the 50 PAL pCO_2 case. The remaining discrepancy may be due to different upward and downward O_2 fluxes used by our model compared to Young et al.'s (2014), since their gross fluxes into and out of the atmosphere are roughly three times larger. Reducing our incoming O_2 flux and O_2 deposition velocity by a factor of 2 decreases the $\Delta^{17}O$ values, as shown by the downward-pointing, pale purple triangles in Figure 6-3. It is therefore likely that increasing our fluxes would achieve a closer match to the results of Young et al. (2014).

6.3.1.2 – Preliminary application to 'Snowball Earth' atmospheres

Bao et al. (2008) use their model to suggest that pCO_2 of 12,000 ppmv could explain the low $\Delta^{17}O$ values observed in Marinoan cap carbonate-associated sulphates (Figure 1-3). Young et al. (2014) use their model to show that the $\Delta^{17}O$ minimum of -1.64‰ (Bao et al., 2009) could only be explained by CO_2 concentrations of 20,000 ppmv, if the GPP was the same as today. They obtain this larger pCO_2 value, partly because of the more recent, more negative observations, but also because their pCO_2-$\Delta^{17}O$ relation is not linear. At high pCO_2, a larger increase in pCO_2 is required to produce the same change in $\Delta^{17}O$. Our model deviates from the linear relation even more, so would suggest that an even larger pCO_2 than 20,000 ppmv would be required, at modern GPP, to produce the very low $\Delta^{17}O$ values at 635 Ma. In fact, the curve of our pCO_2-$\Delta^{17}O$ results seems to start to plateau. We do not increase pCO_2 to

the levels of more than 280 PAL that some authors propose (e.g. Bao et al., 2009; Benn et al., 2015), but the extrapolation of our results along the already-shallowing trend suggests that negative feedbacks in our model would prevent the production of such low $\Delta^{17}O_{O2}$ values, even with the maximum proposed pCO_2. We therefore propose that high pCO_2 alone cannot account for the minimum Cryogenian $\Delta^{17}O_{SO4}$ values.

However, some authors instead consider the minimum could be evidence for reduced primary productivity (Cao and Bao, 2013; Sansjofre et al., 2011). The Young et al. (2014) model can also explain the observations with a lower pCO_2 of 10,000 ppmv if the rates of respiration and photosynthesis are equal to half of the modern values (pale purple dashed line on Figure 6-3). This hypothesis is supported by biogeochemical modelling indicating that pCO_2 was higher than modern but only by roughly an order of magnitude (Mills et al., 2017, 2019). We will therefore also explore the effects of varying pO_2 and GPP on $\Delta^{17}O$ value.

6.3.2 – Case 2: Decreasing pO_2 results

In order to simulate the effects of varying pO_2 on the $\Delta^{17}O$ values of atmospheric species, we vary the O_2 fluxes across the lower boundary. As for Case 1, using a mixing ratio lower boundary condition for O_2 would not be instructive, since the $\Delta^{17}O$ value of tropospheric O_2 is our key output, and would not be allowed to vary freely (Chapter 5). For Case 2, we decreased the upward O_2 flux from 4×10^{13} pu (the base model flux, which produces modern O_2 concentrations at the ground-level) to 10^{11} pu. The deposition velocity dictating the O_2 flux out of the atmosphere remains the same, and the CH_4 flux is held constant at 10^{11} pu for all Case 2 model atmospheres.

Figure 6-4a shows the ground-level O_2 (filled teal circles) and CH_4 (filled orange diamonds) mixing ratios and CO_2 concentrations (filled purple squares) for each model atmosphere, plotted against the input lower boundary O_2 flux, for Case 2. With decreasing O_2 flux, the O_2 mixing ratio also decreases, as expected. This

continues up to a critical flux point – for this suite of model atmospheres, a flux of 4×10^{11} – at which point any further decreases in O_2 flux result in very low O_2 mixing ratios of less than 10^{-9}. Simultaneously, methane mixing ratios for the high-O_2 atmospheres remain between 10^{-7} and 10^{-5}, until the critical O_2 flux point, at which point they increase to around 10^{-3}. This result is similar to that seen in Chapter 3, as there seems to be a large region of O_2 mixing ratio space in which model solutions are not easily produced, separated by a very narrow range of O_2 fluxes in a flux-driven model. A variation in O_2 flux does not greatly affect the CO_2 concentrations when the CO_2 flux remains constant, so variations in pCO_2 are not affecting $\Delta^{17}O$ values to a significant extent here.

Figure 6-4b shows the predicted ground-level O_2 mixing ratios, now on the horizontal axis, plotted against the $\Delta^{17}O$ value of ground-level O_2 (filled teal circles) and CO_2 (filled purple squares). The tropospheric $\Delta^{17}O_{CO2}$ values remain relatively unchanged, decreasing with decreasing O_2 mixing ratio by less than 1‰. However, a decrease in O_2 mixing ratios results in a decrease in $\Delta^{17}O$ to more negative values, reaching a minimum of -15‰. The three model atmospheres with low O_2 mixing ratios resulting from low O_2 fluxes are different: they have $\Delta^{17}O$ values very close to zero, indicating that O-MIF is not being propagated to major O-bearing species under these conditions.

Figure 6-5 shows the model output $\Delta^{17}O$ values of selected species with altitude, for selected O_2 flux inputs. In general, as in Figure 6-4b, a decrease in O_2 flux (and O_2 mixing ratio) results in a decrease in $\Delta^{17}O$ value at all altitudes, for O_2 fluxes between 4×10^{13} pu and 5×10^{11} pu. This is the case for all selected species except for tropospheric H_2O, which has a $\Delta^{17}O$ value held fixed at zero in the model (see Chapter 4). The profiles for the three models with O_2 fluxes of 3×10^{11} pu, 2×10^{11} pu and 10^{11} pu act differently. For ozone, these three models have the highest $\Delta^{17}O$ values in the troposphere and lower stratosphere, but since they do not have the same shape as the profiles for the other fluxes, the values are lower in the upper atmosphere than for the high-O_2 flux models. For all other selected species, $\Delta^{17}O$ values throughout the atmospheric column are close to zero. These atmospheres are

reducing, and have very different chemistries. Due to insufficient O_2, the rate of production of ozone is greatly decreased, and less mass-independent fractionation occurs because the process that produces it has been restricted. The ozone that is produced has O-MIF because we are declaring it to do so when formed, but the small concentrations mean that this is not significantly propagated to other atmospheric species.

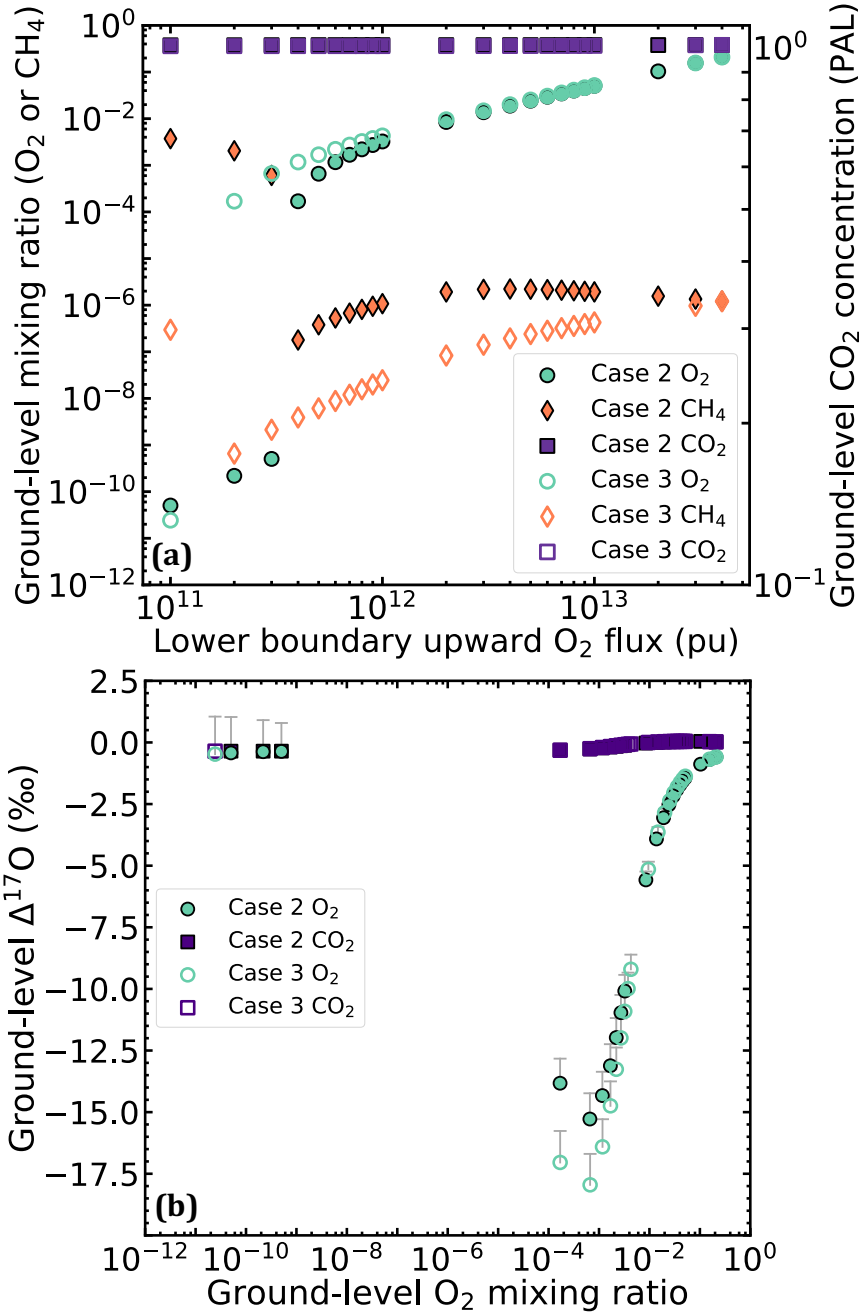

Figure 6-4: ***(a)*** *Ground-level mixing ratios of O_2, CH_4 and CO_2 plotted against lower boundary upward O_2 flux, for Cases 2 (solid points) and 3 (unshaded points).* ***(b)*** *Ground-level $\Delta^{17}O_{O2}$ and $\Delta^{17}O_{CO2}$ values plotted against model-predicted ground-level O_2 mixing ratio, for Cases 2 (solid points) and 3 (unshaded points). Grey bars show values before correction for artificial fractionation is applied.*

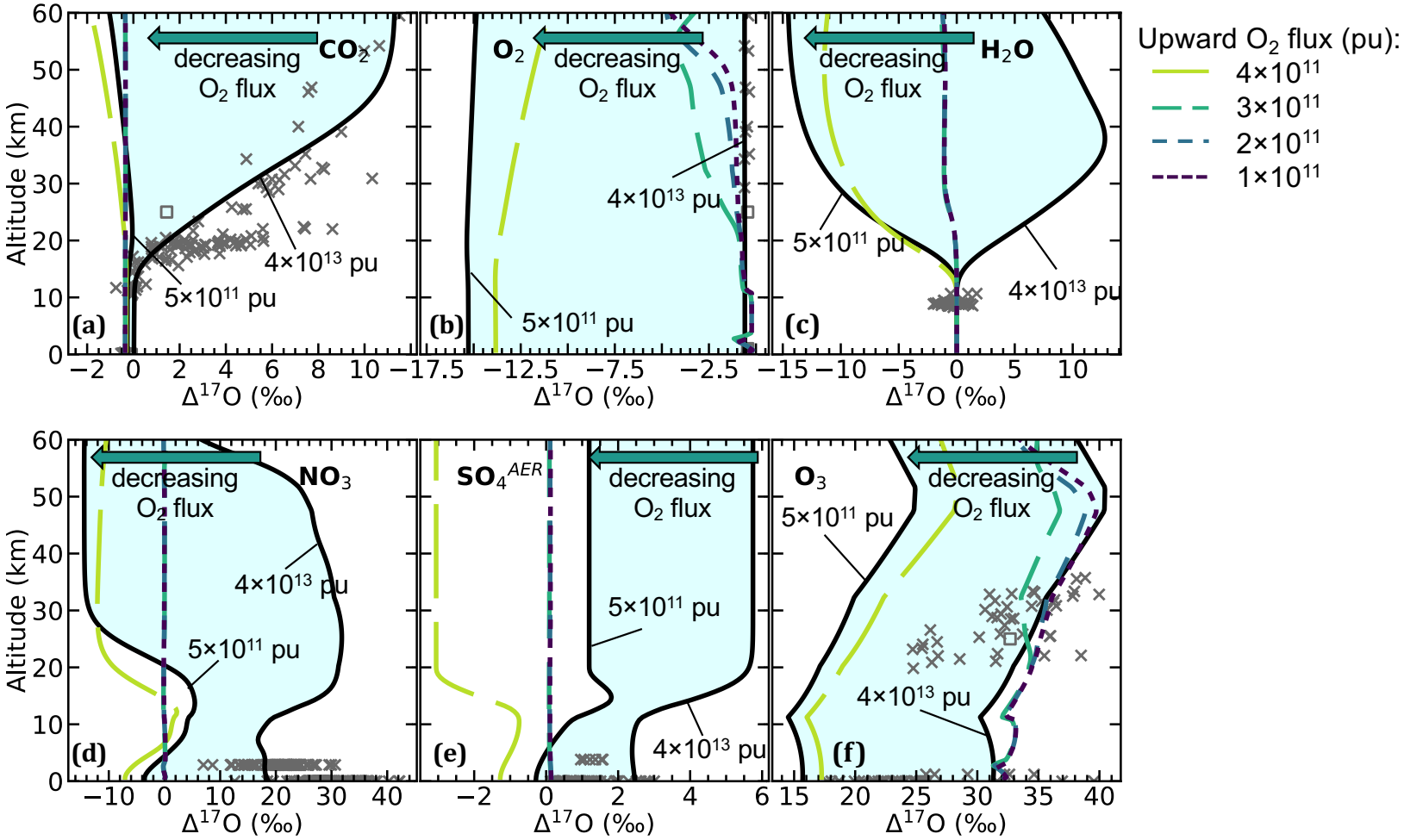

Figure 6-5: Variation of $\Delta^{17}O_{O2}$ with altitude, with varying upward O_2 flux across the lower boundary. Black lines show profiles for model atmospheres with O_2 fluxes of 4×10^{13} pu and 5×10^{11} pu, and green shading shows $\Delta^{17}O$ values with altitude for model atmospheres with O_2 fluxes between these values (individual profiles not shown). Model atmospheres with fluxes of 4×10^{11} pu and less behave differently, so are shown by individual coloured lines, denoted by the key. Modern observations (crosses) and previous model predictions (squares) are shown by the grey points.

Another interesting feature of the decreasing O_2 flux suite is that the model run at the critical flux point (corresponding to a flux of 4×10^{11} pu), has a lower mixing ratio than all the other high-O_2 models, but a slightly less negative $\Delta^{17}O$ value (Figure 6-4). This is also seen in the $\Delta^{17}O$ profiles of O_2, O_3 and stratospheric H_2O and NO_3 (Figure 6-5). For this model, O_2 and O_3 concentrations seem to have decreased to a level at which significantly less ozone is being produced and therefore the anomalous oxygen isotope signal is weaker. It is likely a transitional case, unstable to small perturbations towards either higher- or trace-O_2 cases (see Chapter 3).

Our results from Case 2 suggest that there exists a minimum $\Delta^{17}O$ near -15‰ that can be incorporated into O_2, although this would need to be verified over a larger set of flux cases, combined with considerations of atmospheric stability against perturbations and feedbacks with biological fluxes. We start with the former below.

6.3.3 – Case 3: Decreasing pO_2 with decreasing CH_4 flux

For a third case, we decreased the O_2 flux to achieve a suite of model atmospheres with varying pO_2, as for Case 2, but also decreased the methane flux. The methane flux was decreased to maintain a constant ratio of methane flux to upward O_2 flux, similar to the models in Chapter 3. Our aim was to better simulate processes in the Earth system. Since O_2 and CH_4 are biological fluxes, it is more consistent to vary their fluxes in tandem. The ratio of the upward O_2 flux to the CH_4 flux is the same as for the base model (CH_4:O_2 flux ratio = 1/400). This is a much lower CH_4:O_2 flux ratio than that used in Chapter 3 because here, as explained in Chapter 5, larger upward and downward O_2 fluxes are used, representing shorter-term biological fluxes. We however continue to use the medium-term net CH_4 flux, with no drawdown from the atmosphere. Since most biological methane is oxidised in sediments before it is able to be released from the atmosphere, and since methane is not an oxygen-bearing species whose oxygen isotope ratios must be prescribed carefully, this is an acceptable assumption for the time being (but see discussion in Section 6.4.2). Broadly speaking, Case 3 can be considered as simulating a modern-style Earth

system (e.g. oxic ocean with high sulphate levels stimulating substantial methanotrophy in sediments) but at differing levels of GPP.

Figure 6-4 (unshaded symbols) shows that these model atmospheres are fairly similar to those produced in Case 2. Decreasing O_2 flux results in model atmospheres with decreasing ground-level O_2 mixing ratios, as seen in Figure 6-4a. Again, there is a window of O_2 mixing ratio space in which no model solutions lie, for a narrow flux range. This window is very similar to that seen for the Case 2 results (2×10^{-11} to 2×10^{-4}), and again, reducing atmospheres with high CH_4 mixing ratios are seen alongside a trace O_2 mixing ratio for the lowest flux. The most stark difference is much lower predicted methane mixing ratios for the oxic atmospheres with lower coupled fluxes, which makes sense given the lower fluxes. Another difference between this case and Case 2 is that a lower O_2 flux is required to trigger the jump from higher- to trace-O_2 mixing ratios compared to Case 2. This makes sense, given that the lower CH_4 flux for Case 3 has reduced the flux of reductants into the atmosphere. Again, pCO_2 levels are relatively unaffected by the variations introduced here.

Figure 6-4b shows that the ground-level $\Delta^{17}O_{CO2}$ values do not vary significantly between Cases 2 and 3. For the atmospheres with ground-level O_2 mixing ratios greater than 10^{-2}, the ground-level $\Delta^{17}O_{O2}$ values are also very similar between the two cases, with the Case 3 atmospheres producing slightly more negative $\Delta^{17}O_{O2}$ values at lower O_2 mixing ratios. This could be because, as can be seen in Figure 6- 4a, the O_2 flux required to produce the same O_2 concentration (for O_2 levels below 10^{-2}) is lower for Case 3. The lower O_2 flux therefore results in less dilution of the stratospheric O-MIF signal.

6.3.4 – Case 4: Decreasing pO_2 at various pCO_2

Since much current discussion centres around the combined effects of pO_2 and pCO_2 on $\Delta^{17}O_{O2}$, we produced suites of model atmospheres like those in Case 3 (with decreasing O_2 and CH_4 upward fluxes), with different upward CO_2 fluxes (resulting

in different tropospheric CO_2 concentrations). Since Crockford et al. (2018) vary pCO_2 in their Monte Carlo models between 2 and 30 times PAL, we run suites of models with 10, 20 and 30 times the CO_2 flux used to produce a modern pCO_2 (in the base model). This produces atmospheres with close to 10, 20 and 30 times modern pCO_2. Planavsky et al. (2020) and Young et al. (2014) explore pCO_2 values of higher levels (2-500 PAL and 1-100 PAL respectively). Expansion of our parameter space for these higher 'Snowball Earth'-relevant pCO_2 levels would be an interesting avenue for future investigation in the short-term.

Figure 6-6 shows some extracted data products for Case 4 model results. To facilitate comparison with the geologic record, we estimate the $\Delta^{17}O$ of sedimentary sulphates (those inheriting the negative $\Delta^{17}O$ value from O_2 through weathering; vertical axis), which is plotted against the model-predicted ground-level O_2 mixing ratio (horizontal axis). To estimate the $\Delta^{17}O$ values of sulphates from the model output $\Delta^{17}O$ of tropospheric O_2, we assume lower and upper estimates for the proportion of oxygen atoms in sulphate that come from tropospheric O_2 of 8% and 15% (Balci et al., 2007; Crockford et al., 2018; Planavsky et al., 2020; see review in Section 1.5.2.2), shown by the upper line with circle markers and the lower line with square markers, respectively. The shaded regions therefore show the range of potential $\Delta^{17}O_{SO4}$ values that might be expected to be preserved in evaporites under an atmosphere with the chosen pCO_2, at a certain pO_2. Grey dashed lines show the minimum observed $\Delta^{17}O$ values measured in sedimentary sulphates at two specific intervals – the mid-Proterozoic Sibley basin sulphates from 1.4 Ga (Crockford et al., 2018), and the cap-carbonate-associated sulphates from 635 Ma (Bao et al., 2008). These are the most negative $\Delta^{17}O$ values observed in the geological record and are of particular interest as a proxy for GPP, pO_2, pCO_2 or some combination.

6.4 – Discussion

6.4.1 – Palaeo-O_2 mixing ratios

Our suites of model atmospheres in Cases 2 and 3 show no model atmospheres with predicted O_2 mixing ratios between 5×10^{-10} and 2×10^{-4}. In Chapter 3, similar results led us to propose potential constraints on pO_2 for the geological past. However, we have not exhausted possible combinations of biological fluxes in this chapter, so cannot use the lack of atmospheres with certain mixing ratios to improve on the Chapter 3 constraints in a similar way.

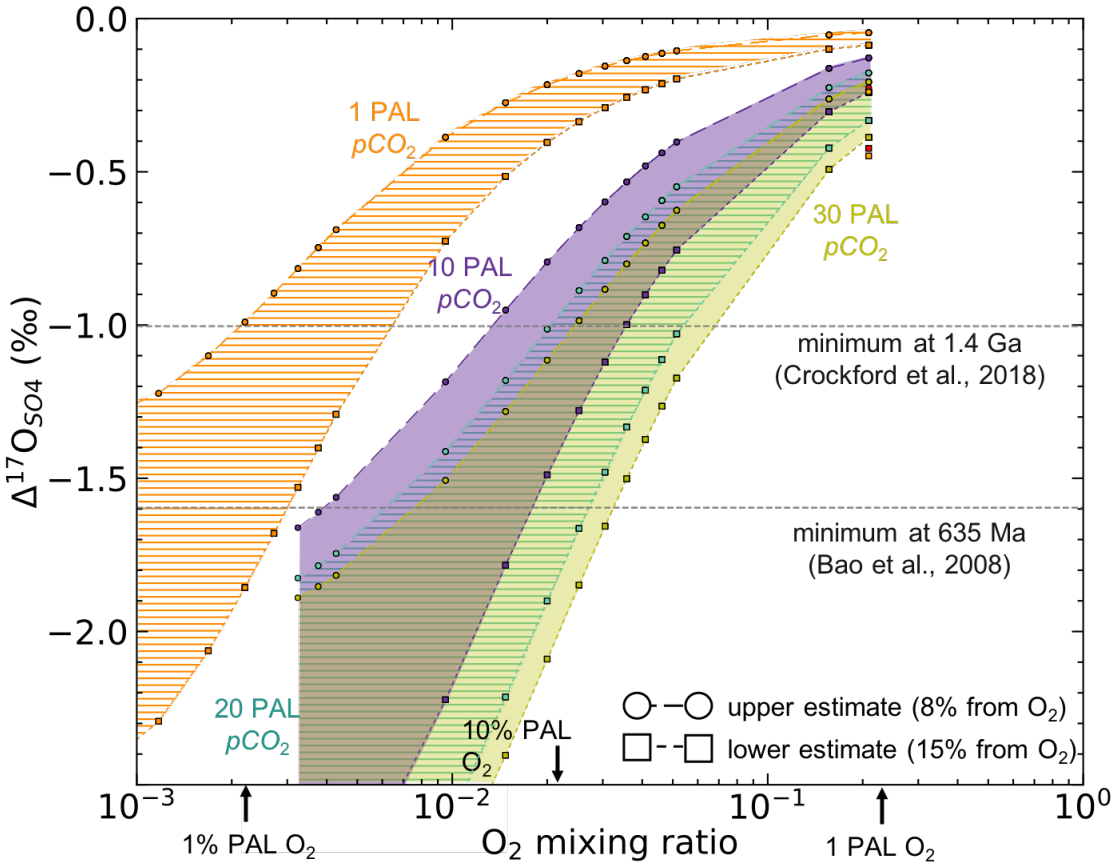

Figure 6-6: Predicted $\Delta^{17}O$ values of geological sulphate for model atmospheres with varying pO_2 at different pCO_2 levels. The $\Delta^{17}O$ values of sulphate are calculated from the $\Delta^{17}O_{O2}$ values at the ground-level of the atmosphere, assuming a minimum of 8% (dashed lines with circular markers) and a maximum of 15% (dotted lines with square markers) of the oxygen atoms from sulphate come from atmospheric oxygen. Shading shows the $\Delta^{17}O$ values between these limits for 1 PAL (orange stripes), 10 PAL (purple), 20 PAL (teal stripes) and 30 PAL (yellow) pCO_2. The single pairs of red and orange markers indicate the $\Delta^{17}O$ values for model atmospheres with 40 PAL and 50 PAL pCO_2, respectively, at modern O_2 levels. Two of the minimum $\Delta^{17}O_{SO4}$ observations from the geological record are shown by the grey dotted lines.

Building on Chapter 3, there are complementary insights that an oxygen isotope photochemical model can offer. If similar suites of model atmospheres with varying O_2 fluxes and GPP are produced in an oxygen isotope model, the predicted $\Delta^{17}O_{O2}$ values can be compared to observations in the geological record to add a potential constraint on O_2 mixing ratios across certain key points in geological history. Here, we discuss how the results presented here might start to address this.

6.4.1.1 – Implications for an ozone layer

Firstly, we have demonstrated in Cases 2 and 3 that trace-O_2 atmospheres produce $\Delta^{17}O_{O2}$ values of zero, within error. Therefore, we do not expect to find non-zero $\Delta^{17}O_{SO4}$ values before the GOE, and any non-zero $\Delta^{17}O_{SO4}$ since the start of the Proterozoic should indicate the presence of an ozone layer. Crockford et al. (2018; 2019) used the assumption that the presence of non-zero $\Delta^{17}O_{SO4}$ since the GOE indicates the presence of an ozone layer to propose a lower limit for Proterozoic pO_2 of 10^{-3} PAL (a mixing ratio of 2.1×10^{-4}), after the results of photochemical models which suggested that this was the minimum pO_2 at which an ozone layer could be formed (e.g. Segura et al., 2003). However, as explained in Chapter 3, the photochemical models on which this assumption was based used fixed mixing ratio boundary conditions, which produce strikingly different results to those presented in Chapter 3 using fixed flux boundary conditions for O_2 and important reducing species. In this subsection, we review the implications of the work in this thesis for this assumption.

In Chapter 3 we concluded that most of our model atmospheres had O_2 mixing ratios of more than 2×10^{-3} or less than 6×10^{-7}, and for the latter, there was no substantial ozone layer. It was possible to produce model atmospheres with an ozone layer with a pO_2 between these mixing ratios, but these atmospheres were unstable to small perturbations in the model atmosphere conditions. Our Chapter 3 conclusions therefore imply that the minimum pO_2 required for non-zero $\Delta^{17}O$ to be formed is 1% PAL, approximately ten times larger than that suggested by Crockford et al. (2018; 2019).

Our oxygen isotope model can also contribute to this discussion. The results from Cases 2 and 3 do produce model atmospheres with O_2 mixing ratios as low as 1.7×10^{-4}, which have non-zero $\Delta^{17}O$ values (Figure 6-4). As a thorough exploration of lower boundary flux parameter space like that in Chapter 3 has not been executed, this lower limit has a higher associated uncertainty, as our lowest pO_2 cases suffered some photochemical instabilities. On the other hand, the lowest $\Delta^{17}O_{SO4}$ values measured in the geological record are ~-1.64‰ (for 635 Ma; Bao et al., 2009). Assuming modern-day pCO_2 and the lowest proposed estimate (8%) of the percentage of sulphate atoms derived from atmospheric oxygen from Balci et al. (2007), this corresponds to a ground-level $\Delta^{17}O_{O2}$ value of -20.5‰, which is lower than the $\Delta^{17}O$ predicted by our lowest oxic pO_2 cases. If we could assume that pCO_2 has been constant at modern levels throughout the Proterozoic and Phanerozoic, this could be proposed as evidence that low $\Delta^{17}O$ observations in the geological record can be explained by pO_2 with a lower limit of $\sim10^{-4}$ However, given that -20.5‰ is a very conservative minimum, and pCO_2 is likely to have been at levels higher than modern levels, especially during the Cryogenian period from which the minimum observation dates (e.g. Bao et al., 2008; Mills et al., 2019; Sheldon, 2006, 2013; see Figure 1-3), the model atmospheres with O_2 mixing ratios of around 10^{-4}-10^{-3} may not necessarily need to be invoked to explain the oxygen isotope signatures.

6.4.1.2 – Further preliminary application to 'Snowball Earth' atmospheres

We discussed in Section 6.3.1.2 that our model results from Case 1 suggest that very high pCO_2 (Bao et al., 2008; 2009; Benn et al., 2015) cannot be the sole cause of the minimum Cryogenian $\Delta^{17}O_{SO4}$ values (-1.64‰). However, as explained in the previous subsection, Figure 6-6 shows that the minimum $\Delta^{17}O$ values can be reproduced by a model with O_2 mixing ratios less than 3×10^{-3} with pCO_2 at values equal to today. Our models with pCO_2 higher than modern (which it is likely to have been; Mills et al., 2017; 2019) require less of a drop in pO_2; however, we suggest that pCO_2 as high as suggested by Bao et al. (2009) and allowed by Young et al. (2014) (see Figure 1-3) is not a prerequisite for the large, negative $\Delta^{17}O_{SO4}$ observations.

Reduced primary productivity, with or without elevated pCO_2, could reproduce the observations for this period.

6.4.1.3 – Mid-Proterozoic atmospheric composition

The lowest $\Delta^{17}O$ values measured in mid-Proterozoic sulphates (recorded in Sibley Basin sediments) is -1.00‰ (according to our $\Delta^{17}O$ definition; Crockford et al., 2018). Planavsky et al. (2020) used their model to propose a best-fit O_2 mixing ratio of $\sim 7.1\times10^{-4}$ (with uncertainty range between 3×10^{-4} and 2×10^{-3}) to produce such low $\Delta^{17}O$. Using sulphate-O_2 incorporation factors between 8% and 15% requires $\Delta^{17}O_{O2}$ values between -6.5‰ and -12.5‰ for the Sibley Basin minimum observation. For Cases 2 and 3, with modern-day pCO_2, we predict such $\Delta^{17}O_{O2}$ values at O_2 mixing ratios of 10^{-3}-7×10^{-3}. Figure 6-6 shows that model atmospheres with more CO_2 can reproduce the observations without the need to invoke such low pO_2. Given that the mid-Proterozoic is likely to have had elevated pCO_2 relative to the modern atmosphere (Kasting, 1987; Kaufman and Xiao, 2003; Sheldon, 2006, 2013; see Figure 1-3), our results suggest that O_2 mixing ratios lower than 10^{-3} are not required to explain the observations. Our lower limit of 10^{-3} is at the upper end of the range proposed by Planavsky et al. (2020).

While a helpful first step, we must discuss a couple of caveats. Firstly, lower $\Delta^{17}O_{SO4}$ would require a lower pO_2, and, while -1.00‰ is the lowest measured $\Delta^{17}O_{SO4}$ value for the mid-Proterozoic at the moment, it cannot be assumed that this is a minimum $\Delta^{17}O_{SO4}$ value for all of the mid-Proterozoic. It is possible that future work will allow for the discovery of more negative O-MIF in the geological record, or that it was present but has not been preserved. While stable to diagenesis (Bao, 2015), the O-MIF signature in sulphate can be erased by biological sulphur cycling, so ought to be considered a conservative tracer (Crockford et al., 2019). Therefore, the minimum $\Delta^{17}O_{SO4}$ values cannot necessarily be taken to be the most negative $\Delta^{17}O_{SO4}$ values possible. Our results show that for a given pCO_2 value, lower O_2 concentrations are required to reproduce lower $\Delta^{17}O$ values, and suggest that explicit knowledge of pCO_2 may be needed to constrain pO_2. Utilising the details of palaeo-constraints and

models of pCO_2, such as those described in Section 1.2 and shown in Figure 1-3, would be an interesting target for honing in on pO_2 over particular intervals of the Proterozoic and Phanerozoic. Future integration of pCO_2 into atmospheric models may, with further development, allow for constraints on the pCO_2/pO_2 ratio for a given $\Delta^{17}O$ observation.

Secondly, we have assumed that 8-15% of the oxygen atoms in sulphate come from atmospheric O_2, but this is a source of uncertainty (see review in Chapter 1, and Section 6.4.3 below). A smaller fraction, or a dilution of MIF-bearing sulphate with oceanic sulphate may mean that observed $\Delta^{17}O_{SO4}$ values are consistent with more negative $\Delta^{17}O_{O2}$ values, and therefore lower pO_2.

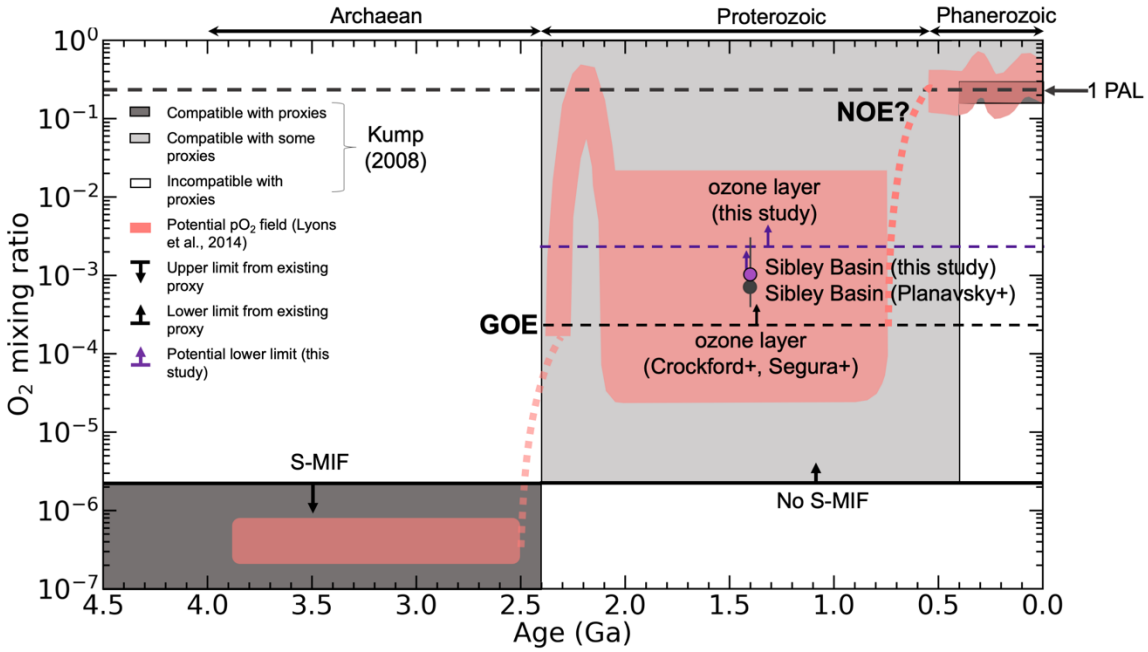

Figure 6-7: Summary and context of Chapter 6 results in terms of palaeo-O_2 levels. Purple point shows minimum O_2 mixing ratio required by our models to reproduce the Sibley sulphate $\Delta^{17}O$ minimum, compared to the estimate of Planavsky et al. *(2020). This lower limit will increase with appropriate inclusion of palaeo-pCO_2 in future work. Purple line and arrow show lower limit for pO_2 required by the presence of an ozone layer, according to our Chapter 3 and Chapter 6 results, compared to those previously used (black line; Crockford* et al., *2018; 2019; Segura* et al., *2003). This is higher than our conservative constraint from the Sibley Basin sulphates, because our study in Chapter 3 suggests that, though a small fraction of model atmospheres are produced with O_2 mixing ratios between 6×10^{-7} and 2×10^{-3}, they may be unstable to small perturbations in flux. However, we show both constraints independently in this figure.*

Therefore, we have shown that the very low Sibley Basin sulphate $\Delta^{17}O$ measurements, dated to 1.4 Ga, could be produced under an atmosphere with an O_2 mixing ratio of 10^{-3} or above, which does not require as low a pO_2 at 1.4 Ga as previous work has proposed. Our model could potentially be applied to other intervals of Earth history for which $\Delta^{17}O$ has been measured, with consideration for existing estimates of pCO_2 (Figure 1-3) to produce a tighter constraint. A summary of our results in the context of palaeo-O_2 levels is shown in Figure 6-7.

6.4.2 – Boundary conditions for O_2 and CH_4

In Cases 2-4, we have produced varying pO_2 by decreasing the O_2 flux and choosing to i) keep the CH_4 flux constant (Case 2); or ii) decrease the CH_4 flux at a constant ratio in relation to the upward O_2 flux (Case 3). However, neither of these CH_4 lower boundary conditions effectively reproduce the way in which biological fluxes were varied for the flux-driven models in Chapter 3. There, we varied the lower boundary upward O_2 flux, with the CH_4 flux varying at a constant CH_4:O_2 flux ratio (between 0.1 and 0.5). However, due to our choice of lower boundary condition for O_2 in this chapter, it is not straightforward to reproduce these model conditions. As explained in Chapter 5, it was necessary to choose high fluxes of O_2 into and out of the model atmosphere, as correct prediction of $\Delta^{17}O$ values of tropospheric O_2 depends on large, short-term biological fluxes of O_2 into and out of the atmosphere. In contrast, medium-term fluxes of O_2 were a more appropriate choice for the Chapter 3 models.

To enable better comparison of model atmospheres here and in Chapter 3, we computed the CH_4:O_2 flux ratio for the models in this chapter by using the ratio of the CH_4 flux to a net O_2 flux equal to the O_2 flux out of the atmosphere subtracted from the O_2 flux into the atmosphere. The O_2 flux out of the atmosphere is not constant, but is linearly dependent on the ground-level concentration, given the deposition velocity specification (Section 2.5). Figure 6-8 shows the mixing ratios of O_2 and CH_4 from Cases 2 and 3, now plotted against the CH_4:O_2 flux ratio calculated in this way. The results from Case 2 (filled symbols) allow a comparison to those in which we incrementally adjusted the CH_4:O_2 flux ratio in Chapter 3, because the flux

ratio varies between 0.1 and 0.5 (though here it is due to varying O_2 flux at constant CH_4 flux, as opposed to varying CH_4 flux at constant O_2 flux, as in Chapter 3). However, all Case 3 CH_4:O_2 flux ratios are less than 0.1, which is roughly the value for the modern atmosphere, which explores parameter space outside of that explored in Chapter 3 (and unlikely to represent Earth's past atmosphere). Furthermore, neither case has a CH_4:O_2 flux ratio held constant, as we did for the Case 1 and 3 models in Chapter 3.

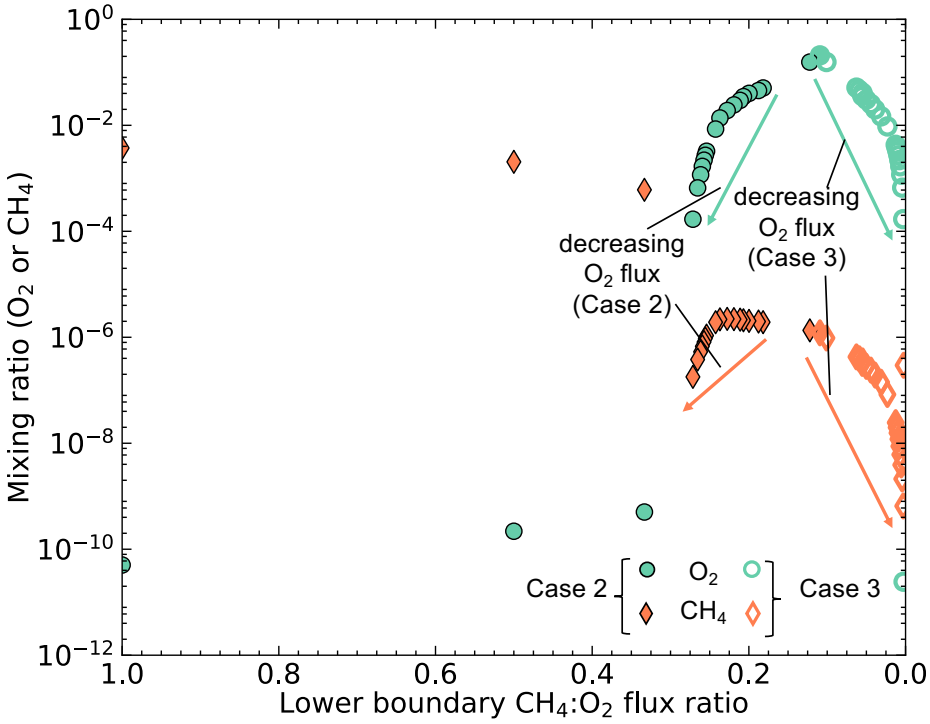

Figure 6-8: Ground-level O_2 and CH_4 mixing ratios plotted against CH_4:O_2 flux (the ratio of the CH_4 flux to the net O_2 flux), for model atmospheres from Cases 2 (filled symbols) and 3 (unfilled symbols). Arrows indicate the direction of decreasing upward gross O_2 flux for the model suites.

We therefore produced a further suite of models, with decreasing O_2 flux, but in which the CH_4 flux was adjusted iteratively such that the CH_4:O_2 flux ratio (in which the O_2 flux is the net O_2 flux across the lower boundary) was held constant at 0.11±0.01 (which is the flux ratio in the base model). These models (Case 5; coloured symbols) are shown in Figure 6-9, in comparison to those of Cases 2 (filled black symbols) and 3 (unfilled black symbols). The results show that (though we chose to

produce fewer model atmospheres) Case 5 is very similar to Case 3, in terms of O_2 mixing ratios and $\Delta^{17}O_{O2}$ values produced. The methane mixing ratios are higher for Case 5 models due to higher CH_4 fluxes in general. The models of Cases 3 and 5 are therefore acceptable as tests for varying GPP (as well as pO_2 as a result), and show lower $\Delta^{17}O$ values with lower GPP/pO_2, under various CH_4 boundary condition choices.

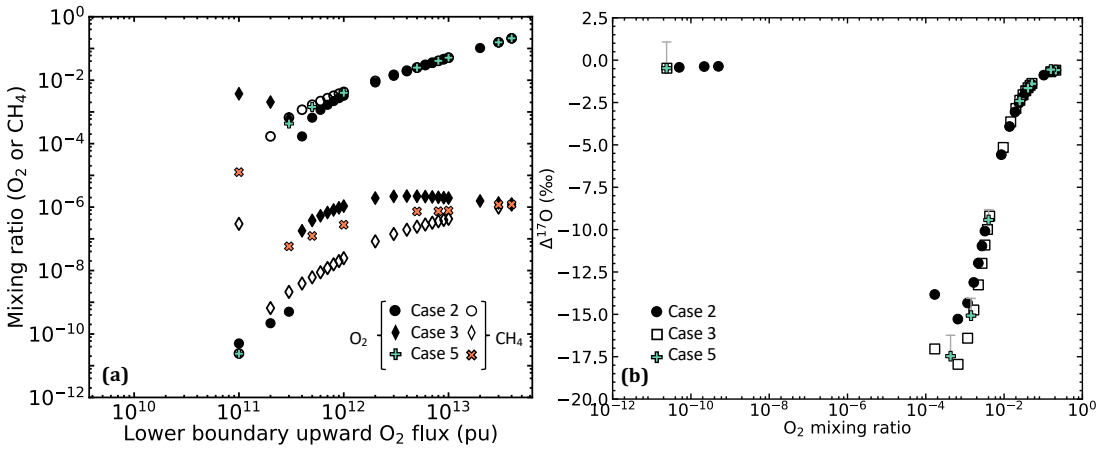

Figure 6-9: Results from Case 5 (coloured symbols) compared to those of Cases 2 (black filled symbols) and 3 (black unfilled symbols). ***(a)*** *Ground-level O_2 and CH_4 mixing ratios with lower boundary O_2 flux.* ***(b)*** *Ground-level $\Delta^{17}O_{O2}$ and $\Delta^{17}O_{CO2}$ with model-predicted ground-level O_2 mixing ratio. The uncorrected model $\Delta^{17}O$ values are shown by the caps of the error bars (if further from the marker than the radius of the marker).*

However, in the box model of Young et al. (2014), 'GPP' is varied by varying the photosynthesis rate (labelled r_p in their model) and the respiration rate constant (labelled k_r) at constant r_p/k_r. This results in a suite of model atmospheres with varying 'GPP' (i.e. r_p and k_r, equivalent to a variation in O_2 turnover), but at constant pO_2 (since r_p/k_r remains constant). The pale purple symbols in Figure 6-3 show that the effect of reducing 'GPP' by a factor of two is a decrease in $\Delta^{17}O_{O2}$ to more negative values, as Young et al. (2014) found using their model (pale purple line on Figure 6-3).

Another notable difference between the results presented in this chapter and those of Chapter 3 is that, in the latter, we decided to include a negative feedback flux with a power law relation to simulate oxidative weathering, after Johnson et al. (2019). Here, we instead use a linear negative feedback flux. However, this is acceptable

because in the short-term, the major downward O_2 flux is due to biological uptake rather than oxidative weathering.

6.4.3 – Uncertainty in the proportion of sulphate atoms from tropospheric O_2

The discussion thus far has shown that pO_2 as low as has been suggested in previous work may not necessarily be required to reproduce the oxygen isotope data in the geological record. For most of the Phanerozoic and Proterozoic, $\Delta^{17}O_{SO4}$ values have not been lower than -0.5‰ (with the exceptions of 4 minimum points in the Proterozoic seen in Figure 1-2). Assumed values for the percentage of sulphate atoms from O_2 of 8-15% require a $\Delta^{17}O$ of initial atmospheric O_2 of no less than -6.25‰. According to the model suites presented here, this minimum value corresponds to an O_2 mixing ratio of no lower than 10^{-3} PAL for most of the Proterozoic, especially so if the carbonate-silicate cycle increases pCO_2 to counteract a less luminous Sun (Kasting, 1993). This could be evidence that oxygen levels have been above this limit since the GOE. However, as discussed above, it could be that more negative $\Delta^{17}O$ values are yet to be discovered or were not preserved. Another possible explanation is that estimates of 8-15% are unsuitable, or even that our understanding of the processes by which sulphide is oxidised by atmospheric O_2 is not correct (Hemingway et al., 2020). The amount of the atmospheric O_2 signal that is preserved in sulphate is uncertain (see review in Chapter 1), and the community would benefit from tighter constraints on this value in the interpretation of geological $\Delta^{17}O$ values.

6.5 – Conclusions

In this chapter, we have explored some of the effects on the $\Delta^{17}O$ values of atmospheric O_2 resulting from atmospheres with varying pCO_2 and pO_2. The $\Delta^{17}O_{O2}$ values decrease with either an increase in pCO_2 or a decrease in pO_2. Differences between our model and previous models at high pCO_2 can be explained by a combination of different mass-independent fractionation factors, our inclusion of

exchange between O_2 and CO_2, and slightly different boundary fluxes for O_2. The models presented here also offer potential constraints on pO_2 and pCO_2 over certain intervals of time. According to our model, O_2 mixing ratios no lower than 10^{-3} need be invoked to explain the mid-Proterozoic $\Delta^{17}O_{SO4}$ minimum at 1.4 Ga. Our model results also suggest that the 635 Ma $\Delta^{17}O_{SO4}$ minimum is unlikely to be explained by high pCO_2 alone, but reduced pO_2 ($< 3\times10^{-2}$) alongside high pCO_2 (not necessarily greater than 30 PAL) may help explain the observations. Future work will involve minimising uncertainty by e.g. including reactions involving important excited-state O_2 species, and a thorough exploration of boundary flux parameter space like that presented in Chapter 3. Nevertheless, we have shown that the oxygen isotope photochemical model is a useful and promising tool for interpreting $\Delta^{17}O$ values in the geological record.

Chapter 7

Conclusions

In this thesis we use and develop a 1-D photochemical model, with an aim to better constrain the evolution of oxygen levels in the atmosphere over Earth history, with some application to carbon dioxide. Our results are summarised in Figure 7-1, which is developed from Figure 1-1 in Chapter 1. In Chapter 3, most of the model atmospheres produced using fixed flux boundary conditions as opposed to traditionally-used mixing ratio boundary conditions had O_2 mixing ratios smaller than 6×10^{-7} or larger than 2×10^{-3}. We proposed that this could offer potential constraints on atmospheric pO_2 over Earth history, since our model suggests that atmospheres with mixing ratios between these values may be unstable to small perturbations in lower boundary fluxes (see purple shading and purple dashed line in Figure 7-1). In particular, we outlined how our results address an area of debate pertaining to Proterozoic pO_2, by suggesting a potential lower limit of 2×10^{-3} (~1% PAL).

For this application to early Earth atmospheres, it would be instructive to build on our study by further exploring the stability of model solutions with pO_2 in the 6×10^{-7} – 2×10^{-3} window. Currently, we have shown that our steady-state model solutions switch from having trace- to high-O_2 levels with very small changes in reducing or oxidising fluxes, but use of a time-dependent model would help us to understand the timescales on which this potentially rapid process might occur. A geologically-fast transition from trace- to high-pO_2 states has been observed by existing time-dependent biogeochemical modelling studies (e.g. Claire et al., 2006), which is likely to be compounded by our atmospheric chemistry feedbacks. This may therefore give further insight into the mechanisms, timescales and potential reversibility of

the GOE. Coupling of our atmospheric model to biogeochemical cycling models at the lower boundary may also help to better simulate the inter-connection between biology, fluxes of biological gases to the atmosphere and atmospheric composition.

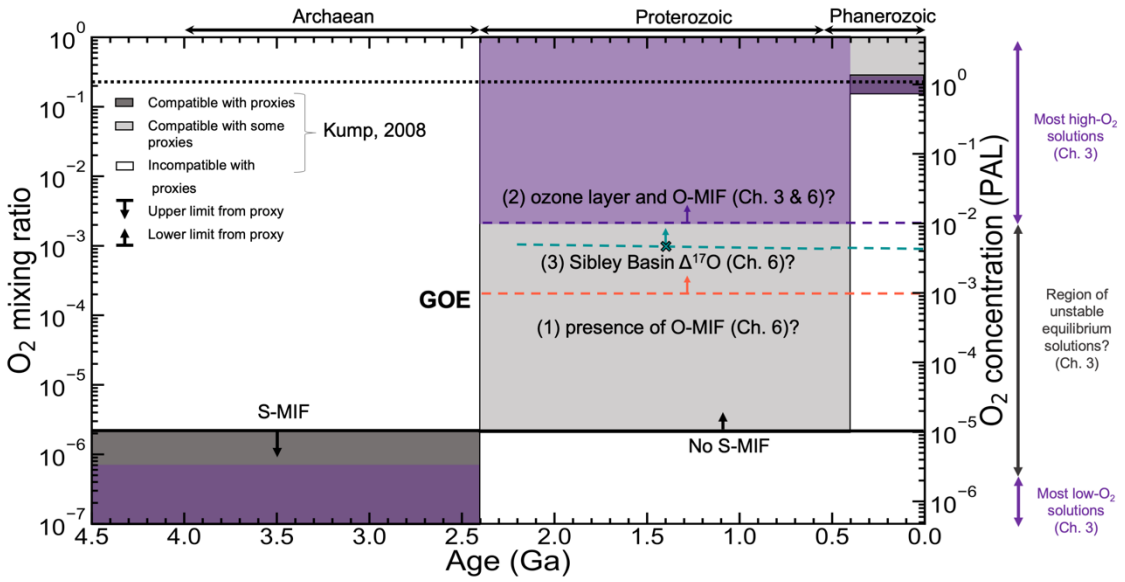

Figure 7-1: Summary and context of thesis results in terms of palaeo-O_2 levels. The left- and right-hand axes indicate O_2 levels as mixing ratios and in PAL, respectively. Grey boxes show ground-level pO_2 compatible with (some) proxies plotted against age, as in Figures 1-1 and 4-9. Purple boxes show ground-level pO_2 compatible with existing proxies and our constraints from the models produced in Chapter 3. Coloured dashed lines show additional constraints from this thesis. Orange dashed line (1) and arrow show lower limit indicated by the results in Chapter 6: 10^{-4} is the lowest O_2 mixing ratio with which $\Delta^{17}O_{O2}$ were non-zero in the models presented there. Purple dashed line (2) shows that the results from Chapter 3, which indicate few oxidised atmosphere model solutions exist with $pO_2 < 2\times10^{-3}$, may increase this lower limit. Teal dashed line (3) shows lowest O_2 mixing ratio required to reproduce the most negative mid-Proterozoic and Phanerozoic $\Delta^{17}O_{SO4}$ values (except for those at ~635 Ma), according to our results in Chapter 6. Present atmospheric levels are indicated by the black dotted line.

We have focussed primarily on the application of the results of Chapter 3 for palaeo-Earth atmospheres, but there are also implications for the characterisation of exoplanet atmospheres. Firstly, the utility of the absorption features of O_3 have been highlighted as a proxy for O_2 (e.g. Des Marais et al., 2002; Leger et al., 1993). Our results in Chapter 3 challenge the classic understanding of the relationship between O_2 and O_3 levels (i.e. the increase in O_3 with O_2 concentrations as shown in Figure 3-1; Kasting and Donahue, 1980; Kasting et al., 1985; Segura et al., 2003), and affect the way in which O_3 detection should be translated into O_2 mixing ratios.

Secondly, if we were to observe Earth from space using the biosignature tools we currently use for exoplanets, which of the model atmospheres from Chapter 3 would we consider to be potentially inhabited? Coupling of our model results to a radiative transfer model (e.g. Kaltenegger et al., 2007; Kaltenegger and Traub, 2009; Meadows and Crisp, 1996; Segura et al., 2003) would reveal the absorption spectra we might observe for the >2000 model solutions. Earth has been inhabited for the majority of its lifetime, but the hypothetical detection of biosignatures for inhabited palaeo-Earth is an area of interest (e.g. Kaltenegger et al., 2020; Rugheimer and Kaltenegger, 2018). How high do O_2 levels (and the fluxes responsible) need to be before oxygenation is observable?

Thirdly, is the two-state behaviour likely to occur on planets orbiting other stars, with different stellar fluxes? Would it occur in our Solar System if the Earth orbited the Sun a little closer or further away? These research questions can be pursued using *Atmos*, which is flexible for use with other types of stars. Of particular interest is the behaviour of atmospheres of planets around M dwarves (e.g. Rugheimer et al., 2015; Rugheimer and Kaltenegger, 2018) since these planets tend to be the most easily observable. Production of model atmospheres with varying fixed flux boundary conditions simulating a range of biological fluxes, followed by collaboration with workers who can produce the absorption spectra that we would expect to see from such atmospheres is a natural follow-up project to Chapter 3; with the launch of JWST on the horizon, models to help interpret absorption spectra are particularly exciting.

In Chapters 4 and 5, we built on our findings from Chapter 3 by developing the model to include the three stable isotopes of oxygen. In Chapter 5, we presented the model, and have demonstrated that it predicts modern $\Delta^{17}O$ values in key species (including O_2, CO_2, O_3, NO_3, H_2O and H_2O_2) for modern Earth atmospheric conditions. We showed the importance of inclusion of various isotope exchange reactions, mass-dependent fractionation effects, and experimentally-determined mass-independent fractionation effects in the formation of ozone. We additionally demonstrate the sensitivity of model output $\Delta^{17}O$ values to environmental

conditions including rainfall, temperature, latitude and the isotopic composition of water vapour, which have previously been shown to result in large variations in observations.

In Chapter 6, we applied the model to reproduce the isotopic signature of atmospheric oxygen preserved in sulphates in the geological record, under various pO_2/pCO_2 conditions. We confirm that non-zero $\Delta^{17}O$ values are only produced in atmospheric O_2 (and therefore preserved in sulphates) in the presence of an ozone layer, which does not appear with trace O_2 concentrations. Our preliminary results show an O_2 mixing ratio window (for $6\times10^{-10} < pO_2 < 1.7\times10^{-4}$), in which no model atmospheres lie, supporting our conclusions from Chapter 3. The lowest O_2 mixing ratio of a model atmosphere with an ozone layer is therefore 1.7×10^{-4}, which is similar to that proposed previously (Crockford et al., 2018; Segura et al. 2003; see orange dashed line in Figure 7-1). However, the minimum $\Delta^{17}O$ values observed in the mid-Proterozoic can be explained with pO_2 values no lower than 10^{-3}, and even higher if pCO_2 greater than modern levels is assumed (see teal dashed line in Figure 7-1). We also find that pO_2 lower than modern is required to reproduce minimum Cryogenian $\Delta^{17}O$ values, implying that they cannot be purely explained by high pCO_2 in the aftermath of a Snowball Earth glaciation.

The development of our oxygen isotope model is a promising step towards better constraining of pO_2 during the Proterozoic and Phanerozoic, as well as understanding processes in the modern atmosphere. In Chapters 4-6, we have described and tuned the model, and discussed preliminary applications, but there are plenty of avenues for future research.

In the immediate-term, further development of the model is important. One of the limitations of the oxygen isotope model is the artificial fractionations produced. As discussed, these are small, but future work will involve further rigorous investigation of the model code with the aim of minimising this source of uncertainty. Two options for this, outlined in Chapter 4, are i) investigating potential improvements with the inclusion of isotopologues with more than one heavy oxygen

isotope (e.g. $^{17}O^{18}O$, $C^{17}O^{17}O$), and ii) adjusting the mixing ratios of oxygen-bearing species such that the total mixing ratio of isotopologues for a species is equal to the mixing ratio of the original, non-substituted species. As well as reducing uncertainty in $\Delta^{17}O$ for key species such as O_2 and CO_2, the removal of artificial fractionations will allow the model to predict $\delta^{17}O$ and $\delta^{18}O$ more accurately for trace species. The oxygen isotope composition of many atmospheric species has not been measured, so this may provide a first prediction of whether and how minor atmospheric components (such as OCS, HSO, SO_2 and CO) inherit O-MIF from ozone.

As suggested in Chapter 5, it would also be valuable to undertake a Monte-Carlo simulation in which some of the chosen parameters (e.g. CO_2 flux MDF, reaction rates of oxygen isotope exchange reactions) are varied, in order to assess the uncertainty in the model output due to our assumed values. As well as quantifying it, it would also be beneficial to address an area of uncertainty highlighted in Chapters 5 and 6: namely, the inclusion of O_2/CO_2 isotope exchange reactions. Our results with varying pCO_2 in Chapter 6 differed from previous box models, in part due to our parametrisation of isotope exchange reactions between CO_2 and $O_2(^1\Delta)/O_2(^1\Sigma)$ through these reactions, having not yet included excited-state O_2 species in the model thus far. It would therefore be instructive to include these species and their isotopic equivalents in the model for future work.

Chapters 1 and 5 highlighted some of the applications of triple oxygen isotope studies to sulphates, nitrates and perchlorates produced in and deposited from the modern atmosphere, and preserved at or near the surface in arid regions. Observations of $\Delta^{17}O$ have been useful in identifying and quantifying oxidation pathways that produce these species, and their global variation. In Chapter 5, we began to test the sensitivity of $\Delta^{17}O_{NO3}$ to some environmental variables, and showed that the individual analyses had affected $\Delta^{17}O$ in the same direction as the data indicate. Future work could involve using the model to predict changes in $\Delta^{17}O$ with combinations of variables, which might initially comprise a Monte-Carlo approach, to continue our study of how a resulting spread in our model output might compare to a spread in observations. Subsequently, we can simultaneously vary multiple

environmental variables in order to predict $\Delta^{17}O$ in specific locations. For example, once the samples we collected in 2017 from the Atacama Desert have been processed (see Chapter 1, Section 1.5.1.2), an interesting project would be the model prediction of $\Delta^{17}O$ variation along the latitudinal transect, by varying the rainfall input, with Atacama-like values for the other environmental variables. As well as an opportunity to explore the relationship between rainfall and $\Delta^{17}O$ in atmospheric nitrates and sulphates, this will allow for fine-tuning of the way rainfall is incorporated in *Atmos*.

High concentrations of sulphates are also found in arid Atacama soils, as well as other extremely dry locations globally (e.g. the Antarctic Dry Valleys). However, as discussed in Chapter 5, our oxygen isotope model does not yet predict $\Delta^{17}O$ of atmospheric sulphate well, due to the lack of incorporation of aqueous-phase oxidation pathways, which are important in the propagation of O-MIF to this species. A priority for future work is therefore the tuning of the model, through the inclusion of the additional oxidation reactions, to better predict atmospheric sulphate. This would aid constraining of the sensitivity of $\Delta^{17}O$ of sulphate to environmental conditions.

For the same reason, it would be interesting to develop the model to predict the isotopic composition of perchlorate, and especially as perchlorate formation pathways are so uncertain. This development would also be of great interest in planetary science, since large concentrations have been found in the Martian regolith; a better understanding of how they are formed could give us insight as to atmospheric conditions necessary to produce them on the red planet (Kounaves et al., 2010). This would involve the incorporation of chlorine species (already included for the model used in Chapter 3; Catling et al., 2010) into the oxygen isotope model. For Chapters 4, 5 and 6, these were neglected because initial investigation found that large artificial fractionations were produced when the additional species and reactions were added. However, atmospheric chlorine is important in the O_x-O_2 system as it catalyses the breakdown of ozone, and therefore affects the concentrations of some of our key species.

Chapter 6 showed results from suites of model atmospheres with varying pCO_2 and pO_2, and this enabled us to consider possible atmospheric compositions required to produce extremely negative O-MIF in the rock record. However, we focussed on two minima only (1.4 Ga and 635 Ma), but much more $\Delta^{17}O$ data has been obtained (see Figure 1-2). In particular, we have not discussed observations from the Phanerozoic in this thesis. Recent work, including work within our research group (Pettigrew et al., 2020; Warke et al., 2020a) has expanded the $\Delta^{17}O_{SO4}$ data for the Phanerozoic, with a particularly noteworthy minimum in the Carboniferous, when it is thought that O_2 levels may have been reduced. Surprisingly low $\Delta^{17}O$ values have also been observed in sulphates in 605 Ga sedimentary exhalative (SEDEX) deposits (Moles et al., 2020). It would be interesting to explore these episodes using the oxygen isotope model to aid interpretation of these data.

To conclude, we have used two approaches - a systematic study of lower boundary conditions in a 1-D photochemical model, and development of an oxygen isotope photochemical model – to put potential constraints on atmospheric evolution. We have demonstrated the utility of our newly-developed model in the field of early-Earth studies, and are excited about its potential to further investigate palaeo-atmospheres and characterise exoplanet atmospheres, as well as its applicability to the modern atmosphere.

References

Aiuppa, A., Shinohara, H., Tamburello, G., Giudice, G., Liuzzo, M. and Moretti, R., 2011. Hydrogen in the gas plume of an open-vent volcano, Mount Etna, Italy. *Journal of Geophysical Research: Solid Earth*, *116*(B10).

Alcott, L.J., Mills, B.J. and Poulton, S.W., 2019. Stepwise Earth oxygenation is an inherent property of global biogeochemical cycling. *Science*, *366*(6471), pp.1333-1337.

Alexander, B., Allman, D.J., Amos, H.M., Fairlie, T.D., Dachs, J., Hegg, D.A. and Sletten, R.S., 2012. Isotopic constraints on the formation pathways of sulfate aerosol in the marine boundary layer of the subtropical northeast Atlantic Ocean. *Journal of Geophysical Research: Atmospheres*, *117*(D6).

Alexander, B., Hastings, M.G., Allman, D.J., Dachs, J., Thornton, J.A. and Kunasek, S.A., 2009b. Quantifying atmospheric nitrate formation pathways based on a global model of the oxygen isotopic composition (Δ 17 O) of atmospheric nitrate. *Atmospheric Chemistry and Physics*, *9*(14), pp.5043-5056.

Alexander, B., Park, R.J., Jacob, D.J. and Gong, S., 2009a. Transition metal-catalyzed oxidation of atmospheric sulfur: Global implications for the sulfur budget. *Journal of Geophysical Research: Atmospheres*, *114*(D2).

Alexander, B., Savarino, J., Barkov, N.I., Delmas, R.J. and Thiemens, M.H., 2002. Climate driven changes in the oxidation pathways of atmospheric sulfur. *Geophysical research letters*, *29*(14), pp.30-1.

Alexander, B., Savarino, J., Kreutz, K.J. and Thiemens, M.H., 2004. Impact of preindustrial biomass-burning emissions on the oxidation pathways of tropospheric sulfur and nitrogen. *Journal of Geophysical Research: Atmospheres*, *109*(D8).

Alexander, B., Thiemens, M.H., Farquhar, J., Kaufman, A.J., Savarino, J. and Delmas, R.J., 2003. East Antarctic ice core sulfur isotope measurements over a complete glacial-interglacial cycle. *Journal of Geophysical Research: Atmospheres*, *108*(D24).

Alexander, B., Vollmer, M.K., Jackson, T., Weiss, R.F. and Thiemens, M.H., 2001. Stratospheric CO2 isotopic anomalies and SF6 and CFC tracer concentrations in the Arctic polar vortex. *Geophysical Research Letters*, *28*(21), pp.4103-4106.

Anderson, S.M., Hülsebusch, D. and Mauersberger, K., 1997. Surprising rate coefficients for four isotopic variants of O + O_2 + M. *The Journal of Chemical Physics*, *107*(14), pp.5385-5392.

Arnold, G.L., Anbar, A.D., Barling, J. and Lyons, T.W., 2004. Molybdenum isotope evidence for widespread anoxia in mid-Proterozoic oceans. S*cience*, *304*(5667), pp.87-90.

Atkinson, R., Baulch, D.L., Cox, R.A., Crowley, J.N., Hampson, R.F., Hynes, R.G., Jenkin, M.E., Rossi, M.J. and Troe, J., 2004. Evaluated kinetic and photochemical data for atmospheric chemistry: Volume I-gas phase reactions of Ox, HOx, NOx and SOx species. *Atmospheric chemistry and physics*, *4*(6), pp.1461-1738.

Bakakas Mayika, K., Moussavou, M., Prave, A.R., Lepland, A., Mbina, M. and Kirsimäe, K., The Paleoproterozoic Francevillian succession of Gabon and the Lomagundi-Jatuli event. *Geology*. https://doi.org/10.1130/G47651.1.

Balci, N., Shanks III, W.C., Mayer, B. and Mandernack, K.W., 2007. Oxygen and sulfur isotope systematics of sulfate produced by bacterial and abiotic oxidation of pyrite. *Geochimica et Cosmochimica Acta*, *71*(15), pp.3796-3811.

Bao, H., 2015. Sulfate: a time capsule for Earth's O_2, O_3, and H_2O. *Chemical Geology*, *395*, pp.108-118.

Bao, H., Campbell, D.A., Bockheim, J.G. and Thiemens, M.H., 2000. Origins of sulphate in Antarctic dry-valley soils as deduced from anomalous ^{17}O compositions. *Nature*, *407*(6803), pp.499-502.

Bao, H., Cao, X. and Hayles, J.A., 2016. Triple oxygen isotopes: fundamental relationships and applications. *Annual Review of Earth and Planetary Sciences*, *44*, pp.463-492.

Bao, H., Chen, Z.Q. and Zhou, C., 2012. An ^{17}O record of late Neoproterozoic glaciation in the Kimberley region, Western Australia. *Precambrian Research*, *216*, pp.152-161.

Bao, H., Fairchild, I.J., Wynn, P.M. and Spötl, C., 2009. Stretching the envelope of past surface environments: Neoproterozoic glacial lakes from Svalbard. *Science*, *323*(5910), pp.119-122.

Bao, H. and Gu, B., 2004. Natural perchlorate has a unique oxygen isotope signature, *Environmental Science and Technology*, 38(19), pp. 5073–5077.

Bao, H., Lyons, J.R. and Zhou, C., 2008. Triple oxygen isotope evidence for elevated CO_2 levels after a Neoproterozoic glaciation. *Nature*, *453*(7194), pp.504-506.

Bao, H. and Marchant, D. R., 2006. Quantifying sulfate components and their variations in soils of the McMurdo Dry Valleys, Antarctica, *Journal of Geophysical Research Atmospheres*, 111(16), pp. 1–13. doi: 10.1029/2005JD006669.

Bao, H., Michalski, G.M. and Thiemens, M.H., 2001. Sulfate oxygen-17 anomalies in desert varnishes. *Geochimica et Cosmochimica Acta*, *65*(13), pp.2029-2036.

Barkan, E. and Luz, B., 2005. High precision measurements of $^{17}O/^{16}O$ and $^{18}O/^{16}O$ ratios in H_2O, *Rapid Communications in Mass Spectrometry*, 19(24), pp. 3737–3742. doi: 10.1002/rcm.2250.

Barkan, E. and Luz, B., 2012. High-precision measurements of $^{17}O/^{16}O$ and $^{18}O/^{16}O$ ratios in CO_2. *Rapid communications in mass spectrometry*, *26*(23), pp.2733-2738.

Bekker, A. and Holland, H.D., 2012. Oxygen overshoot and recovery during the early Paleoproterozoic. *Earth and Planetary Science Letters*, *317*, pp.295-304.

Bekker, A., Holland, H.D., Wang, P.L., Rumble III, D., Stein, H.J., Hannah, J.L., Coetzee, L.L. and Beukes, N.J., 2004. Dating the rise of atmospheric oxygen. *Nature*, *427*(6970), pp.117-120.

Bellefroid, E.J., Hood, A.V.S., Hoffman, P.F., Thomas, M.D., Reinhard, C.T. and Planavsky, N.J., 2018. Constraints on Paleoproterozoic atmospheric oxygen levels. *Proceedings of the National Academy of Sciences*, *115*(32), pp.8104-8109.

Bender, M., Sowers, T. and Labeyrie, L., 1994. The Dole effect and its variations during the last 130,000 years as measured in the Vostok ice core. *Global Biogeochemical Cycles*, *8*(3), pp.363-376.

Benn, D.I., Le Hir, G., Bao, H., Donnadieu, Y., Dumas, C., Fleming, E.J., Hambrey, M.J., McMillan, E.A., Petronis, M.S., Ramstein, G. and Stevenson, C.T., 2015. Orbitally forced ice sheet fluctuations during the Marinoan Snowball Earth glaciation. *Nature Geoscience*, *8*(9), pp.704-707.

Bergman, N.M., Lenton, T.M. and Watson, A.J., 2004. COPSE: a new model of biogeochemical cycling over Phanerozoic time. *American Journal of Science*, *304*(5), pp.397-437.

Berner, R.A., 2006. GEOCARBSULF: a combined model for Phanerozoic atmospheric O_2 and CO_2. *Geochimica et Cosmochimica Acta*, *70*(23), pp.5653-5664.

Berner, R.A., 2009. Phanerozoic atmospheric oxygen: New results using the GEOCARBSULF model. *American Journal of Science*, *309*(7), pp.603-606.

Berner, R.A., Beerling, D.J., Dudley, R., Robinson, J.M. and Wildman Jr, R.A., 2003. Phanerozoic atmospheric oxygen. *Annual Review of Earth and Planetary Sciences*, *31*(1), pp.105-134.

Berner, R.A. and Canfield, D.E., 1989. A new model for atmospheric oxygen over Phanerozoic time. *American Journal of Science*, *289*(4), pp.333-361.

Bhattacharya, S.K., Pandey, A. and Savarino, J., 2008. Determination of intramolecular isotope distribution of ozone by oxidation reaction with silver metal. *Journal of Geophysical Research: Atmospheres*, *113*(D3).

Blättler, C.L., Claire, M.W., Prave, A.R., Kirsimäe, K., Higgins, J.A., Medvedev, P.V., Romashkin, A.E., Rychanchik, D.V., Zerkle, A.L., Paiste, K. and Kreitsmann, T., 2018. Two-billion-year-old evaporites capture Earth's great oxidation. *Science*, *360*(6386), pp.320-323.

Blunier, T., Barnett, B., Bender, M.L. and Hendricks, M.B., 2002. Biological oxygen productivity during the last 60,000 years from triple oxygen isotope measurements. *Global Biogeochemical Cycles*, *16*(3), pp.3-1.

Boering, K.A., Jackson, T., Hoag, K.J., Cole, A.S., Perri, M.J., Thiemens, M. and Atlas, E., 2004. Observations of the anomalous oxygen isotopic composition of carbon dioxide in the lower stratosphere and the flux of the anomaly to the troposphere. *Geophysical Research Letters*, *31*(3).

Böhlke, J.K., Ericksen, G.E. and Revesz, K., 1997. Stable isotope evidence for an atmospheric origin of desert nitrate deposits in northern Chile and southern California, USA. *chemical geology*, *136*(1-2), pp.135-152.

Broecker, W.S. and Van Donk, J., 1970. Insolation changes, ice volumes, and the O^{18} record in deep-sea cores. *Reviews of Geophysics*, *8*(1), pp.169-198.

Brunner, B., Einsiedl, F., Arnold, G.L., Müller, I., Templer, S. and Bernasconi, S.M., 2012. The reversibility of dissimilatory sulphate reduction and the cell-internal multi-step reduction of sulphite to sulphide: insights from the oxygen isotope composition of sulphate. *Isotopes in environmental and health studies*, *48*(1), pp.33-54.

Burkholder, J.B., Sander, S.P., Abbatt, J.P.D., Barker, J.R., Huie, R.E., Kolb, C.E., Kurylo, M.J., Orkin, V.L., Wilmouth, D.M. and Wine, P.H., 2015. *Chemical Kinetics and Photochemical Data for Use in Atmospheric Studies: Evaluation Number 18*. Pasadena, CA: Jet Propulsion Laboratory, National Aeronautics and Space Administration, 2015.

Canfield, D.E., 1998. A new model for Proterozoic ocean chemistry. *Nature*, *396*(6710), pp.450-453.

Canfield, D.E., 2004. The evolution of the Earth surface sulfur reservoir. *American Journal of Science*, *304*(10), pp.839-861.

Canfield, D.E., 2005. The early history of atmospheric oxygen: homage to Robert M. Garrels. *Annu. Rev. Earth Planet. Sci.*, *33*, pp.1-36.

Canfield, D.E., Zhang, S., Frank, A.B., Wang, X., Wang, H., Su, J., Ye, Y. and Frei, R., 2018. Highly fractionated chromium isotopes in Mesoproterozoic-aged shales and atmospheric oxygen. *Nature communications*, *9*(1), pp.1-11.

Cao, X. and Bao, H., 2013. Dynamic model constraints on oxygen-17 depletion in atmospheric O_2 after a snowball Earth. *Proceedings of the National Academy of Sciences*, *110*(36), pp.14546-14550.

Cao, X. and Liu, Y., 2011. Equilibrium mass-dependent fractionation relationships for triple oxygen isotopes. *Geochimica et Cosmochimica Acta*, *75*(23), pp.7435-7445.

Catling, D.C. and Claire, M.W., 2005. How Earth's atmosphere evolved to an oxic state: a status report. *Earth and Planetary Science Letters*, *237*(1-2), pp.1-20.

Catling, D.C., Claire, M.W. and Zahnle, K.J., 2007. Anaerobic methanotrophy and the rise of atmospheric oxygen. *Philosophical Transactions of the Royal Society A: Mathematical, Physical and Engineering Sciences*, *365*(1856), pp.1867-1888.

Catling, D.C., Claire, M.W., Zahnle, K.J., Quinn, R.C., Clark, B.C., Hecht, M.H. and Kounaves, S., 2010. Atmospheric origins of perchlorate on Mars and in the Atacama. *Journal of Geophysical Research: Planets*, *115*(E1).

Catling, D.C. and Kasting, J.F., 2017. *Atmospheric evolution on inhabited and lifeless worlds*. Cambridge University Press.

Chapman, S., 1930. XXXV. On ozone and atomic oxygen in the upper atmosphere. *The London, Edinburgh, and Dublin Philosophical Magazine and Journal of Science*, *10*(64), pp.369-383.

Claire, M., 2008. *Quantitative modeling of the rise in atmospheric oxygen*. University of Washington.

Claire, M.W., Catling, D.C. and Zahnle, K.J., 2006. Biogeochemical modelling of the rise in atmospheric oxygen. *Geobiology*, *4*(4), pp.239-269.

Claire, M.W., Kasting, J.F., Domagal-Goldman, S.D., Stüeken, E.E., Buick, R. and Meadows, V.S., 2014. Modeling the signature of sulfur mass-independent fractionation produced in the Archean atmosphere. *Geochimica et Cosmochimica Acta*, *141*, pp.365-380.

Cloud, P.E., 1968. Atmospheric and hydrospheric evolution on the primitive Earth. *Science*, *160*(3829), pp.729-736.

Cole, D.B., Mills, D.B., Erwin, D.H., Sperling, E.A., Porter, S.M., Reinhard, C.T. and Planavsky, N.J., 2020. On the co-evolution of surface oxygen levels and animals. *Geobiology*, *18*(3), pp.260-281.

Cole, D.B., Reinhard, C.T., Wang, X., Gueguen, B., Halverson, G.P., Gibson, T., Hodgskiss, M.S., McKenzie, N.R., Lyons, T.W. and Planavsky, N.J., 2016. A shale-hosted Cr isotope record of low atmospheric oxygen during the Proterozoic. *Geology*, *44*(7), pp.555-558.

Crockford, P.W., Hayles, J.A., Bao, H., Planavsky, N.J., Bekker, A., Fralick, P.W., Halverson, G.P., Bui, T.H., Peng, Y. and Wing, B.A., 2018. Triple oxygen isotope evidence for limited mid-Proterozoic primary productivity. *Nature*, *559*(7715), pp.613-616.

Crockford, P.W., Kunzmann, M., Bekker, A., Hayles, J., Bao, H., Halverson, G.P., Peng, Y., Bui, T.H., Cox, G.M., Gibson, T.M. and Wörndle, S., 2019. Claypool continued: Extending the isotopic record of sedimentary sulfate. *Chemical Geology*, *513*, pp.200-225.

Crowe, S.A., Paris, G., Katsev, S., Jones, C., Kim, S.T., Zerkle, A.L., Nomosatryo, S., Fowle, D.A., Adkins, J.F., Sessions, A.L. and Farquhar, J., 2014. Sulfate was a trace constituent of Archean seawater. *Science*, *346*(6210), pp.735-739.

Dahl, T.W. and Arens, S.K., 2020. The impacts of land plant evolution on Earth's climate and oxygenation state–An interdisciplinary review. *Chemical Geology*, p.119665.

Dahl, T.W., Hammarlund, E.U., Anbar, A.D., Bond, D.P., Gill, B.C., Gordon, G.W., Knoll, A.H., Nielsen, A.T., Schovsbo, N.H. and Canfield, D.E., 2010. Devonian rise in atmospheric oxygen correlated to the radiations of terrestrial plants and large predatory fish. *Proceedings of the National Academy of Sciences*, *107*(42), pp.17911-17915.

Daines, S.J. and Lenton, T.M., 2016. The effect of widespread early aerobic marine ecosystems on methane cycling and the Great Oxidation. *Earth and Planetary Science Letters*, *434*, pp.42-51.

Daines, S.J., Mills, B.J. and Lenton, T.M., 2017. Atmospheric oxygen regulation at low Proterozoic levels by incomplete oxidative weathering of sedimentary organic carbon. *Nature Communications*, *8*(1), pp.1-11.

Danielache, S.O., Eskebjerg, C., Johnson, M.S., Ueno, Y. and Yoshida, N., 2008. High-precision spectroscopy of ^{32}S, ^{33}S, and ^{34}S sulfur dioxide: Ultraviolet absorption cross sections and isotope effects. *Journal of Geophysical Research: Atmospheres*, *113*(D17).

Dasgupta, P.K., Martinelango, P.K., Jackson, W.A., Anderson, T.A., Tian, K., Tock, R.W. and Rajagopalan, S., 2005. The origin of naturally occurring perchlorate: the role of atmospheric processes. *Environmental Science & Technology*, *39*(6), pp.1569-1575.

Des Marais, D.J., Harwit, M.O., Jucks, K.W., Kasting, J.F., Lin, D.N., Lunine, J.I., Schneider, J., Seager, S., Traub, W.A. and Woolf, N.J., 2002. Remote sensing of planetary properties and biosignatures on extrasolar terrestrial planets. *Astrobiology*, *2*(2), pp.153-181.

Domagal-Goldman, S.D., Segura, A., Claire, M.W., Robinson, T.D. and Meadows, V.S., 2014. Abiotic ozone and oxygen in atmospheres similar to prebiotic Earth. *The Astrophysical Journal*, *792*(2), p.90.

Driese, S.G., Jirsa, M.A., Ren, M., Brantley, S.L., Sheldon, N.D., Parker, D. and Schmitz, M., 2011. Neoarchean paleoweathering of tonalite and metabasalt:

Implications for reconstructions of 2.69 Ga early terrestrial ecosystems and paleoatmospheric chemistry. *Precambrian Research*, *189*(1-2), pp.1-17.

Ehhalt, D., Prather, M., Dentener, F., Derwent, R., Dlugokencky, E.J., Holland, E., Isaksen, I., Katima, J., Kirchhoff, V., Matson, P. and Midgley, P., 2001. *Atmospheric chemistry and greenhouse gases* (No. PNNL-SA-39647). Pacific Northwest National Lab. (PNNL), Richland, WA (United States).

Endo, Y., Danielache, S.O., Ueno, Y., Hattori, S., Johnson, M.S., Yoshida, N. and Kjaergaard, H.G., 2015. Photoabsorption cross-section measurements of ^{32}S, ^{33}S, ^{34}S, and ^{36}S sulfur dioxide from 190 to 220 nm. *Journal of Geophysical Research: Atmospheres*, *120*(6), pp.2546-2557.

Ericksen, G.E., 1983. The Chilean Nitrate Deposits. *American Scientist*, *71*(4), pp.366-374.

Erwin, D.H., Laflamme, M., Tweedt, S.M., Sperling, E.A., Pisani, D. and Peterson, K.J., 2011. The Cambrian conundrum: early divergence and later ecological success in the early history of animals. *Science*, *334*(6059), pp.1091-1097.

Eugster, H.P., 1966. Sodium carbonate-bicarbonate minerals as indicators of Pco_2. *Journal of Geophysical Research*, *71*(14), pp.3369-3377.

Farquhar, J., Bao, H. and Thiemens, M., 2000. Atmospheric influence of Earth's earliest sulfur cycle. *Science*, *289*(5480), pp.756-758.

Farquhar, J., Zerkle, A.L. and Bekker, A., 2014. Geologic and geochemical constraints on Earth's early atmosphere. In: Holland, H.D. and Turekian, K.K. (Eds), Treatise on Geochemistry: Reference Module in Earth Systems and Environmental Sciences. Second Edition, Vol. 6: The Atmosphere – History. Elsevier, p91-138.

Feichter, J., Kjellström, E., Rodhe, H., Dentener, F., Lelieveldi, J. and Roelofs, G.J., 1996. Simulation of the tropospheric sulfur cycle in a global climate model. *Atmospheric Environment*, *30*(10-11), pp.1693-1707.

Figge, R.A. and White, J.W., 1995. High-resolution holocene and late glacial atmospheric CO_2 record: variability tied to changes in thermohaline circulation. *Global Biogeochemical Cycles*, *9*(3), pp.391-403.

Finlayson-Pitts, B.J. and Pitts Jr, J.N., 2000. *Chemistry of the Upper and Lower Atmosphere: Theory, Experiments, and Applications*. Academic Press.

Fiorella, R.P. and Sheldon, N.D., 2017. Equable end Mesoproterozoic climate in the absence of high CO_2. *Geology*, *45*(3), pp.231-234.

Fischer, W.W., Hemp, J. and Johnson, J.E., 2016. Evolution of oxygenic photosynthesis. *Annual Review of Earth and Planetary Sciences*, *44*, pp.647-683.

Fletcher, B.J., Beerling, D.J., Brentnall, S.J. and Royer, D.L., 2005. Fossil bryophytes as recorders of ancient CO_2 levels: experimental evidence and a Cretaceous case study. *Global Biogeochemical Cycles*, *19*(3).

Fleurat-Lessard, P., Grebenshchikov, S.Y., Schinke, R., Janssen, C. and Krankowsky, D., 2003. Isotope dependence of the O+ O_2 exchange reaction: Experiment and theory. *The Journal of chemical physics*, *119*(9), pp.4700-4712.

Frei, R., Gaucher, C., Poulton, S.W. and Canfield, D.E., 2009. Fluctuations in Precambrian atmospheric oxygenation recorded by chromium isotopes. *Nature*, *461*(7261), pp.250-253.

Früchtl, M., Janssen, C. and Röckmann, T., 2015. Experimental study on isotope fractionation effects in visible photolysis of O_3 and in the O+ O_3 odd oxygen sink reaction. *Journal of Geophysical Research: Atmospheres*, *120*(9), pp.4398-4416.

Geng, L., Cole-Dai, J., Alexander, B., Erbland, J., Savarino, J., Schauer, A.J., Steig, E.J., Lin, P., Fu, Q. and Zatko, M.C., 2014. On the origin of the occasional spring nitrate peak in Greenland snow. *Atmos. Chem. Phys*, *14*, pp.13361-13376.

Gibson, T.M., Shih, P.M., Cumming, V.M., Fischer, W.W., Crockford, P.W., Hodgskiss, M.S., Wörndle, S., Creaser, R.A., Rainbird, R.H., Skulski, T.M. and Halverson,

G.P., 2018. Precise age of Bangiomorpha pubescens dates the origin of eukaryotic photosynthesis. *Geology*, *46*(2), pp.135-138.

Gilleaudeau, G.J., Frei, R., Kaufman, A.J., Kah, L.C., Azmy, K., Bartley, J.K., Chernyavskiy, P. and Knoll, A.H., 2016. Oxygenation of the mid-Proterozoic atmosphere: clues from chromium isotopes in carbonates. *Geochem. Perspect. Lett*, *2*(2), pp.178-187.

Gillon, M., Triaud, A.H., Demory, B.O., Jehin, E., Agol, E., Deck, K.M., Lederer, S.M., De Wit, J., Burdanov, A., Ingalls, J.G. and Bolmont, E., 2017. Seven temperate terrestrial planets around the nearby ultracool dwarf star TRAPPIST-1. *Nature*, *542*(7642), pp.456-460.

Giorgi, F. and Chameides, W.L., 1985. The rainout parameterization in a photochemical model. *Journal of Geophysical Research: Atmospheres*, *90*(D5), pp.7872-7880.

Glasspool, I.J. and Scott, A.C., 2010. Phanerozoic concentrations of atmospheric oxygen reconstructed from sedimentary charcoal. *Nature Geoscience*, *3*(9), pp.627-630.

Glasspool, I.J., Scott, A.C., Waltham, D., Pronina, N.V. and Shao, L., 2015. The impact of fire on the Late Paleozoic Earth system. *Frontiers in Plant Science*, *6*, p.756.

Goldblatt, C., Lenton, T.M. and Watson, A.J., 2006. Bistability of atmospheric oxygen and the Great Oxidation. *Nature*, *443*(7112), pp.683-686.

Gregory, B.S., Claire, M.W. and Rugheimer, S., 2019. Photochemical Modelling of Atmospheric Oxygen Levels Reveals Three Stable States [Abstract], *Goldschmidt Abstracts*, 2019, 1201.

Gregory, B.S., Claire, M.W. and Rugheimer, S., 2021. Photochemical modelling of atmospheric oxygen levels confirms two stable states. *Earth and Planetary Science Letters*, *561*, 116818.

Guenther, J., Erbacher, B., Krankowsky, D. and Mauersberger, K., 1999. Pressure dependence of two relative ozone formation rate coefficients. *Chemical Physics Letters*, *306*(5-6), pp.209-213.

Guy, R.D., Fogel, M.L. and Berry, J.A., 1993. Photosynthetic fractionation of the stable isotopes of oxygen and carbon. *Plant Physiology*, *101*(1), pp.37-47.

Guzmán-Marmolejo, A., Segura, A. and Escobar-Briones, E., 2013. Abiotic production of methane in terrestrial planets. *Astrobiology*, *13*(6), pp.550-559.

Habicht, K.S., Gade, M., Thamdrup, B., Berg, P. and Canfield, D.E., 2002. Calibration of sulfate levels in the Archean ocean. *Science*, *298*(5602), pp.2372-2374.

Haqq-Misra, J.D., Domagal-Goldman, S.D., Kasting, P.J. and Kasting, J.F., 2008. A revised, hazy methane greenhouse for the Archean Earth. *Astrobiology*, *8*(6), pp.1127-1137.

Harman, C.E., Felton, R., Hu, R., Domagal-Goldman, S.D., Segura, A., Tian, F. and Kasting, J.F., 2018. Abiotic O_2 levels on planets around F, G, K, and M stars: effects of lightning-produced catalysts in eliminating oxygen false positives. *The Astrophysical Journal*, *866*(1), p.56.

Hartmann, D.L., 1994. *Global Physical Climatology (International geophysics; v. 56)*. Academic Press.

Hayes, J.M., Strauss, H. and Kaufman, A.J., 1999. The abundance of ^{13}C in marine organic matter and isotopic fractionation in the global biogeochemical cycle of carbon during the past 800 Ma. *Chemical Geology*, *161*(1-3), pp.103-125.

Hemingway, J.D., Olson, H., Turchyn, A.V., Tipper, E.T., Bickle, M.J. and Johnston, D.T., 2020. Triple oxygen isotope insight into terrestrial pyrite oxidation. *Proceedings of the National Academy of Sciences*, *117*(14), pp.7650-7657.

Hitchcock, D.R. and Lovelock, J.E., 1967. Life detection by atmospheric analysis. *Icarus*, *7*(1-3), pp.149-159.

Hofmann, M.E., Horváth, B. and Pack, A., 2012. Triple oxygen isotope equilibrium fractionation between carbon dioxide and water. *Earth and Planetary Science Letters*, *319*, pp.159-164.

Hoffman, P.F., Kaufman, A.J., Halverson, G.P. and Schrag, D.P., 1998. A Neoproterozoic snowball earth. *science*, *281*(5381), pp.1342-1346.

Holland, H.D., 1962. Model for the evolution of the Earth's atmosphere. *Petrologic studies: a volume in honor of A.F. Buddington*.

Holland H.D.,1994. Early Proterozoic atmospheric change. In: Bengtson S., ed. 1994. *Early life on earth. Nobel Symposium. vol. 84*. Columbia University Press; New York, NY. pp. 237–244.

Holland, H.D., 2002. Volcanic gases, black smokers, and the Great Oxidation Event. *Geochimica et Cosmochimica acta*, *66*(21), pp.3811-3826.

Hsu, C.C., Mebel, A.M. and Lin, M.C., 1996. Ab initio molecular orbital study of the HCO+ O_2 reaction: Direct versus indirect abstraction channels. *The Journal of ChemicalPphysics*, *105*(6), pp.2346-2352.

Izon, G., Zerkle, A.L., Williford, K.H., Farquhar, J., Poulton, S.W. and Claire, M.W., 2017. Biological regulation of atmospheric chemistry en route to planetary oxygenation. *Proceedings of the National Academy of Sciences*, *114*(13), pp.E2571-E2579.

Jackson, W.A., Böhlke, J.K., Gu, B., Hatzinger, P.B. and Sturchio, N.C., 2010. Isotopic composition and origin of indigenous natural perchlorate and co-occurring nitrate in the southwestern United States. *Environmental science & technology*, *44*(13), pp.4869-4876.

Jagniecki, E.A., Lowenstein, T.K., Jenkins, D.M. and Demicco, R.V., 2015. Eocene atmospheric CO_2 from the nahcolite proxy. *Geology*, *43*(12), pp.1075-1078.

Janssen, C., 2005. Intramolecular isotope distribution in heavy ozone ($^{16}O^{18}O^{16}O$ and $^{16}O^{16}O^{18}O$). *Journal of Geophysical Research: Atmospheres*, *110*(D8).

Janssen, C., Guenther, J., Krankowsky, D. and Mauersberger, K., 2003. Temperature dependence of ozone rate coefficients and isotopologue fractionation in ^{16}O–^{18}O oxygen mixtures. *Chemical Physics Letters*, *367*(1-2), pp.34-38.

Janssen, C., Guenther, J., Mauersberger, K. and Krankowsky, D., 2001. Kinetic origin of the ozone isotope effect: a critical analysis of enrichments and rate coefficients. *Physical Chemistry Chemical Physics*, *3*(21), pp.4718-4721.

Johnson, A.C., Romaniello, S.J., Reinhard, C.T., Gregory, D.D., Garcia-Robledo, E., Revsbech, N.P., Canfield, D.E., Lyons, T.W. and Anbar, A.D., 2019. Experimental determination of pyrite and molybdenite oxidation kinetics at nanomolar oxygen concentrations. *Geochimica et Cosmochimica Acta*, *249*, pp.160-172.

Johnston, J.C. and Thiemens, M.H., 1997. The isotopic composition of tropospheric ozone in three environments. *Journal of Geophysical Research: Atmospheres*, *102*(D21), pp.25395-25404.

Johnson, J.E., Gerpheide, A., Lamb, M.P. and Fischer, W.W., 2014. O2 constraints from Paleoproterozoic detrital pyrite and uraninite. *Bulletin*, *126*(5-6), pp.813-830.

Kah, L.C. and Riding, R., 2007. Mesoproterozoic carbon dioxide levels inferred from calcified cyanobacteria. *Geology*, *35*(9), pp.799-802.

Kaltenegger, L. and Traub, W.A., 2009. Transits of Earth-like planets. *The Astrophysical Journal*, *698*(1), p.519.

Kaltenegger, L., Lin, Z. and Madden, J., 2020. High-resolution Transmission Spectra of Earth Through Geological Time. *The Astrophysical Journal Letters*, *892*(1), L17.

Kaltenegger, L., Traub, W.A. and Jucks, K.W., 2007. Spectral evolution of an Earth-like planet. *The Astrophysical Journal*, *658*(1), p.598.

Karhu, J.A., 1993. Paleoproterozoic evolution of the carbon isotope ratios of sedimentary carbonates in the Fennoscandian Shield. *Geological Survey of Finland Bulletin,* 371, pp. 1-87.

Karhu, J.A. and Holland, H.D., 1996. Carbon isotopes and the rise of atmospheric oxygen. *Geology*, *24*(10), pp.867-870.

Kasting, J.F., 1987. Theoretical constraints on oxygen and carbon dioxide concentrations in the Precambrian atmosphere. *Precambrian research*, *34*(3-4), pp.205-229.

Kasting, J.F., 1990. Bolide impacts and the oxidation state of carbon in the Earth's early atmosphere. *Origins of Life and Evolution of the Biosphere*, *20*(3-4), pp.199-231.

Kasting, J.F., 1993. Earth's early atmosphere. *Science*, *259*(5097), pp.920-926.

Kasting, J.F. and Donahue, T.M., 1980. The evolution of atmospheric ozone. *Journal of Geophysical Research: Oceans*, *85*(C6), pp.3255-3263.

Kasting, J.F., Holland, H.D. and Pinto, J.P., 1985. Oxidant abundances in rainwater and the evolution of atmospheric oxygen. *Journal of Geophysical Research: Atmospheres*, *90*(D6), pp.10497-10510.

Kaufman, A.J., Knoll, A.H. and Narbonne, G.M., 1997. Isotopes, ice ages, and terminal Proterozoic earth history. *Proceedings of the National Academy of Sciences*, *94*(13), pp.6600-6605.

Kaufman, A.J. and Xiao, S., 2003. High CO 2 levels in the Proterozoic atmosphere estimated from analyses of individual microfossils. *Nature*, *425*(6955), pp.279-282.

Kaye, J.A. and Strobel, D.F., 1983. Enhancement of heavy ozone in the Earth's atmosphere?. *Journal of Geophysical Research: Oceans*, *88*(C13), pp.8447-8452.

Kennedy, M.J., 1996. Stratigraphy, sedimentology, and isotopic geochemistry of Australian Neoproterozoic postglacial cap dolostones; deglaciation, $\delta^{13}C$ excursions, and carbonate precipitation. *Journal of sedimentary Research*, *66*(6), pp.1050-1064.

Kharecha, P., Kasting, J. and Siefert, J., 2005. A coupled atmosphere–ecosystem model of the early Archean Earth. *Geobiology*, *3*(2), pp.53-76.

KIDA Kinetic Database for Astrochemistry, 2020. *KIDA: Kinetic Database for Atrochemistry.* [online] Available at: http://kida.astrophy.u-bordeaux.fr. [Accessed 2017- 2020].

Killingsworth, B.A., Hayles, J.A., Zhou, C. and Bao, H., 2013. Sedimentary constraints on the duration of the Marinoan Oxygen-17 Depletion (MOSD)

event. *Proceedings of the National Academy of Sciences*, *110*(44), pp.17686-17690.

Klein, C., 2005. Some Precambrian banded iron-formations (BIFs) from around the world: Their age, geologic setting, mineralogy, metamorphism, geochemistry, and origins. *American Mineralogist*, *90*(10), pp.1473-1499.

Knoll, A.H., Kaufman, A.J. and Semikhatov, M.A., 1995. The carbon-isotopic composition of Proterozoic carbonates: Riphean successions from Northwestern Siberia (Anabar massif, Turukhansk uplift). *American Journal of Science*, *295*(7), p.823.

Kohl, I. and Bao, H., 2011. Triple-oxygen-isotope determination of molecular oxygen incorporation in sulfate produced during abiotic pyrite oxidation (pH= 2–11). *Geochimica et Cosmochimica Acta*, *75*(7), pp.1785-1798.

Kounaves, S.P., Hecht, M.H., Kapit, J., Gospodinova, K., DeFlores, L., Quinn, R.C., Boynton, W.V., Clark, B.C., Catling, D.C., Hredzak, P. and Ming, D.W., 2010. Wet Chemistry experiments on the 2007 Phoenix Mars Scout Lander mission: Data analysis and results. *Journal of Geophysical Research: Planets*, *115*(E1).

Krankowsky, D., Bartecki, F., Klees, G.G., Mauersberger, K., Schellenbach, K. and Stehr, J., 1995. Measurement of heavy isotope enrichment in tropospheric ozone. *Geophysical Research Letters*, *22*(13), pp.1713-1716.

Krankowsky, D., Lämmerzahl, P. and Mauersberger, K., 2000. Isotopic measurements of stratospheric ozone. *Geophysical research letters*, *27*(17), pp.2593-2595.

Krankowsky, D., Lämmerzahl, P., Mauersberger, K., Janssen, C., Tuzson, B. and Röckmann, T., 2007. Stratospheric ozone isotope fractionations derived from collected samples. *Journal of Geophysical Research: Atmospheres*, *112*(D8).

Krause, A.J., Mills, B.J., Zhang, S., Planavsky, N.J., Lenton, T.M. and Poulton, S.W., 2018. Stepwise oxygenation of the Paleozoic atmosphere. *Nature communications*, *9*(1), pp.1-10.

Kump, L.R., 2008. The rise of atmospheric oxygen. *Nature*, *451*(7176), pp.277-278.

Kunasek, S.A., Alexander, B., Steig, E.J., Hastings, M.G., Gleason, D.J. and Jarvis, J.C., 2008. Measurements and modeling of $\Delta^{17}O$ of nitrate in snowpits from Summit, Greenland. *Journal of Geophysical Research: Atmospheres*, *113*(D24).

Kunasek, S.A., Alexander, B., Steig, E.J., Sofen, E.D., Jackson, T.L., Thiemens, M.H., McConnell, J.R., Gleason, D.J. and Amos, H.M., 2010. Sulfate sources and oxidation chemistry over the past 230 years from sulfur and oxygen isotopes of sulfate in a West Antarctic ice core. *Journal of Geophysical Research: Atmospheres*, *115*(D18).

Laakso, T.A. and Schrag, D.P., 2017. A theory of atmospheric oxygen. *Geobiology, 15(3)*, pp.366-384.

Lämmerzahl, P., Röckmann, T., Brenninkmeijer, C.A., Krankowsky, D. and Mauersberger, K., 2002. Oxygen isotope composition of stratospheric carbon dioxide. *Geophysical Research Letters*, *29*(12), pp.23-1.

Lederberg, J., 1965. Signs of life. *Nature*, *207*(4992), pp.9-13.

Lee, C.C.W., Savarino, J. and Thiemens, M.H., 2001. Mass independent oxygen isotopic composition of atmospheric sulfate: Origin and implications for the present and past atmosphere of Earth and Mars. *Geophysical research letters*, *28*(9), pp.1783-1786.

Lee, C.C.W. and Thiemens, M.H., 2001. The $\delta^{17}O$ and $\delta^{18}O$ measurements of atmospheric sulfate from a coastal and high alpine region: A mass-independent isotopic anomaly. *Journal of Geophysical Research: Atmospheres*, *106*(D15), pp.17359-17373.

Léger, A., Pirre, M. and Marceau, F.J., 1993. Search for primitive life on a distant planet: relevance of O_2 and O_3 detections. *Astronomy and Astrophysics*, *277*, p.309.

Lenton T. M., 2013. Fire feedbacks on atmospheric oxygen. In: Belcher C. M. ed., 2013. *Fire Phenomena and the Earth System: An Interdisciplinary Guide to Fire Science*. Chichester: John Wiley and Sons, Ltd. Ch.15, 289–308.

Lenton, T.M., Dahl, T.W., Daines, S.J., Mills, B.J., Ozaki, K., Saltzman, M.R. and Porada, P., 2016. Earliest land plants created modern levels of atmospheric oxygen. *Proceedings of the National Academy of Sciences*, *113*(35), pp.9704-9709.

Lenton, T.M. and Daines, S.J., 2017. Biogeochemical transformations in the history of the ocean. *Annual Review of Marine Science*, *9*, pp.31-58.

Lenton, T.M., Daines, S.J. and Mills, B.J., 2018. COPSE reloaded: an improved model of biogeochemical cycling over Phanerozoic time. *Earth-Science Reviews*, *178*, pp.1-28.

Lepland, A., Melezhik, V.A., Papineau, D., Romashkin, A.E. and Joosu, L., 2013. 7.7 The Earliest Phosphorites: Radical Change in the Phosphorus Cycle During the Palaeoproterozoic. In *Reading the Archive of Earth's Oxygenation* (pp. 1275-1296). Springer, Berlin, Heidelberg.

Liang, M.C., Blake, G.A., Lewis, B.R. and Yung, Y.L., 2007. Oxygen isotopic composition of carbon dioxide in the middle atmosphere. *Proceedings of the National Academy of Sciences*, *104*(1), pp.21-25.

Liang, M.C., Irion, F.W., Weibel, J.D., Miller, C.E., Blake, G.A. and Yung, Y.L., 2006. Isotopic composition of stratospheric ozone. *Journal of Geophysical Research: Atmospheres*, *111*(D2).

Liang, M.C., Mahata, S., Laskar, A.H. and Bhattacharya, S.K., 2017a. Spatiotemporal variability of oxygen isotope anomaly in near surface air CO_2 over urban, semi-urban and ocean areas in and around Taiwan. *Aerosol and Air Quality Research*, *17*(3), pp.706-720.

Liang, M.C., Mahata, S., Laskar, A.H., Thiemens, M.H. and Newman, S., 2017b. Oxygen isotope anomaly in tropospheric CO_2 and implications for CO_2 residence time in the atmosphere and gross primary productivity. *Scientific reports*, *7*(1), pp.1-12.

Lovelock, J.E., 1965. A physical basis for life detection experiments. *Nature*, *207*(997), pp.568-570.

Luz, B., Barkan, E., Bender, M.L., Thiemens, M.H. and Boering, K.A., 1999. Triple-isotope composition of atmospheric oxygen as a tracer of biosphere productivity. *Nature*, *400*(6744), pp.547-550.

Lyons, J. R., 2001. Transfer of mass-independent fractionation in ozone to other oxygen-containing radicals in the atmosphere, 28(17), pp. 3231–3234.

Lyons, T.W., Reinhard, C.T. and Planavsky, N.J., 2014. The rise of oxygen in Earth's early ocean and atmosphere. *Nature*, *506*(7488), pp.307-315.

Manabe, S. and Wetherald, R.T., 1967. Thermal equilibrium of the atmosphere with a given distribution of relative humidity. *Journal of the Atmospheric Sciences.* 24(3), pp. 241-259.

Manion, J.A., Huie, R.E., Levin, R.D., Burgess Jr, D.R., Orkin, V.L., Tsang, W., McGivern, W.S., Hudgens, J.W., Knyazev, V.D., Atkinson, D.B. and Chai, E., 2015. NIST Chemical Kinetics Database, NIST Standard Reference Database 17, Version 7.0 (Web Version), Release 1.6. 8, Data Version 2015.09. *National Inst. of Standards and Technology, Gaithersburg, MD, http://kinetics. nist. gov*.

Marrero, T.R. and Mason, E.A., 1972. Gaseous diffusion coefficients. *Journal of Physical and Chemical Reference Data*, *1*(1), pp.3-118.

Massie, S.T. and Hunten, D.M., 1981. Stratospheric eddy diffusion coefficients from tracer data. *Journal of Geophysical Research: Oceans*, *86*(C10), pp.9859-9868.

Mauersberger, K., 1987. Ozone isotope measurements in the stratosphere. *Geophysical Research Letters*, *14*(1), pp.80-83.

Mauersberger, K., Erbacher, B., Krankowsky, D., Günther, J. and Nickel, R., 1999. Ozone isotope enrichment: Isotopomer-specific rate coefficients. *Science*, *283*(5400), pp.370-372.

Mauersberger, K., Lämmerzahl, P. and Krankowsky, D., 2001. Stratospheric ozone isotope enrichments—revisited. *Geophysical Research Letters*, *28*(16), pp.3155-3158.

McCabe, J.R., Savarino, J., Alexander, B., Gong, S. and Thiemens, M.H., 2006. Isotopic constraints on non-photochemical sulfate production in the Arctic winter. *Geophysical research letters*, *33*(5).

McCabe, J.R., Thiemens, M.H. and Savarino, J., 2007. A record of ozone variability in South Pole Antarctic snow: Role of nitrate oxygen isotopes. *Journal of Geophysical Research: Atmospheres*, *112*(D12).

Meadows, V.S. and Crisp, D., 1996. Ground-based near-infrared observations of the Venus nightside: The thermal structure and water abundance near the surface. *Journal of Geophysical Research: Planets*, *101*(E2), pp.4595-4622.

Michalski, G., Bhattacharya, S.K. and Girsch, G., 2014. NO_x cycle and the tropospheric ozone isotope anomaly: an experimental investigation. *Atmospheric Chemistry & Physics*, *14*(10).

Michalski, G., Bockheim, J.G., Kendall, C. and Thiemens, M., 2005. Isotopic composition of Antarctic Dry Valley nitrate: Implications for NO_y sources and cycling in Antarctica. *Geophysical Research Letters*, *32*(13).

Michalski, G., Böhlke, J.K. and Thiemens, M., 2004b. Long term atmospheric deposition as the source of nitrate and other salts in the Atacama Desert, Chile: New evidence from mass-independent oxygen isotopic compositions. *Geochimica et Cosmochimica Acta*, *68*(20), pp.4023-4038.

Michalski, G., Meixner, T., Fenn, M., Hernandez, L., Sirulnik, A., Allen, E. and Thiemens, M., 2004a. Tracing atmospheric nitrate deposition in a complex semiarid ecosystem using $\Delta^{17}O$. *Environmental Science & Technology*, *38*(7), pp.2175-2181.

Michalski, G., Scott, Z., Kabiling, M. and Thiemens, M.H., 2003. First measurements and modeling of $\Delta^{17}O$ in atmospheric nitrate. *Geophysical Research Letters*, *30*(16), p.1870.

Michalski, G. and Thiemens M. H., 2000. Mass independent fractionation in nitrate aerosols, *EOS, Transactions of the American Geophysical Union*, 81 (48), Fall Meet. Suppl., Abstract A11b-13, p.F120.

Mills, B.J., Krause, A.J., Scotese, C.R., Hill, D.J., Shields, G.A. and Lenton, T.M., 2019. Modelling the long-term carbon cycle, atmospheric CO_2, and Earth surface temperature from late Neoproterozoic to present day. *Gondwana Research*, *67*, pp.172-186.

Mills, B.J., Scotese, C.R., Walding, N.G., Shields, G.A. and Lenton, T.M., 2017. Elevated CO_2 degassing rates prevented the return of Snowball Earth during the Phanerozoic. *Nature communications*, *8*(1), pp.1-7.

Mitchell, R.L. and Sheldon, N.D., 2010. The~ 1100 Ma Sturgeon Falls paleosol revisited: Implications for Mesoproterozoic weathering environments and atmospheric CO_2 levels. *Precambrian Research*, *183*(4), pp.738-748.

Mix, A.C. and Ruddiman, W.F., 1984. Oxygen-isotope analyses and Pleistocene ice volumes. *Quaternary Research*, *21*(1), pp.1-20.

Moles, N.R., Boyce, A.J., Selby D., Warke, M.R., Gregory, B., and Claire, M.W. (2020). Global seawater sulfate isotope composition and atmospheric-biosphere evolution constrained at 605 Ma by pyrite Re-Os dating and $\delta^{34}S$, $\delta^{18}O$ and $\Delta^{17}O$ analyses of the Aberfeldy stratiform barite deposits, Scotland [Abstract], *Sulfur in the Earth system conference.* Geological Society of London, 16-17 November.

Morin, S., Savarino, J., Bekki, S., Gong, S. and Bottenheim, J.W., 2007. Signature of Arctic surface ozone depletion events in the isotope anomaly ($\Delta^{17}O$) of atmospheric nitrate.

Morin, S., Savarino, J., Frey, M.M., Domine, F., Jacobi, H.W., Kaleschke, L. and Martins, J.M., 2009. Comprehensive isotopic composition of atmospheric nitrate in the Atlantic Ocean boundary layer from 65 S to 79 N. *Journal of Geophysical Research: Atmospheres*, *114*(D5).

Murakami, T., Sreenivas, B., Sharma, S.D. and Sugimori, H., 2011. Quantification of atmospheric oxygen levels during the Paleoproterozoic using paleosol compositions and iron oxidation kinetics. *Geochimica et Cosmochimica Acta*, *75*(14), pp.3982-4004.

Nagel, O.W., Waldron, S. and Jones, H.G., 2001. An off-line implementation of the stable isotope technique for measurements of alternative respiratory pathway activities. *Plant Physiology*, *127*(3), pp.1279-1286.

NASA Exoplanet Exploration Program and the Jet Propulsion Laboratory, 2020. *NASA Exoplanet Exploration: Planets Beyond Our Solar System.* [online] Available at: https://exoplanets.nasa.gov. [Accessed 4 September 2020].

Ndengué, S., Madronich, S., Gatti, F., Meyer, H.D., Motapon, O. and Jost, R., 2014. Ozone photolysis: Strong isotopologue/isotopomer selectivity in the stratosphere. *Journal of Geophysical Research: Atmospheres*, *119*(7), pp.4286-4302.

Och, L.M. and Shields-Zhou, G.A., 2012. The Neoproterozoic oxygenation event: environmental perturbations and biogeochemical cycling. *Earth-Science Reviews*, *110*(1-4), pp.26-57.

Ozaki, K., Reinhard, C.T. and Tajika, E., 2019. A sluggish mid-Proterozoic biosphere and its effect on Earth's redox balance. *Geobiology*, *17*(1), pp.3-11.

Paiste, K., Lepland, A., Zerkle, A.L., Kirsimäe, K., Kreitsmann, T., Mänd, K., Romashkin, A.E., Rychanchik, D.V. and Prave, A.R., 2020. Identifying global vs. basinal controls on Paleoproterozoic organic carbon and sulfur isotope records. *Earth-Science Reviews*, p.103230.

Papineau, D., 2010. Global biogeochemical changes at both ends of the Proterozoic: insights from phosphorites. *Astrobiology*, *10*(2), pp.165-181.

Pavlov, A.A., Hurtgen, M.T., Kasting, J.F. and Arthur, M.A., 2003. Methane-rich Proterozoic atmosphere? *Geology*, *31*(1), pp.87-90.

Pavlov, A.A. and Kasting, J.F., 2002. Mass-independent fractionation of sulfur isotopes in Archean sediments: strong evidence for an anoxic Archean atmosphere. *Astrobiology*, *2*(1), pp.27-41.

Pearson, P.N. and Palmer, M.R., 2000. Atmospheric carbon dioxide concentrations over the past 60 million years. *Nature*, *406*(6797), pp.695-699.

Peng, Y., Bao, H., Zhou, C. and Yuan, X., 2011. ^{17}O-depleted barite from two Marinoan cap dolostone sections, South China. *Earth and Planetary Science Letters*, *305*(1-2), pp.21-31.

Pierrehumbert, R.T., 2004. High levels of atmospheric carbon dioxide necessary for the termination of global glaciation. *Nature*, *429*(6992), pp.646-649.

Planavsky, N.J., Bekker, A., Hofmann, A., Owens, J.D. and Lyons, T.W., 2012. Sulfur record of rising and falling marine oxygen and sulfate levels during the Lomagundi event. *Proceedings of the National Academy of Sciences*, *109*(45), pp.18300-18305.

Planavsky, N.J., Cole, D.B., Isson, T.T., Reinhard, C.T., Crockford, P.W., Sheldon, N.D. and Lyons, T.W., 2018. A case for low atmospheric oxygen levels during Earth's middle history. *Emerging Topics in Life Sciences*, *2*(2), pp.149-159.

Planavsky, N.J., Reinhard, C.T., Isson, T.T., Ozaki, K. and Crockford, P.W., 2020. Large Mass-Independent Oxygen Isotope Fractionations in Mid-Proterozoic Sediments: Evidence for a Low-Oxygen Atmosphere?. *Astrobiology*, *20*(5), pp.628-636.

Planavsky, N.J., Reinhard, C.T., Wang, X., Thomson, D., McGoldrick, P., Rainbird, R.H., Johnson, T., Fischer, W.W. and Lyons, T.W., 2014. Low Mid-Proterozoic atmospheric oxygen levels and the delayed rise of animals. *science*, *346*(6209), pp.635-638.

Popp, B.N., Takigiku, R., Hayes, J.M., Louda, J.W. and Baker, E.W., 1989. The post-Paleozoic chronology and mechanism of ^{13}C depletion in primary marine organic matter. *American Journal of Science*, *289*(4), pp.436-454.

Rasmussen, B. and Buick, R., 1999. Redox state of the Archean atmosphere: evidence from detrital heavy minerals in ca. 3250–2750 Ma sandstones from the Pilbara Craton, Australia. *Geology*, *27*(2), pp.115-118.

Royer, D.L., 2001. Stomatal density and stomatal index as indicators of paleoatmospheric CO_2 concentration. *Review of Palaeobotany and Palynology*, *114*(1-2), pp.1-28.

Royer, D.L., 2014. Atmospheric CO_2 and O_2 during the Phanerozoic: Tools, patterns, and impacts. In: Holland, H.D. and Turekian, K.K. (Eds), Treatise on Geochemistry: Reference Module in Earth Systems and Environmental Sciences. Second Edition, Vol. 6: The Atmosphere – History. Elsevier, p251-267.

Royer, D.L., Donnadieu, Y., Park, J., Kowalczyk, J. and Godderis, Y., 2014. Error analysis of CO_2 and O_2 estimates from the long-term geochemical model GEOCARBSULF. *American Journal of Science*, *314*(9), pp.1259-1283.

Rugheimer, S. and Kaltenegger, L., 2018. Spectra of Earth-like planets through geological evolution around FGKM stars. *The Astrophysical Journal*, *854*(1), p.19.

Rugheimer, S., Kaltenegger, L., Segura, A., Linsky, J. and Mohanty, S., 2015. Effect of UV radiation on the spectral fingerprints of Earth-like planets orbiting M stars. *The Astrophysical Journal*, *809*(1), p.57.

Rye, R. and Holland, H.D., 1998. Paleosols and the evolution of atmospheric oxygen: a critical review. *American Journal of Science*, *298*(8), p.621.

Sagan, C. and Mullen, G., 1972. Earth and Mars: Evolution of atmospheres and surface temperatures. *Science*, *177*(4043), pp.52-56.

Sander, S.P., Golden, D.M., Kurylo, M.J., Moortgat, G.K., Wine, P.H., Ravishankara, A.R., Kolb, C.E., Molina, M.J., Finlayson-Pitts, B.J., Huie, R.E. and Orkin, V.L., 2006. *Chemical kinetics and photochemical data for use in atmospheric studies evaluation number 15*. Pasadena, CA: Jet Propulsion Laboratory, National Aeronautics and Space Administration, 2006.

Sansjofre, P., Ader, M., Trindade, R.I.F., Elie, M., Lyons, J., Cartigny, P. and Nogueira, A.C.R., 2011. A carbon isotope challenge to the snowball Earth. *Nature*, *478*(7367), pp.93-96.

Savarino, J., Bhattacharya, S.K., Morin, S., Baroni, M. and Doussin, J.F., 2008. The NO+ O_3 reaction: A triple oxygen isotope perspective on the reaction dynamics

and atmospheric implications for the transfer of the ozone isotope anomaly. *The Journal of chemical physics*, *128*(19), p.194303.

Savarino, J., Kaiser, J., Morin, S., Sigman, D.M. and Thiemens, M.H., 2007. Nitrogen and oxygen isotopic constraints on the origin of atmospheric nitrate in coastal Antarctica. *Atmospheric Chemistry and Physics*, *7*(8), pp.1925-1945.

Savarino, J., Lee, C.C. and Thiemens, M.H., 2000. Laboratory oxygen isotopic study of sulfur (IV) oxidation: Origin of the mass-independent oxygen isotopic anomaly in atmospheric sulfates and sulfate mineral deposits on Earth. *Journal of Geophysical Research: Atmospheres*, *105*(D23), pp.29079-29088.

Savarino, J., Morin, S., Erbland, J., Grannec, F., Patey, M.D., Vicars, W., Alexander, B. and Achterberg, E.P., 2013. Isotopic composition of atmospheric nitrate in a tropical marine boundary layer. *Proceedings of the National Academy of Sciences*, *110*(44), pp.17668-17673.

Savarino, J. and Thiemens, M.H., 1999. Analytical procedure to determine both $\delta^{18}O$ and $\delta^{17}O$ of H_2O_2 in natural water and first measurements. *Atmospheric Environment*, *33*(22), pp.3683-3690.

Schlesinger, W.H. and Bernhardt, E.S., 2013. *Biogeochemistry: An analysis of global change*. 3rd Edn. Elsevier, Waltham, MA.

Schmidt, P.W. and Williams, G.E., 1995. The Neoproterozoic climatic paradox: equatorial palaeolatitude for Marinoan glaciation near sea level in South Australia. *Earth and Planetary Science Letters*, *134*(1-2), pp.107-124.

Schröder, S., Bekker, A., Beukes, N.J., Strauss, H. and Van Niekerk, H.S., 2008. Rise in seawater sulphate concentration associated with the Paleoproterozoic positive carbon isotope excursion: evidence from sulphate evaporites in the~ 2.2–2.1 Gyr shallow-marine Lucknow Formation, South Africa. *Terra Nova*, *20*(2), pp.108-117.

Segura, A., Kasting, J.F., Meadows, V., Cohen, M., Scalo, J., Crisp, D., Butler, R.A. and Tinetti, G., 2005. Biosignatures from Earth-like planets around M dwarfs. *Astrobiology*, *5*(6), pp.706-725.

Segura, A., Krelove, K., Kasting, J.F., Sommerlatt, D., Meadows, V., Crisp, D., Cohen, M. and Mlawer, E., 2003. Ozone concentrations and ultraviolet fluxes on Earth-like planets around other stars. *Astrobiology*, *3*(4), pp.689-708.

Sehested, J., Nielsen, O.J., Egsgaard, H., Larsen, N.W., Andersen, T.S. and Pedersen, T., 1998. Kinetic study of the formation of isotopically substituted ozone in argon. *Journal of Geophysical Research: Atmospheres*, *103*(D3), pp.3545-3552.

Shackleton, N., 1967. Oxygen isotope analyses and Pleistocene temperatures re-assessed. *Nature*, *215*(5096), pp.15-17.

Sheldon, N.D., 2006. Precambrian paleosols and atmospheric CO_2 levels. *Precambrian Research*, *147*(1-2), pp.148-155.

Sheldon, N.D., 2013. Causes and consequences of low atmospheric pCO_2 in the Late Mesoproterozoic. *Chemical Geology*, *362*, pp.224-231.

Shen, J., Wyness, A.J., Claire, M.W. and Zerkle, A.L., 2021. Spatial Variability of Microbial Communities and Salt Distributions Across a Latitudinal Aridity Gradient in the Atacama Desert. *Microbial Ecology*, pp.1-17.

Shields-Zhou, G. and Och, L., 2011. The case for a Neoproterozoic oxygenation event: geochemical evidence and biological consequences. *GSA Today*, *21*(3), pp.4-11.

Simonaitis, R. and Heicklen, J., 1975. Perchloric acid: A possible sink for stratospheric chlorine. *Planetary and Space Science*, *23*(11), pp.1567-1569.

Sofen, E.D., Alexander, B. and Kunasek, S.A., 2011. The impact of anthropogenic emissions on atmospheric sulfate production pathways, oxidants, and ice core $\Delta^{17}O(SO_4^{2-})$. *Atmospheric Chemistry and Physics*, *11*(7), p.3565.

Sofen, E.D., Alexander, B., Steig, E.J., Thiemens, M.H., Kunasek, S.A., Amos, H.M., Schauer, A.J., Hastings, M.G., Bautista, J., Jackson, T.L. and Vogel, L.E., 2014.

WAIS Divide ice core suggests sustained changes in the atmospheric formation pathways of sulfate and nitrate since the 19th century in the extratropical Southern Hemisphere. *Atmospheric Chemistry and Physics*, *14*(11), pp.5749-5769.

Sridharan, U.C., Klein, F.S. and Kaufman, F., 1985. Detailed course of the O+ HO_2 reaction. *The Journal of chemical physics*, *82*(1), pp.592-593.

Thiemens, M.H., 2006. History and applications of mass-independent isotope effects. *Annu. Rev. Earth Planet. Sci.*, *34*, pp.217-262.

Thiemens, M.H., Chakraborty, S. and Dominguez, G., 2012. The physical chemistry of mass-independent isotope effects and their observation in nature. *Annual Review of Physical Chemistry*, *63*, pp.155-177.

Thiemens, M.H., Chakraborty, S. and Jackson, T.L., 2014. Decadal $\Delta^{17}O$ record of tropospheric CO2: Verification of a stratospheric component in the troposphere. *Journal of Geophysical Research: Atmospheres*, *119*(10), pp.6221-6229.

Thiemens, M.H. and Heidenreich, J.E., 1983. The mass-independent fractionation of oxygen: A novel isotope effect and its possible cosmochemical implications. *Science*, *219*(4588), pp.1073-1075.

Thiemens, M.H., Jackson, T.L. and Brenninkmeijer, C.A., 1995a. Observation of a mass independent oxygen isotopic composition in terrestrial stratospheric CO_2, the link to ozone chemistry, and the possible occurrence in the Martian atmosphere. *Geophysical Research Letters*, *22*(3), pp.255-257.

Thiemens, M.H., Jackson, T., Zipf, E.C., Erdman, P.W. and van Egmond, C., 1995b. Carbon dioxide and oxygen isotope anomalies in the mesosphere and stratosphere. *Science*, *270*(5238), pp.969-972.

Tostevin, R. and Mills, B.J., 2020. Reconciling proxy records and models of Earth's oxygenation during the Neoproterozoic and Palaeozoic. *Interface Focus*, *10*(4), p.20190137.

U.S. Standard Atmosphere, 1976, U.S. Government Printing Office, Washington, D.C., 1976.

Utsunomiya, S., Murakami, T., Nakada, M. and Kasama, T., 2003. Iron oxidation state of a 2.45-Byr-old paleosol developed on mafic volcanics. *Geochimica et Cosmochimica Acta*, *67*(2), pp.213-221.

Vicars, W.C. and Savarino, J., 2014. Quantitative constraints on the ^{17}O-excess ($\Delta^{17}O$) signature of surface ozone: Ambient measurements from 50 N to 50 S using the nitrite-coated filter technique. *Geochimica et Cosmochimica Acta*, *135*, pp.270-287.

Wakelam, V., Herbst, E., Loison, J.C., Smith, I.W.M., Chandrasekaran, V., Pavone, B., Adams, N.G., Bacchus-Montabonel, M.C., Bergeat, A., Béroff, K., Bierbaum, V.M., Chabot, M., Dalgarno, A., van Dishoeck, E. F., Faure, A., Geppert, W. D., Gerlich, D., Galli, D., Hébrard, E., Hersant, F., Hockson K. M., Honvault, P., Klippenstein, S. J., Le Picard, S., Nyman, G., Pernot, P., Schlemmer, S., Selsis, F., Sims, I. R., Talbi, D., Tennyson, J., Troe, J., Wester, R., and Wiesenfeld, L., 2012. A kinetic database for astrochemistry (KIDA). *The Astrophysical Journal Supplement Series*, *199*(1), p.21.

Warke, M.R., Di Rocco, T., Zerkle, A.L., Lepland, A., Prave, A.R., Martin, A.P., Ueno, Y., Condon, D.J. and Claire, M.W., 2020b. The Great Oxidation Event preceded a Paleoproterozoic "snowball Earth". *Proceedings of the National Academy of Sciences*.

Warke, M., Pettigrew, R., Millward, D., Raine, R., Clarke, S., Peng, Y., Bao, H., and Claire, M., 2020a. Spatiotemporal $\Delta^{17}O$ variability in the rock record, EGU General Assembly 2020, Online, 4–8 May 2020, EGU2020-5752, https://doi.org/10.5194/egusphere-egu2020-5752.

Warneck, P., 2000. *Chemistry of the natural atmosphere*. Academic Press.

Warneck, P. and Williams, J., 2012. *The atmospheric Chemist's companion: numerical data for use in the atmospheric sciences*. Springer Science & Business Media.

Welp, L.R., Lee, X., Kim, K., Griffis, T.J., Billmark, K.A. and Baker, J.M., 2008. $\delta^{18}O$ of water vapour, evapotranspiration and the sites of leaf water evaporation in a soybean canopy. *Plant, Cell & Environment*, *31*(9), pp.1214-1228.

Wen, J. and Thiemens, M.H., 1993. Multi-isotope study of the O (^1D)+ CO_2 exchange and stratospheric consequences. *Journal of Geophysical Research: Atmospheres*, *98*(D7), pp.12801-12808.

White, J.W.C., Ciais, P., Figge, R.A., Kenny, R. and Markgraf, V., 1994. A high-resolution record of atmospheric CO_2 content from carbon isotopes in peat. *Nature*, *367*(6459), pp.153-156.

Wiegel, A.A., Cole, A.S., Hoag, K.J., Atlas, E.L., Schauffler, S.M. and Boering, K.A., 2013. Unexpected variations in the triple oxygen isotope composition of stratospheric carbon dioxide. *Proceedings of the National Academy of Sciences*, *110*(44), pp.17680-17685.

Wing, B.A., 2013. A cold, hard look at ancient oxygen. *Proceedings of the National Academy of Sciences*, *110*(36), pp.14514-14515.

Wolf, E.T. and Toon, O.B., 2014. Controls on the Archean climate system investigated with a global climate model. *Astrobiology*, *14*(3), pp.241-253.

Woodward, F.I., 1987. Stomatal numbers are sensitive to increases in CO_2 from pre-industrial levels. *Nature*, *327*(6123), pp.617-618.

Yankovsky, V.A. and Manuilova, R.O., 2006. Model of daytime emissions of electronically-vibrationally excited products of O_3 and O_2 photolysis: application to ozone retrieval. *Ann. Geophys.*, 24, pp. 2823–2839.

Young, E.D., Galy, A. and Nagahara, H., 2002. Kinetic and equilibrium mass-dependent isotope fractionation laws in nature and their geochemical and cosmochemical significance. *Geochimica et Cosmochimica Acta*, *66*(6), pp.1095-1104.

Young, E.D., Yeung, L.Y. and Kohl, I.E., 2014. On the$\Delta^{17}O$ budget of atmospheric O_2. *Geochimica et Cosmochimica Acta*, *135*, pp.102-125.

Yu, J., Elderfield, H. and Hönisch, B., 2007. B/Ca in planktonic foraminifera as a proxy for surface seawater pH. *Paleoceanography*, *22*(2).

Yung, Y.L., DeMore, W.B. and Pinto, J.P., 1991. Isotopic exchange between carbon dioxide and ozone via O(^{1}D) in the stratosphere. *Geophysical Research Letters*, *18*(1), pp.13-16.

Yung, Y.L., Lee, A.Y., Irion, F.W., DeMore, W.B. and Wen, J., 1997. Carbon dioxide in the atmosphere: Isotopic exchange with ozone and its use as a tracer in the middle atmosphere. *Journal of Geophysical Research: Atmospheres*, *102*(D9), pp.10857-10866.

Zachos, J.C., Dickens, G.R. and Zeebe, R.E., 2008. An early Cenozoic perspective on greenhouse warming and carbon-cycle dynamics. *Nature*, *451*(7176), pp.279-283.

Zahnle, K.J., Catling, D.C. and Claire, M.W., 2013. The rise of oxygen and the hydrogen hourglass. *Chemical Geology*, *362*, pp.26-34.

Zahnle, K., Claire, M. and Catling, D., 2006. The loss of mass-independent fractionation in sulfur due to a Palaeoproterozoic collapse of atmospheric methane. *Geobiology*, *4*(4), pp.271-283.

Zerkle, A.L., Claire, M.W., Domagal-Goldman, S.D., Farquhar, J. and Poulton, S.W., 2012. A bistable organic-rich atmosphere on the Neoarchaean Earth. *Nature Geoscience*, *5*(5), pp.359-363.

Appendix A

Supplementary Material for Chapter 3

Appendix A.1: Photolysis rates for Case 1 example atmospheres

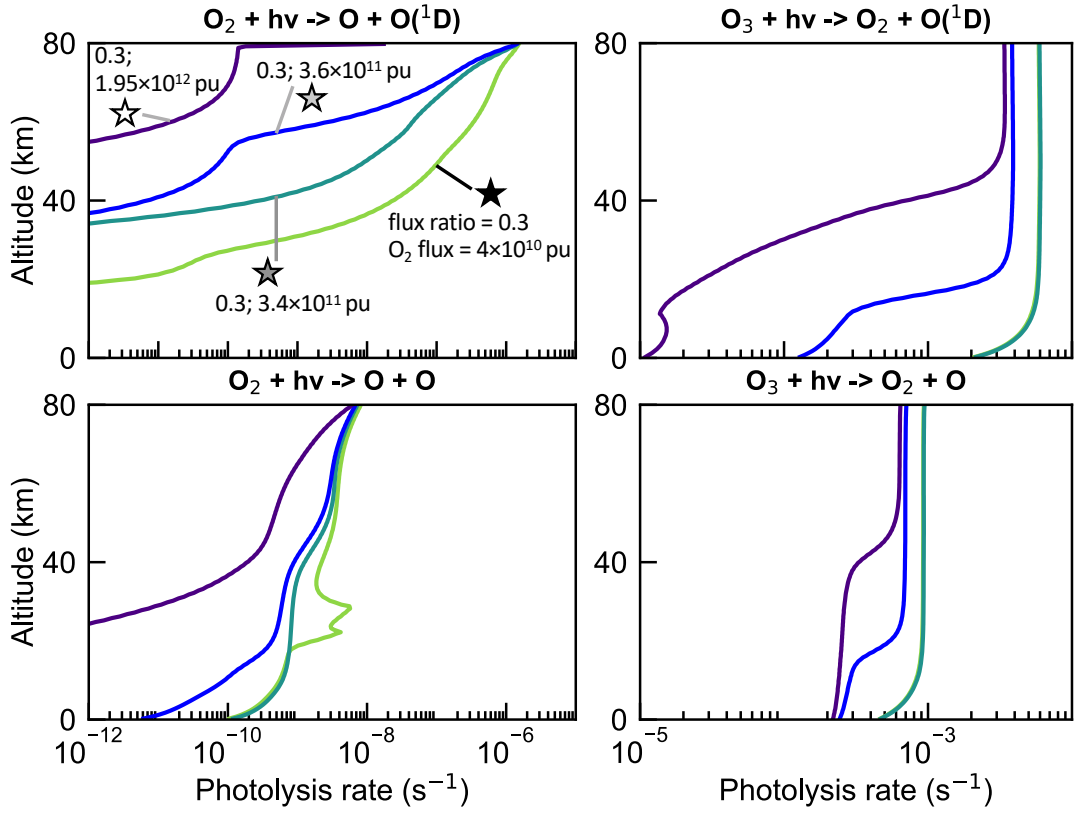

Figure A-1: O_2 and O_3 photolysis rates for the example atmospheres in panels (i) – (iv) in Figure 3-2d.

Appendix A.2: Further supplementary material for Chapter 3

Further supplementary material for Chapter 3 can be found at https://doi.org/10.1016/j.epsl.2021.116818. This includes:

- Lower boundary conditions for key species for all model runs (Table C1; CSV file).
- Appendix E: Model input temperature and eddy diffusion profiles (NC file).

Model output data is available at Mendeley Data at http://dx.doi.org/10.17632/pd659h3fmd.1.
Please note that for the output lower boundary fluxes, if a certain species has a combined deposition velocity and flux boundary condition, only the calculated flux out of the atmosphere is saved in the output file. The upward fluxes in these cases can be found in Table C1.

Appendix B

Lower boundary condition tables

The following tables show the lower boundary conditions for the models in Chapter 3 (Table C-1) and Chapters 5 and 6 (Table C-2). In the second column, a number is given to denote each type of lower boundary condition, as follows: 1 = fixed mixing ratio; 2 = fixed flux; 3 = fixed deposition velocity; and 4 = fixed flux distributed over height, with deposition velocity. Fluxes are given in 'pu' ('photochemical units'; 1 pu = 1 molecule cm^{-2} s^{-1}).

At the upper boundary (representative of the top of the atmosphere), constant effusion velocity boundary conditions of zero are set for all species except N, which is allocated a constant influx of 10^8 pu from above, and H and H_2, which are allocated molecular diffusion terms.

Boundary conditions are those used by Catling et al. (2010; after Segura et al. (2005)) and Domagal-Goldman et al. (2014), with only minor changes. The H_2S and SO_2 fluxes are from the 'modern low' values in Zahnle et al. (2006).

* N_2 has an inert boundary condition set as the remainder of an assumed one bar atmosphere after accounting for the mixing ratios of major species.

Table B-1: Lower boundary conditions for species in models described in Chapter 3. See main text for further details for O_2, CH_4, CO, H_2, N_2O, H_2S and SO_2.

Species	Lower boundary condition	Mixing ratio	Flux (pu)	Deposition velocity (cm s^{-1})	Flux distribution height (km)
Long-lived species					
O	3	-	-	1	-
O_2	1, 2, 4 (see text)	0.21-2.1×10^{-11}	2×10^{10} – 3×10^{13}	0 – 2.3×10^{-8}	0.5
H_2O	3	-	-	0	-
H	3	-	-	1	-
OH	3	-	-	1	-
HO_2	3	-	-	1	-
H_2O_2	3	-	-	0.2	-
H_2	1, 2 (see text)	5.3×10^{-7}	1.22×10^{8}	-	-
CO	1, 2 (see text)	1.1×10^{-7}	2.65×10^{11}	-	-
HCO	3	-	-	1	-
H_2CO	3	-	-	0.2	-
CH_4	1, 2 (see text)	1.8×10^{-6}	2×10^{9} – 1.5×10^{13}	-	-
CH_3	3	-	-	1	-
C_2H_6	3	-	-	0	-
NO	3	-	-	3×10^{-4}	-
NO_2	3	-	-	3×10^{-3}	-
HNO	3	-	-	1	-
H_2S	2	-	10^{8}		-
HS	3	-	-	0	-
S	3	-	-	0	-
SO	3	-	-	0	-
SO_2	4	-	10^{9}	1	20
H_2SO_4	3	-	-	1	-
HSO	3	-	-	1	-
S_2	3	-	-	0	-
S_4	3	-	-	0	-
SO_3	3	-	-	0	-
OCS	3	-	-	0	-
S_3	3	-	-	0	-
O_3	3	-	-	0.7	-
HNO_3	3	-	-	0.2	-
N	3	-	-	0	-
NO_3	3	-	-	0	-
N_2O	1, 2 (see text)	3.1×10^{-7}	4.11×10^{8}	0	-

HO_2NO_2	3	-	-	0.2	-
N_2O_5	3	-	-	0	-
CH_3O	3	-	-	0	-
CH_3ONO	3	-	-	0	-
CH_3ONO_2	3	-	-	0	-
CH_2ONO_2	3	-	-	0	-
$CH_3O_2NO_2$	3	-	-	0.2	-
CH_3O_2	3	-	-	0	-
CH_3OH	3	-	-	0	-
CH_2O_2	3	-	-	0	-
CH_3OOH	3	-	-	0.2	-
CH_2OOH	3	-	-	0	-
CH_2OH	3	-	-	0	-
CH_2ClO	3	-	-	0	-
$CHClO$	3	-	-	0	-
CH_3Cl	2	-	3×10^{8}	0	-
CCl_4	2	-	2×10^{5}	0	-
CCl_3	3	-	-	0	-
CCl_3O_2	3	-	-	0	-
$COCl_2$	3	-	-	0	-
CCl_3NO_4	3	-	-	0	-
ClO	3	-	-	0.5	-
$HOCl$	3	-	-	0.5	-
Cl_2	3	-	-	0	-
$OClO$	3	-	-	0	-
$ClOO$	3	-	-	0	-
$ClONO$	3	-	-	0	-
$ClONO_2$	3	-	-	0.5	-
$ClNO$	3	-	-	0	-
$ClNO_2$	3	-	-	0	-
CH_2Cl	3	-	-	0	-
CH_2ClO_2	3	-	-	0	-
CH_2OCl	3	-	-	0	-
HCl	4	-	10^{8}	0.2	10
Cl	3	-	-	1	-
Cl_2O_2	3	-	-	0	-
ClO_3	3	-	-	0	-
Cl_2O	3	-	-	0	-
$HClO_4$	3	-	-	0.2	-
Cl_2O_4	3	-	-	0	-
SO_4^{AER}	3	-	-	0.1	-
$S8^{AER}$	3	-	-	0.1	-
Inert species					
CO_2	1	2.8×10^{-4}	-	-	-
N_2	See text	~0.8	-	-	-
Short-lived species					

HNO_2	N/A	-	-	-	-
$O(^1D)$	N/A	-	-	-	-
$CH_2(^1)$	N/A	-	-	-	-
$CH_2(^3)$	N/A	-	-	-	-
C_2H_5	N/A	-	-	-	-
$SO_2(^1B)$	N/A	-	-	-	-
$SO_2(^3B)$	N/A	-	-	-	-
HSO_3	N/A	-	-	-	-
OCS_2	N/A	-	-	-	-

Table B-2: Lower boundary conditions for species in models developed in Chapter 5 (Case 17 summary model), and used in Chapter 6. See text of Chapters 5 & 6 for further details for O_2, CH_4, and CO_2. Here, 'O' denotes a ^{16}O atom, while 'P' and 'Q' denote ^{17}O and ^{18}O respectively.

Species	Lower boundary condition	1 - Mixing ratio	2 - Flux (pu)	3 - Deposition velocity (cm s^{-1})	4 - Flux distribution height (km)
Long-lived species					
O	3	-	-	1	-
P	3			1	-
Q	3			1	-
O_2	4 (see text)	-	4×10^{13}	7.56×10^{-6}	0.5
OP	4 (see text)	-	3.0482×10^{10}	7.49×10^{-6}	0.5
OQ	4 (see text)	-	1.6084×10^{11}	7.425×10^{-6}	0.5
H_2O	3	-	-	0	-
H_2P	3	-	-	0	-
H_2Q	3	-	-	0	-
H	3	-	-	1	-
OH	3	-	-	1	-
PH	3	-	-	1	-
QH	3	-	-	1	-
HO_2	3	-	-	1	-
HOP	3	-	-	1	-
HOQ	3	-	-	1	-
H_2O_2	3	-	-	0.2	-
H_2OP	3	-	-	0.2	-
H_2OQ	3	-	-	0.2	-
H_2	2 (see text)	-	2.38×10^{9}	-	-
CO	2 (see text)	-	3.15×10^{11}	-	-
CP	2 (see text)	-	1.197×10^{8}	-	-
CQ	2 (see text)	-	3.6×10^{8}	-	-
HCO	3	-	-	1	-
HCP	3	-	-	1	-
HCQ	3	-	-	1	-

H_2CO	3	-	-	0.2	-
H_2CP	3	-	-	0.2	-
H_2CQ	3	-	-	0.2	-
CH_4	2 (see text)	-	$2.5\times108 - 10^{11}$	-	-
CH_3	3	-	-	1	-
C_2H_6	3	-	-	0	-
NO	3	-	-	3×10^{-4}	-
NP	3	-	-	3×10^{-4}	-
NQ	3	-	-	3×10^{-4}	-
NO_2	3	-	-	3×10^{-3}	-
NOP	3	-	-	3×10^{-3}	-
NOQ	3	-	-	3×10^{-3}	-
HNO	3	-	-	1	-
HNP	3	-	-	1	-
HNQ	3	-	-	1	-
H_2S	2	-	10^8		-
HS	3	-	-	0	-
S	3	-	-	0	-
SO	3	-	-	0	-
SP	3	-	-	0	-
SQ	3	-	-	0	-
SO_2	4	-	10^9	1	20
SOP	4	-	7.6×10^5	1	20
SOQ	4	-	4×10^6	1	20
H_2SO_4	3	-	-	1	-
H_2SOOOP	3	-	-	1	-
H_2SOOOQ	3	-	-	1	-
HSO	3	-	-	1	-
HSP	3	-	-	1	-
HSQ	3	-	-	1	-
S_2	3	-	-	0	-
S_4	3	-	-	0	-
SO_3	3	-	-	0	-
SOOP	3	-	-	0	-
SOOQ	3	-	-	0	-
OCS	3	-	-	0	-
PCS	3	-	-	0	-
QCS	3	-	-	0	-
S_3	3	-	-	0	-
O_3	3	-	-	0.7	-
OOP	3	-	-	0.7	-
OOQ	3	-	-	0.7	-
HNO_3	3	-	-	0.2	-
HNOOP	3	-	-	0.2	-
HNOOQ	3	-	-	0.2	-

N	3	-	-	0	-
NO_3	3	-	-	0.2	-
NOOP	3	-	-	0.2	-
NOOQ	3	-	-	0.2	-
N_2O	2 (see text)	-	1.06×10^{9}	-	-
N_2P	2 (see text)	-	4.028×10^{5}	-	-
N_2Q	2 (see text)	-	2.12×10^{6}	-	-
HO_2NO_2	3	-	-	0.2	-
HO_2NOP	3	-	-	0.2	-
HO_2NOQ	3	-	-	0.2	-
N_2O_5	3	-	-	0	-
N_2O_4P	3	-	-	0	-
N_2O_4Q	3	-	-	0	-
SO_4^{AER}	3	-	-	0.1	-
$SOOOP^{AER}$	3	-	-	0.1	-
$SOOOQ^{AER}$	3	-	-	0.1	-
S_8^{AER}	3	-	-	0.1	-
CO_2	4 (see text)	-	2.2×10^{13}	3.2×10^{-3}	0.5
COP	4 (see text)	-	1.707509013×10^{10}	3.2×10^{-3}	0.5
COQ	4 (see text)	-	9.1608×10^{10}	3.2×10^{-3}	0.5
$SO_2(^1B)$	0	-	-	0	-
$SOP(^1B)$	0	-	-	0	-
$SOQ(^1B)$	0	-	-	0	-
$SO_2(^3B)$	0	-	-	0	-
$SOP(^3B)$	0	-	-	0	-
$SOQ(^3B)$	0	-	-	0	-
Inert species					
N_2	See text	~0.8	-	-	-
Short-lived species					
HNO_2	N/A	-	-	-	-
HNOP	N/A	-	-	-	-
HNOQ	N/A	-	-	-	-
$O(^1D)$	N/A	-	-	-	-
$P(^1D)$	N/A	-	-	-	-
$Q(^1D)$	N/A	-	-	-	-
$CH_2(^1)$	N/A	-	-	-	-
$CH_2(^3)$	N/A	-	-	-	-
C_2H_5	N/A	-	-	-	-
HSO_3	N/A	-	-	-	-
HSOOP	N/A	-	-	-	-
HSOOQ	N/A	-	-	-	-
OCS_2	N/A	-	-	-	-
PCS_2	N/A	-	-	-	-
QCS_2	N/A	-	-	-	-

Appendix B.1: References:

Kasting, J.F. and Donahue, T.M., 1980. The evolution of atmospheric ozone. *Journal of Geophysical Research: Oceans*, *85*(C6), pp.3255-3263.

Kasting, J.F., Holland, H.D. and Pinto, J.P., 1985. Oxidant abundances in rainwater and the evolution of atmospheric oxygen. *Journal of Geophysical Research: Atmospheres*, *90*(D6), pp.10497-10510.

Segura, A., Krelove, K., Kasting, J.F., Sommerlatt, D., Meadows, V., Crisp, D., Cohen, M. and Mlawer, E., 2003. Ozone concentrations and ultraviolet fluxes on Earth-like planets around other stars. *Astrobiology*, *3*(4), pp.689-708.

Zahnle, K., Claire, M. and Catling, D., 2006. The loss of mass-independent fractionation in sulfur due to a Palaeoproterozoic collapse of atmospheric methane. *Geobiology*, *4*(4), pp.271-283.

Appendix C

Reaction rate tables for the model developed in this thesis

Table C-1: Reaction rates for the 1-D oxygen isotope photochemical model developed in this thesis. Specifically, this is the 'Case 17' model developed in Chapter 5 and used in Chapter 6.

Note that 'P' and 'Q' refer to ^{17}O and ^{18}O respectively, while 'O' refers here to ^{16}O.

Note that fractionations are incorporated into the O_3 formation reactions (reactions 78-82) when the model is run, so are not shown here. For the fractionation factors by which the rates here are multiplied, see Chapter 5. This is also the case for the mass-dependent fractionations incorporated for all two- and three- body reactions.

Rxn #	Reaction	Rate [$cm^3\ s^{-1}$]	Source
1	$O(^1D) + H_2O \rightarrow OH + OH$	$1.63 \times 10^{-10} \cdot \exp(60.0/T)$	*A*,1
2	$O(^1D) + H_2P \rightarrow OH + PH$	$1.63 \times 10^{-10} \cdot \exp(60.0/T)$	*A*,1
3	$P(^1D) + H_2O \rightarrow OH + PH$	$1.63 \times 10^{-10} \cdot \exp(60.0/T)$	*A*,1
4	$O(^1D) + H_2Q \rightarrow OH + QH$	$1.63 \times 10^{-10} \cdot \exp(60.0/T)$	*A*,1
5	$Q(^1D) + H_2O \rightarrow OH + QH$	$1.63 \times 10^{-10} \cdot \exp(60.0/T)$	*A*,1
6	$O(^1D) + H_2 \rightarrow OH + H$	1.20×10^{-10}	*A*,1
7	$P(^1D) + H_2 \rightarrow PH + H$	1.20×10^{-10}	*A*,1
8	$Q(^1D) + H_2 \rightarrow QH + H$	1.20×10^{-10}	*A*,1
9	$H_2 + O \rightarrow OH + H$	$3.44 \times 10^{-13} \cdot (T/300)^{2.67} \cdot \exp(-3160.0/T)$	*B*,1
10	$H_2 + P \rightarrow PH + H$	$3.44 \times 10^{-13} \cdot (T/300)^{2.67} \cdot \exp(-3160.0/T)$	*B*,1
11	$H_2 + Q \rightarrow QH + H$	$3.44 \times 10^{-13} \cdot (T/300)^{2.67} \cdot \exp(-3160.0/T)$	*B*,1
12	$OH + H_2 \rightarrow H_2O + H$	$2.80 \times 10^{-12} \cdot \exp(-1800.0/T)$	*A*,1
13	$PH + H_2 \rightarrow H_2P + H$	$2.80 \times 10^{-12} \cdot \exp(-1800.0/T)$	*A*,1
14	$QH + H_2 \rightarrow H_2Q + H$	$2.80 \times 10^{-12} \cdot \exp(-1800.0/T)$	*A*,1
15	$H + O_3 \rightarrow OH + O_2$	$1.40 \times 10^{-10} \cdot \exp(-470.0/T)$	*A*,1
16	$H + OOP \rightarrow PH + O_2$	$0.3333333 \times 1.40 \times 10^{-10} \cdot \exp(-470.0/T)$	*A*,1
17	$H + OOP \rightarrow OH + OP$	$0.6666667 \times 1.40 \times 10^{-10} \cdot \exp(-470.0/T)$	*A*,1
18	$H + OOQ \rightarrow QH + O_2$	$0.333333333 \times 1.40 \times 10^{-10} \cdot \exp(-470.0/T)$	*A*,1
19	$H + OOQ \rightarrow OH + OQ$	$0.666666667 \times 1.40 \times 10^{-10} \cdot \exp(-470.0/T)$	*A*,1
20	$H + O_2 \rightarrow HO_2$	$k_0 = 4.40 \times 10^{-32} \cdot (T/300)^{-1.3}$ $k_\infty = 7.50 \times 10^{-11} \cdot (T/300)^{0.2}$	*A*,2
21	$H + OP \rightarrow HOP$	$k_0 = 4.40 \times 10^{-32} \cdot (T/300)^{-1.3}$ $k_\infty = 7.50 \times 10^{-11} \cdot (T/300)^{0.2}$	*A*,2

Rxn #	Reaction	Rate [$cm^3\ s^{-1}$]	Source
22	$H + OQ \rightarrow HOQ$	$\begin{cases} k_0 = 4.40 \times 10^{-32} \cdot (T/300)^{-1.3} \\ k_\infty = 7.50 \times 10^{-11} \cdot (T/300)^{0.2} \end{cases}$	*A*,2
23	$H + HO_2 \rightarrow H_2 + O_2$	6.90×10^{-12}	*A*,1
24	$H + HOP \rightarrow H_2 + OP$	6.90×10^{-12}	*A*,1
25	$H + HOQ \rightarrow H_2 + OQ$	6.90×10^{-12}	*A*,1
26	$H + HO_2 \rightarrow O + H_2O$	1.60×10^{-12}	*A*,1
27	$H + HOP \rightarrow P + H_2O$	$0.5 \times 1.60 \times 10^{-12}$	*A*,1
28	$H + HOP \rightarrow O + H_2P$	$0.5 \times 1.60 \times 10^{-12}$	*A*,1
29	$H + HOQ \rightarrow Q + H_2O$	$0.5 \times 1.60 \times 10^{-12}$	*A*,1
30	$H + HOQ \rightarrow O + H_2Q$	$0.5 \times 1.60 \times 10^{-12}$	*A*,1
31	$H + HO_2 \rightarrow OH + OH$	7.20×10^{-11}	*A*,1
32	$H + HOP \rightarrow OH + PH$	7.20×10^{-11}	*A*,1
33	$H + HOQ \rightarrow OH + QH$	7.20×10^{-11}	*A*,1
34	$O + OH \rightarrow O_2 + H$	$1.80 \times 10^{-11} \cdot \exp(180.0/T)$	*A*,1
35	$O + PH \rightarrow OP + H$	$1.80 \times 10^{-11} \cdot \exp(180.0/T)$	*A*,1
36	$P + OH \rightarrow OP + H$	$1.80 \times 10^{-11} \cdot \exp(180.0/T)$	*A*,1
37	$O + QH \rightarrow OQ + H$	$1.80 \times 10^{-11} \cdot \exp(180.0/T)$	*A*,1
38	$Q + OH \rightarrow OQ + H$	$1.80 \times 10^{-11} \cdot \exp(180.0/T)$	*A*,1
39	$OH + HO_2 \rightarrow H_2O + O_2$	$4.80 \times 10^{-11} \cdot \exp(250.0/T)$	*A*,1
40	$OH + HOP \rightarrow H_2O + OP$	$4.80 \times 10^{-11} \cdot \exp(250.0/T)$	*A*,1
41	$PH + HO_2 \rightarrow H_2P + O_2$	$4.80 \times 10^{-11} \cdot \exp(250.0/T)$	*A*,1
42	$OH + HOQ \rightarrow H_2O + OQ$	$4.80 \times 10^{-11} \cdot \exp(250.0/T)$	*A*,1
43	$QH + HO_2 \rightarrow H_2Q + O_2$	$4.80 \times 10^{-11} \cdot \exp(250.0/T)$	*A*,1
44	$OH + O_3 \rightarrow HO_2 + O_2$	$1.70 \times 10^{-12} \cdot \exp(-940.0/T)$	*A*,1
45	$PH + O_3 \rightarrow HOP + O_2$	$1.70 \times 10^{-12} \cdot \exp(-940.0/T)$	*A*,1
46	$OH + OOP \rightarrow HOP + O_2$	$0.3333333 \times 1.70 \times 10^{-12} \cdot \exp(-940.0/T)$	*A*,1
47	$OH + OOP \rightarrow HO_2 + OP$	$0.6666667 \times 1.70 \times 10^{-12} \cdot \exp(-940.0/T)$	*A*,1

Rxn #	Reaction	Rate [$cm^3\ s^{-1}$]	Source
48	$QH + O_3 \rightarrow HOQ + O_2$	$1.70 \times 10^{-12} \cdot \exp(-940.0/T)$	*A*,1
49	$OH + OOQ \rightarrow HOQ + O_2$	$0.333333333 \times 1.70 \times 10^{-12} \cdot \exp(-940.0/T)$	*A*,1
50	$OH + OOQ \rightarrow HO_2 + OQ$	$0.666666667 \times 1.70 \times 10^{-12} \cdot \exp(-940.0/T)$	*A*,1
51	$O + HO_2 \rightarrow OH + O_2$	$3.00 \times 10^{-11} \cdot \exp(200.0/T)$	*A*,1
52	$P + HO_2 \rightarrow OH + OP$	$3.00 \times 10^{-11} \cdot \exp(200.0/T)$	*A*,1
53	$O + HOP \rightarrow PH + O_2$	$0.5 \times 3.00 \times 10^{-11} \cdot \exp(200.0/T)$	*A*,1
54	$O + HOP \rightarrow OH + OP$	$0.5 \times 3.00 \times 10^{-11} \cdot \exp(200.0/T)$	*A*,1
55	$Q + HO_2 \rightarrow OH + OQ$	$3.00 \times 10^{-11} \cdot \exp(200.0/T)$	*A*,1
56	$O + HOQ \rightarrow QH + O_2$	$0.5 \times 3.00 \times 10^{-11} \cdot \exp(200.0/T)$	*A*,1
57	$O + HOQ \rightarrow OH + OQ$	$0.5 \times 3.00 \times 10^{-11} \cdot \exp(200.0/T)$	*A*,1
58	$HO_2 + O_3 \rightarrow OH + O_2 + O_2$	$1.00 \times 10^{-14} \cdot \exp(-490.0/T)$	*A*,1
59	$HOP + O_3 \rightarrow OH + O_2 + OP$	$1.00 \times 10^{-14} \cdot \exp(-490.0/T)$	*A*,1
60	$HO_2 + OOP \rightarrow PH + O_2 + O_2$	$0.3333333 \times 1.00 \times 10^{-14} \cdot \exp(-490.0/T)$	*A*,1
61	$HO_2 + OOP \rightarrow OH + O_2 + OP$	$0.6666667 \times 1.00 \times 10^{-14} \cdot \exp(-490.0/T)$	*A*,1
62	$HOQ + O_3 \rightarrow OH + O_2 + OQ$	$1.00 \times 10^{-14} \cdot \exp(-490.0/T)$	*A*,1
63	$HO_2 + OOQ \rightarrow QH + O_2 + O_2$	$0.333333333 \times 1.00 \times 10^{-14} \cdot \exp(-490.0/T)$	*A*,1
64	$HO_2 + OOQ \rightarrow OH + O_2 + OQ$	$0.666666667 \times 1.00 \times 10^{-14} \cdot \exp(-490.0/T)$	*A*,1
65	$HO_2 + HO_2 \rightarrow H_2O_2 + O_2$	sum of biomolecular and trimolecular following JPL18-B13	*A*
66	$HO_2 + HOP \rightarrow H_2OP + O_2$	rates doubled - isotopic self-reaction	*A*
67	$HO_2 + HOP \rightarrow H_2O_2 + OP$	rates doubled - isotopic self-reaction	*A*
68	$HO_2 + HOQ \rightarrow H_2OQ + O_2$	rates doubled - isotopic self-reaction	*A*
69	$HO_2 + HOQ \rightarrow H_2O_2 + OQ$	rates doubled - isotopic self-reaction	*A*
70	$OH + H_2O_2 \rightarrow H_2O + HO_2$	1.80×10^{-12}	*A*,1
71	$OH + H_2OP \rightarrow H_2O + HOP$	1.80×10^{-12}	*A*,1
72	$PH + H_2O_2 \rightarrow H_2P + HO_2$	1.80×10^{-12}	*A*,1
73	$OH + H_2OQ \rightarrow H_2O + HOQ$	1.80×10^{-12}	*A*,1
74	$QH + H_2O_2 \rightarrow H_2Q + HO_2$	1.80×10^{-12}	*A*,1

Rxn #	Reaction	Rate [$cm^3\ s^{-1}$]	Source
75	$O + O \rightarrow O_2$	$k_0 = 9.46 \times 10^{-34} \cdot \exp(485.0/T)$ $k_\infty = 1.00 \times 10^{-10}$	*C*,2
76	$O + P \rightarrow OP$	$k_0 = 1.89 \times 10^{-33} \cdot \exp(485.0/T)$ $k_\infty = 2.00 \times 10^{-10}$	*C*,2
77	$O + Q \rightarrow OQ$	$k_0 = 1.89 \times 10^{-33} \cdot \exp(485.0/T)$ $k_\infty = 2.00 \times 10^{-10}$	*C*,2
78	$O + O_2 \rightarrow O_3$	$k_0 = 6.00 \times 10^{-34} \cdot (T/300)^{-2.4}$ $k_\infty = 1.00 \times 10^{-10}$	*A*,2
79	$P + O_2 \rightarrow OOP$	$k_0 = 6.00 \times 10^{-34} \cdot (T/300)^{-2.4}$ $k_\infty = 1.00 \times 10^{-10}$	*A*,2
80	$O + OP \rightarrow OOP$	$k_0 = 6.00 \times 10^{-34} \cdot (T/300)^{-2.4}$ $k_\infty = 1.00 \times 10^{-10}$	*A*,2
81	$Q + O_2 \rightarrow OOQ$	$k_0 = 6.00 \times 10^{-34} \cdot (T/300)^{-2.4}$ $k_\infty = 1.00 \times 10^{-10}$	*A*,2
82	$O + OQ \rightarrow OOQ$	$k_0 = 6.00 \times 10^{-34} \cdot (T/300)^{-2.4}$ $k_\infty = 1.00 \times 10^{-10}$	*A*,2
83	$O + O_3 \rightarrow O_2 + O_2$	$8.00 \times 10^{-12} \cdot \exp(-2060.0/T)$	*A*,1
84	$P + O_3 \rightarrow O_2 + OP$	$8.00 \times 10^{-12} \cdot \exp(-2060.0/T)$	*A*,1
85	$O + OOP \rightarrow O_2 + OP$	$8.00 \times 10^{-12} \cdot \exp(-2060.0/T)$	*A*,1
86	$Q + O_3 \rightarrow O_2 + OQ$	$8.00 \times 10^{-12} \cdot \exp(-2060.0/T)$	*A*,1
87	$O + OOQ \rightarrow O_2 + OQ$	$8.00 \times 10^{-12} \cdot \exp(-2060.0/T)$	*A*,1
88	$OH + OH \rightarrow H_2O + O$	1.80×10^{-12}	*A*,1
89	$OH + PH \rightarrow H_2O + P$	$0.5 \times 3.60 \times 10^{-12}$	*A*,1

Rxn #	Reaction	Rate [$cm^3\ s^{-1}$]	Source
90	$OH + PH \rightarrow H_2P + O$	$0.5 \times 3.60 \times 10^{-12}$	*A*,1
91	$OH + QH \rightarrow H_2O + Q$	$0.5 \times 3.60 \times 10^{-12}$	*A*,1
92	$OH + QH \rightarrow H_2Q + O$	$0.5 \times 3.60 \times 10^{-12}$	*A*,1
93	$O(^1D) + N_2 \rightarrow O + N_2$	$2.15 \times 10^{-11} \cdot \exp(110.0/T)$	*A*,1
94	$P(^1D) + N_2 \rightarrow P + N_2$	$2.15 \times 10^{-11} \cdot \exp(110.0/T)$	*A*,1
95	$Q(^1D) + N_2 \rightarrow Q + N_2$	$2.15 \times 10^{-11} \cdot \exp(110.0/T)$	*A*,1
96	$O(^1D) + O_2 \rightarrow O + O_2$	$3.30 \times 10^{-11} \cdot \exp(55.0/T)$	*A*,1
97	$P(^1D) + O_2 \rightarrow P + O_2$	$0.333333333 \times 3.30 \times 10^{-11} \cdot \exp(55.0/T)$	*A*,1
98	$O(^1D) + OP \rightarrow O + OP$	$0.666666667 \times 3.30 \times 10^{-11} \cdot \exp(55.0/T)$	*A*,1
99	$Q(^1D) + O_2 \rightarrow Q + O_2$	$0.333333333 \times 3.30 \times 10^{-11} \cdot \exp(55.0/T)$	*A*,1
100	$O(^1D) + OQ \rightarrow O + OQ$	$0.666666667 \times 3.30 \times 10^{-11} \cdot \exp(55.0/T)$	*A*,1
101	$P(^1D) + O_2 \rightarrow O + OP$	$0.666666667 \times 3.30 \times 10^{-11} \cdot \exp(55.0/T)$	*A*,1
102	$O(^1D) + OP \rightarrow P + O_2$	$0.333333333 \times 3.30 \times 10^{-11} \cdot \exp(55.0/T)$	*A*,1
103	$Q(^1D) + O_2 \rightarrow O + OQ$	$0.666666667 \times 3.30 \times 10^{-11} \cdot \exp(55.0/T)$	*A*,1
104	$O(^1D) + OQ \rightarrow Q + O_2$	$0.333333333 \times 3.30 \times 10^{-11} \cdot \exp(55.0/T)$	*A*,1
105	$O_2 + h\nu \rightarrow O + O(^1D)$	$6.70 \times 10^{+00}$	*D*,3
106	$O_2 + h\nu \rightarrow O + O$	2.55×10^{-03}	*D*,3
107	$OP + h\nu \rightarrow O + P(^1D)$	2.60×10^{-03}	*D*,3
108	$OP + h\nu \rightarrow P + O(^1D)$	1.34×10^{-02}	*D*,3
109	$OP + h\nu \rightarrow O + P$	1.39×10^{-02}	*D*,3
110	$OQ + h\nu \rightarrow O + Q(^1D)$	$3.93 \times 10^{+01}$	*D*,3
111	$OQ + h\nu \rightarrow Q + O(^1D)$	1.54×10^{-02}	*D*,3
112	$OQ + h\nu \rightarrow O + Q$	8.39×10^{-02}	*D*,3
113	$H_2O + h\nu \rightarrow H + OH$	8.13×10^{-01}	*E*,3
114	$H_2P + h\nu \rightarrow H + PH$	2.98×10^{-04}	*E*,3
115	$H_2Q + h\nu \rightarrow H + QH$	1.51×10^{-03}	*E*,3
116	$O_3 + h\nu \rightarrow O_2 + O(^1D)$	7.47×10^{-06}	*E*,3

Rxn #	Reaction	Rate [cm^3 s^{-1}]	Source
117	$O_3 + h\nu \rightarrow O_2 + O$	3.11×10^{-09}	*E*,3
118	$OOP + h\nu \rightarrow OP + O(^1D)$	1.68×10^{-08}	*E*,3
119	$OOP + h\nu \rightarrow O_2 + P(^1D)$	$7.74 \times 10^{+03}$	*E*,3
120	$OOP + h\nu \rightarrow OP + O$	$3.21 \times 10^{+00}$	*E*,3
121	$OOP + h\nu \rightarrow O_2 + P$	$6.41 \times 10^{+00}$	*E*,3
122	$OOQ + h\nu \rightarrow OQ + O(^1D)$	$1.72 \times 10^{+01}$	*E*,3
123	$OOQ + h\nu \rightarrow O_2 + Q(^1D)$	$3.43 \times 10^{+01}$	*E*,3
124	$OOQ + h\nu \rightarrow OQ + O$	$2.13 \times 10^{+02}$	*E*,3
125	$OOQ + h\nu \rightarrow O_2 + Q$	1.64×10^{-01}	*E*,3
126	$H_2O_2 + h\nu \rightarrow OH + OH$	8.80×10^{-01}	*E*,3
127	$H_2OP + h\nu \rightarrow OH + PH$	1.99×10^{-03}	*E*,3
128	$H_2OQ + h\nu \rightarrow OH + QH$	1.55×10^{-06}	*E*,3
129	$CO_2 + h\nu \rightarrow CO + O$	8.30×10^{-06}	*E*,3
130	$CO_2 + h\nu \rightarrow CO + O(^1D)$	4.61×10^{-04}	*E*,3
131	$COP + h\nu \rightarrow CP + O$	1.79×10^{-07}	*E*,3
132	$COP + h\nu \rightarrow CO + P$	1.79×10^{-07}	*E*,3
133	$COP + h\nu \rightarrow CP + O(^1D)$	9.62×10^{-07}	*E*,3
134	$COP + h\nu \rightarrow CO + P(^1D)$	9.62×10^{-07}	*E*,3
135	$COQ + h\nu \rightarrow CQ + O$	2.07×10^{-02}	*E*,3
136	$COQ + h\nu \rightarrow CO + Q$	1.61×10^{-05}	*E*,3
137	$COQ + h\nu \rightarrow CQ + O(^1D)$	8.66×10^{-05}	*E*,3
138	$COQ + h\nu \rightarrow CO + Q(^1D)$	$8.07 \times 10^{+03}$	*E*,3
139	$OH + CO \rightarrow H + CO_2$	Proceeds via HOCO intermediate (JPL-18 3body note D1) - duplicated below for HS + CS	*A*
140	$OH + CP \rightarrow H + COP$		*A*
141	$PH + CO \rightarrow H + COP$		*A*
142	$OH + CQ \rightarrow H + COQ$		*A*
143	$QH + CO \rightarrow H + COQ$		*A*

Rxn #	Reaction	Rate [cm^3 s^{-1}]	Source
144	CO + O → CO_2	$k_0 = 6.51 \times 10^{-33} \cdot \exp(-2188.0/T)$ $k_\infty = 1.00 \times 10^{-10}$	*F*,2
145	CP + O → COP	$k_0 = 6.51 \times 10^{-33} \cdot \exp(-2188.0/T)$ $k_\infty = 1.00 \times 10^{-10}$	*F*,2
146	CO + P → COP	$k_0 = 6.51 \times 10^{-33} \cdot \exp(-2188.0/T)$ $k_\infty = 1.00 \times 10^{-10}$	*F*,2
147	CQ + O → COQ	$k_0 = 6.51 \times 10^{-33} \cdot \exp(-2188.0/T)$ $k_\infty = 1.00 \times 10^{-10}$	*F*,2
148	CO + Q → COQ	$k_0 = 6.51 \times 10^{-33} \cdot \exp(-2188.0/T)$ $k_\infty = 1.00 \times 10^{-10}$	*F*,2
149	H + CO → HCO	$k_0 = 5.29 \times 10^{-34} \cdot \exp(-373.0/T)$ $k_\infty = 1.00 \times 10^{-10}$	*G*,2
150	H + CP → HCP	$k_0 = 5.29 \times 10^{-34} \cdot \exp(-373.0/T)$ $k_\infty = 1.00 \times 10^{-10}$	*G*,2
151	H + CQ → HCQ	$k_0 = 5.29 \times 10^{-34} \cdot \exp(-373.0/T)$ $k_\infty = 1.00 \times 10^{-10}$	*G*,2
152	H + HCO → H_2 + CO	1.83×10^{-10}	*G*,1
153	H + HCP → H_2 + CP	1.83×10^{-10}	*G*,1
154	H + HCQ → H_2 + CQ	1.83×10^{-10}	*G*,1
155	HCO + HCO → H_2CO + CO	4.48×10^{-11}	*G*,1
156	HCO + HCP → H_2CO + CP	$0.5 \times 8.96 \times 10^{-11}$	*G*,1
157	HCO + HCP → H_2CP + CO	$0.5 \times 8.96 \times 10^{-11}$	*G*,1
158	HCO + HCQ → H_2CO + CQ	$0.5 \times 8.96 \times 10^{-11}$	*G*,1

Rxn #	Reaction	Rate [cm^3 s^{-1}]	Source
159	HCO + HCQ → H_2CQ + CO	$0.5 \times 8.96 \times 10^{-11}$	*G*,1
160	OH + HCO → H_2O + CO	1.80×10^{-10}	*G*,1
161	PH + HCO → H_2P + CO	1.80×10^{-10}	*G*,1
162	OH + HCP → H_2O + CP	1.80×10^{-10}	*G*,1
163	QH + HCO → H_2Q + CO	1.80×10^{-10}	*G*,1
164	OH + HCQ → H_2O + CQ	1.80×10^{-10}	*G*,1
165	O + HCO → H + CO_2	5.00×10^{-11}	*G*,1
166	O + HCP → H + COP	5.00×10^{-11}	*G*,1
167	P + HCO → H + COP	5.00×10^{-11}	*G*,1
168	O + HCQ → H + COQ	5.00×10^{-11}	*G*,1
169	Q + HCO → H + COQ	5.00×10^{-11}	*G*,1
170	O + HCO → OH + CO	5.00×10^{-11}	*G*,1
171	P + HCO → PH + CO	5.00×10^{-11}	*G*,1
172	O + HCP → OH + CP	5.00×10^{-11}	*G*,1
173	Q + HCO → QH + CO	5.00×10^{-11}	*G*,1
174	O + HCQ → OH + CQ	5.00×10^{-11}	*G*,1
175	H_2CO + hν → H_2 + CO	$3.32 \times 10^{+00}$	*E*,3
176	H_2CO + hν → HCO + H	$2.92 \times 10^{+00}$	*E*,3
177	H_2CP + hν → H_2 + CP	$1.78 \times 10^{+01}$	*E*,3
178	H_2CP + hν → HCP + H	$1.46 \times 10^{+01}$	*E*,3
179	H_2CQ + hν → H_2 + CQ	1.82×10^{-07}	*E*,3
180	H_2CQ + hν → HCQ + H	1.41×10^{-10}	*E*,3
181	HCO + hν → H + CO	1.00×10^{-02}	*H*,1
182	HCP + hν → H + CP	1.00×10^{-02}	*H*,1
183	HCQ + hν → H + CQ	1.00×10^{-02}	*H*,1
184	H_2CO + H → H_2 + HCO	$2.16 \times 10^{-12} \cdot (T/300)^{1.62} \cdot \exp(-1090.0/T)$	*G*,1
185	H_2CP + H → H_2 + HCP	$2.16 \times 10^{-12} \cdot (T/300)^{1.62} \cdot \exp(-1090.0/T)$	*G*,1

Rxn #	Reaction	Rate [cm^3 s^{-1}]	Source
186	$H_2CQ + H \rightarrow H_2 + HCQ$	$2.16 \times 10^{-12} \cdot (T/300)^{1.62} \cdot \exp(-1090.0/T)$	*G*,1
187	$H + H \rightarrow H_2$	$k_0 = 8.85 \times 10^{-33} \cdot (T/300)^{-0.6}$ $k_\infty = 1.00 \times 10^{-10}$	*I*,2
188	$HCO + O_2 \rightarrow CO + HO_2$	5.20×10^{-12}	*A*,1
189	$HCO + OP \rightarrow CO + HOP$	5.20×10^{-12}	*A*,1
190	$HCP + O_2 \rightarrow CP + HO_2$	5.20×10^{-12}	*A*,1
191	$HCO + OQ \rightarrow CO + HOQ$	5.20×10^{-12}	*A*,1
192	$HCQ + O_2 \rightarrow CQ + HO_2$	5.20×10^{-12}	*A*,1
193	$OH + H_2CO \rightarrow H_2O + HCO$	$5.50 \times 10^{-12} \cdot \exp(125.0/T)$	*A*,1
194	$PH + H_2CO \rightarrow H_2P + HCO$	$5.50 \times 10^{-12} \cdot \exp(125.0/T)$	*A*,1
195	$OH + H_2CP \rightarrow H_2O + HCP$	$5.50 \times 10^{-12} \cdot \exp(125.0/T)$	*A*,1
196	$QH + H_2CO \rightarrow H_2Q + HCO$	$5.50 \times 10^{-12} \cdot \exp(125.0/T)$	*A*,1
197	$OH + H_2CQ \rightarrow H_2O + HCQ$	$5.50 \times 10^{-12} \cdot \exp(125.0/T)$	*A*,1
198	$H + OH \rightarrow H_2O$	$k_0 = 6.78 \times 10^{-31} \cdot (T/300)^{-2}$ $k_\infty = 1.00 \times 10^{-10}$	*G*,2
199	$H + PH \rightarrow H_2P$	$k_0 = 6.78 \times 10^{-31} \cdot (T/300)^{-2}$ $k_\infty = 1.00 \times 10^{-10}$	*G*,2
200	$H + QH \rightarrow H_2Q$	$k_0 = 6.78 \times 10^{-31} \cdot (T/300)^{-2}$ $k_\infty = 1.00 \times 10^{-10}$	*G*,2
201	$OH + OH \rightarrow H_2O_2$	$k_0 = 6.90 \times 10^{-31} \cdot (T/300)^{-1}$ $k_\infty = 2.60 \times 10^{-11}$	*A*,2
202	$OH + PH \rightarrow H_2OP$	$k_0 = 1.38 \times 10^{-30} \cdot (T/300)^{-1}$ $k_\infty = 5.20 \times 10^{-11}$	*A*,2

Rxn #	Reaction	Rate [$cm^3\ s^{-1}$]	Source
203	$OH + QH \rightarrow H_2OQ$	$\begin{cases} k_0 = 1.38 \times 10^{-30} \cdot (T/300)^{-1} \\ k_\infty = 5.20 \times 10^{-11} \end{cases}$	A,2
204	$H_2CO + O \rightarrow HCO + OH$	$3.40 \times 10^{-11} \cdot \exp(\text{-}1600.0/T)$	J,1
205	$H_2CP + O \rightarrow HCP + OH$	$3.40 \times 10^{-11} \cdot \exp(\text{-}1600.0/T)$	J,1
206	$H_2CO + P \rightarrow HCO + PH$	$3.40 \times 10^{-11} \cdot \exp(\text{-}1600.0/T)$	J,1
207	$H_2CQ + O \rightarrow HCQ + OH$	$3.40 \times 10^{-11} \cdot \exp(\text{-}1600.0/T)$	J,1
208	$H_2CO + Q \rightarrow HCO + QH$	$3.40 \times 10^{-11} \cdot \exp(\text{-}1600.0/T)$	J,1
209	$O + H_2O_2 \rightarrow OH + HO_2$	$1.40 \times 10^{-12} \cdot \exp(\text{-}2000.0/T)$	A,1
210	$O + H_2OP \rightarrow OH + HOP$	$1.40 \times 10^{-12} \cdot \exp(\text{-}2000.0/T)$	A,1
211	$P + H_2O_2 \rightarrow PH + HO_2$	$1.40 \times 10^{-12} \cdot \exp(\text{-}2000.0/T)$	A,1
212	$O + H_2OQ \rightarrow OH + HOQ$	$1.40 \times 10^{-12} \cdot \exp(\text{-}2000.0/T)$	A,1
213	$Q + H_2O_2 \rightarrow QH + HO_2$	$1.40 \times 10^{-12} \cdot \exp(\text{-}2000.0/T)$	A,1
214	$HO_2 + h\nu \rightarrow OH + O$	7.45×10^{-11}	E,3
215	$HOP + h\nu \rightarrow PH + O$	7.53×10^{-10}	E,3
216	$HOP + h\nu \rightarrow OH + P$	3.97×10^{-10}	E,3
217	$HOQ + h\nu \rightarrow QH + O$	3.35×10^{-05}	E,3
218	$HOQ + h\nu \rightarrow OH + Q$	1.37×10^{-08}	E,3
219	$HNO_2 + h\nu \rightarrow NO + OH$	1.70×10^{-03}	K,1
220	$HNOP + h\nu \rightarrow NP + OH$	$0.5 \times 1.70 \times 10^{-03}$	K,1
221	$HNOP + h\nu \rightarrow NO + PH$	$0.5 \times 1.70 \times 10^{-03}$	K,1
222	$HNOQ + h\nu \rightarrow NQ + OH$	$0.5 \times 1.70 \times 10^{-03}$	K,1
223	$HNOQ + h\nu \rightarrow NO + QH$	$0.5 \times 1.70 \times 10^{-03}$	K,1
224	$HNO_3 + h\nu \rightarrow NO_2 + OH$	1.38×10^{-08}	E,3
225	$HNOOP + h\nu \rightarrow NOP + OH$	2.77×10^{-08}	E,3
226	$HNOOP + h\nu \rightarrow NO_2 + PH$	7.28×10^{-08}	E,3
227	$HNOOQ + h\nu \rightarrow NOQ + OH$	7.39×10^{-08}	E,3
228	$HNOOQ + h\nu \rightarrow NO_2 + QH$	1.48×10^{-07}	E,3

Rxn #	Reaction	Rate [$cm^3\ s^{-1}$]	Source
229	$NO + h\nu \rightarrow N + O$	$2.13 \times 10^{+02}$	*D*,3
230	$NP + h\nu \rightarrow N + P$	7.65×10^{-02}	*D*,3
231	$NQ + h\nu \rightarrow N + Q$	8.23×10^{-02}	*D*,3
232	$NO_2 + h\nu \rightarrow NO + O$	8.23×10^{-02}	*E*,3
233	$NOP + h\nu \rightarrow NP + O$	3.82×10^{-01}	*E*,3
234	$NOP + h\nu \rightarrow NO + P$	4.40×10^{-01}	*E*,3
235	$NOQ + h\nu \rightarrow NQ + O$	4.40×10^{-01}	*E*,3
236	$NOQ + h\nu \rightarrow NO + Q$	2.69×10^{-08}	*E*,3
237	$OH + CH_4 \rightarrow CH_3 + H_2O$	$2.45 \times 10^{-12} \cdot \exp(-1775.0/T)$	*A*,1
238	$PH + CH_4 \rightarrow CH_3 + H_2P$	$2.45 \times 10^{-12} \cdot \exp(-1775.0/T)$	*A*,1
239	$QH + CH_4 \rightarrow CH_3 + H_2Q$	$2.45 \times 10^{-12} \cdot \exp(-1775.0/T)$	*A*,1
240	$O(^1D) + CH_4 \rightarrow CH_3 + OH$	$0.95 \times 1.75 \times 10^{-10}$	*L*,1
241	$P(^1D) + CH_4 \rightarrow CH_3 + PH$	$0.95 \times 1.75 \times 10^{-10}$	*L*,1
242	$Q(^1D) + CH_4 \rightarrow CH_3 + QH$	$0.95 \times 1.75 \times 10^{-10}$	*L*,1
243	$O(^1D) + CH_4 \rightarrow H_2CO + H_2$	$0.05 \times 1.75 \times 10^{-10}$	*L*,1
244	$P(^1D) + CH_4 \rightarrow H_2CP + H_2$	$0.05 \times 1.75 \times 10^{-10}$	*L*,1
245	$Q(^1D) + CH_4 \rightarrow H_2CQ + H_2$	$0.05 \times 1.75 \times 10^{-10}$	*L*,1
246	$^1CH_2 + CH_4 \rightarrow CH_3 + CH_3$	3.60×10^{-11}	*M*,1
247	$^1CH_2 + O_2 \rightarrow H + CO + OH$	$0.5 \times 4.10 \times 10^{-11} \cdot \exp(-750.0/T)$	*N*,1
248	$^1CH_2 + OP \rightarrow H + CP + OH$	$0.25 \times 4.10 \times 10^{-11} \cdot \exp(-750.0/T)$	*N*,1
249	$^1CH_2 + OP \rightarrow H + CO + PH$	$0.25 \times 4.10 \times 10^{-11} \cdot \exp(-750.0/T)$	*N*,1
250	$^1CH_2 + OQ \rightarrow H + CQ + OH$	$0.25 \times 4.10 \times 10^{-11} \cdot \exp(-750.0/T)$	*N*,1
251	$^1CH_2 + OQ \rightarrow H + CO + QH$	$0.25 \times 4.10 \times 10^{-11} \cdot \exp(-750.0/T)$	*N*,1
252	$^1CH_2 + O_2 \rightarrow H_2 + CO_2$	$0.5 \times 4.10 \times 10^{-11} \cdot \exp(-750.0/T)$	*N*,1
253	$^1CH_2 + OP \rightarrow H_2 + COP$	$0.5 \times 4.10 \times 10^{-11} \cdot \exp(-750.0/T)$	*N*,1
254	$^1CH_2 + OQ \rightarrow H_2 + COQ$	$0.5 \times 4.10 \times 10^{-11} \cdot \exp(-750.0/T)$	*N*,1
255	$^1CH_2 + N_2 \rightarrow {}^3CH_2 + N_2$	1.00×10^{-11}	*G*,1

Rxn #	Reaction	Rate [$cm^3\ s^{-1}$]	Source
256	$^3CH_2 + H_2 \rightarrow CH_3 + H$	5.00×10^{-15}	*O*,1
257	$^3CH_2 + CH_4 \rightarrow CH_3 + CH_3$	$7.13 \times 10^{-12} \cdot \exp(-5050.0/T)$	*G*,1
258	$^3CH_2 + O_2 \rightarrow HCO + OH$	$4.10 \times 10^{-11} \cdot \exp(-750.0/T)$	*M*,1
259	$^3CH_2 + OP \rightarrow HCP + OH$	$0.5 \times 4.10 \times 10^{-11} \cdot \exp(-750.0/T)$	*M*,1
260	$^3CH_2 + OP \rightarrow HCO + PH$	$0.5 \times 4.10 \times 10^{-11} \cdot \exp(-750.0/T)$	*M*,1
261	$^3CH_2 + OQ \rightarrow HCQ + OH$	$0.5 \times 4.10 \times 10^{-11} \cdot \exp(-750.0/T)$	*M*,1
262	$^3CH_2 + OQ \rightarrow HCO + QH$	$0.5 \times 4.10 \times 10^{-11} \cdot \exp(-750.0/T)$	*M*,1
263	$CH_3 + O_2 \rightarrow H_2CO + OH$	3.00×10^{-16}	*J*,1
264	$CH_3 + OP \rightarrow H_2CP + OH$	$0.5 \times 3.00 \times 10^{-16}$	*J*,1
265	$CH_3 + OP \rightarrow H_2CO + PH$	$0.5 \times 3.00 \times 10^{-16}$	*J*,1
266	$CH_3 + OQ \rightarrow H_2CQ + OH$	$0.5 \times 3.00 \times 10^{-16}$	*J*,1
267	$CH_3 + OQ \rightarrow H_2CO + QH$	$0.5 \times 3.00 \times 10^{-16}$	*J*,1
268	$CH_3 + O \rightarrow H_2CO + H$	1.10×10^{-10}	*J*,1
269	$CH_3 + P \rightarrow H_2CP + H$	1.10×10^{-10}	*J*,1
270	$CH_3 + Q \rightarrow H_2CQ + H$	1.10×10^{-10}	*J*,1
271	$CH_3 + CH_3 \rightarrow C_2H_6$	$k_0 = 1.13 \times 10^{-25} \cdot (T/300)^{-3.75} \cdot \exp(-494.0/T)$ $k_\infty = 7.42 \times 10^{-11} \cdot (T/300)^{-0.69} \cdot \exp(-88.0/T)$	*G*,2
272	$CH_3 + h\nu \rightarrow {}^3CH_2 + H$	1.00×10^{-05}	*K*,1
273	$CH_3 + H \rightarrow CH_4$	$k_0 = 2.63 \times 10^{-28} \cdot (T/300)^{-2.98} \cdot \exp(-635.0/T)$ $k_\infty = 3.50 \times 10^{-10}$	*G*,2
274	$CH_3 + HCO \rightarrow CH_4 + CO$	9.30×10^{-11}	*P*,1
275	$CH_3 + HCP \rightarrow CH_4 + CP$	9.30×10^{-11}	*P*,1
276	$CH_3 + HCQ \rightarrow CH_4 + CQ$	9.30×10^{-11}	*P*,1
277	$CH_3 + HNO \rightarrow CH_4 + NO$	$1.85 \times 10^{-11} \cdot (T/300)^{0.6} \cdot \exp(-176.0/T)$	*Q*,1
278	$CH_3 + HNP \rightarrow CH_4 + NP$	$1.85 \times 10^{-11} \cdot (T/300)^{0.6} \cdot \exp(-176.0/T)$	*Q*,1
279	$CH_3 + HNQ \rightarrow CH_4 + NQ$	$1.85 \times 10^{-11} \cdot (T/300)^{0.6} \cdot \exp(-176.0/T)$	*Q*,1

Rxn #	Reaction	Rate [cm^3 s^{-1}]	Source
280	$CH_3 + H_2CO \rightarrow CH_4 + HCO$	$1.12 \times 10^{-14} \cdot (T/300)^{3.36} \cdot \exp(-2170.0/T)$	*G*,1
281	$CH_3 + H_2CP \rightarrow CH_4 + HCP$	$1.12 \times 10^{-14} \cdot (T/300)^{3.36} \cdot \exp(-2170.0/T)$	*G*,1
282	$CH_3 + H_2CQ \rightarrow CH_4 + HCQ$	$1.12 \times 10^{-14} \cdot (T/300)^{3.36} \cdot \exp(-2170.0/T)$	*G*,1
283	$H + NO \rightarrow HNO$	$k_0 = 1.34 \times 10^{-31} \cdot (T/300)^{-1.32} \cdot \exp(-370.0/T)$ $k_\infty = 2.44 \times 10^{-10} \cdot (T/300)^{-0.41}$	*R*,2
284	$H + NP \rightarrow HNP$	$k_0 = 1.34 \times 10^{-31} \cdot (T/300)^{-1.32} \cdot \exp(-370.0/T)$ $k_\infty = 2.44 \times 10^{-10} \cdot (T/300)^{-0.41}$	*R*,2
285	$H + NQ \rightarrow HNQ$	$k_0 = 1.34 \times 10^{-31} \cdot (T/300)^{-1.32} \cdot \exp(-370.0/T)$ $k_\infty = 2.44 \times 10^{-10} \cdot (T/300)^{-0.41}$	*R*,2
286	$N + N \rightarrow N_2$	$k_0 = 4.10 \times 10^{-34}$ $k_\infty = 1.00 \times 10^{-10}$	*G*,2
287	$N + O_2 \rightarrow NO + O$	$1.50 \times 10^{-11} \cdot \exp(-3600.0/T)$	*A*,1
288	$N + OP \rightarrow NP + O$	$0.5 \times 1.50 \times 10^{-11} \cdot \exp(-3600.0/T)$	*A*,1
289	$N + OP \rightarrow NO + P$	$0.5 \times 1.50 \times 10^{-11} \cdot \exp(-3600.0/T)$	*A*,1
290	$N + OQ \rightarrow NQ + O$	$0.5 \times 1.50 \times 10^{-11} \cdot \exp(-3600.0/T)$	*A*,1
291	$N + OQ \rightarrow NO + Q$	$0.5 \times 1.50 \times 10^{-11} \cdot \exp(-3600.0/T)$	*A*,1
292	$N + O_3 \rightarrow NO + O_2$	$0.00 \times 10^{+00}$	*A*,1
293	$N + OOP \rightarrow NO + OP$	$0.6666667 \times 0.00 \times 10^{+00}$	*A*,1
294	$N + OOP \rightarrow NP + O_2$	$0.3333333 \times 0.00 \times 10^{+00}$	*A*,1
295	$N + OOQ \rightarrow NO + OQ$	$0.666666667 \times 0.00 \times 10^{+00}$	*A*,1
296	$N + OOQ \rightarrow NQ + O_2$	$0.333333333 \times 0.00 \times 10^{+00}$	*A*,1
297	$N + OH \rightarrow NO + H$	$5.00 \times 10^{-11} \cdot \exp(-6.0/T)$	*G*,1
298	$N + PH \rightarrow NP + H$	$5.00 \times 10^{-11} \cdot \exp(-6.0/T)$	*G*,1
299	$N + QH \rightarrow NQ + H$	$5.00 \times 10^{-11} \cdot \exp(-6.0/T)$	*G*,1
300	$N + NO \rightarrow N_2 + O$	$2.10 \times 10^{-11} \cdot \exp(100.0/T)$	*A*,1

Rxn #	Reaction	Rate [$cm^3\ s^{-1}$]	Source
301	$N + NP \rightarrow N_2 + P$	$2.10 \times 10^{-11} \cdot \exp(100.0/T)$	*A*,1
302	$N + NQ \rightarrow N_2 + Q$	$2.10 \times 10^{-11} \cdot \exp(100.0/T)$	*A*,1
303	$NO + O_3 \rightarrow NO_2 + O_2$	$3.00 \times 10^{-12} \cdot \exp(-1500.0/T)$	*A*,1
304	$NP + O_3 \rightarrow NOP + O_2$	$3.00 \times 10^{-12} \cdot \exp(-1500.0/T)$	*A*,1
305	$NO + OOP \rightarrow NOP + O_2$	$0.3333333 \times 3.00 \times 10^{-12} \cdot \exp(-1500.0/T)$	*A*,1
306	$NO + OOP \rightarrow NO_2 + OP$	$0.6666667 \times 3.00 \times 10^{-12} \cdot \exp(-1500.0/T)$	*A*,1
307	$NQ + O_3 \rightarrow NOQ + O_2$	$3.00 \times 10^{-12} \cdot \exp(-1500.0/T)$	*A*,1
308	$NO + OOQ \rightarrow NOQ + O_2$	$0.3333333 \times 3.00 \times 10^{-12} \cdot \exp(-1500.0/T)$	*A*,1
309	$NO + OOQ \rightarrow NO_2 + OQ$	$0.6666667 \times 3.00 \times 10^{-12} \cdot \exp(-1500.0/T)$	*A*,1
310	$O + NO \rightarrow NO_2$	$k_0 = 9.00 \times 10^{-32} \cdot (T/300)^{-1.5}$ $k_\infty = 3.00 \times 10^{-11}$	*A*,2
311	$O + NP \rightarrow NOP$	$k_0 = 9.00 \times 10^{-32} \cdot (T/300)^{-1.5}$ $k_\infty = 3.00 \times 10^{-11}$	*A*,2
312	$P + NO \rightarrow NOP$	$k_0 = 9.00 \times 10^{-32} \cdot (T/300)^{-1.5}$ $k_\infty = 3.00 \times 10^{-11}$	*A*,2
313	$O + NQ \rightarrow NOQ$	$k_0 = 9.00 \times 10^{-32} \cdot (T/300)^{-1.5}$ $k_\infty = 3.00 \times 10^{-11}$	*A*,2
314	$Q + NO \rightarrow NOQ$	$k_0 = 9.00 \times 10^{-32} \cdot (T/300)^{-1.5}$ $k_\infty = 3.00 \times 10^{-11}$	*A*,2
315	$HO_2 + NO \rightarrow NO_2 + OH$	$3.30 \times 10^{-12} \cdot \exp(270.0/T)$	*A*,1
316	$HOP + NO \rightarrow NO_2 + PH$	$0.5 \times 3.30 \times 10^{-12} \cdot \exp(270.0/T)$	*A*,1
317	$HOP + NO \rightarrow NOP + OH$	$0.5 \times 3.30 \times 10^{-12} \cdot \exp(270.0/T)$	*A*,1
318	$HO_2 + NP \rightarrow NOP + OH$	$3.30 \times 10^{-12} \cdot \exp(270.0/T)$	*A*,1
319	$HOQ + NO \rightarrow NO_2 + QH$	$0.5 \times 3.30 \times 10^{-12} \cdot \exp(270.0/T)$	*A*,1
320	$HOQ + NO \rightarrow NOQ + OH$	$0.5 \times 3.30 \times 10^{-12} \cdot \exp(270.0/T)$	*A*,1

Rxn #	Reaction	Rate [$cm^3\ s^{-1}$]	Source
321	$HO_2 + NQ \rightarrow NOQ + OH$	$3.30 \times 10^{-12} \cdot \exp(270.0/\mathrm{T})$	*A*,1
322	$OH + NO \rightarrow HNO_2$	$k_0 = 7.00 \times 10^{-31} \cdot (T/300)^{-2.6}$ $k_\infty = 3.60 \times 10^{-11} \cdot (T/300)^{-0.1}$	*A*,2
323	$OH + NP \rightarrow HNOP$	$k_0 = 7.00 \times 10^{-31} \cdot (T/300)^{-2.6}$ $k_\infty = 3.60 \times 10^{-11} \cdot (T/300)^{-0.1}$	*A*,2
324	$PH + NO \rightarrow HNOP$	$k_0 = 7.00 \times 10^{-31} \cdot (T/300)^{-2.6}$ $k_\infty = 3.60 \times 10^{-11} \cdot (T/300)^{-0.1}$	*A*,2
325	$OH + NQ \rightarrow HNOQ$	$k_0 = 7.00 \times 10^{-31} \cdot (T/300)^{-2.6}$ $k_\infty = 3.60 \times 10^{-11} \cdot (T/300)^{-0.1}$	*A*,2
326	$QH + NO \rightarrow HNOQ$	$k_0 = 7.00 \times 10^{-31} \cdot (T/300)^{-2.6}$ $k_\infty = 3.60 \times 10^{-11} \cdot (T/300)^{-0.1}$	*A*,2
327	$O + NO_2 \rightarrow NO + O_2$	$5.10 \times 10^{-12} \cdot \exp(210.0/\mathrm{T})$	*A*,1
328	$P + NO_2 \rightarrow NO + OP$	$5.10 \times 10^{-12} \cdot \exp(210.0/\mathrm{T})$	*A*,1
329	$O + NOP \rightarrow NP + O_2$	$0.5 \times 5.10 \times 10^{-12} \cdot \exp(210.0/\mathrm{T})$	*A*,1
330	$O + NOP \rightarrow NO + OP$	$0.5 \times 5.10 \times 10^{-12} \cdot \exp(210.0/\mathrm{T})$	*A*,1
331	$Q + NO_2 \rightarrow NO + OQ$	$5.10 \times 10^{-12} \cdot \exp(210.0/\mathrm{T})$	*A*,1
332	$O + NOQ \rightarrow NQ + O_2$	$0.5 \times 5.10 \times 10^{-12} \cdot \exp(210.0/\mathrm{T})$	*A*,1
333	$O + NOQ \rightarrow NO + OQ$	$0.5 \times 5.10 \times 10^{-12} \cdot \exp(210.0/\mathrm{T})$	*A*,1
334	$OH + NO_2 \rightarrow HNO_3$	$k_0 = 1.80 \times 10^{-30} \cdot (T/300)^{-3}$ $k_\infty = 2.80 \times 10^{-11}$	*J*,2
335	$PH + NO_2 \rightarrow HNOOP$	$k_0 = 1.80 \times 10^{-30} \cdot (T/300)^{-3}$ $k_\infty = 2.80 \times 10^{-11}$	*J*,2
336	$OH + NOP \rightarrow HNOOP$	$k_0 = 1.80 \times 10^{-30} \cdot (T/300)^{-3}$ $k_\infty = 2.80 \times 10^{-11}$	*J*,2

Rxn #	Reaction	Rate [$cm^3\ s^{-1}$]	Source
337	$QH + NO_2 \rightarrow HNOOQ$	$k_0 = 1.80 \times 10^{-30} \cdot (T/300)^{-3}$ $k_\infty = 2.80 \times 10^{-11}$	J,2
338	$OH + NOQ \rightarrow HNOOQ$	$k_0 = 1.80 \times 10^{-30} \cdot (T/300)^{-3}$ $k_\infty = 2.80 \times 10^{-11}$	J,2
339	$H + NO_2 \rightarrow OH + NO$	$4.00 \times 10^{-10} \cdot \exp(-340.0/T)$	A,1
340	$H + NOP \rightarrow PH + NO$	$0.5 \times 4.00 \times 10^{-10} \cdot \exp(-340.0/T)$	A,1
341	$H + NOP \rightarrow OH + NP$	$0.5 \times 4.00 \times 10^{-10} \cdot \exp(-340.0/T)$	A,1
342	$H + NOQ \rightarrow QH + NO$	$0.5 \times 4.00 \times 10^{-10} \cdot \exp(-340.0/T)$	A,1
343	$H + NOQ \rightarrow OH + NQ$	$0.5 \times 4.00 \times 10^{-10} \cdot \exp(-340.0/T)$	A,1
344	$HCO + NO \rightarrow HNO + CO$	1.35×10^{-11}	S,1
345	$HCO + NP \rightarrow HNP + CO$	1.35×10^{-11}	S,1
346	$HCP + NO \rightarrow HNO + CP$	1.35×10^{-11}	S,1
347	$HCO + NQ \rightarrow HNQ + CO$	1.35×10^{-11}	S,1
348	$HCQ + NO \rightarrow HNO + CQ$	1.35×10^{-11}	S,1
349	$HNO + h\nu \rightarrow NO + H$	1.70×10^{-03}	S,1
350	$HNP + h\nu \rightarrow NP + H$	1.70×10^{-03}	S,1
351	$HNQ + h\nu \rightarrow NQ + H$	1.70×10^{-03}	S,1
352	$H + HNO \rightarrow H_2 + NO$	$3.01 \times 10^{-11} \cdot \exp(-500.0/T)$	T,1
353	$H + HNP \rightarrow H_2 + NP$	$3.01 \times 10^{-11} \cdot \exp(-500.0/T)$	T,1
354	$H + HNQ \rightarrow H_2 + NQ$	$3.01 \times 10^{-11} \cdot \exp(-500.0/T)$	T,1
355	$O + HNO \rightarrow OH + NO$	$3.80 \times 10^{-11} \cdot (T/300)^{-0.08}$	G,1
356	$O + HNP \rightarrow OH + NP$	$3.80 \times 10^{-11} \cdot (T/300)^{-0.08}$	G,1
357	$P + HNO \rightarrow PH + NO$	$3.80 \times 10^{-11} \cdot (T/300)^{-0.08}$	G,1
358	$O + HNQ \rightarrow OH + NQ$	$3.80 \times 10^{-11} \cdot (T/300)^{-0.08}$	G,1
359	$Q + HNO \rightarrow QH + NO$	$3.80 \times 10^{-11} \cdot (T/300)^{-0.08}$	G,1
360	$OH + HNO \rightarrow H_2O + NO$	$8.00 \times 10^{-11} \cdot \exp(-500.0/T)$	T,1

Rxn #	Reaction	Rate [$cm^3\ s^{-1}$]	Source
361	$OH + HNP \rightarrow H_2O + NP$	$8.00 \times 10^{-11} \cdot \exp(-500.0/T)$	T,1
362	$PH + HNO \rightarrow H_2P + NO$	$8.00 \times 10^{-11} \cdot \exp(-500.0/T)$	T,1
363	$OH + HNQ \rightarrow H_2O + NQ$	$8.00 \times 10^{-11} \cdot \exp(-500.0/T)$	T,1
364	$QH + HNO \rightarrow H_2Q + NO$	$8.00 \times 10^{-11} \cdot \exp(-500.0/T)$	T,1
365	$OH + HNO_2 \rightarrow H_2O + NO_2$	$1.80 \times 10^{-11} \cdot \exp(-390.0/T)$	A,1
366	$OH + HNOP \rightarrow H_2O + NOP$	$1.80 \times 10^{-11} \cdot \exp(-390.0/T)$	A,1
367	$PH + HNO_2 \rightarrow H_2P + NO_2$	$1.80 \times 10^{-11} \cdot \exp(-390.0/T)$	A,1
368	$OH + HNOQ \rightarrow H_2O + NOQ$	$1.80 \times 10^{-11} \cdot \exp(-390.0/T)$	A,1
369	$QH + HNO_2 \rightarrow H_2Q + NO_2$	$1.80 \times 10^{-11} \cdot \exp(-390.0/T)$	A,1
370	$CH_4 + O \rightarrow CH_3 + OH$	$8.41 \times 10^{-12} \cdot (T/300)^{1.56} \cdot \exp(-4280.0/T)$	G,1
371	$CH_4 + P \rightarrow CH_3 + PH$	$8.41 \times 10^{-12} \cdot (T/300)^{1.56} \cdot \exp(-4280.0/T)$	G,1
372	$CH_4 + Q \rightarrow CH_3 + QH$	$8.41 \times 10^{-12} \cdot (T/300)^{1.56} \cdot \exp(-4280.0/T)$	G,1
373	$^1CH_2 + H_2 \rightarrow CH_3 + H$	1.20×10^{-10}	G,1
374	$^1CH_2 + H_2 \rightarrow {}^3CH_2 + H_2$	1.26×10^{-11}	G,1
375	$^1CH_2 + CO_2 \rightarrow H_2CO + CO$	1.00×10^{-12}	U,1
376	$^1CH_2 + COP \rightarrow H_2CP + CO$	$0.5 \times 1.00 \times 10^{-12}$	U,1
377	$^1CH_2 + COP \rightarrow H_2CO + CP$	$0.5 \times 1.00 \times 10^{-12}$	U,1
378	$^1CH_2 + COQ \rightarrow H_2CQ + CO$	$0.5 \times 1.00 \times 10^{-12}$	U,1
379	$^1CH_2 + COQ \rightarrow H_2CO + CQ$	$0.5 \times 1.00 \times 10^{-12}$	U,1
380	$^3CH_2 + O \rightarrow CO + H + H$	$0.599 \times 3.40 \times 10^{-10} \cdot \exp(-270.0/T)$	G,1
381	$^3CH_2 + P \rightarrow CP + H + H$	$0.6 \times 3.40 \times 10^{-10} \cdot \exp(-270.0/T)$	G,1
382	$^3CH_2 + Q \rightarrow CQ + H + H$	$0.6 \times 3.40 \times 10^{-10} \cdot \exp(-270.0/T)$	G,1
383	$^3CH_2 + CO_2 \rightarrow H_2CO + CO$	3.90×10^{-14}	O,1
384	$^3CH_2 + COP \rightarrow H_2CP + CO$	$0.5 \times 3.90 \times 10^{-14}$	O,1
385	$^3CH_2 + COP \rightarrow H_2CO + CP$	$0.5 \times 3.90 \times 10^{-14}$	O,1
386	$^3CH_2 + COQ \rightarrow H_2CQ + CO$	$0.5 \times 3.90 \times 10^{-14}$	O,1
387	$^3CH_2 + COQ \rightarrow H_2CO + CQ$	$0.5 \times 3.90 \times 10^{-14}$	O,1

Rxn #	Reaction	Rate [$cm^3\ s^{-1}$]	Source
388	$OH + C_2H_6 \rightarrow H_2O + C_2H_5$	$7.66 \times 10^{-12} \cdot \exp(-1020.0/T)$	*A*,1
389	$PH + C_2H_6 \rightarrow H_2P + C_2H_5$	$7.66 \times 10^{-12} \cdot \exp(-1020.0/T)$	*A*,1
390	$QH + C_2H_6 \rightarrow H_2Q + C_2H_5$	$7.66 \times 10^{-12} \cdot \exp(-1020.0/T)$	*A*,1
391	$C_2H_6 + O \rightarrow C_2H_5 + OH$	$8.63 \times 10^{-12} \cdot (T/300)^{1.5} \cdot \exp(-2920.0/T)$	*G*,1
392	$C_2H_6 + P \rightarrow C_2H_5 + PH$	$8.63 \times 10^{-12} \cdot (T/300)^{1.5} \cdot \exp(-2920.0/T)$	*G*,1
393	$C_2H_6 + Q \rightarrow C_2H_5 + QH$	$8.63 \times 10^{-12} \cdot (T/300)^{1.5} \cdot \exp(-2920.0/T)$	*G*,1
394	$C_2H_6 + O(^1D) \rightarrow C_2H_5 + OH$	3.40×10^{-10}	*V*,1
395	$C_2H_6 + P(^1D) \rightarrow C_2H_5 + PH$	3.40×10^{-10}	*V*,1
396	$C_2H_6 + Q(^1D) \rightarrow C_2H_5 + QH$	3.40×10^{-10}	*V*,1
397	$C_2H_5 + HCO \rightarrow C_2H_6 + CO$	7.21×10^{-11}	*W*,1
398	$C_2H_5 + HCP \rightarrow C_2H_6 + CP$	7.21×10^{-11}	*W*,1
399	$C_2H_5 + HCQ \rightarrow C_2H_6 + CQ$	7.21×10^{-11}	*W*,1
400	$C_2H_5 + HNO \rightarrow C_2H_6 + NO$	$1.60 \times 10^{-12} \cdot \exp(-1000.0/T)$	*X*,1
401	$C_2H_5 + HNP \rightarrow C_2H_6 + NP$	$1.60 \times 10^{-12} \cdot \exp(-1000.0/T)$	*X*,1
402	$C_2H_5 + HNQ \rightarrow C_2H_6 + NQ$	$1.60 \times 10^{-12} \cdot \exp(-1000.0/T)$	*X*,1
403	$C_2H_5 + O_2 \rightarrow CH_3 + HCO + OH$	1.00×10^{-14}	*J*,1
404	$C_2H_5 + OP \rightarrow CH_3 + HCP + OH$	$0.5 \times 1.00 \times 10^{-14}$	*J*,1
405	$C_2H_5 + OP \rightarrow CH_3 + HCO + PH$	$0.5 \times 1.00 \times 10^{-14}$	*J*,1
406	$C_2H_5 + OQ \rightarrow CH_3 + HCQ + OH$	$0.5 \times 1.00 \times 10^{-14}$	*J*,1
407	$C_2H_5 + OQ \rightarrow CH_3 + HCO + QH$	$0.5 \times 1.00 \times 10^{-14}$	*J*,1
408	$CO + O(^1D) \rightarrow CO + O$	$4.70 \times 10^{-11} \cdot \exp(63.0/T)$	*Y*,1
409	$CP + O(^1D) \rightarrow CP + O$	$4.70 \times 10^{-11} \cdot \exp(63.0/T)$	*Y*,1
410	$CO + P(^1D) \rightarrow CO + P$	$4.70 \times 10^{-11} \cdot \exp(63.0/T)$	*Y*,1
411	$CQ + O(^1D) \rightarrow CQ + O$	$4.70 \times 10^{-11} \cdot \exp(63.0/T)$	*Y*,1
412	$CO + Q(^1D) \rightarrow CO + Q$	$4.70 \times 10^{-11} \cdot \exp(63.0/T)$	*Y*,1
413	$HNO_3 + OH \rightarrow H_2O + NO_3$	See JPL-18 note C 9	*A*
414	$HNOOP + OH \rightarrow H_2O + NOOP$		*A*

Rxn #	Reaction	Rate [$cm^3\ s^{-1}$]	Source
415	$HNO_3 + PH \rightarrow H_2P + NO_3$		*A*
416	$HNOOQ + OH \rightarrow H_2O + NOOQ$		*A*
417	$HNO_3 + QH \rightarrow H_2Q + NO_3$		*A*
418	$N + HO_2 \rightarrow NO + OH$	2.20×10^{-11}	*Z*,1
419	$N + HOP \rightarrow NP + OH$	$0.5 \times 2.20 \times 10^{-11}$	*Z*,1
420	$N + HOP \rightarrow NO + PH$	$0.5 \times 2.20 \times 10^{-11}$	*Z*,1
421	$N + HOQ \rightarrow NQ + OH$	$0.5 \times 2.20 \times 10^{-11}$	*Z*,1
422	$N + HOQ \rightarrow NO + QH$	$0.5 \times 2.20 \times 10^{-11}$	*Z*,1
423	$HO_2 + NO_2 \rightarrow HNO_2 + O_2$	5.00×10^{-16}	*A*,1
424	$HOP + NO_2 \rightarrow HNO_2 + OP$	5.00×10^{-16}	*A*,1
425	$HO_2 + NOP \rightarrow HNOP + O_2$	5.00×10^{-16}	*A*,1
426	$HOQ + NO_2 \rightarrow HNO_2 + OQ$	5.00×10^{-16}	*A*,1
427	$HO_2 + NOQ \rightarrow HNOQ + O_2$	5.00×10^{-16}	*A*,1
428	$SO + h\nu \rightarrow S + O$	2.07×10^{-11}	*E*,3
429	$SP + h\nu \rightarrow S + P$	1.11×10^{-11}	*E*,3
430	$SQ + h\nu \rightarrow S + Q$	2.22×10^{-11}	*E*,3
431	$H_2S + h\nu \rightarrow HS + H$	1.11×10^{-10}	*E*,3
432	$SO_2 + h\nu \rightarrow SO + O$	5.91×10^{-11}	*E*,3
433	$SO_2 + h\nu \rightarrow {}^1SO_2$	1.18×10^{-10}	*E*,3
434	$SO_2 + h\nu \rightarrow {}^3SO_2$	4.66×10^{-11}	*E*,3
435	$SOP + h\nu \rightarrow SP + O$	3.60×10^{-14}	*E*,3
436	$SOP + h\nu \rightarrow SO + P$	3.60×10^{-14}	*E*,3
437	$SOP + h\nu \rightarrow {}^1SOP$	1.92×10^{-13}	*E*,3
438	$SOP + h\nu \rightarrow {}^3SOP$	1.92×10^{-13}	*E*,3
439	$SOQ + h\nu \rightarrow SQ + O$	1.19×10^{-15}	*E*,3
440	$SOQ + h\nu \rightarrow SO + Q$	9.19×10^{-19}	*E*,3
441	$SOQ + h\nu \rightarrow {}^1SOQ$	4.86×10^{-19}	*E*,3

Rxn #	Reaction	Rate [$cm^3\ s^{-1}$]	Source
442	$SOQ + h\nu \rightarrow {}^3SOQ$	4.92×10^{-18}	*E*,3
443	$SO + O_2 \rightarrow SO_2 + O$	$1.60 \times 10^{-13} \cdot \exp(-2280.0/T)$	*A*,1
444	$SP + O_2 \rightarrow SOP + O$	$1.60 \times 10^{-13} \cdot \exp(-2280.0/T)$	*A*,1
445	$SO + OP \rightarrow SOP + O$	$0.5 \times 1.60 \times 10^{-13} \cdot \exp(-2280.0/T)$	*A*,1
446	$SO + OP \rightarrow SO_2 + P$	$0.5 \times 1.60 \times 10^{-13} \cdot \exp(-2280.0/T)$	*A*,1
447	$SQ + O_2 \rightarrow SOQ + O$	$1.60 \times 10^{-13} \cdot \exp(-2280.0/T)$	*A*,1
448	$SO + OQ \rightarrow SOQ + O$	$0.5 \times 1.60 \times 10^{-13} \cdot \exp(-2280.0/T)$	*A*,1
449	$SO + OQ \rightarrow SO_2 + Q$	$0.5 \times 1.60 \times 10^{-13} \cdot \exp(-2280.0/T)$	*A*,1
450	$SO + HO_2 \rightarrow SO_2 + OH$	2.80×10^{-11}	*a*,1
451	$SP + HO_2 \rightarrow SOP + OH$	2.80×10^{-11}	*a*,1
452	$SO + HOP \rightarrow SOP + OH$	$0.5 \times 2.80 \times 10^{-11}$	*a*,1
453	$SO + HOP \rightarrow SO_2 + PH$	$0.5 \times 2.80 \times 10^{-11}$	*a*,1
454	$SQ + HO_2 \rightarrow SOQ + OH$	2.80×10^{-11}	*a*,1
455	$SO + HOQ \rightarrow SOQ + OH$	$0.5 \times 2.80 \times 10^{-11}$	*a*,1
456	$SO + HOQ \rightarrow SO_2 + QH$	$0.5 \times 2.80 \times 10^{-11}$	*a*,1
457	$SO + O \rightarrow SO_2$	$k_0 = 5.10 \times 10^{-31}$ $k_\infty = 5.31 \times 10^{-11}$	*b*,2
458	$SP + O \rightarrow SOP$	$k_0 = 5.10 \times 10^{-31}$ $k_\infty = 5.31 \times 10^{-11}$	*b*,2
459	$SO + P \rightarrow SOP$	$k_0 = 5.10 \times 10^{-31}$ $k_\infty = 5.31 \times 10^{-11}$	*b*,2
460	$SQ + O \rightarrow SOQ$	$k_0 = 5.10 \times 10^{-31}$ $k_\infty = 5.31 \times 10^{-11}$	*b*,2
461	$SO + Q \rightarrow SOQ$	$k_0 = 5.10 \times 10^{-31}$ $k_\infty = 5.31 \times 10^{-11}$	*b*,2

Rxn #	Reaction	Rate [$cm^3\ s^{-1}$]	Source
462	$OH + SO \rightarrow H + SO_2$	$2.70 \times 10^{-11} \cdot \exp(335.0/T)$	*A*,1
463	$PH + SO \rightarrow H + SOP$	$2.70 \times 10^{-11} \cdot \exp(335.0/T)$	*A*,1
464	$OH + SP \rightarrow H + SOP$	$2.70 \times 10^{-11} \cdot \exp(335.0/T)$	*A*,1
465	$QH + SO \rightarrow H + SOQ$	$2.70 \times 10^{-11} \cdot \exp(335.0/T)$	*A*,1
466	$OH + SQ \rightarrow H + SOQ$	$2.70 \times 10^{-11} \cdot \exp(335.0/T)$	*A*,1
467	$OH + SO_2 \rightarrow HSO_3$	$k_0 = 3.30 \times 10^{-31} \cdot (T/300)^{-4.3}$ $k_\infty = 1.60 \times 10^{-12}$	*A*,2
468	$PH + SO_2 \rightarrow HSOOP$	$k_0 = 3.30 \times 10^{-31} \cdot (T/300)^{-4.3}$ $k_\infty = 1.60 \times 10^{-12}$	*A*,2
469	$OH + SOP \rightarrow HSOOP$	$k_0 = 3.30 \times 10^{-31} \cdot (T/300)^{-4.3}$ $k_\infty = 1.60 \times 10^{-12}$	*A*,2
470	$QH + SO_2 \rightarrow HSOOQ$	$k_0 = 3.30 \times 10^{-31} \cdot (T/300)^{-4.3}$ $k_\infty = 1.60 \times 10^{-12}$	*A*,2
471	$OH + SOQ \rightarrow HSOOQ$	$k_0 = 3.30 \times 10^{-31} \cdot (T/300)^{-4.3}$ $k_\infty = 1.60 \times 10^{-12}$	*A*,2
472	$O + SO_2 \rightarrow SO_3$	$k_0 = 1.80 \times 10^{-33} \cdot (T/300)^{2}$ $k_\infty = 4.20 \times 10^{-14} \cdot (T/300)^{1.8}$	*A*,2
473	$P + SO_2 \rightarrow SOOP$	$k_0 = 1.80 \times 10^{-33} \cdot (T/300)^{2}$ $k_\infty = 4.20 \times 10^{-14} \cdot (T/300)^{1.8}$	*A*,2
474	$O + SOP \rightarrow SOOP$	$k_0 = 1.80 \times 10^{-33} \cdot (T/300)^{2}$ $k_\infty = 4.20 \times 10^{-14} \cdot (T/300)^{1.8}$	*A*,2
475	$Q + SO_2 \rightarrow SOOQ$	$k_0 = 1.80 \times 10^{-33} \cdot (T/300)^{2}$ $k_\infty = 4.20 \times 10^{-14} \cdot (T/300)^{1.8}$	*A*,2

Rxn #	Reaction	Rate [$cm^3\ s^{-1}$]	Source
476	O + SOQ → SOOQ	$k_0 = 1.80 \times 10^{-33} \cdot (T/300)^2$ $k_\infty = 4.20 \times 10^{-14} \cdot (T/300)^{1.8}$	*A*,2
477	$SO_3 + H_2O \rightarrow H_2SO_4$	1.20×10^{-15}	*A*,1
478	$SOOP + H_2O \rightarrow$ H2SOOOP	1.20×10^{-15}	*A*,1
479	$SO_3 + H_2P \rightarrow$ H2SOOOP	1.20×10^{-15}	*A*,1
480	$SOOQ + H_2O \rightarrow$ H2SOOOQ	1.20×10^{-15}	*A*,1
481	$SO_3 + H_2Q \rightarrow$ H2SOOOQ	1.20×10^{-15}	*A*,1
482	$HSO_3 + O_2 \rightarrow HO_2 + SO_3$	$1.30 \times 10^{-12} \cdot \exp(-330.0/T)$	*A*,1
483	$HSOOP + O_2 \rightarrow HO_2 +$ SOOP	$1.30 \times 10^{-12} \cdot \exp(-330.0/T)$	*A*,1
484	$HSO_3 + OP \rightarrow HOP + SO_3$	$1.30 \times 10^{-12} \cdot \exp(-330.0/T)$	*A*,1
485	$HSOOQ + O_2 \rightarrow HO_2 +$ SOOQ	$1.30 \times 10^{-12} \cdot \exp(-330.0/T)$	*A*,1
486	$HSO_3 + OQ \rightarrow HOQ + SO_3$	$1.30 \times 10^{-12} \cdot \exp(-330.0/T)$	*A*,1
487	$HSO_3 + OH \rightarrow H_2O + SO_3$	1.00×10^{-11}	*a*,1
488	$HSOOP + OH \rightarrow H_2O +$ SOOP	1.00×10^{-11}	*a*,1
489	$HSO_3 + PH \rightarrow H_2P + SO_3$	1.00×10^{-11}	*a*,1
490	$HSOOQ + OH \rightarrow H_2O +$ SOOQ	1.00×10^{-11}	*a*,1
491	$HSO_3 + QH \rightarrow H_2Q + SO_3$	1.00×10^{-11}	*a*,1
492	$HSO_3 + H \rightarrow H_2 + SO_3$	1.00×10^{-11}	*a*,1
493	$HSOOP + H \rightarrow H_2 +$ SOOP	1.00×10^{-11}	*a*,1
494	$HSOOQ + H \rightarrow H_2 +$ SOOQ	1.00×10^{-11}	*a*,1
495	$HSO_3 + O \rightarrow OH + SO_3$	1.00×10^{-11}	*a*,1
496	$HSOOP + O \rightarrow OH +$ SOOP	1.00×10^{-11}	*a*,1
497	$HSO_3 + P \rightarrow PH + SO_3$	1.00×10^{-11}	*a*,1
498	$HSOOQ + O \rightarrow OH +$ SOOQ	1.00×10^{-11}	*a*,1
499	$HSO_3 + Q \rightarrow QH + SO_3$	1.00×10^{-11}	*a*,1
500	$OH + H_2S \rightarrow HS + H_2O$	$6.10 \times 10^{-12} \cdot \exp(-75.0/T)$	*A*,1
501	$PH + H_2S \rightarrow HS + H_2P$	$6.10 \times 10^{-12} \cdot \exp(-75.0/T)$	*A*,1

Rxn #	Reaction	Rate [cm^3 s^{-1}]	Source
502	QH + H_2S → HS + H_2Q	$6.10 \times 10^{-12} \cdot \exp(-75.0/T)$	*A*,1
503	H_2S + H → H_2 + HS	$3.66 \times 10^{-12} \cdot (T/300)^{1.94} \cdot \exp(-455.0/T)$	*c*,1
504	O + H_2S → OH + HS	$9.20 \times 10^{-12} \cdot \exp(-1800.0/T)$	*A*,1
505	P + H_2S → PH + HS	$9.20 \times 10^{-12} \cdot \exp(-1800.0/T)$	*A*,1
506	Q + H_2S → QH + HS	$9.20 \times 10^{-12} \cdot \exp(-1800.0/T)$	*A*,1
507	O + HS → SO + H	7.00×10^{-11}	*A*,1
508	P + HS → SP + H	7.00×10^{-11}	*A*,1
509	Q + HS → SQ + H	7.00×10^{-11}	*A*,1
510	HS + O_2 → OH + SO	4.00×10^{-19}	*A*,1
511	HS + OP → PH + SO	$0.5 \times 4.00 \times 10^{-19}$	*A*,1
512	HS + OP → OH + SP	$0.5 \times 4.00 \times 10^{-19}$	*A*,1
513	HS + OQ → QH + SO	$0.5 \times 4.00 \times 10^{-19}$	*A*,1
514	HS + OQ → OH + SQ	$0.5 \times 4.00 \times 10^{-19}$	*A*,1
515	HS + HO_2 → H_2S + O_2	1.00×10^{-11}	*d*,1
516	HS + HOP → H_2S + OP	1.00×10^{-11}	*d*,1
517	HS + HOQ → H_2S + OQ	1.00×10^{-11}	*d*,1
518	HS + HS → H_2S + S	1.50×10^{-11}	*e*,1
519	HS + HCO → H_2S + CO	5.00×10^{-11}	*a*,1
520	HS + HCP → H_2S + CP	5.00×10^{-11}	*a*,1
521	HS + HCQ → H_2S + CQ	5.00×10^{-11}	*a*,1
522	HS + H → H_2 + S	2.00×10^{-11}	*f*,1
523	HS + S → H + S_2	5.00×10^{-12}	*g*,1
524	S + O_2 → SO + O	$1.60 \times 10^{-12} \cdot \exp(100.0/T)$	*A*,1
525	S + OP → SP + O	$0.5 \times 1.60 \times 10^{-12} \cdot \exp(100.0/T)$	*A*,1
526	S + OP → SO + P	$0.5 \times 1.60 \times 10^{-12} \cdot \exp(100.0/T)$	*A*,1
527	S + OQ → SQ + O	$0.5 \times 1.60 \times 10^{-12} \cdot \exp(100.0/T)$	*A*,1
528	S + OQ → SO + Q	$0.5 \times 1.60 \times 10^{-12} \cdot \exp(100.0/T)$	*A*,1

Rxn #	Reaction	Rate [$cm^3\ s^{-1}$]	Source
529	$OH + S \rightarrow H + SO$	6.60×10^{-11}	*A*,1
530	$PH + S \rightarrow H + SP$	6.60×10^{-11}	*A*,1
531	$QH + S \rightarrow H + SQ$	6.60×10^{-11}	*A*,1
532	$S + HCO \rightarrow HS + CO$	4.00×10^{-11}	*h*,1
533	$S + HCP \rightarrow HS + CP$	4.00×10^{-11}	*h*,1
534	$S + HCQ \rightarrow HS + CQ$	4.00×10^{-11}	*h*,1
535	$S + HO_2 \rightarrow HS + O_2$	5.00×10^{-12}	*a*,1
536	$S + HOP \rightarrow HS + OP$	5.00×10^{-12}	*a*,1
537	$S + HOQ \rightarrow HS + OQ$	5.00×10^{-12}	*a*,1
538	$S + HO_2 \rightarrow SO + OH$	5.00×10^{-12}	*a*,1
539	$S + HOP \rightarrow SP + OH$	$0.5 \times 5.00 \times 10^{-12}$	*a*,1
540	$S + HOP \rightarrow SO + PH$	$0.5 \times 5.00 \times 10^{-12}$	*a*,1
541	$S + HOQ \rightarrow SQ + OH$	$0.5 \times 5.00 \times 10^{-12}$	*a*,1
542	$S + HOQ \rightarrow SO + QH$	$0.5 \times 5.00 \times 10^{-12}$	*a*,1
543	$S + S \rightarrow S_2$	$\begin{cases} k_0 = 1.00 \times 10^{-33} \cdot \exp(206.0/T) \\ k_\infty = 2.26 \times 10^{-14} \cdot \exp(415.0/T) \end{cases}$	*i*,2
544	$S_2 + O \rightarrow S + SO$	1.66×10^{-11}	*j*,1
545	$S_2 + P \rightarrow S + SP$	1.66×10^{-11}	*j*,1
546	$S_2 + Q \rightarrow S + SQ$	1.66×10^{-11}	*j*,1
547	$HS + H_2CO \rightarrow H_2S + HCO$	$5.50 \times 10^{-12} \cdot \exp(125.0/T)$	*k*,1
548	$HS + H_2CP \rightarrow H_2S + HCP$	$5.50 \times 10^{-12} \cdot \exp(125.0/T)$	*k*,1
549	$HS + H_2CQ \rightarrow H_2S + HCQ$	$5.50 \times 10^{-12} \cdot \exp(125.0/T)$	*k*,1
550	$S_2 + h\nu \rightarrow S + S$	2.59×10^{-18}	*E*,3
551	$S + S_2 \rightarrow S_3$	$\begin{cases} k_0 = 1.65 \times 10^{-33} \cdot \exp(144.0/T) \\ k_\infty = 1.38 \times 10^{-14} \cdot \exp(450.0/T) \end{cases}$	*l*,2

Rxn #	Reaction	Rate [$cm^3\ s^{-1}$]	Source
552	$S_2 + S_2 \rightarrow S_4$	$k_0 = 2.50 \times 10^{-30}$ $k_\infty = 5.00 \times 10^{-11}$	m,2
553	$S + S_3 \rightarrow S_4$	$k_0 = 1.65 \times 10^{-33} \cdot \exp(144.0/T)$ $k_\infty = 1.38 \times 10^{-14} \cdot \exp(450.0/T)$	n,2
554	$S_4 + S_4 \rightarrow S_8^{aer}$	$k_0 = 2.50 \times 10^{-30}$ $k_\infty = 5.00 \times 10^{-11}$	o,2
555	$S_4 + h\nu \rightarrow S_2 + S_2$	$6.78 \times 10^{+04}$	p,3
556	$S_3 + h\nu \rightarrow S_2 + S$	$4.90 \times 10^{+01}$	p,3
557	$SO_3 + h\nu \rightarrow SO_2 + O$	$2.46 \times 10^{+02}$	E,3
558	$SOOP + h\nu \rightarrow SOP + O$	$4.12 \times 10^{+04}$	E,3
559	$SOOP + h\nu \rightarrow SO_2 + P$	$1.41 \times 10^{+01}$	E,3
560	$SOOQ + h\nu \rightarrow SOQ + O$	$3.71 \times 10^{+01}$	E,3
561	$SOOQ + h\nu \rightarrow SO_2 + Q$	$6.04 \times 10^{+01}$	E,3
562	$^1SO_2 + M \rightarrow {}^3SO_2 + M$	1.00×10^{-12}	q,1
563	$^1SOP + M \rightarrow {}^3SOP + M$	1.00×10^{-12}	q,1
564	$^1SOQ + M \rightarrow {}^3SOQ + M$	1.00×10^{-12}	q,1
565	$^1SO_2 + M \rightarrow SO_2 + M$	1.00×10^{-11}	q,1
566	$^1SOP + M \rightarrow SOP + M$	1.00×10^{-11}	q,1
567	$^1SOQ + M \rightarrow SOQ + M$	1.00×10^{-11}	q,1
568	$^1SO_2 + h\nu \rightarrow {}^3SO_2 + h\nu$	$1.50 \times 10^{+03}$	q,1
569	$^1SOP + h\nu \rightarrow {}^3SOP + h\nu$	$1.50 \times 10^{+03}$	q,1
570	$^1SOQ + h\nu \rightarrow {}^3SOQ + h\nu$	$1.50 \times 10^{+03}$	q,1
571	$^1SO_2 + h\nu \rightarrow SO_2 + h\nu$	$2.20 \times 10^{+04}$	q,1
572	$^1SOP + h\nu \rightarrow SOP + h\nu$	$2.20 \times 10^{+04}$	q,1
573	$^1SOQ + h\nu \rightarrow SOQ + h\nu$	$2.20 \times 10^{+04}$	q,1
574	$^1SO_2 + O_2 \rightarrow SO_3 + O$	1.00×10^{-16}	r,1

Rxn #	Reaction	Rate [$cm^3\ s^{-1}$]	Source
575	$^1SOP + O_2 \rightarrow SOOP + O$	1.00×10^{-16}	r,1
576	$^1SO_2 + OP \rightarrow SOOP + O$	$0.5 \times 1.00 \times 10^{-16}$	r,1
577	$^1SO_2 + OP \rightarrow SO_3 + P$	$0.5 \times 1.00 \times 10^{-16}$	r,1
578	$^1SOQ + O_2 \rightarrow SOOQ + O$	1.00×10^{-16}	r,1
579	$^1SO_2 + OQ \rightarrow SOOQ + O$	$0.5 \times 1.00 \times 10^{-16}$	r,1
580	$^1SO_2 + OQ \rightarrow SO_3 + Q$	$0.5 \times 1.00 \times 10^{-16}$	r,1
581	$^1SO_2 + SO_2 \rightarrow SO_3 + SO$	4.00×10^{-12}	q,1
582	$^1SOP + SO_2 \rightarrow SOOP + SO$	4.00×10^{-12}	q,1
583	$^1SO_2 + SOP \rightarrow SOOP + SO$	$0.5 \times 4.00 \times 10^{-12}$	q,1
584	$^1SO_2 + SOP \rightarrow SO_3 + SP$	$0.5 \times 4.00 \times 10^{-12}$	q,1
585	$^1SOQ + SO_2 \rightarrow SOOQ + SO$	4.00×10^{-12}	q,1
586	$^1SO_2 + SOQ \rightarrow SOOQ + SO$	$0.5 \times 4.00 \times 10^{-12}$	q,1
587	$^1SO_2 + SOQ \rightarrow SO_3 + SQ$	$0.5 \times 4.00 \times 10^{-12}$	q,1
588	$^3SO_2 + M \rightarrow SO_2 + M$	1.50×10^{-13}	q,1
589	$^3SOP + M \rightarrow SOP + M$	1.50×10^{-13}	q,1
590	$^3SOQ + M \rightarrow SOQ + M$	1.50×10^{-13}	q,1
591	$^3SO_2 + h\nu \rightarrow SO_2 + h\nu$	$1.13 \times 10^{+03}$	q,1
592	$^3SOP + h\nu \rightarrow SOP + h\nu$	$1.13 \times 10^{+03}$	q,1
593	$^3SOQ + h\nu \rightarrow SOQ + h\nu$	$1.13 \times 10^{+03}$	q,1
594	$^3SO_2 + SO_2 \rightarrow SO_3 + SO$	7.00×10^{-14}	q,1
595	$^3SOP + SO_2 \rightarrow SOOP + SO$	7.00×10^{-14}	q,1
596	$^3SO_2 + SOP \rightarrow SOOP + SO$	$0.5 \times 7.00 \times 10^{-14}$	q,1
597	$^3SO_2 + SOP \rightarrow SO_3 + SP$	$0.5 \times 7.00 \times 10^{-14}$	q,1
598	$^3SOQ + SO_2 \rightarrow SOOQ + SO$	7.00×10^{-14}	q,1
599	$^3SO_2 + SOQ \rightarrow SOOQ + SO$	$0.5 \times 7.00 \times 10^{-14}$	q,1
600	$^3SO_2 + SOQ \rightarrow SO_3 + SQ$	$0.5 \times 7.00 \times 10^{-14}$	q,1
601	$SO + NO_2 \rightarrow SO_2 + NO$	1.40×10^{-11}	A,1

Rxn #	Reaction	Rate [$cm^3\ s^{-1}$]	Source
602	$SP + NO_2 \rightarrow SOP + NO$	1.40×10^{-11}	*A*,1
603	$SO + NOP \rightarrow SOP + NO$	$0.5 \times 1.40 \times 10^{-11}$	*A*,1
604	$SO + NOP \rightarrow SO_2 + NP$	$0.5 \times 1.40 \times 10^{-11}$	*A*,1
605	$SQ + NO_2 \rightarrow SOQ + NO$	1.40×10^{-11}	*A*,1
606	$SO + NOQ \rightarrow SOQ + NO$	$0.5 \times 1.40 \times 10^{-11}$	*A*,1
607	$SO + NOQ \rightarrow SO_2 + NQ$	$0.5 \times 1.40 \times 10^{-11}$	*A*,1
608	$SO + O_3 \rightarrow SO_2 + O_2$	$3.40 \times 10^{-12} \cdot \exp(-1100.0/T)$	*A*,1
609	$SP + O_3 \rightarrow SOP + O_2$	$3.40 \times 10^{-12} \cdot \exp(-1100.0/T)$	*A*,1
610	$SO + OOP \rightarrow SOP + O_2$	$0.3333333 \times 3.40 \times 10^{-12} \cdot \exp(-1100.0/T)$	*A*,1
611	$SO + OOP \rightarrow SO_2 + OP$	$0.6666667 \times 3.40 \times 10^{-12} \cdot \exp(-1100.0/T)$	*A*,1
612	$SQ + O_3 \rightarrow SOQ + O_2$	$3.40 \times 10^{-12} \cdot \exp(-1100.0/T)$	*A*,1
613	$SO + OOQ \rightarrow SOQ + O_2$	$0.3333333 \times 3.40 \times 10^{-12} \cdot \exp(-1100.0/T)$	*A*,1
614	$SO + OOQ \rightarrow SO_2 + OQ$	$0.6666667 \times 3.40 \times 10^{-12} \cdot \exp(-1100.0/T)$	*A*,1
615	$HO_2 + SO_2 \rightarrow SO_3 + OH$	1.00×10^{-18}	*A*,1
616	$HOP + SO_2 \rightarrow SOOP + OH$	$0.5 \times 1.00 \times 10^{-18}$	*A*,1
617	$HOP + SO_2 \rightarrow SO_3 + PH$	$0.5 \times 1.00 \times 10^{-18}$	*A*,1
618	$HO_2 + SOP \rightarrow SOOP + OH$	1.00×10^{-18}	*A*,1
619	$HOQ + SO_2 \rightarrow SOOQ + OH$	$0.5 \times 1.00 \times 10^{-18}$	*A*,1
620	$HOQ + SO_2 \rightarrow SO_3 + QH$	$0.5 \times 1.00 \times 10^{-18}$	*A*,1
621	$HO_2 + SOQ \rightarrow SOOQ + OH$	1.00×10^{-18}	*A*,1
622	$HS + O_3 \rightarrow HSO + O_2$	$9.00 \times 10^{-12} \cdot \exp(-280.0/T)$	*A*,1
623	$HS + OOP \rightarrow HSP + O_2$	$0.3333333 \times 9.00 \times 10^{-12} \cdot \exp(-280.0/T)$	*A*,1
624	$HS + OOP \rightarrow HSO + OP$	$0.6666667 \times 9.00 \times 10^{-12} \cdot \exp(-280.0/T)$	*A*,1
625	$HS + OOQ \rightarrow HSQ + O_2$	$0.3333333 \times 9.00 \times 10^{-12} \cdot \exp(-280.0/T)$	*A*,1
626	$HS + OOQ \rightarrow HSO + OQ$	$0.6666667 \times 9.00 \times 10^{-12} \cdot \exp(-280.0/T)$	*A*,1
627	$HS + NO_2 \rightarrow HSO + NO$	$2.90 \times 10^{-11} \cdot \exp(250.0/T)$	*A*,1
628	$HS + NOP \rightarrow HSP + NO$	$0.5 \times 2.90 \times 10^{-11} \cdot \exp(250.0/T)$	*A*,1

Rxn #	Reaction	Rate [$cm^3\ s^{-1}$]	Source
629	$HS + NOP \rightarrow HSO + NP$	$0.5 \times 2.90 \times 10^{-11} \cdot \exp(250.0/T)$	A,1
630	$HS + NOQ \rightarrow HSQ + NO$	$0.5 \times 2.90 \times 10^{-11} \cdot \exp(250.0/T)$	A,1
631	$HS + NOQ \rightarrow HSO + NQ$	$0.5 \times 2.90 \times 10^{-11} \cdot \exp(250.0/T)$	A,1
632	$S + O_3 \rightarrow SO + O_2$	1.20×10^{-11}	A,1
633	$S + OOP \rightarrow SP + O_2$	$0.3333333 \times 1.20 \times 10^{-11}$	A,1
634	$S + OOP \rightarrow SO + OP$	$0.6666667 \times 1.20 \times 10^{-11}$	A,1
635	$S + OOQ \rightarrow SQ + O_2$	$0.3333333 \times 1.20 \times 10^{-11}$	A,1
636	$S + OOQ \rightarrow SO + OQ$	$0.6666667 \times 1.20 \times 10^{-11}$	A,1
637	$SO + SO \rightarrow SO_2 + S$	2.00×10^{-15}	s,1
638	$SO + SP \rightarrow SOP + S$	4.00×10^{-15}	s,1
639	$SO + SQ \rightarrow SOQ + S$	4.00×10^{-15}	s,1
640	$SO_3 + SO \rightarrow SO_2 + SO_2$	2.00×10^{-15}	t,1
641	$SOOP + SO \rightarrow SO_2 + SOP$	2.00×10^{-15}	t,1
642	$SO_3 + SP \rightarrow SO_2 + SOP$	2.00×10^{-15}	t,1
643	$SOOQ + SO \rightarrow SO_2 + SOQ$	2.00×10^{-15}	t,1
644	$SO_3 + SQ \rightarrow SO_2 + SOQ$	2.00×10^{-15}	t,1
645	$S + CO_2 \rightarrow SO + CO$	1.00×10^{-20}	u,1
646	$S + COP \rightarrow SP + CO$	$0.5 \times 1.00 \times 10^{-20}$	u,1
647	$S + COP \rightarrow SO + CP$	$0.5 \times 1.00 \times 10^{-20}$	u,1
648	$S + COQ \rightarrow SQ + CO$	$0.5 \times 1.00 \times 10^{-20}$	u,1
649	$S + COQ \rightarrow SO + CQ$	$0.5 \times 1.00 \times 10^{-20}$	u,1
650	$HCO + SO \rightarrow HSO + CO$	5.20×10^{-12}	v,1
651	$HCP + SO \rightarrow HSO + CP$	5.20×10^{-12}	v,1
652	$HCO + SP \rightarrow HSP + CO$	5.20×10^{-12}	v,1
653	$HCQ + SO \rightarrow HSO + CQ$	5.20×10^{-12}	v,1
654	$HCO + SQ \rightarrow HSQ + CO$	5.20×10^{-12}	v,1

Rxn #	Reaction	Rate [cm^3 s^{-1}]	Source
655	H + SO → HSO	$k_0 = 4.40 \times 10^{-32} \cdot (T/300)^{-1.3}$ $k_\infty = 7.50 \times 10^{-11} \cdot (T/300)^{0.2}$	*w*,2
656	H + SP → HSP	$k_0 = 4.40 \times 10^{-32} \cdot (T/300)^{-1.3}$ $k_\infty = 7.50 \times 10^{-11} \cdot (T/300)^{0.2}$	*w*,2
657	H + SQ → HSQ	$k_0 = 4.40 \times 10^{-32} \cdot (T/300)^{-1.3}$ $k_\infty = 7.50 \times 10^{-11} \cdot (T/300)^{0.2}$	*w*,2
658	HSO + hν → HS + O	$2.13 \times 10^{+02}$	*x*,3
659	HSP + hν → HS + P	$1.38 \times 10^{+03}$	*x*,3
660	HSQ + hν → HS + Q	4.96×10^{-01}	*x*,3
661	HSO + NO → HNO + SO	1.00×10^{-15}	*J*,1
662	HSP + NO → HNO + SP	1.00×10^{-15}	*J*,1
663	HSO + NP → HNP + SO	1.00×10^{-15}	*J*,1
664	HSQ + NO → HNO + SQ	1.00×10^{-15}	*J*,1
665	HSO + NQ → HNQ + SO	1.00×10^{-15}	*J*,1
666	HSO + OH → H_2O + SO	$4.80 \times 10^{-11} \cdot \exp(250.0/T)$	*y*,1
667	HSP + OH → H_2O + SP	$4.80 \times 10^{-11} \cdot \exp(250.0/T)$	*y*,1
668	HSO + PH → H_2P + SO	$4.80 \times 10^{-11} \cdot \exp(250.0/T)$	*y*,1
669	HSQ + OH → H_2O + SQ	$4.80 \times 10^{-11} \cdot \exp(250.0/T)$	*y*,1
670	HSO + QH → H_2Q + SO	$4.80 \times 10^{-11} \cdot \exp(250.0/T)$	*y*,1
671	HSO + H → S + H_2O	1.60×10^{-12}	*z*,1
672	HSP + H → S + H_2P	1.60×10^{-12}	*z*,1
673	HSQ + H → S + H_2Q	1.60×10^{-12}	*z*,1
674	HSO + H → HS + OH	7.20×10^{-11}	*z*,1
675	HSP + H → HS + PH	7.20×10^{-11}	*z*,1
676	HSQ + H → HS + QH	7.20×10^{-11}	*z*,1
677	HSO + H → H_2 + SO	6.90×10^{-12}	*z*,1

Rxn #	Reaction	Rate [cm^3 s^{-1}]	Source
678	HSP + H → H_2 + SP	6.90×10^{-12}	*z*,1
679	HSQ + H → H_2 + SQ	6.90×10^{-12}	*z*,1
680	HSO + HS → H_2S + SO	3.00×10^{-11}	*Á*,1
681	HSP + HS → H_2S + SP	3.00×10^{-11}	*Á*,1
682	HSQ + HS → H_2S + SQ	3.00×10^{-11}	*Á*,1
683	HSO + O → OH + SO	$3.00 \times 10^{-11} \cdot \exp(200.0/T)$	*Â*,1
684	HSP + O → OH + SP	$3.00 \times 10^{-11} \cdot \exp(200.0/T)$	*Â*,1
685	HSO + P → PH + SO	$3.00 \times 10^{-11} \cdot \exp(200.0/T)$	*Â*,1
686	HSQ + O → OH + SQ	$3.00 \times 10^{-11} \cdot \exp(200.0/T)$	*Â*,1
687	HSO + Q → QH + SO	$3.00 \times 10^{-11} \cdot \exp(200.0/T)$	*Â*,1
688	HSO + S → HS + SO	3.00×10^{-11}	*a*,1
689	HSP + S → HS + SP	3.00×10^{-11}	*a*,1
690	HSQ + S → HS + SQ	3.00×10^{-11}	*a*,1
691	H + OCS → CO + HS	$9.07 \times 10^{-12} \cdot \exp(-1940.0/T)$	*Ã*,1
692	H + PCS → CP + HS	$9.07 \times 10^{-12} \cdot \exp(-1940.0/T)$	*Ã*,1
693	H + QCS → CQ + HS	$9.07 \times 10^{-12} \cdot \exp(-1940.0/T)$	*Ã*,1
694	HS + CO → OCS + H	$4.15 \times 10^{-14} \cdot \exp(-7660.0/T)$	*Ä*,1
695	HS + CP → PCS + H	$4.15 \times 10^{-14} \cdot \exp(-7660.0/T)$	*Ä*,1
696	HS + CQ → QCS + H	$4.15 \times 10^{-14} \cdot \exp(-7660.0/T)$	*Ä*,1
697	$O(^1D)$ + OCS → CO + SO	3.00×10^{-10}	*Å*,1
698	$P(^1D)$ + OCS → CO + SP	3.00×10^{-10}	*Å*,1
699	$O(^1D)$ + PCS → CP + SO	3.00×10^{-10}	*Å*,1
700	$Q(^1D)$ + OCS → CO + SQ	3.00×10^{-10}	*Å*,1
701	$O(^1D)$ + QCS → CQ + SO	3.00×10^{-10}	*Å*,1
702	O + OCS → CO + SO	$2.10 \times 10^{-11} \cdot \exp(-2200.0/T)$	*A*,1
703	P + OCS → CO + SP	$2.10 \times 10^{-11} \cdot \exp(-2200.0/T)$	*A*,1

Rxn #	Reaction	Rate [cm^3 s^{-1}]	Source
704	O + PCS → CP + SO	$2.10 \times 10^{-11} \cdot \exp(-2200.0/T)$	*A*,1
705	Q + OCS → CO + SQ	$2.10 \times 10^{-11} \cdot \exp(-2200.0/T)$	*A*,1
706	O + QCS → CQ + SO	$2.10 \times 10^{-11} \cdot \exp(-2200.0/T)$	*A*,1
707	O + OCS → S + CO_2	$8.33 \times 10^{-11} \cdot \exp(-5530.0/T)$	*A*,1
708	O + PCS → S + COP	$8.33 \times 10^{-11} \cdot \exp(-5530.0/T)$	*A*,1
709	P + OCS → S + COP	$8.33 \times 10^{-11} \cdot \exp(-5530.0/T)$	*A*,1
710	O + QCS → S + COQ	$8.33 \times 10^{-11} \cdot \exp(-5530.0/T)$	*A*,1
711	Q + OCS → S + COQ	$8.33 \times 10^{-11} \cdot \exp(-5530.0/T)$	*A*,1
712	OCS + S → CO + S_2	$1.90 \times 10^{-14} \cdot (T/300)^{3.97} \cdot \exp(-580.0/T)$	Æ,1
713	PCS + S → CP + S_2	$1.90 \times 10^{-14} \cdot (T/300)^{3.97} \cdot \exp(-580.0/T)$	Æ,1
714	QCS + S → CQ + S_2	$1.90 \times 10^{-14} \cdot (T/300)^{3.97} \cdot \exp(-580.0/T)$	Æ,1
715	OH + OCS → CO_2 + HS	$7.20 \times 10^{-14} \cdot \exp(-1070.0/T)$	*J*,1
716	PH + OCS → COP + HS	$7.20 \times 10^{-14} \cdot \exp(-1070.0/T)$	*J*,1
717	OH + PCS → COP + HS	$7.20 \times 10^{-14} \cdot \exp(-1070.0/T)$	*J*,1
718	QH + OCS → COQ + HS	$7.20 \times 10^{-14} \cdot \exp(-1070.0/T)$	*J*,1
719	OH + QCS → COQ + HS	$7.20 \times 10^{-14} \cdot \exp(-1070.0/T)$	*J*,1
720	CO + S → OCS	$k_0 = 6.51 \times 10^{-33} \cdot \exp(-2188.0/T)$ $k_\infty = 1.00 \times 10^{-10}$	Ç,2
721	CP + S → PCS	$k_0 = 6.51 \times 10^{-33} \cdot \exp(-2188.0/T)$ $k_\infty = 1.00 \times 10^{-10}$	Ç,2
722	CQ + S → QCS	$k_0 = 6.51 \times 10^{-33} \cdot \exp(-2188.0/T)$ $k_\infty = 1.00 \times 10^{-10}$	Ç,2
723	OCS + hν → CO + S	$1.71 \times 10^{+00}$	*E*,3
724	PCS + hν → CP + S	$2.47 \times 10^{+00}$	*E*,3
725	QCS + hν → CQ + S	$9.15 \times 10^{+00}$	*E*,3
726	HO_2 + H_2S → H_2O + HSO	3.00×10^{-15}	*J*,1

Rxn #	Reaction	Rate [$cm^3\ s^{-1}$]	Source
727	$HOP + H_2S \rightarrow H_2P + HSO$	$0.5 \times 3.00 \times 10^{-15}$	*J*,1
728	$HOP + H_2S \rightarrow H_2O + HSP$	$0.5 \times 3.00 \times 10^{-15}$	*J*,1
729	$HOQ + H_2S \rightarrow H_2Q + HSO$	$0.5 \times 3.00 \times 10^{-15}$	*J*,1
730	$HOQ + H_2S \rightarrow H_2O + HSQ$	$0.5 \times 3.00 \times 10^{-15}$	*J*,1
731	$OCS + S \rightarrow OCS_2$	$k_0 = 9.72 \times 10^{-25} \cdot (T/300)^{-6.98} \cdot \exp(-6046.0/T)$ $k_\infty = 3.50 \times 10^{-11} \cdot (T/300)^{-8.22} \cdot \exp(-4206.0/T)$	Æ,2
732	$PCS + S \rightarrow PCS2$	$k_0 = 9.72 \times 10^{-25} \cdot (T/300)^{-6.98} \cdot \exp(-6046.0/T)$ $k_\infty = 3.50 \times 10^{-11} \cdot (T/300)^{-8.22} \cdot \exp(-4206.0/T)$	Æ,2
733	$QCS + S \rightarrow QCS2$	$k_0 = 9.72 \times 10^{-25} \cdot (T/300)^{-6.98} \cdot \exp(-6046.0/T)$ $k_\infty = 3.50 \times 10^{-11} \cdot (T/300)^{-8.22} \cdot \exp(-4206.0/T)$	Æ,2
734	$OCS_2 + S \rightarrow OCS + S_2$	5.00×10^{-12}	*È*,1
735	$PCS2 + S \rightarrow PCS + S_2$	5.00×10^{-12}	*È*,1
736	$QCS2 + S \rightarrow QCS + S_2$	5.00×10^{-12}	*È*,1
737	$S_3 + O \rightarrow S_2 + SO$	1.00×10^{-16}	*É*,1
738	$S_3 + P \rightarrow S_2 + SP$	1.00×10^{-16}	*É*,1
739	$S_3 + Q \rightarrow S_2 + SQ$	1.00×10^{-16}	*É*,1
740	$S_4 + O \rightarrow S_3 + SO$	1.00×10^{-16}	*É*,1
741	$S_4 + P \rightarrow S_3 + SP$	1.00×10^{-16}	*É*,1
742	$S_4 + Q \rightarrow S_3 + SQ$	1.00×10^{-16}	*É*,1
743	$OCS_2 + CO \rightarrow OCS + OCS$	3.00×10^{-12}	*Á*,1
744	$PCS2 + CO \rightarrow OCS + PCS$	3.00×10^{-12}	*Á*,1
745	$OCS_2 + CP \rightarrow OCS + PCS$	3.00×10^{-12}	*Á*,1
746	$QCS2 + CO \rightarrow OCS + QCS$	3.00×10^{-12}	*Á*,1
747	$OCS_2 + CQ \rightarrow OCS + QCS$	3.00×10^{-12}	*Á*,1
748	$C_2H_5 + H \rightarrow CH_3 + CH_3$	6.00×10^{-11}	*B*,1

Rxn #	Reaction	Rate [$cm^3\ s^{-1}$]	Source
749	$C_2H_5 + O \rightarrow CH_3 + HCO + H$	3.00×10^{-11}	$\hat{E}$,1
750	$C_2H_5 + P \rightarrow CH_3 + HCP + H$	3.00×10^{-11}	$\hat{E}$,1
751	$C_2H_5 + Q \rightarrow CH_3 + HCQ + H$	3.00×10^{-11}	$\hat{E}$,1
752	$C_2H_5 + OH \rightarrow CH_3 + HCO + H_2$	4.00×10^{-11}	$\ddot{E}$,1
753	$C_2H_5 + PH \rightarrow CH_3 + HCP + H_2$	4.00×10^{-11}	$\ddot{E}$,1
754	$C_2H_5 + QH \rightarrow CH_3 + HCQ + H_2$	4.00×10^{-11}	$\ddot{E}$,1
755	$CH_4 + h\nu \rightarrow {}^1CH_2 + H_2$	1.36×10^{-07}	E,3
756	$CH_4 + h\nu \rightarrow CH_3 + H$	5.61×10^{-11}	E,3
757	$CH_4 + h\nu \rightarrow {}^3CH_2 + H + H$	5.61×10^{-11}	E,3
758	$O + HNO_3 \rightarrow OH + NO_3$	3.00×10^{-17}	A,1
759	$P + HNO_3 \rightarrow PH + NO_3$	3.00×10^{-17}	A,1
760	$O + HNOOP \rightarrow OH + NOOP$	3.00×10^{-17}	A,1
761	$Q + HNO_3 \rightarrow QH + NO_3$	3.00×10^{-17}	A,1
762	$O + HNOOQ \rightarrow OH + NOOQ$	3.00×10^{-17}	A,1
763	$O + N_2O_5 \rightarrow NO_2 + NO_2 + O_2$	3.00×10^{-16}	A,1
764	$P + N_2O_5 \rightarrow NO_2 + NO_2 + OP$	3.00×10^{-16}	A,1
765	$O + N_2O_4P \rightarrow NOP + NO_2 + O_2$	$0.8 \times 3.00 \times 10^{-16}$	A,1
766	$O + N_2O_4P \rightarrow NO_2 + NO_2 + OP$	$0.2 \times 3.00 \times 10^{-16}$	A,1
767	$Q + N_2O_5 \rightarrow NO_2 + NO_2 + OQ$	3.00×10^{-16}	A,1
768	$O + N_2O_4Q \rightarrow NOQ + NO_2 + O_2$	$0.8 \times 3.00 \times 10^{-16}$	A,1
769	$O + N_2O_4Q \rightarrow NO_2 + NO_2 + OQ$	$0.2 \times 3.00 \times 10^{-16}$	A,1
770	$NO_2 + NO_3 \rightarrow N_2O_5$	$\begin{cases} k_0 = 2.40 \times 10^{-30} \cdot (T/300)^{-3} \\ k_\infty = 1.60 \times 10^{-12} \cdot (T/300)^{-0.1} \end{cases}$	A,2
771	$NOP + NO_3 \rightarrow N_2O_4P$	$\begin{cases} k_0 = 2.40 \times 10^{-30} \cdot (T/300)^{-3} \\ k_\infty = 1.60 \times 10^{-12} \cdot (T/300)^{-0.1} \end{cases}$	A,2

Rxn #	Reaction	Rate [$cm^3\ s^{-1}$]	Source
772	$NO_2 + NOOP \rightarrow N_2O_4P$	$k_0 = 2.40 \times 10^{-30} \cdot (T/300)^{-3}$ $k_\infty = 1.60 \times 10^{-12} \cdot (T/300)^{-0.1}$	*A*,2
773	$NOQ + NO_3 \rightarrow N_2O_4Q$	$k_0 = 2.40 \times 10^{-30} \cdot (T/300)^{-3}$ $k_\infty = 1.60 \times 10^{-12} \cdot (T/300)^{-0.1}$	*A*,2
774	$NO_2 + NOOQ \rightarrow N_2O_4Q$	$k_0 = 2.40 \times 10^{-30} \cdot (T/300)^{-3}$ $k_\infty = 1.60 \times 10^{-12} \cdot (T/300)^{-0.1}$	*A*,2
775	$N_2O_5 + M \rightarrow NO_3 + NO_2 + M$	see IUPAC datasheet	*Ì*
776	$N_2O_4P + M \rightarrow NOOP + NO_2 + M$		*Ì*
777	$N_2O_4P + M \rightarrow NO_3 + NOP + M$		*Ì*
778	$N_2O_4Q + M \rightarrow NOOQ + NO_2 + M$		*Ì*
779	$N_2O_4Q + M \rightarrow NO_3 + NOQ + M$		*Ì*
780	$NO_2 + NO_3 \rightarrow NO + NO_2 + O_2$	$4.50 \times 10^{-14} \cdot \exp(-1260.0/T)$	*A*,1
781	$NOP + NO_3 \rightarrow NO + NO_2 + OP$	$0.5 \times 4.50 \times 10^{-14} \cdot \exp(-1260.0/T)$	*A*,1
782	$NOP + NO_3 \rightarrow NP + NO_2 + O_2$	$0.5 \times 4.50 \times 10^{-14} \cdot \exp(-1260.0/T)$	*A*,1
783	$NO_2 + NOOP \rightarrow NO + NOP + O_2$	$0.6666667 \times 4.50 \times 10^{-14} \cdot \exp(-1260.0/T)$	*A*,1
784	$NO_2 + NOOP \rightarrow NO + NO_2 + OP$	$0.3333333 \times 4.50 \times 10^{-14} \cdot \exp(-1260.0/T)$	*A*,1
785	$NOQ + NO_3 \rightarrow NO + NO_2 + OQ$	$0.5 \times 4.50 \times 10^{-14} \cdot \exp(-1260.0/T)$	*A*,1
786	$NOQ + NO_3 \rightarrow NQ + NO_2 + O_2$	$0.5 \times 4.50 \times 10^{-14} \cdot \exp(-1260.0/T)$	*A*,1
787	$NO_2 + NOOQ \rightarrow NO + NOQ + O_2$	$0.6666667 \times 4.50 \times 10^{-14} \cdot \exp(-1260.0/T)$	*A*,1
788	$NO_2 + NOOQ \rightarrow NO + NO_2 + OQ$	$0.3333333 \times 4.50 \times 10^{-14} \cdot \exp(-1260.0/T)$	*A*,1
789	$NO_2 + O_3 \rightarrow NO_3 + O_2$	$1.20 \times 10^{-13} \cdot \exp(-2450.0/T)$	*A*,1
790	$NOP + O_3 \rightarrow NOOP + O_2$	$1.20 \times 10^{-13} \cdot \exp(-2450.0/T)$	*A*,1
791	$NO_2 + OOP \rightarrow NOOP + O_2$	$0.3333333 \times 1.20 \times 10^{-13} \cdot \exp(-2450.0/T)$	*A*,1
792	$NO_2 + OOP \rightarrow NO_3 + OP$	$0.6666667 \times 1.20 \times 10^{-13} \cdot \exp(-2450.0/T)$	*A*,1
793	$NOQ + O_3 \rightarrow NOOQ + O_2$	$1.20 \times 10^{-13} \cdot \exp(-2450.0/T)$	*A*,1

Rxn #	Reaction	Rate [$cm^3\ s^{-1}$]	Source
794	$NO_2 + OOQ \rightarrow NOOQ + O_2$	$0.3333333 \times 1.20 \times 10^{-13} \cdot \exp(-2450.0/T)$	*A*,1
795	$NO_2 + OOQ \rightarrow NO_3 + OQ$	$0.6666667 \times 1.20 \times 10^{-13} \cdot \exp(-2450.0/T)$	*A*,1
796	$NO_3 + NO_3 \rightarrow NO_2 + NO_2 + O_2$	$8.50 \times 10^{-13} \cdot \exp(-2450.0/T)$	*A*,1
797	$NO_3 + NOOP \rightarrow NOP + NO_2 + O_2$	$0.6666667 \times 1.70 \times 10^{-12} \cdot \exp(-2450.0/T)$	*A*,1
798	$NO_3 + NOOP \rightarrow NO_2 + NO_2 + OP$	$0.3333333 \times 1.70 \times 10^{-12} \cdot \exp(-2450.0/T)$	*A*,1
799	$NO_3 + NOOQ \rightarrow NOQ + NO_2 + O_2$	$0.6666667 \times 1.70 \times 10^{-12} \cdot \exp(-2450.0/T)$	*A*,1
800	$NO_3 + NOOQ \rightarrow NO_2 + NO_2 + OQ$	$0.3333333 \times 1.70 \times 10^{-12} \cdot \exp(-2450.0/T)$	*A*,1
801	$HO_2 + NO_2 \rightarrow HO_2NO_2$	$k_0 = 1.90 \times 10^{-31} \cdot (T/300)^{-3.4}$ $k_\infty = 4.00 \times 10^{-12} \cdot (T/300)^{-0.3}$	*A*,2
802	$HOP + NO_2 \rightarrow HO_2NOP$	$k_0 = 1.90 \times 10^{-31} \cdot (T/300)^{-3.4}$ $k_\infty = 4.00 \times 10^{-12} \cdot (T/300)^{-0.3}$	*A*,2
803	$HO_2 + NOP \rightarrow HO_2NOP$	$k_0 = 1.90 \times 10^{-31} \cdot (T/300)^{-3.4}$ $k_\infty = 4.00 \times 10^{-12} \cdot (T/300)^{-0.3}$	*A*,2
804	$HOQ + NO_2 \rightarrow HO_2NOQ$	$k_0 = 1.90 \times 10^{-31} \cdot (T/300)^{-3.4}$ $k_\infty = 4.00 \times 10^{-12} \cdot (T/300)^{-0.3}$	*A*,2
805	$HO_2 + NOQ \rightarrow HO_2NOQ$	$k_0 = 1.90 \times 10^{-31} \cdot (T/300)^{-3.4}$ $k_\infty = 4.00 \times 10^{-12} \cdot (T/300)^{-0.3}$	*A*,2
806	$O + HO_2NO_2 \rightarrow OH + NO_2 + O_2$	$7.80 \times 10^{-11} \cdot \exp(-3400.0/T)$	*J*,1
807	$P + HO_2NO_2 \rightarrow PH + NO_2 + O_2$	$7.80 \times 10^{-11} \cdot \exp(-3400.0/T)$	*J*,1
808	$O + HO_2NOP \rightarrow OH + NOP + O_2$	$0.5 \times 7.80 \times 10^{-11} \cdot \exp(-3400.0/T)$	*J*,1
809	$O + HO_2NOP \rightarrow OH + NO_2 + OP$	$0.5 \times 7.80 \times 10^{-11} \cdot \exp(-3400.0/T)$	*J*,1
810	$Q + HO_2NO_2 \rightarrow QH + NO_2 + O_2$	$7.80 \times 10^{-11} \cdot \exp(-3400.0/T)$	*J*,1
811	$O + HO_2NOQ \rightarrow OH + NOQ + O_2$	$0.5 \times 7.80 \times 10^{-11} \cdot \exp(-3400.0/T)$	*J*,1
812	$O + HO_2NOQ \rightarrow OH + NO_2 + OQ$	$0.5 \times 7.80 \times 10^{-11} \cdot \exp(-3400.0/T)$	*J*,1
813	$OH + HO_2NO_2 \rightarrow H_2O + NO_2 + O_2$	$1.30 \times 10^{-12} \cdot \exp(380.0/T)$	*J*,1

Rxn #	Reaction	Rate [$cm^3\ s^{-1}$]	Source
814	$PH + HO_2NO_2 \rightarrow H_2P + NO_2 + O_2$	$1.30 \times 10^{-12} \cdot \exp(380.0/T)$	*J*,1
815	$OH + HO_2NOP \rightarrow H_2O + NOP + O_2$	$0.5 \times 1.30 \times 10^{-12} \cdot \exp(380.0/T)$	*J*,1
816	$OH + HO_2NOP \rightarrow H_2O + NO_2 + OP$	$0.5 \times 1.30 \times 10^{-12} \cdot \exp(380.0/T)$	*J*,1
817	$QH + HO_2NO_2 \rightarrow H_2Q + NO_2 + O_2$	$1.30 \times 10^{-12} \cdot \exp(380.0/T)$	*J*,1
818	$OH + HO_2NOQ \rightarrow H_2O + NOQ + O_2$	$0.5 \times 1.30 \times 10^{-12} \cdot \exp(380.0/T)$	*J*,1
819	$OH + HO_2NOQ \rightarrow H_2O + NO_2 + OQ$	$0.5 \times 1.30 \times 10^{-12} \cdot \exp(380.0/T)$	*J*,1
820	$HO_2NO_2 + M \rightarrow HO_2 + NO_2 + M$	see IUPAC datasheet	*Ì*
821	$HO_2NOP + M \rightarrow HOP + NO_2 + M$	HO2NOP represents HOPNO2 and HO2NOP.	*Ì*
822	$HO_2NOP + M \rightarrow HO_2 + NOP + M$	HO2NOP represents HOPNO2 and HO2NOP.	*Ì*
823	$HO_2NOQ + M \rightarrow HOQ + NO_2 + M$	HO2NOP represents HOPNO2 and HO2NOP.	*Ì*
824	$HO_2NOQ + M \rightarrow HO_2 + NOQ + M$	HO2NOP represents HOPNO2 and HO2NOP.	*Ì*
825	$HO_2NO_2 + h\nu \rightarrow HO_2 + NO_2$	3.00×10^{-10}	*E*,3
826	$HO_2NO_2 + h\nu \rightarrow OH + NO_3$	3.00×10^{-10}	*E*,3
827	$HO_2NOP + h\nu \rightarrow HOP + NO_2$	$1.78 \times 10^{+06}$	*E*,3
828	$HO_2NOP + h\nu \rightarrow HO_2 + NOP$	$6.87 \times 10^{+02}$	*E*,3
829	$HO_2NOP + h\nu \rightarrow PH + NO_3$	$3.68 \times 10^{+03}$	*E*,3
830	$HO_2NOP + h\nu \rightarrow OH + NOOP$	$4.80 \times 10^{+05}$	*E*,3
831	$HO_2NOQ + h\nu \rightarrow HOQ + NO_2$	$6.17 \times 10^{+01}$	*E*,3
832	$HO_2NOQ + h\nu \rightarrow HO_2 + NOQ$	$2.46 \times 10^{+02}$	*E*,3
833	$HO_2NOQ + h\nu \rightarrow QH + NO_3$	$3.30 \times 10^{+02}$	*E*,3
834	$HO_2NOQ + h\nu \rightarrow OH + NOOQ$	$1.31 \times 10^{+03}$	*E*,3
835	$N_2O_5 + h\nu \rightarrow NO_3 + NO_2$	$1.23 \times 10^{+02}$	*E*,3
836	$N_2O_5 + h\nu \rightarrow NO_3 + NO + O$	$1.23 \times 10^{+02}$	*E*,3
837	$N_2O_4P + h\nu \rightarrow NOOP + NO_2$	$6.60 \times 10^{+02}$	*E*,3
838	$N_2O_4P + h\nu \rightarrow NO_3 + NOP$	$6.55 \times 10^{+02}$	*E*,3
839	$N_2O_4P + h\nu \rightarrow NOOP + NO + O$	$2.23 \times 10^{+06}$	*E*,3
840	$N_2O_4P + h\nu \rightarrow NO_3 + NP + O$	$7.94 \times 10^{+04}$	*E*,3

Rxn #	Reaction	Rate [$cm^3\ s^{-1}$]	Source
841	$N_2O_4P + h\nu \rightarrow NO_3 + NO + P$	$8.61 \times 10^{+02}$	*E*,3
842	$N_2O_4Q + h\nu \rightarrow NOOQ + NO_2$	$8.61 \times 10^{+02}$	*E*,3
843	$N_2O_4Q + h\nu \rightarrow NO_3 + NOQ$	$6.14 \times 10^{+01}$	*E*,3
844	$N_2O_4Q + h\nu \rightarrow NOOQ + NO + O$	$4.61 \times 10^{+03}$	*E*,3
845	$N_2O_4Q + h\nu \rightarrow NO_3 + NQ + O$	$4.61 \times 10^{+03}$	*E*,3
846	$N_2O_4Q + h\nu \rightarrow NO_3 + NO + Q$	$3.29 \times 10^{+02}$	*E*,3
847	$C_2H_6 + h\nu \rightarrow {}^3CH_2 + {}^3CH_2 + H_2$	$3.65 \times 10^{+01}$	*Í*,3
848	$C_2H_6 + h\nu \rightarrow CH_4 + {}^1CH_2$	1.41×10^{-02}	*Í*,3
849	$O + NO_3 \rightarrow O_2 + NO_2$	1.00×10^{-11}	*A*,1
850	$P + NO_3 \rightarrow OP + NO_2$	1.00×10^{-11}	*A*,1
851	$O + NOOP \rightarrow O_2 + NOP$	$0.6666667 \times 1.00 \times 10^{-11}$	*A*,1
852	$O + NOOP \rightarrow OP + NO_2$	$0.3333333 \times 1.00 \times 10^{-11}$	*A*,1
853	$Q + NO_3 \rightarrow OQ + NO_2$	1.00×10^{-11}	*A*,1
854	$O + NOOQ \rightarrow O_2 + NOQ$	$0.6666667 \times 1.00 \times 10^{-11}$	*A*,1
855	$O + NOOQ \rightarrow OQ + NO_2$	$0.3333333 \times 1.00 \times 10^{-11}$	*A*,1
856	$HO_2 + NO_3 \rightarrow OH + NO_2 + O_2$	3.50×10^{-12}	*A*,1
857	$HOP + NO_3 \rightarrow PH + NO_2 + O_2$	$0.5 \times 3.50 \times 10^{-12}$	*A*,1
858	$HOP + NO_3 \rightarrow OH + NO_2 + OP$	$0.5 \times 3.50 \times 10^{-12}$	*A*,1
859	$HO_2 + NOOP \rightarrow OH + NO_2 + OP$	$0.3333333 \times 3.50 \times 10^{-12}$	*A*,1
860	$HO_2 + NOOP \rightarrow OH + NOP + O_2$	$0.6666667 \times 3.50 \times 10^{-12}$	*A*,1
861	$HOQ + NO_3 \rightarrow QH + NO_2 + O_2$	$0.5 \times 3.50 \times 10^{-12}$	*A*,1
862	$HOQ + NO_3 \rightarrow OH + NO_2 + OQ$	$0.5 \times 3.50 \times 10^{-12}$	*A*,1
863	$HO_2 + NOOQ \rightarrow OH + NO_2 + OQ$	$0.3333333 \times 3.50 \times 10^{-12}$	*A*,1
864	$HO_2 + NOOQ \rightarrow OH + NOQ + O_2$	$0.6666667 \times 3.50 \times 10^{-12}$	*A*,1
865	$NO + NO_3 \rightarrow NO_2 + NO_2$	$1.50 \times 10^{-11} \cdot \exp(170.0/T)$	*A*,1
866	$NP + NO_3 \rightarrow NO_2 + NOP$	$1.50 \times 10^{-11} \cdot \exp(170.0/T)$	*A*,1
867	$NO + NOOP \rightarrow NO_2 + NOP$	$1.50 \times 10^{-11} \cdot \exp(170.0/T)$	*A*,1

Rxn #	Reaction	Rate [$cm^3\ s^{-1}$]	Source
868	$NQ + NO_3 \rightarrow NO_2 + NOQ$	$1.50 \times 10^{-11} \cdot \exp(170.0/T)$	*A*,1
869	$NO + NOOQ \rightarrow NO_2 + NOQ$	$1.50 \times 10^{-11} \cdot \exp(170.0/T)$	*A*,1
870	$O + NO_2 \rightarrow NO_3$	$k_0 = 2.50 \times 10^{-31} \cdot (T/300)^{-1.8}$ $k_\infty = 2.20 \times 10^{-11} \cdot (T/300)^{-0.7}$	*A*,2
871	$P + NO_2 \rightarrow NOOP$	$k_0 = 2.50 \times 10^{-31} \cdot (T/300)^{-1.8}$ $k_\infty = 2.20 \times 10^{-11} \cdot (T/300)^{-0.7}$	*A*,2
872	$O + NOP \rightarrow NOOP$	$k_0 = 2.50 \times 10^{-31} \cdot (T/300)^{-1.8}$ $k_\infty = 2.20 \times 10^{-11} \cdot (T/300)^{-0.7}$	*A*,2
873	$Q + NO_2 \rightarrow NOOQ$	$k_0 = 2.50 \times 10^{-31} \cdot (T/300)^{-1.8}$ $k_\infty = 2.20 \times 10^{-11} \cdot (T/300)^{-0.7}$	*A*,2
874	$O + NOQ \rightarrow NOOQ$	$k_0 = 2.50 \times 10^{-31} \cdot (T/300)^{-1.8}$ $k_\infty = 2.20 \times 10^{-11} \cdot (T/300)^{-0.7}$	*A*,2
875	$OH + NO_3 \rightarrow HO_2 + NO_2$	2.20×10^{-11}	*A*,1
876	$PH + NO_3 \rightarrow HOP + NO_2$	2.20×10^{-11}	*A*,1
877	$OH + NOOP \rightarrow HO_2 + NOP$	$0.6666667 \times 2.20 \times 10^{-11}$	*A*,1
878	$OH + NOOP \rightarrow HOP + NO_2$	$0.3333333 \times 2.20 \times 10^{-11}$	*A*,1
879	$QH + NO_3 \rightarrow HOQ + NO_2$	2.20×10^{-11}	*A*,1
880	$OH + NOOQ \rightarrow HO_2 + NOQ$	$0.6666667 \times 2.20 \times 10^{-11}$	*A*,1
881	$OH + NOOQ \rightarrow HOQ + NO_2$	$0.3333333 \times 2.20 \times 10^{-11}$	*A*,1
882	$NO_3 + h\nu \rightarrow NO + O_2$	7.48×10^{-02}	*E*,3
883	$NO_3 + h\nu \rightarrow NO_2 + O$	$2.71 \times 10^{+04}$	*E*,3
884	$NOOP + h\nu \rightarrow NP + O_2$	$5.15 \times 10^{+03}$	*E*,3
885	$NOOP + h\nu \rightarrow NO + OP$	$2.24 \times 10^{+01}$	*E*,3
886	$NOOP + h\nu \rightarrow NOP + O$	$1.12 \times 10^{+01}$	*E*,3
887	$NOOP + h\nu \rightarrow NO_2 + P$	$4.26 \times 10^{+00}$	*E*,3

Rxn #	Reaction	Rate [$cm^3\ s^{-1}$]	Source
888	$NOOQ + h\nu \rightarrow NQ + O_2$	$2.13 \times 10^{+00}$	*E*,3
889	$NOOQ + h\nu \rightarrow NO + OQ$	$1.20 \times 10^{+02}$	*E*,3
890	$NOOQ + h\nu \rightarrow NOQ + O$	$6.00 \times 10^{+01}$	*E*,3
891	$NOOQ + h\nu \rightarrow NO_2 + Q$	$2.28 \times 10^{+01}$	*E*,3
892	$N + NO_2 \rightarrow N_2O + O$	$5.80 \times 10^{-12} \cdot \exp(220.0/T)$	*A*,1
893	$N + NOP \rightarrow N2P + O$	$0.5 \times 5.80 \times 10^{-12} \cdot \exp(220.0/T)$	*A*,1
894	$N + NOP \rightarrow N_2O + P$	$0.5 \times 5.80 \times 10^{-12} \cdot \exp(220.0/T)$	*A*,1
895	$N + NOQ \rightarrow N2Q + O$	$0.5 \times 5.80 \times 10^{-12} \cdot \exp(220.0/T)$	*A*,1
896	$N + NOQ \rightarrow N_2O + Q$	$0.5 \times 5.80 \times 10^{-12} \cdot \exp(220.0/T)$	*A*,1
897	$O(^1D) + N_2 \rightarrow N_2O$	$k_0 = 2.80 \times 10^{-36} \cdot (T/300)^{-0.9}$ $k_\infty = 1.00 \times 10^{-10}$	*A*,2
898	$P(^1D) + N_2 \rightarrow N2P$	$k_0 = 2.80 \times 10^{-36} \cdot (T/300)^{-0.9}$ $k_\infty = 1.00 \times 10^{-10}$	*A*,2
899	$Q(^1D) + N_2 \rightarrow N2Q$	$k_0 = 2.80 \times 10^{-36} \cdot (T/300)^{-0.9}$ $k_\infty = 1.00 \times 10^{-10}$	*A*,2
900	$O(^1D) + N_2O \rightarrow N_2 + O_2$	$0.39 \times 1.19 \times 10^{-10} \cdot \exp(20.0/T)$	*A*,1
901	$P(^1D) + N_2O \rightarrow N_2 + OP$	$0.39 \times 1.19 \times 10^{-10} \cdot \exp(20.0/T)$	*A*,1
902	$O(^1D) + N2P \rightarrow N_2 + OP$	$0.39 \times 1.19 \times 10^{-10} \cdot \exp(20.0/T)$	*A*,1
903	$Q(^1D) + N_2O \rightarrow N_2 + OQ$	$0.39 \times 1.19 \times 10^{-10} \cdot \exp(20.0/T)$	*A*,1
904	$O(^1D) + N2Q \rightarrow N_2 + OQ$	$0.39 \times 1.19 \times 10^{-10} \cdot \exp(20.0/T)$	*A*,1
905	$O(^1D) + N_2O \rightarrow NO + NO$	$0.61 \times 1.19 \times 10^{-10} \cdot \exp(20.0/T)$	*A*,1
906	$P(^1D) + N_2O \rightarrow NO + NP$	$0.61 \times 1.19 \times 10^{-10} \cdot \exp(20.0/T)$	*A*,1
907	$O(^1D) + N2P \rightarrow NO + NP$	$0.61 \times 1.19 \times 10^{-10} \cdot \exp(20.0/T)$	*A*,1
908	$Q(^1D) + N_2O \rightarrow NO + NQ$	$0.61 \times 1.19 \times 10^{-10} \cdot \exp(20.0/T)$	*A*,1
909	$O(^1D) + N2Q \rightarrow NO + NQ$	$0.61 \times 1.19 \times 10^{-10} \cdot \exp(20.0/T)$	*A*,1
910	$N_2O + h\nu \rightarrow N_2 + O(^1D)$	$1.14 \times 10^{+01}$	*E*,3

Rxn #	Reaction	Rate [cm^3 s^{-1}]	Source
911	N2P + hν $\rightarrow$ N_2 + P(^{1}D)	1.16×10^{-10}	E,3
912	N2Q + hν $\rightarrow$ N_2 + Q(^{1}D)	9.07×10^{-14}	E,3
913	$^3CH_2$ + O $\rightarrow$ CO + H_2	$0.4 \times 3.40 \times 10^{-10} \cdot \exp(-270.0/T)$	G,1
914	$^3CH_2$ + P $\rightarrow$ CP + H_2	$0.4 \times 3.40 \times 10^{-10} \cdot \exp(-270.0/T)$	G,1
915	$^3CH_2$ + Q $\rightarrow$ CQ + H_2	$0.4 \times 3.40 \times 10^{-10} \cdot \exp(-270.0/T)$	G,1
916	CO_2 + O(^{1}D) $\rightarrow$ CO_2 + O	$7.50 \times 10^{-11} \cdot \exp(115.0/T)$	A,1
917	COP + O(^{1}D) $\rightarrow$ COP + O	$0.666666667 \times 7.50 \times 10^{-11} \cdot \exp(115.0/T)$	A,1
918	COP + O(^{1}D) $\rightarrow$ CO_2 + P	$0.333333333 \times 7.50 \times 10^{-11} \cdot \exp(115.0/T)$	A,1
919	CO_2 + P(^{1}D) $\rightarrow$ COP + O	$0.666666667 \times 7.50 \times 10^{-11} \cdot \exp(115.0/T)$	A,1
920	CO_2 + P(^{1}D) $\rightarrow$ CO_2 + P	$0.333333333 \times 7.50 \times 10^{-11} \cdot \exp(115.0/T)$	A,1
921	COQ + O(^{1}D) $\rightarrow$ COQ + O	$0.666666667 \times 7.50 \times 10^{-11} \cdot \exp(115.0/T)$	A,1
922	COQ + O(^{1}D) $\rightarrow$ CO_2 + Q	$0.333333333 \times 7.50 \times 10^{-11} \cdot \exp(115.0/T)$	A,1
923	CO_2 + Q(^{1}D) $\rightarrow$ COQ + O	$0.666666667 \times 7.50 \times 10^{-11} \cdot \exp(115.0/T)$	A,1
924	CO_2 + Q(^{1}D) $\rightarrow$ CO_2 + Q	$0.333333333 \times 7.50 \times 10^{-11} \cdot \exp(115.0/T)$	A,1
925	O + OP $\rightarrow$ P + O_2	$1.73 \times 10^{-12} \cdot (T/300)^{1.1} \cdot \exp(-16.8/T)$	$\hat{I}$,1
926	P + O_2 $\rightarrow$ O + OP	$3.40 \times 10^{-12} \cdot (T/300)^{1.1}$	$\hat{I}$,1
927	O + OQ $\rightarrow$ Q + O_2	$1.75 \times 10^{-12} \cdot (T/300)^{1.1} \cdot \exp(-32.0/T)$	$\hat{I}$,1
928	Q + O_2 $\rightarrow$ O + OQ	$3.40 \times 10^{-12} \cdot (T/300)^{1.1}$	$\hat{I}$,1
929	OP + CO_2 $\rightarrow$ O_2 + COP	$0.5 \times 2.00 \times 10^{-28}$	$\ddot{I}$,1
930	O_2 + COP $\rightarrow$ OP + CO_2	$0.5 \times 2.00 \times 10^{-28}$	$\ddot{I}$,1
931	OQ + CO_2 $\rightarrow$ O_2 + COQ	$0.5 \times 2.00 \times 10^{-28}$	$\ddot{I}$,1
932	O_2 + COQ $\rightarrow$ OQ + CO_2	$0.5 \times 2.00 \times 10^{-28}$	$\ddot{I}$,1

1: cm^3 $molecules^{-2}$ s^{-1}

2: These reaction rates take the form: k(M,T) = $k_0(T)[M]/[1 + k_0(T)[m]/k_\infty(T)] \cdot 0.6\hat{}[1 + [log_{10}[k_0(T)[M]/k_\infty(T)]]^2]^{-1}$, where $k_0(T)$ has units of cm^6 $molecules^{-2}$ s^{-1} and $k_\infty(T)$ has units of cm^3 $molecules^{-2}$ s^{-1}.

3: The photolysis rates presented here are taken from the uppermost layer in the model. Caution: the rates in the upper

atmosphere are not good indicators for rates in the lower atmosphere.

[A]JPL-18; [B]Baulch et al. (1992); [C]Campbell et al. (1972) ; high pressure rate assumed; [D]Allen and Frederick (1982); [E]JPL-06; [F]Slanger et al. 1972 ; high pressure rate assumed; [G]KIDA; [H]Pinto et al. [1980] (note this is photolysis); [I]Baulch et al. (1992); high pressure rate assumed; [J]JPL-18 ; products assumed; [K]Zahnle et al. (2006) - photolysis as 2BODY; [L]JPL-18 ; branching ratios adjusted; [M]Zhanle et al. (2006); [N]Baulch et al. (1994); [O]Tsang and Hampson (1986); [P]Krasnoperov et al. 2005 ; products assumed; [Q]Choi and Lin (2005); [R]Tsang and Hampson (1991); [S]Dammeier et al. (2007); [T]Tsang and Herron (1991); [U]Zahnle (1986); [V]Dillion et al. (2007) ; products assumed; [W]Baggot et al. (1987); [X]Zahnle (1986) estimated; [Y]Davidson et al. (1978); [Z]!Brune et al. 1983 - PRODUCTS ASSUMED; [a]Kasting (1990); [b]Singleton et al. (1988); [c]Pen et al. (1999); [d]Stachnik and Molina (1987); [e]Schofield (1973); Tiee (1981); [f]Tiee (1981); [g]Nicholas et al. (1979); [h]Loison et al. (2012); [i]Du et al. (2008) / Babikov et al. (2017); [j]Singleton (1998); [k]assumed equal to OH + H2CO; [l]Du et al. (2011); [m]Langford and Oldershaw (1972) ; high pressure limit assumed; [n]Assumed equal to S + S2; [o]Assumed equal to S2 + S2; [p]Pavlov et al (2001); [q]Turco et al. (1982); [r]Toon et al. (1987); [s]avg of Chung+1975 and Martinez+1983 measurements; [t]Chung et al. (1975); [u]Yung and DeMore (1982); [v]assumed equal to HCO + O2 → HO2 + CO; [w]assumed equal to H+O2+M → HO2+M; [x]assumed equal to HO2 + hv; [y]assumed same as OH + HO2 → H2O + O2; [z]Assumed same as H + HO2 → O + H2O; [Á]Zhanle et al. (2006), estimated; [Â]assumed same as O + HO2; [Ã]Lee et al. (1977); [Ä]Kurbanov et al. (1995); [Å]Gauthier et al. (1975); [Æ]Lu et al. (2006); [Ç]assumed equal to O + CO + M; [È]estimated from Basco et al. (1967); [É]Assumed equal to rate for S2+O; [Ê]Tsang and Hampson (1986) ; products assumed; [Ë]Zhanle et al. (2006), products assumed; [Ì]IUPAC; [Í]JPL-06; products assumed; [Î]Rate from Fleurat-Lessard et al. (2003); equilibrium constant for fractionation from Kaye and Strobel (1983); [Ï]Upper rate of O2(1D)+CO2 from JPL-18 assumed, corrected for larger mixing ratio of O2 wrt. O2(1D) (see Ch. 5);